Technical report

Backus-Gilbert footprint matching methodology applied on MWI and ICI observations

TR/BG/MWI-ICI Issue 1.0, Rev. 1

Contents

II Backus-Gilbert footprint matching methodology: Algorithm and toolbox description   47

III Application on MWI and ICI data   108

1 Executive summary

The Backus-Gilbert footprint matching methodology has been applied on the Micro-Wave Imager (MWI) and the Ice Cloud Imager (ICI), that are two instruments that will be flown on board of the EUMETSAT Polar System - Second Generation (EPS-SG) satellites. The MWI and ICI will be hosted on the same EPS-SG platforms, providing radiances at microwave (MW) and sub-mm-wave frequencies (MWI will have 18 frequency channels ranging from 18.7 to 183.31 GHz, and ICI 11 channels between 183.31 and 664 GHz). Both ICI and MWI will be conically scanning instruments having a novel scanning pattern designed to obtain footprint sizes between 10 to 50 km for the MWI channels and around 16 km for the ICI channels.

MWI / ICI will provide 1402 / 784 samples per scan and channel, and each channel provides a continues coverage of the swath (approximately 1500 km wide). The exact geolocation of coincident samples differs between channels, but the time integration of individual samples is performed over a time period shorter than the time period necessary to sweep a single projected field of view (FOV). This allows for a footprint matching procedure by remapping of the original data, in order to prepare the data for Level2 processing or Calibration and Validation activities (Cal/Val).

A toolbox for such remappings has been developed, and the toolbox is based on the Backus-Gilbert methodology ([Backus and Gilbert, 1970] [Stogryn, 1978]). In short, the Backus-Gilbert methodology can be used to obtain a set of optimal weighting coefficients for neighboring samples, to create a remapped representation of the data matching a specified target footprint. A remapped value is a linear weighted combination of data of the channel of concern. The weights are found, after a trade-off analysis, by minimization of a penalty function that considers both the effective noise of the remapped data and the fit to the target footprint. In general, the derivation of optimal set of weighting coefficients can be a computational demanding task, and these are channel specific, depends on both scan position and varies slightly with orbital variations. However, an "operational" footprint remapping can deploy a set of precalculated weighting coefficients, and that dramatically decrease the computational burden.

A simulated MWI and ICI Level1B dataset, covering four reference Metop-A orbits, has also been generated. The simulation takes into account of MWI and ICI instrument characteristics, attitude steering of the platform, surface emissivities and topography, absorption properties of atmospheric species, and cloud and precipitation. The toolbox and the simulated MWI and ICI Level1B dataset were further used for studying details, including various types of bias assessments, of the footprint matching application on MWI and ICI.

The study cover technical aspects of the remapping, e.g. identification of how many scan lines that need to taken into account in various type of remappings, how to treat the remapping around swath edges (the various channels have slightly different swath widths), and what type of simplifications that can be performed without introducing any significant errors. Prior to this study, it has been decided that MWI-3V and ICI-1 is the target channel of MWI and ICI, respectively, and the focus is therefore on the remapping onto the FOV(s) of these channels.

Some important aspects that have been resolved are:

- Minimum number of scans to include in the remapping calculation

- Generally, both effective noise and the fit error to the target footprint decreases by the inclusion of an increasing amount of samples in the remapping calculation. The fit-error is here of most concern, as a low noise error is less challenging to obtain (except for MWI-1 and MWI-2 channels). There is no strict requirement on the fit-error, but a reasonable aim is that the fit-error should be low within the -30 dB (main beam) footprint (semi-circular with a radius of around 50 and 25 km for MWI and ICI, respectively). This gives roughly that the footprints of the samples to be included should at least cover this footprint. The situation is different for remapping of MWI-1 and MWI-2 samples onto the MWI-3V FOV, where the resolution must be enhanced, and hence samples outside the "main beam" footprint must be included. The following recommendations are given:

- Remapping of samples from MWI channels (MWI-3 to MWI-18) onto MWI-3V FOV: all samples within 40 or 55 km from the geolocation of the target footprint (corresponding to 9 or 12 scan lines in the center part of the scan) is the minimum and recommended choice, respectively, to be included.

- Remapping of samples from MWI channels (MWI-1 to MWI-2) onto MWI-3V FOV: all samples within 90 km from the geolocation of the target footprint (corresponding to 20 scan lines in the center part of the scan) is recommended to be included. However, the performance of the remapping of samples from MWI-1 and MWI-2 channels onto the MWI-3V FOVs is limited. The remapping results in clear fit-errors, even within the main beam, and primarily only the resolution in the across-track direction was possible to enhance, while at the same time keeping the effective noise at an acceptable level. On top of this, the remapping here results in that relatively large sidelobes are introduced. The usefulness of these remapped observations, for Level2 processing, can therefore be questionable. An alternative approach can be to remap MWI-1 and MWI-2 samples onto a modified MWI-3V FOV, using the effective MWI-1V antenna pattern as target (i.e. not aiming for increasing the resolution).

- Remapping of samples from ICI channels and MWI-8 to MWI-18 channels onto ICI-1 FOV: all samples within 30 km from the geolocation of the target footprint (corresponding to 7 scan lines in the center part of the scan) is recommended to be included

- Treatment around swath edges and number of achievable FOVs

- ICI: samples from all channels can be remapped (without too high errors) onto ICI-1 FOVs for scan angles between about 59° to -59° (or sample numbers between about 64 and 721). The effective noise of the remapped observations are here well below the required Level1B noise levels. A remapping to every third scan position gives that the distance (center to center) and overlap between two such footprints is about 8.1 km and 40 %, respectively. This approximately match the along-track characteristic (the distance between two scan lines is about 9 km). This remapping frequency (every third scan position between scan position 64 and 721) results in 220 different FOVs per scan.

– MWI: samples from most MWI channels can be remapped onto MWI-3V FOVs for scan angles between about -66° to 65° (scan position 37 to 1273). The effective noise of the remapped observations are here well below the required Level1B noise levels for the MWI-3 to MWI-18 channels. The performance of the remapping of samples from MWI-1 and MWI-2 channels onto the MWI-3V FOVs is limited, as described above, but the performance is quite stable over most of the MWI-1V scan angle range of -66° to 65°, although some additional performance degradation is found above 62° (the performance is not symmetric around the two swath edges due to azimuth offset angles between the channels). The distance between two MWI-3V samples is about 1.6 km and a remapping to every sixth scan position results in that the separation between two FOVs approximately match the along-track separation, but it also results in a large overlap between two FOVs (about 65 %). A remapping to every eighth scan position gives that the distance (center to center) and overlap between two such footprints is about 12.8 km and just below 50 %, respectively. This remapping frequency (every 8th scan position between scan position 37 and 1273) results in 155 different FOVs per scan.

- Remapping sensitivity to orbital / yaw angle variations

  – The platform altitude varies between about 820 to 850 km throughout a given orbit, and the platform attitude will follow the local normal pointing law and the swath will be centered around the sub-nadir orbit track. It was found that an optimal set of weighting coefficients varies sightly throughput the orbit, but the errors introduced by neglecting this fact is negligible small for most situations. The orbital variation dependency can be understood as the optimal weights derived around a given position of the sensor and for a specific remapping results in that the target FOV(s) is matched at the surface (that is located a distance r from the sensor). Now, if these weights are applied at a different sensor position, e.g. at a position where the sensor altitude is greater, than the target footprint is still matched at a distance r from the sensor, but that is now not on the surface, but a bit above the surface. This has practically no impact if the "native" and target channels viewing angles are more or less identical (as e.g for ICI-1 and ICI-3). However, if these viewing angles differs, it will be an offset between the geolocation of the "center" of the two footprints. Errors introduced by applying only a single set of weighting coefficients derived from a scan where the sensor altitude is around 835 km were assessed, and it was found that greatest errors (mean and $\pm\,1\,\sigma$ error of 0 K and 0.03 K) occur for the remapping of samples from ICI-4 and ICI-11 channels into the ICI-1 FOV(s). The error introduced by simplifying the remapping calculation should be uncorrelated to other error sources like $NE\Delta T$, and hence more or less negligible.

- Remapping sensitivity to scan synchronization

  – The performance of the remapping of samples from MWI channels onto the FOV of ICI-1 was studied, taking into account that the MWI and ICI scan rotation is clockwise and counterclockwise, respectively, as seen from zenith side of the platform. The performance (noise and fit errors) was found to be comparable for the situation

where the start time of MWI and ICI scans occur at the same time and when the start time of the MWI scan is delayed by half the scan duration time. Thus, it appears that the start time of the MWI scan, relative to start time of the ICI scan is not a critical issue, as long as there is no drift over time.

- Simplifications for channels with similar characteristic

  – Some MWI channels and some ICI channels have similar viewing angles and antenna patterns (e.g. ICI-1, ICI-2, and ICI-3). It was found it is possible to simplify the remapping calculation by applying e.g. weighting coefficients derived for ICI-2 on ICI-3 without introducing any significant errors. This will reduce the number of set of weighting coefficients that need to be derived for an operational processing, and possibly also decrease the computational burden.

Biases of samples convolved to target FOVs have been assessed. In general, a remapped MWI / ICI observation can be seen as an estimate of the antenna temperature of the channel of concern, as "measured" from the target viewing angle and antenna pattern. The dataset of detailed MWI and ICI simulations is used to estimate both "true" and remapped antenna temperatures, and that allowed for inter-channel and inter-FOV bias assessments.

A bias-free convolution has been demonstrated as long as the remapping does not involve a change in incidence angle (i.e. when the incidence angle of the samples to be remapped agree to that of the target channel). However, several MWI and ICI channels have an incidence angle that do not exactly match that of the target (the variation in incidence angle is around 1.2° and 2.0° among the channels for MWI and ICI, respectively), and hence, non-negligible biases, even for cloud free conditions, were found for some of the channels. The reason for this is due to the fact that both surface emissivity / reflectivity and atmospheric transmission varies with incidence angle (and with surface type and atmospheric condition), and this is not taken into account by the Backus-Gilbert footprint resampling methodology.

The cloud free bias were found to be state dependent, but no significant inter-FOV biases (or scan position dependent biases) were found for any channel within the ICI-1 scan angle range of 59° to -59° and MWI-3V scan angle range of -66° to 65° where the remapping is anticipated to work well (low noise and fit-error). Outside this range some inter-FOV biases were seen in the data.

For ICI, the cloud free bias is greatest for the the dual polarized channels around 243 and 664 GHz, where a state varying clear sky bias around 0.4 to 0.6 K was found, whereas the bias is more or less negligible small for the remaining ICI channels.

Some of the MWI channels are significantly sensitive to the surface, and the cloud free bias therefore varies with surface type. The greatest cloud free bias, around 0.8 K, was found for MWI-8V and over an ocean surface, whereas the bias over land was found to be significantly lower. However, biases derived for channels with a strong surface sensitivity must be treated with care, as the surface reflectivity is in general complicated to model, in particular for land surfaces. The surface emissivity tool TELSEM was deployed in the simulation for generating the dataset, and the bias over land presented here depends, clearly, on how accurate the incidence angle dependency in TELSEM is. Non-negligible biases were also found for a couple of other MWI channels, e.g. MWI-14, with less surface sensitivity.

	Backus-Gilbert footprint matching methodology applied on MWI and ICI observations	**Code:** TR/BG/MWI-ICI
MoHHoW		**Issue:** 1.0
		Date: June 5, 2019
		File: optimal-interpolation-applied.tex
		Page: 9 / 200

Inter-channel biases between samples from ICI-1 / MWI-14, ICI-2 / MWI-17, and ICI-3 / MWI-18 convolved to the ICI-1 FOV were assessed. These pairs of channels are overlapping in frequency range, and are, hence, handy to compare in a Cal/Val activity. It was found that ICI "observations" are about 0.1 K warmer than that of MWI, that is due to the fact that ICI samples are having a lower incidence angle $\sim 0.3°$).

Clouds within the FOV can have a non negligible influence, on top of the cloud free bias, and the impact varies between channels and phase of cloud. For MWI, the impact of liquid phase clouds tend to decrease the bias related to surface emissivity / reflectivity variation with incidence angle, as the observation becomes less sensitive to the surface contribution. The impact of cloud ice tends to be to increase the bias. Cloud ice will have an impact both through a "pure" incidence angle difference effect (up to about 2 K for ICI-4 and ICI-11 channels) that applies to a homogeneous cloud layer, but also at the edges of areas with hydrometeors where even higher errors were found. This is also related to differences in viewing angles, and due to the fact that slightly different parts of the atmosphere may be observed by the the target channel and the samples convolved to the target FOV. This gives primarily that samples around cloud system edges may be biased (low or high).

Thus, samples from the various MWI and ICI channels remapped onto the MWI-3V and ICI-1 FOVs were found to be biased, as the remapping algorithm does not compensate for the original difference in incidence angle. This should be taken into account of in Level2 processing. The bias related to the pure incidence angle difference effect, that applies to a homogeneous state, should be possible to take into account of by applying the original incidence angle for each channel in the retrieval calculation. The bias related to the fact that slightly different parts of the atmosphere are observed by the various channels and for a given FOV is a bit more challenging to take into account. This type of bias was found to be most significant for ICI channels 4 and 11, and less pronounced for MWI channels. The ICI retrieval algorithm is based on a precalculated retrieval database consisting of synthetic states and corresponding simulated ICI observations. The ICI channel and scanning characteristic can potentially be taken into account when generating this retrieval database, but this requires that the simulation is based on 3-dimensional varying states. Alternatively, the bias can be taken into account of by increasing the noise values for the ICI-4 and ICI-11 channels in the retrieval calculation.

2 Introduction

2.1 Purpose of this document

The Micro-Wave Imager (MWI) and the Ice Cloud Imager (ICI) are two instruments that will be flown on board of the EUMETSAT Polar System - Second Generation (EPS-SG) satellites. The objectives of these EPS-SG instruments are to provide precipitation, cloud, cloud ice, and snowfall imaging for numerical weather prediction and climate monitoring in the 2020 to mid-2040's time-frame. The MWI and ICI will be hosted on the same EPS-SG platforms, providing radiances at microwave (MW) and sub-mm-wave frequencies (MWI will have 18 frequency channels ranging from 18.7 GHz to 183.31 GHz, and ICI 11 channels between 183.31 GHz and 664 GHz). Both ICI and MWI will be conically scanning instruments having a novel scanning pattern designed to obtain footprint sizes between 10 to 50 km for the MWI channels and around 16 km for the ICI channels. At a given moment, the various channels of MWI and ICI will not view towards exactly the same direction. The time integration is performed over a time period shorter than the time period necessary to sweep a single projected field of view (FOV). This effectively gives that consecutive scans contain observations with partially overlapping footprints. These samples can be remapped into target FOV(s) by the application of a footprint resampling technique, in order to prepare the data for Level 2 processing or Calibration and Validation Activities (Cal/Val). One such technique is the Backus-Gilbert (BG) methodology ([Backus and Gilbert, 1970] [Stogryn, 1978]), that has successfully been applied for footprint-matching between various satellite data channels (e.g Bennartz [2000] and Maeda and Imaoka [2016]), but the application to MWI and ICI observation is novel.

This document is developed as part of a study *Application of optimal interpolation procedures to EPS-SG MWI and ICI*, and the objective of this document is to describe the BG footprint matching methodology applied on MWI and ICI observations. Both a simulated MWI and ICI Level1B dataset, covering four reference Metop-A orbits, and a software remapping toolbox were developed for this purpose. The aim of this document is to describe this dataset and toolbox, as well as the characteristics and limitations of the remapping applied on MWI and ICI observation.

2.2 Structure of this document

This document is divided into three parts. The first part describes how a simulated MWI and ICI Level1B dataset, covering four reference Metop-A orbits, was generated. That is, part 1 describes, in order, MWI and ICI characteristics relevant for the study, data used for the simulation, and the setup of the simulation.

Part 2 describes the basis of the BG footprint matching methodology and a software remapping toolbox for MWI and ICI observations. This includes a description of all algorithms involved.

Part 3 describes important aspects of the BG footprint matching methodology applied on MWI and ICI observations including derived remapping characteristic. This is followed by a bias assessment, where the main focus is to assess biases for clear sky condition, but biases/noise for cloudy condition is also covered.
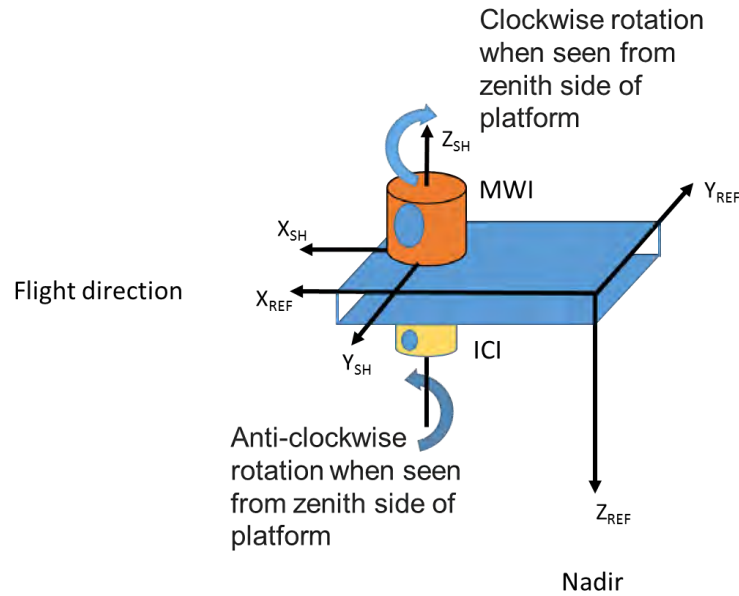
Figure 1: Basic MWI and ICI geometries, with respect to the satellite platform.

Part I

Simulation of MWI and ICI Level1B data

3 MWI and ICI

3.1 MWI and ICI characteristics

The MWI will be a conically scanning instrument radiometer observing in the microwave region. Characteristics relevant for the study are described in Table 1, Table 3, and Table 4. Figure 3 and 4 give an overview of the scanning pattern on ground.

The ICI will be a conical scanning radiometer observing in the microwave and sub-mm wave range, and charactecteristics are presented in Table 2, Table 3, and Table 5. Figure 5 and 6 gives an overview of the scanning pattern on ground.

The radiometric sensitivity ($NE\Delta T$) values presented in Table 1 and Table 2 do not apply to individual samples, but are based on the time required for each instrument to scan over a distance equivalent to the half power beam width (HPBW or -3[dB]) footprint in the across track direction when scanning at 45[rpm].

	Backus-Gilbert footprint matching methodology applied on MWI and ICI observations	**Code:** TR/BG/MWI-ICI
		Issue: 1.0
		Date: June 5, 2019
		File: optimal-interpolation-applied.tex
		Page: 12 / 200

Table 1: MWI instrument characteristics.

Channel ID	Channel	Frequency [GHz]	NEΔT [K]	Polarization	Footprint Size at -3 dB [km]/ HPBW @850 km [degrees]
1	MWI-1	18.7	0.8	V	50 / 1.67
2	MWI-1	18.7	0.8	H	50 / 1.67
3	MWI-2	23.8	0.7	V	50 / 1.67
4	MWI-2	23.8	0.7	H	50 / 1.67
5	MWI-3	31.4	0.9	V	30 / 1.0
6	MWI-3	31.4	0.9	H	30 / 1.0
7	MWI-4	50.3	1.1	V	30 / 1.0
8	MWI-4	50.3	1.1	H	30 / 1.0
9	MWI-5	52.610	1.1	V	30 / 1.0
10	MWI-5	52.610	1.1	H	30 / 1.0
11	MWI-6	53.24	1.1	V	30 / 1.0
12	MWI-6	53.24	1.1	H	30 / 1.0
13	MWI-7	53.750	1.1	V	30 / 1.0
14	MWI-7	53.750	1.1	H	30 / 1.0
15	MWI-8	89	1.1	V	10 / 0.33
16	MWI-8	89	1.1	H	10 / 0.33
17	MWI-9	118.7503 ± 3.2	1.3	V	10 / 0.33
18	MWI-10	118.7503 ± 2.1	1.3	V	10 / 0.33
19	MWI-11	118.7503 ± 1.4	1.3	V	10 / 0.33
20	MWI-12	118.7503 ± 1.2	1.3	V	10 / 0.33
21	MWI-13	165.5 ± 0.75	1.2	V	10 / 0.33
22	MWI-14	183.31 ± 7.0	1.3	V	10 / 0.33
23	MWI-15	183.31 ± 6.1	1.2	V	10 / 0.33
24	MWI-16	183.31 ± 4.9	1.2	V	10 / 0.33
25	MWI-17	183.31 ± 3.4	1.2	V	10 / 0.33
26	MWI-18	183.31 ± 2.0	1.3	V	10 / 0.33

	Backus-Gilbert footprint matching methodology applied on MWI and ICI observations	**Code:** TR/BG/MWI-ICI
		Issue: 1.0
		Date: June 5, 2019
		File: optimal-interpolation-applied.tex
		Page: 13 / 200

Table 2: ICI instrument characteristics.

Channel ID	Channel	Frequency [GHz]	NEΔT [K]	Polarization	Footprint Size at -3 dB [km]/ HPBW @850 km [degrees]
1	ICI-1	183.31 ± 7.0	0.8	V	16 / 0.5
2	ICI-2	183.31 ± 3.4	0.8	V	16 / 0.5
3	ICI-3	183.31 ± 2.0	0.8	V	16 / 0.5
4	ICI-4	243.2 ± 2.5	0.7	V	16 / 0.5
5	ICI-4	243.2 ± 2.5	0.7	H	16 / 0.5
6	ICI-5	325.15 ± 9.5	1.2	V	16 / 0.5
7	ICI-6	325.15 ± 3.5	1.3	V	16 / 0.5
8	ICI-7	325.15 ± 1.5	1.5	V	16 / 0.5
9	ICI-8	448.0 ± 7.2	1.4	V	16 / 0.5
10	ICI-9	448.0 ± 3.0	1.6	V	16 / 0.5
11	ICI-10	448.0 ± 1.4	2.0	V	16 / 0.5
12	ICI-11	664.0 ± 4.2	1.6	V	16 / 0.5
13	ICI-11	664.0 ± 4.2	1.6	H	16 / 0.5

	Backus-Gilbert footprint matching methodology applied on MWI and ICI observations	**Code:** TR/BG/MWI-ICI
MoHHoW		**Issue:** 1.0
		Date: June 5, 2019
		File: optimal-interpolation-applied.tex
		Page: 14 / 200

Table 3: MWI and ICI characteristics.

Earth view angle	Scene viewing angle (azimuth) of ≥130°. (≥65° on each side of orbital plane).
Incidence angle [°]	53±2
Scan speed (rpm)	45
Footprint overlap (Along-track, [%])	ICI ≥ 40, MWI ≥ 20
Satellite Altitude [Km]	822 (min) / 850 (max)
Number of samples in the Earth view (MWI / ICI)	1402 / 784
Sample integration time (MWI / ICI, [ms])	0.392 / 0.661
Rotation as seen from zenith side of platform (MWI / ICI)	Clockwise / Counterclockwise
Starting angle of each scan rotation [°] (MWI / ICI) (0° is aligned with the X_{SH} direction shown in Figure 1.)	149.73 / 226.762
Start window angle [°] (MWI / ICI)	285.740 / 70.0
End window angle [°] (MWI / ICI)	74.26 / 290.0
Main tilt angle of the antenna [°] (MWI / ICI) (θ_{OBA} shown in Figure 2.)	44.81782 / 44.767

Table 4: MWI scan angle offsets.

Channel ID	Channel	Elevation Offset [°]	Azimuth Offset [°]
1	MWI-1V	-0.21436	-7.09015
2	MWI-1H	-0.21509	-7.09439
3	MWI-2V	-0.21991	-7.16206
4	MWI-2H	-0.22017	-7.15770
5	MWI-3V	-0.07794	4.22445
6	MWI-3H	-0.07799	4.22587
7	MWI-4V	-0.28916	8.51205
8	MWI-4H	-0.28696	8.50953
9	MWI-5V	-0.28916	8.51205
10	MWI-5H	-0.28696	8.50953
11	MWI-6V	-0.28916	8.51205
12	MWI-6H	-0.28696	8.50953
13	MWI-7V	-0.28916	8.51205
14	MWI-7H	-0.28696	8.50953
15	MWI-8V	0.43213	-1.16522
16	MWI-8H	0.43213	-1.16522
17	MWI-9	-0.00452	0.89802
18	MWI-10	-0.00452	0.89802
19	MWI-11	-0.00452	0.89802
20	MWI-12	-0.00452	0.89802
21	MWI-13	-0.98839	-2.38986
22	MWI-14	-0.95929	-0.53027
23	MWI-15	-0.95929	-0.53027
24	MWI-16	-0.95929	-0.53027
25	MWI-17	-0.95929	-0.53027
26	MWI-18	-0.95929	-0.53027

Table 5: ICI scan angle offsets.

Channel ID	Channel	Elevation Offset [°]	Azimuth Offset [°]
1	ICI-1	-0.7801282	0.000000
2	ICI-2	-0.7801282	0.000000
3	ICI-3	-0.7801282	0.000000
4	ICI-4V	0.71056695	-3.39767815
5	ICI-4H	0.7308017	3.3846293
6	ICI-5	-0.82190055	-2.22634105
7	ICI-6	-0.82190055	-2.22634105
8	ICI-7	-0.82190055	-2.22634105
9	ICI-8	-0.8221742	2.2402233
10	ICI-9	-0.8221742	2.2402233
11	ICI-10	-0.8221742	2.2402233
12	ICI-11V	0.7522477	-1.3670384
13	ICI-11H	0.8755013	0.9408979
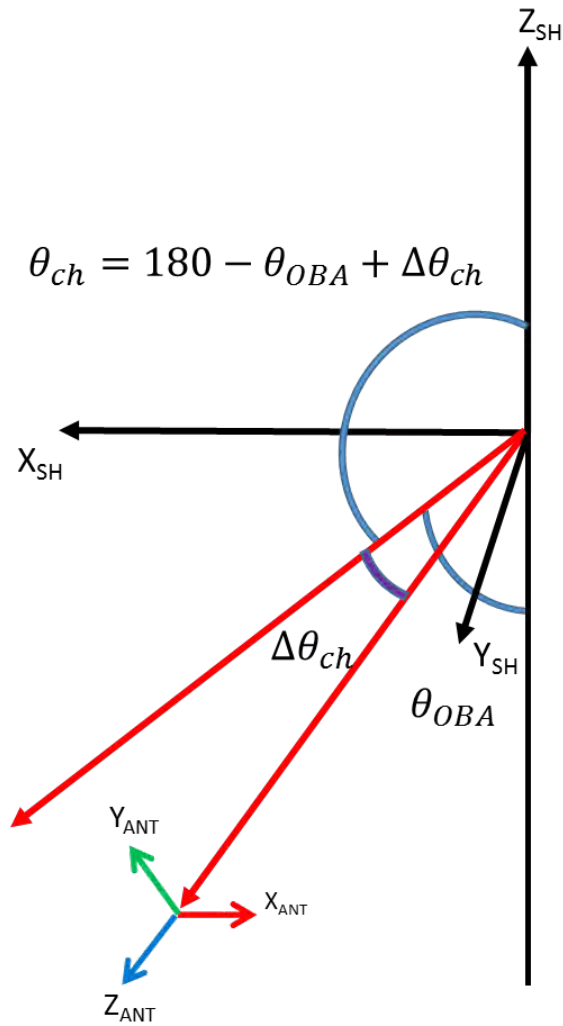
Figure 2: Elevation angles, and description of sensor head (SH) reference coordinate system (x-axis is aligned with flight direction taking into account of yaw steering) and antenna (ANT) reference coordinate systems (z-axis is aligned with the antenna boresight direction).

	Backus-Gilbert footprint matching methodology applied on MWI and ICI observations	**Code**: TR/BG/MWI-ICI
		Issue: 1.0
		Date: June 5, 2019
		File: optimal-interpolation-applied.tex
		Page: 18 / 200
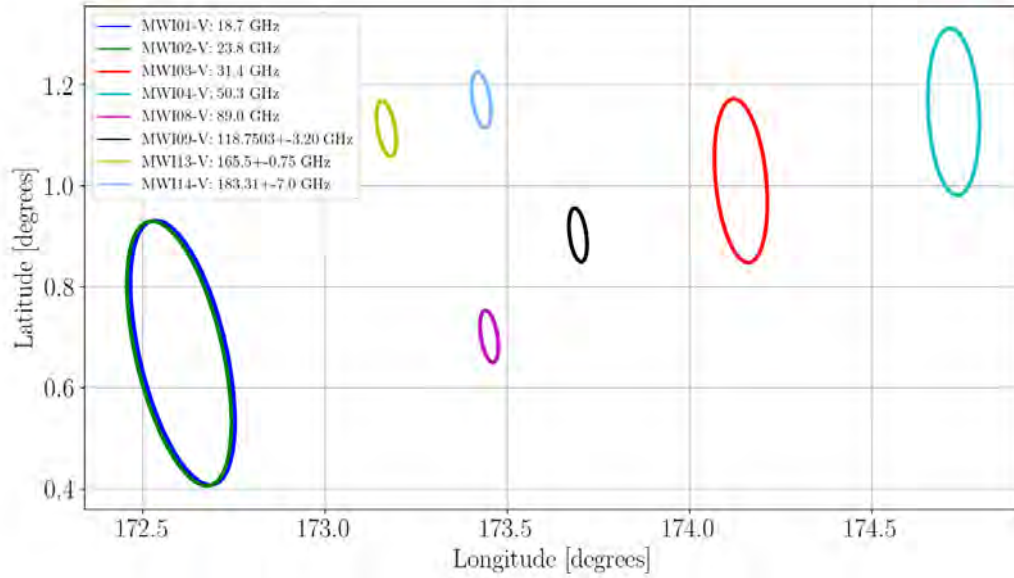
Figure 3: The figure shows the instantaneous, relative positions of -3-dB footprints on the geoid for some MWI channels.
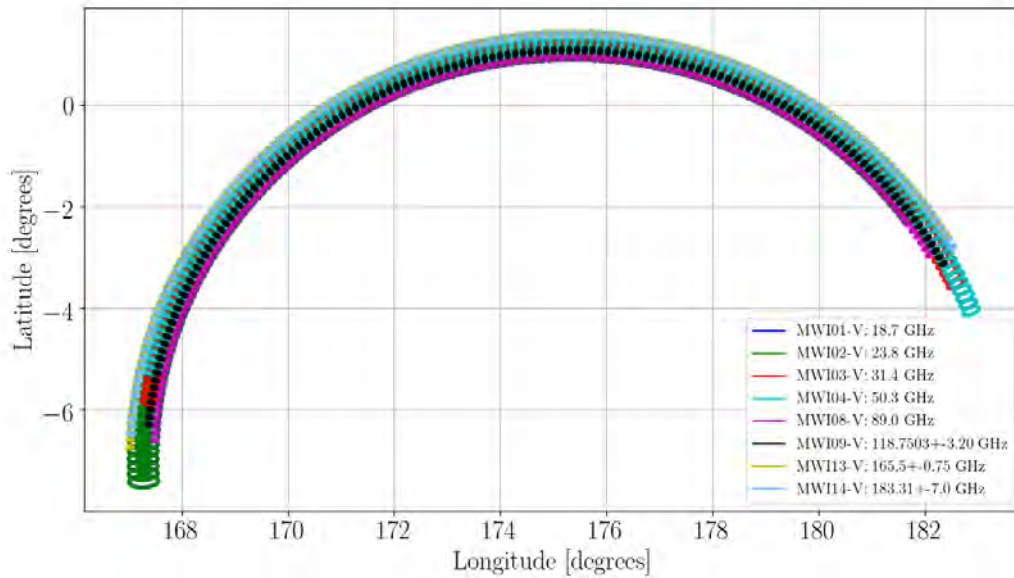
Figure 4: The figure shows the relative positions of -3-dB footprints on geoid for some MWI channels and for every 10th sample of a complete scan.
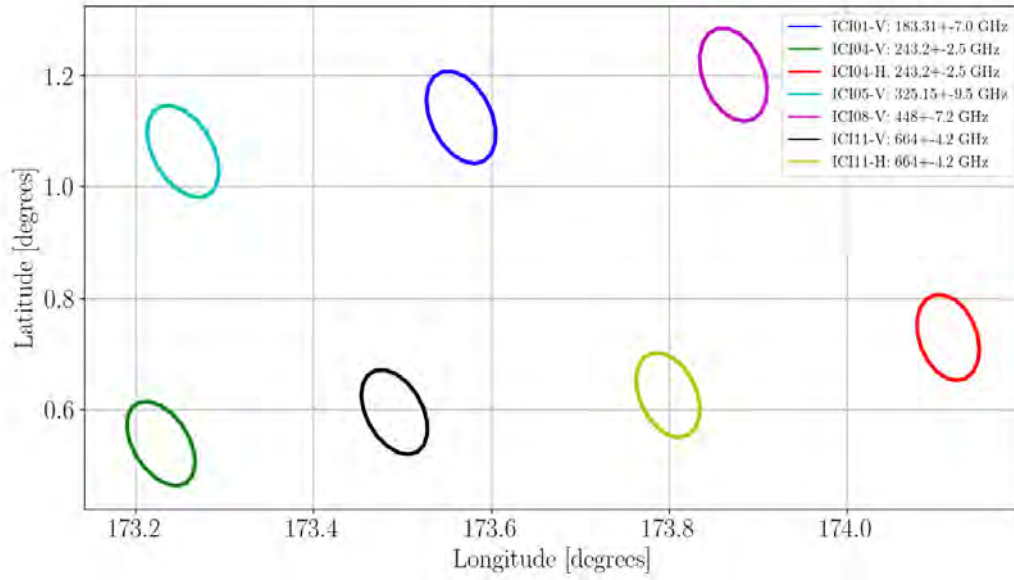
Figure 5: The figure shows the instantaneous, relative positions of -3-dB footprints on the geoid for some ICI channels.
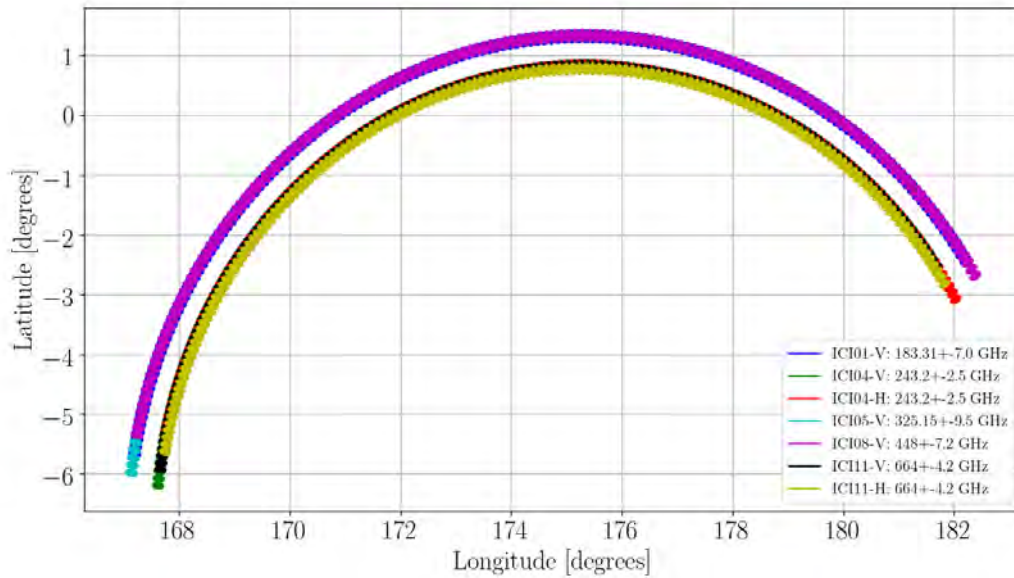
Figure 6: The figure shows the relative positions of -3-dB footprints on geoid for some ICI channels and for every 5th sample of a complete scan.

Table 6: Reference Metop-A orbits.

Orbit Number	Time Interval (UTC, Format:YYYY-MM-DD HH:MM:SS)	Comment
4655	2007-09-12 08:43:03 to 2007-09-12 10:22:03	First summer orbit
4656	2007-09-12 10:22:03 to 2007-09-12 12:04:03	Second summer orbit
6985	2008-02-23 08:46:03 to 2008-02-23 10:28:03	Winter orbit
9744	2008-09-04 13:37:26 to 2008-09-04 15:16:22	Tropical cyclone Ike

4   Data

This section just describes the sources to data. Processing and modifications of the data are treated in later sections.

4.1   Orbit and attitude data

Details of the four reference Metop-A orbits considered in the study are described in Table 6, and displayed in Figure 7. Orbit state vectors are needed for the generation of the Level1B dataset. The Pyorbital package (`https://pyorbital.readthedocs.io/en/latest/`) was deployed to perform orbit propagation calculation for those orbits. Pyorbital is a python package that can calculate orbit state vectors (cartesian position and velocity vectors in an Earth-centred inertial, ECI, coordinate frame) for a given time using a TLE file as input.

4.2   Surface and atmosphere data

4.2.1   ERA5

ERA5 is a reanalysis project made by ECMWF[1] that provides hourly estimates of a large number of atmospheric, land and oceanic climate variables. The data cover the Earth on a $0.25°$ (about $30\,\text{km}$) grid and resolve the atmosphere from the surface up to a height of $80\,\text{km}$. It was found that surface rain and snowfall rates were required input (see below). Unfortunately, these quantities are not provided as analysis data, and it was necessary to make use of forecast data. Forecast data are given with an hourly resolution, and data from the following date and hours are used for the various orbits:

- orbit 4655 and 4656:
  08:00:00/09:00:00/10:00:00/11:00:00/12:00:00/13:00:00 from forecast@2007-09-12T06:00:00

- orbit 6985:
  08:00:00/09:00:00/10:00:00/11:00:00 from forecast @2008-02-23T06:00:00

---

[1]`climate.copernicus.eu/climate-reanalysis`
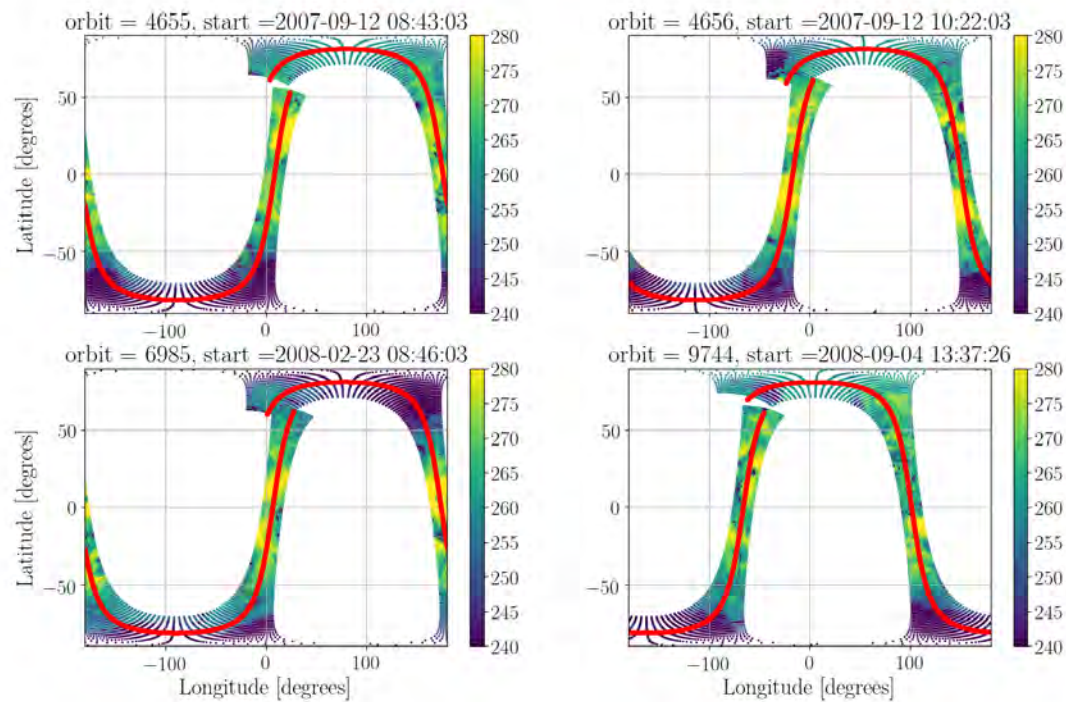
Figure 7: Calculated satellite positions for the four reference Metop-A orbits, and actual MHS channel 5 (190[GHz]) observations in the background.

- orbit 9744:
  13:00:00/14:00:00/15:00:00/16:00:00 from forecast @2008-09-04T06:00:00

The following "surface" parameters are used in the simulations:

- two meter temperature,

- ten meter u component wind,

- ten meter v component wind,

- sea surface temperature,

- sea ice cover,

- ice temperature layer 1,

- large-scale rain rate,

- convective rain rate,

- large-scale snowfall rate water equivalent.

- convective snowfall rate water equivalent,

The following atmospheric parameters are used in the simulations:

- temperature,

- geopotential,

- specific humidity,

- specific cloud ice water content,

- specific cloud liquid water content,

- specific rain water content (large-scale),

- specific snow water content (large-scale).

The ERA5 data were retrieved using the ECMWF WebAPI [2].

4.2.2   Convective precipitation database

ERA5 provides information on the mass of several hydrometeor classes: cloud liquid water, large-scale rain, cloud ice content and large-scale snow. Internally in the model there exist two additional hydrometeor classes: convective rain and convective snowfall. These later two classes are treated differently, they are prognostic variables of flux type. As a consequence, these two classes are not part of ERA5's set of variables. To cover the convective classes in an approximate manner, Alan Geer (at ECMWF) was kind enough to compile a database of 24248 large-scale and convective flux profiles. These combinations of flux profiles were extracted from a run of the IFS model. The selection was based on collocations with AMSR2, where data having significant convective precipitation was selected in a random manner.

4.3   Topography and surface type data

GTOPO30[3] is a global digital elevation model (DEM) with a horizontal grid spacing of 30 arc seconds (approximately 1 km), and is used in the simulation.

A surface type mask based on the "Global Self-consistent Hierarchical High-resolution Geography Database" (GSHHG) is used to categorise surface type (land or water). The GSHHG land-water mask is obtained through GMT, the Generic Mapping Tools.

5   Simulation of Level1b data

5.1   Overview

The generation of simulated Level1b antenna temperatures has three main steps:

---

[2]https://confluence.ecmwf.int//display/WEBAPI/Access+ECMWF+Public+Datasets
[3]lta.cr.usgs.gov/GTOPO30
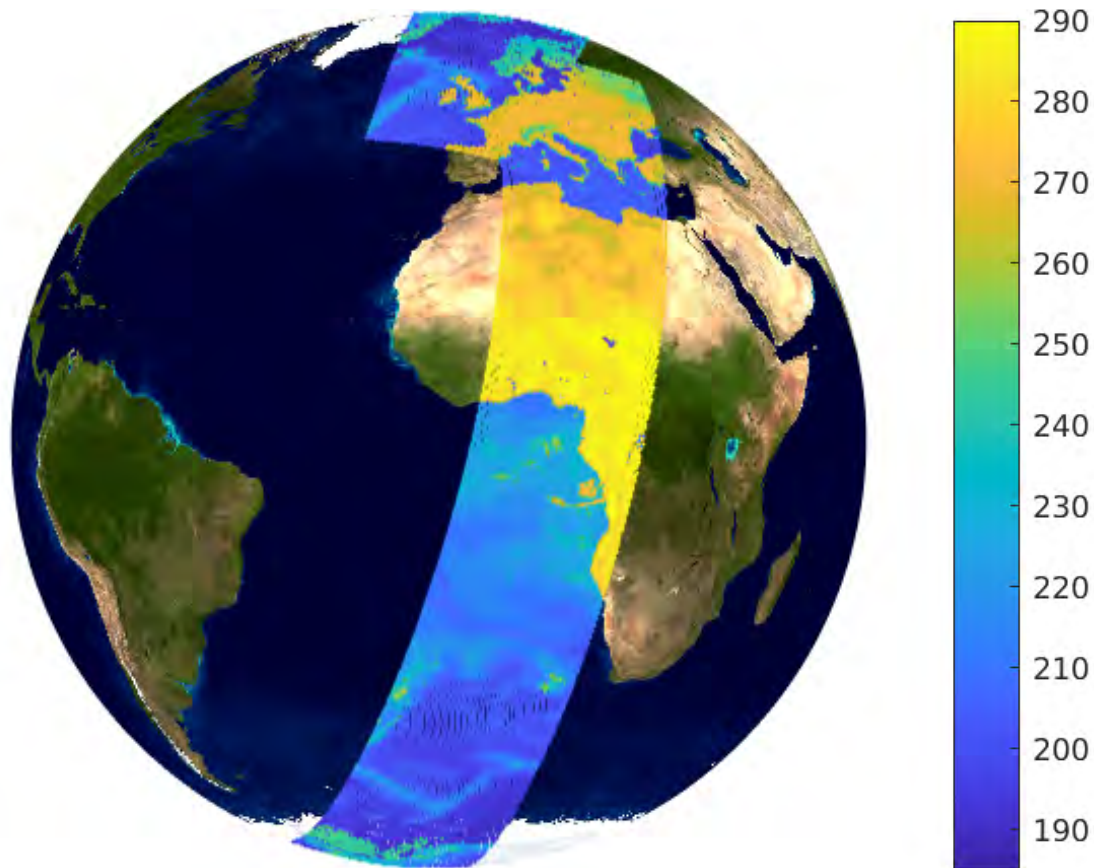
Figure 8: Example on "swath Tb-data". Data for a part of orbit 6985, 31.4 GHz and a geocentric zenith angle of 127° (at ellipsoid level) are shown. The first Stokes element is displayed (that equals mean of V and H polarisation.) The start and end parts of the swath grid are partly overlapping.

1. A lookup-table of pencil beam brightness temperatures, covering the swath for a complete orbit, is generated (Figure 8). These lookup-tables are denoted as "swath Tb-data". The data contain also geolocation information, both with respect to the reference ellipsoid and the Earth's surface.

2. A "scanning dataset" is created, containing sensor position and antenna boresight viewing direction for each channel / scan / sample within the orbit. This dataset contains also a description of effective antenna patterns to apply, i.e. including the broadening due to the azimuthal movement inside the integration time.

3. Final data are obtained by using the information in the scanning dataset to interpolate and integrate swath Tb-data. This gives the antenna temperature of each channel / scan / sample within the file, with associated geolocation information. These datasets are denoted as the Ta-data for short.

This approach allows to derive antenna temperatures for various scan configurations, without

	Backus-Gilbert footprint matching methodology applied on MWI and ICI observations	Code: TR/BG/MWI-ICI
		Issue: 1.0
		Date: June 5, 2019
		File: optimal-interpolation-applied.tex
		Page: 24 / 200

having to perform new radiative transfer calculation.

The basic objective of the study is to implement a "remapping" toolbox. To support this objective it is critical that the accuracy in step 2 and 3 is very high. This is a requirement to test remapping for various conditions. That is, it must be possible to answer the question, does the output of the toolbox agree with simulations mimicking the measurement conditions assumed in the remapping? The output of step 1 shall of course give a fair description of the radiance field reaching the sensor, but the accuracy of these data are not critical for the study objective. For example, even a systematic error of 10 K should be of no importance at all with respect to the testing of the remapping toolbox.

5.2 Basic radiative transfer setup

5.2.1 Software

The core calculations are performed by ARTS (Atmospheric Radiative Transfer System) v2.3.x [Eriksson et al., 2011, Buehler et al., 2018]. The version used at the time of writing is v2.3.1127. The background data manipulation is performed in Matlab (both R2016b and R2017b tested and used). Some functions from Matlab's mapping toolbox are used. The Atmlab package (can be obtained by the ARTS web site) is also used. (Note that ARTS and Matlab are only used for internal purposes. The remapping toolbox will by Python-only.)

5.2.2 Geometrical aspects

The WGS-84 reference ellipsoid is applied throughout. Of special concern is the fact that ARTS operates with geocentric coordinates, while input and orbit data are specified geodetic coordinates. All calculations involving geodetic coordinates are performed in Matlab (using functions from the mapping toolbox). The geodetic and geocentric versions of latitudes and zenith angles differ. In this document, all latitudes are geodetic. Zenith angles are also geodetic, if not stated differently.

Inside ARTS the surface altitude is defined on the same latitude and longitude grids as applied for the atmospheric quantities, and the surface altitude is treated to vary linearly between grid points. To match the treatment inside ARTS, the input topography from GTOPO30 is interpolated to the grid of ERA5. That is, the topography is effectively represented at a resolution of about 30 km (but note that e.g. shorelines are represented at about 2 km resolution, see below).

5.2.3 Surface types and emissivities

A surface type mask is generated. This mask has a 1 min resolution (about 2 km), following the GSHHG data. The mask is first set to discriminate between water and land. Note that GSHHG provides a description of lakes, not only land/sea. A third surface type is considered, sea-ice. Locations covered by sea-ice are determined using ERA5's sea-ice concentration. A simple algorithm is applied: The ERA5 sea-ice concentration (30 km resolution) is interpolated to the GSHHG-based grid (2 km resolution). Inside each ERA5 grid cell, the positions with the highest interpolated sea-ice fractions are set to be covered with sea-ice. The fraction set to
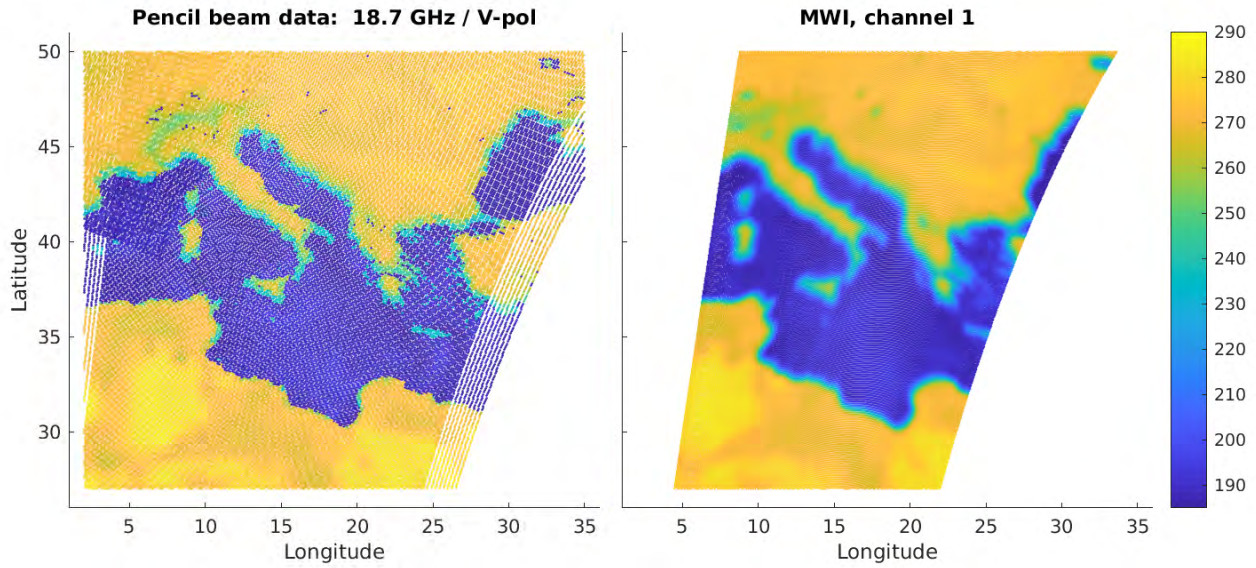
Figure 9: Left: Part of the swath Tb-data of orbit 6985 (the geocentric zenith angle, at the ellipsoid level, is 127°). Right: Final Ta-data of MWI channel 1 (that is V-polarised) for the displayed part of the orbit.

be sea-ice follows the original sea-concentration. That is, if the ERA5 sea-ice concentration is 25%, a forth of the surface type mask values inside the region will flag sea-ice. This procedure will tend to place the sea-ice inside a ERA5 grid cell along the border to the neighbouring grid cell having the highest sea-ice concentration.

The emissivity of open water is set according to TESSEM2 (Tool to Estimate Sea-Surface Emissivity from Microwaves to sub-Millimeter waves, Prigent et al. [2017]). The effective temperature for this surface type is set to ERA5's sea surface temperature. The 10 meter wind speed of ERA5 is considered, i.e. it is provided to TESSEM2.

The emissivity of land is set following TELSEM2 (A Tool to Estimate Land Surface Emissivities at Microwave frequencies, Aires et al. [2011]). Several modifications of the information provided by TELSEM2 were necessary. First of all, geographical positions flagged as land by GSHHG are not always covered by TELSEM2, for example, small islands. The ARTS interface to TELSEM2 was extended to handle this, by adding a nearest neighbour interpolation. That is, the closest value provided by TELSEM2 is applied. The TELSEM2 data appear to be derived as footprint averages. This means that the emissivity given for positions close to shorelines (both lake and sea ones) can be a mean of the emissivity of land and water, while for these simulations the land-only emissivity is the desired quantity. Influence of water decreases the TELSEM2 value, and as a rough "fix" the land emissivity is not allowed to be below 0.8. That is, if TELSEM2 reports a value below 0.8, the value is rejected and 0.8 is applied instead. The effective temperature for land is taken as ERA5's 2 m temperature.

The impact of the TELSEM2 "water contamination" can be seen in Fig. 9. The relative low brightness temperatures of e.g. Majorca, Crete and the west coast of Italy originate in relative low land emissivities, compared to the land areas away from any sea (besides the Alps).

All sea-ice is assumed to be covered by snow, and a generic snow emissivity of 0.9 is assumed.
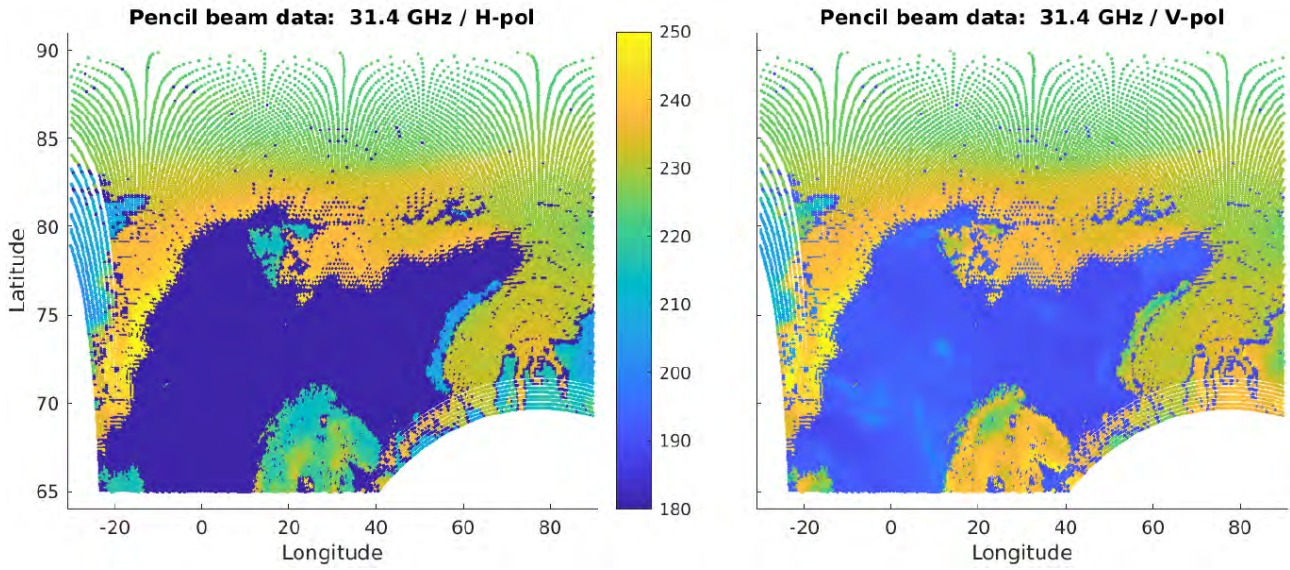
Figure 10: Further example on Tb-data from orbit 6895 (31.4 GHz, at H- (left) and V-polarisation (right)). Here a region centred close to Svalbard is shown, to illustrate how sea-ice are represented in the simulations. The colorbar is common for the two panels.

The effective temperature for this surface type is taken as ERA5's "ice temperature layer 1". Example results including sea-ice are displayed in Fig. 10.

5.2.4   Absorption models for atmospheric species

Absorption and emission of water vapour are considered following the "absorption model" of Rosenkranz [1998]. This model is in ARTS denoted as *H2O-PWR98*. For oxygen and nitrogen, *O2-PWR98* and *N2-SelfContStandardType* were used, that both are mainly based on [Rosenkranz, 1993]. See the ARTS documentation for details.

5.2.5   Cloud and precipitation

Cloud liquid water is assumed to cause no scattering, a valid assumption at microwave frequencies. This hydrometeor class is below denoted as liquid water content (LWC). The absorption model of Ellison [2007] is applied for LWC.

Estimation of convective rain and snowfall is described below. Large-scale and convective rain are summed up to form a rain water content (RWC) hydrometeor class. The drop size distribution of Abel and Boutle [2012] is assumed for RWC. For both LWC and RWC, zero mass content is enforced at temperature below 240 K.

Cloud ice water, large-scale snow and convective snow are summed up to form a generic ice water content (IWC) hydrometeor class. The tropical version of the particle size distribution (PSD) of Field et al. [2007] is assumed for IWC. This selection of PSD is based on Geer and Baordo [2014]. IWC is allowed to be non-zero between 200 and 277.15 K.

Particle single scattering data are taken from the database presented by Eriksson et al. [2018]. For RWC the liquid sphere habit (ID 25) is applied, while for IWC the large plate

aggregate (ID 20) is used. The "standard habit" version of the data is used, that e.g. helps ARTS to better represent the temperature variation of the scattering properties. Geer and Baordo [2014] were not followed regarding selection of ice habit, as more realistic particle data now are at hand. In addition, the "sector snowflake" recommended by Geer and Baordo [2014] (considering frequencies up to $190\,\mathrm{GHz}$) has been found to give an excess of scattering at $664\,\mathrm{GHz}$ (Fox et al. [2018] and unpublished results).

As mentioned, ERA5 does not provide data on the vertical distribution of "convective rain and snow" and these two components are estimated based on their surface fluxes and the "database" provided by Alan Geer. Flux profiles from this database are considered and included according to this scheme:

- The database is only considered where the ERA5 surface flux due to convective rain and snow exceeds a threshold value, l. This value is set to $l = 10^{-6}\,\mathrm{kg/m^2}$.

- Only database profiles from within $10°$ in latitude, from the ERA5 position, are considered.

- The ERA5 and database surface convective rain fluxes must both be below l, or agree within 25%.

- The same match is demanded for surface convective snow.

- If the above filtering results in no match, no convective precipitation is added.

- If the filtering leaves a single database entry, these convective flux profiles are selected.

- If the filtering leaves multiple database entries, the large-scale snow and rain profiles are compared. The database entry with the smallest deviation is selected (the deviation is measured in terms of the 2-norm).

- Flux profiles are converted to mass contents by assuming a constant fall speed of $1\,\mathrm{m/s}$. For rain the fall speed is assumed to be directly proportional to the flux, varying from $2.5\,\mathrm{m/s}$ to $8\,\mathrm{m/s}$ (at the maximum flux found in the database).

5.3   Generation of swath Tb-data

5.3.1   Swath grid

As a first step, a "swath grid" is created. This grid is rectangular and is centred around the satellite's nadir track. Accordingly, the dimensions of the grid are along-track and across-track. The along-track grid is an equally spaced vector. The across-track has one value at zero, and is symmetric with respect to the nadir track. An equally spaced grid is used out to an across-distance of $1100\,\mathrm{km}$. Extra points are added out to $1300\,\mathrm{km}$, to cover the far-wing parts of the antenna pattern of the first MWI channels. The same spacing is applied along-track and in the centre part of the across-track dimension. This spacing is set to $12.5\,\mathrm{km}$. The second across-spacing is set to $25\,\mathrm{km}$.

	Backus-Gilbert footprint matching methodology applied on MWI and ICI observations	**Code:** TR/BG/MWI-ICI
		Issue: 1.0
		Date: June 5, 2019
		File: optimal-interpolation-applied.tex
		Page: 28 / 200

Table 7: Dimensions and grids of the Tb-data lookup-table.

Dimension	Grid
Along-track	0, 12.5, 25.0, 37.5 … . km
Across-track	[-1300:25:-1125,-1100:12.5:1100 1125:25:1300] km
Incidence angle	[116° 127° 137°]
Frequency	26, one per unique channel
Stokes	I and Q elements

The geographical position for the nadir track (i.e. zero across-track distance) is obtained by interpolating the orbit data. The geographical coordinates of across-track distance are calculated with Matlab's function `track1`[4], that returns the latitude and longitude along a great circle (the start azimuth of the great circle is the satellite's heading ±90°). All these geographical positions are geodetic, at 0 m above the reference ellipsoid. If these positions actually form a perfectly rectangular grid is not critical, as final data are extracted by "unstructured grid" interpolation.

5.3.2 Radiative transfer calculations

As indicated above, the swath Tb-data consists of a lookup-table of pencil beam brightness temperatures. This lookup-table has dimensions: Stokes element, frequency, along-track distance, across-track distance and zenith angle (Table 7). The latitude and longitude (at ellipsoid level) for each swath grid position are known, they are part of the definition of the swath grid.

The lookup-table is filled as follows. For each swath grid position, radiative transfer calculations are done for three (geocentric) zenith angles (116°, 127° and 137°). A single azimuth direction is used, determined as the azimuth towards the satellite for the middle zenith angle. The zenith angle refers here to the angle between the viewing direction and local (geocentric) zenith, at the intersection with reference ellipsoid. For each zenith and azimuth combination, the matching combination of satellite position and line-of-sight (LOS) is determined. These calculations are done using functions from Atmlab.

For memory and efficiency reasons, the complete Tb-data are not calculated in a single ARTS call. The swath is divided into rectangular latitude-longitude regions. The surface and atmosphere of the region is created by incorporating ERA5 and other data, as described above. Margins are added in both latitude and longitude, to make sure that no "edge effects" slip into the simulations, and that the propagation path from the satellite enters the model atmosphere from the top (and not from the side).

All the radiative transfer calculations for one "region" is done in a single ARTS call, where ARTS is given a 3D atmospheric view. It is far too costly too handle the hydrometeor scattering in 3D and an "independent beam approximation" is used. In short, the propagation paths from the sensor down to the surface are determined and the atmosphere and surface are "sampled" along the path. This forms a set of 1D atmospheres that are given to the RT4 (a.k.a. polradtran) scattering solver [Evans and Stephens, 1995]. RT4 is "polarised", and data for V and H polarisation are obtained in one calculation. Example results are found in Figures 8 and

---

[4]See `mathworks.com/help/map/ref/track1.html`.

	Backus-Gilbert footprint matching methodology applied on MWI and ICI observations	Code:	TR/BG/MWI-ICI
		Issue:	1.0
		Date:	June 5, 2019
		File:	optimal-interpolation-applied.tex
		Page:	29 / 200

9.

Among the details here, it is stressed that the lookup-table holds data for the position where a line-of-sight intersects the reference ellipsoid, but ARTS' ray tracing considers topography. Over land, this means that the data of the different zenith angles matches different surface positions, and that even the surface type can differ between the angles (land or lake). The geographical position of the surface intersection are stored as part of the Tb-data.

5.4 Scanning simulation

The aim of the scanning simulation is to generate a dataset containing sensor positions and antenna boresight viewing directions for each channel / scan / sample within a given orbit. This requires a modelling of the scanning rotation of the MWI and ICI instruments and the orbit propagation. Knowledge of orbit state vectors are required to take into account of the Metop-A / Metop-SG s/c platform attitude steering.

5.4.1 Orbit state vectors

The Pyorbital package [5] was deployed to perform orbit propagation calculation for those orbits. Pyorbital is a python package that is built around the latest version of the *Simplified General Perturbations* (SGP4) algorithm [6], and can calculate orbit state vectors (Cartesian position and velocity vectors in an Earth-centred inertial, ECI, coordinate frame) for a given time using a two line element set or TLE file [7] as input.

The ECI frame used by Pyorbital is true equator, mean equinox (TEME) although it does not use the conventional mean equinox. The ECI coordinate system is defined as a Cartesian coordinate system, where the coordinates are defined as the distance from the origin along the three orthogonal axes. The z axis runs along the Earth's rotational axis pointing North (for the epoch of the TLE file and accounting for precession but not nutation), the x axis points in the direction of the vernal equinox (see Figure 11 and further explanation in Sect. D: Coordinate System in Vallado et al. [2006]).

For further use of positions in this coordinate system, it is recommended to first transform them to a standard coordinate frame, where the pseudo Earth-fixed (PEF) coordinate frame is the closest one. The transformation to PEF coordinate frame (which implies that polar motion is neglected) is achieved by a rotation around the Z-axis using Greenwich Mean Sidereal Time (GMST)

$$\mathbf{r}_{pef} = \mathbf{R}_{pef-to-eci}^{T} \cdot \mathbf{r}_{eci} \tag{1}$$

and

$$\mathbf{v}_{pef} = \frac{\partial}{\partial t} \left(\mathbf{R}_{pef-to-eci}^{T} \cdot \mathbf{r}_{eci} \right) = \mathbf{R}_{pef-to-eci}^{T} \cdot \mathbf{v}_{eci} + \frac{d\mathbf{R}_{eci-to-pef}^{T}}{dt} \cdot \mathbf{r}_{eci} \tag{2}$$

where $\mathbf{r}_{pef}$ and $\mathbf{v}_{pef}$ is the position and velocity vector, respectively, in PEF frame, and $\mathbf{r}_{eci}$ and $\mathbf{v}_{eci}$ is the position and velocity vector, respectively, in the ECI frame. The rotation matrix

---

[5] https://pyorbital.readthedocs.io/en/latest/
[6] http://www.celestrak.com/publications/AIAA/2006-6753/
[7] https://en.wikipedia.org/wiki/Two-line_element_set

		Code:	TR/BG/MWI-ICI
MollioW	**Backus-Gilbert footprint matching methodology applied on MWI and ICI observations**	Issue:	1.0
		Date:	June 5, 2019
		File:	optimal-interpolation-applied.tex
		Page:	30 / 200
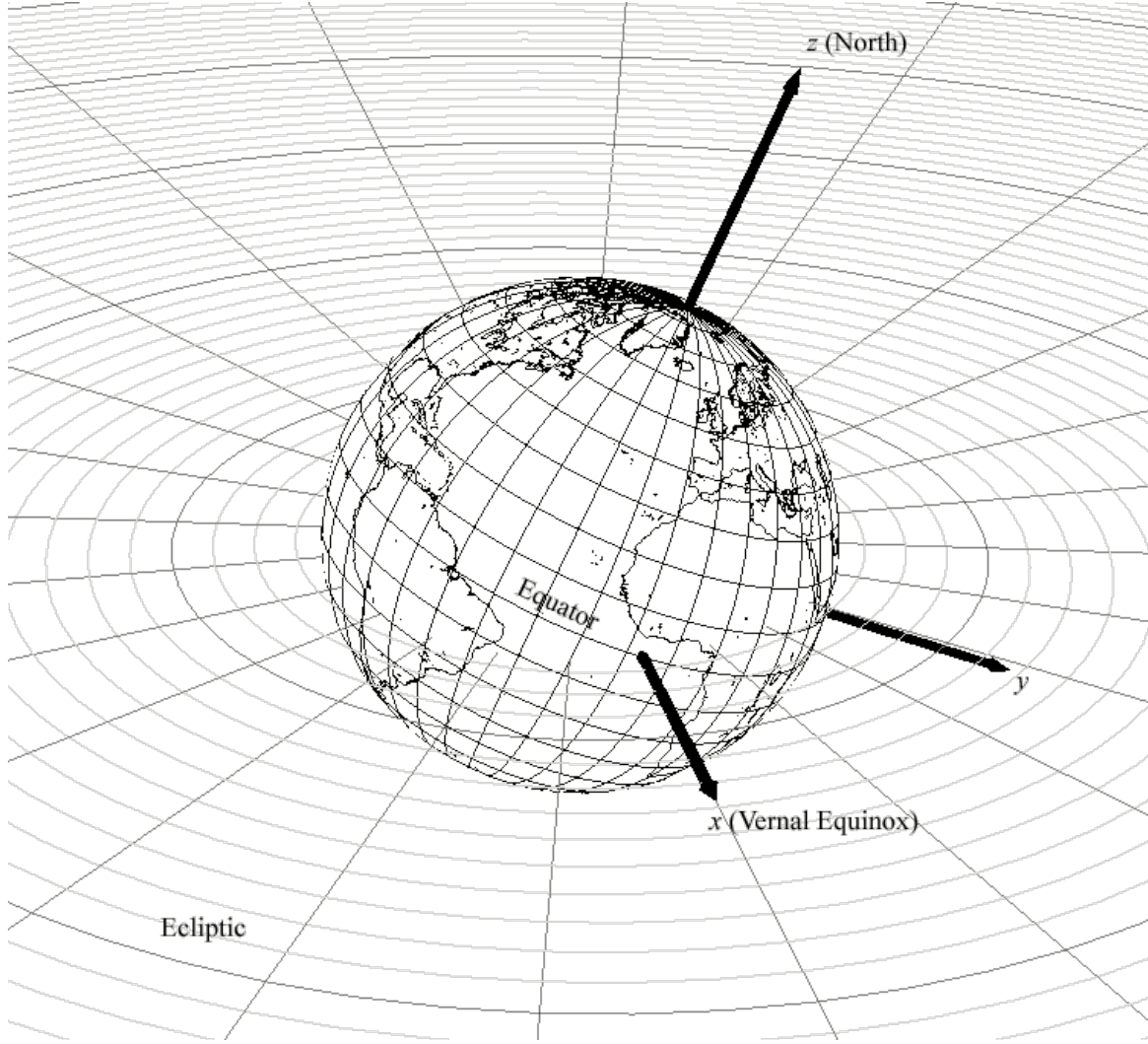
Figure 11: Earth-centered inertial (ECI) coordinate system applied by orbit propagation calculation.

$\mathbf{R}_{pef-to-eci}$ is described by

$$\mathbf{R}_{pef-to-eci} = \begin{bmatrix} cos(\theta_{gmst}) & -sin(\theta_{gmst}) & 0 \\ sin(\theta_{gmst}) & cos(\theta_{gmst}) & 0 \\ 0 & 0 & 1 \end{bmatrix} \tag{3}$$

and

$$\frac{d\mathbf{R}_{pef-to-eci}}{dt} = \Omega_e \cdot \begin{bmatrix} -sin(\theta_{gmst}) & -cos(\theta_{gmst}) & 0 \\ cos(\theta_{gmst}) & -sin(\theta_{gmst}) & 0 \\ 0 & 0 & 0 \end{bmatrix} \tag{4}$$

where θ_{gmst} is the Greenwich mean sidereal utc time [radians] as defined by Eq. 2 in Vallado et al. [2006], and and Ω_e is $\frac{d\theta}{dt}$ or the angular velocity of Earth.

The tranformation from a PEF coordinate to an Earth-centered Earth-fixed (ECEF) coordinate system can then be achieved by (Appendix C in Vallado et al. [2006]),

$$\mathbf{r}_{ecef} = \mathbf{R}_{ecef-to-pef}^T \mathbf{r}_{pef} \tag{5}$$

and

$$\mathbf{v}_{ecef} = \mathbf{R}_{ecef-to-pef}^T \mathbf{v}_{pef} \tag{6}$$

where $\mathbf{R}_{ecef-to-pef}$ is the transformation matrix that accounts for polar motion and can be described by

$$\mathbf{R}_{ecef-to-pef} = \begin{bmatrix} 1 & 0 & 0 \\ 0 & cos(y_p) & -sin(y_p) \\ 0 & sin(y_p) & cos(y_p) \end{bmatrix} \cdot \begin{bmatrix} cos(x_p) & 0 & sin(x_p) \\ 0 & 1 & 0 \\ -sin(x_p) & 0 & cos(x_p) \end{bmatrix} \tag{7}$$

where x_p and y_p are polar motion coeffecients which can not be predicted theoretically, but data to estimate these can be obtained from *International Earth Rotation and Reference Systems Service* (IERS) bulletins [8]. However, polar motions are small (x_p and y_p coeffecients are typically smaller than half an arcsecond), and polar motions are neglected in this study, i.e. we assume $\mathbf{r}_{pef} = \mathbf{r}_{ecef}$, $\mathbf{v}_{pef} = \mathbf{v}_{ecef}$, and $\mathbf{R}_{pef-to-eci} = \mathbf{R}_{ecef-to-eci}$. The resulting error in position vector from this assumption is typically smaller than 20[m], and this is smaller than the accuracy of the error of the orbit propagator, which is stated to be about 1[km] / day (which translate to a $\sim$ 70[m] / 100[minutes]). Obtained orbit positions was compared to EUmetsat's reference data for Metop-A positions, and differences were found to be smaller than 50[m], which was deemed sufficient for the purpose of the study.

5.4.2 Attitude

The Metop-SG s/c platform will in routine operation be attitude controlled in such a way that its z-axis is pointing towards the local geodetic nadir direction and its x-axis (or nose) is aligned with the velocity vector relative to Earth surface. Thus, for a given viewing direction, $\vec{r}_{ref}$, in the s/c coordinate frame (where the x-axis is aligned with the flight direction, as described in Figure 1) we can obtain the viewing direction, $\vec{r}_{ecef}$, in the Earth Centered Earth Fixed (ECEF) coordinate frame by

$$\vec{r}_{ecef} = \mathbf{R}_{ecef-to-ref}^T \cdot \vec{r}_{ref} \tag{8}$$

where

$$\mathbf{R}_{ecef-to-ref} = \begin{bmatrix} \vec{u}_x & \vec{u}_y & \vec{u}_z \end{bmatrix}^T \tag{9}$$

and $\vec{u}_z$ is the local geodetic nadir pointing vector,

$$\vec{u}_y = \vec{u}_z \times \vec{v}_{ecef}, \tag{10}$$

and

$$\vec{u}_x = \vec{u}_y \times \vec{u}_z. \tag{11}$$

---

[8] urlhttps://www.iers.org/IERS/EN/Publications/Bulletins/bulletins.html

The resulting platform pitch, roll and yaw angles, are in fact not needed by any calculation, but can be obtained from the rotation matrix, $\mathbf{R}_{lof-to-ref}$ which relates directions in the local orbit frame (lof) to the s/c nominal frame

$$\mathbf{R}_{lof-to-ref} = \mathbf{R}_{ecef-to-ref} \cdot \mathbf{R}^T_{ecef-to-eci} \cdot \mathbf{R}^T_{eci-to-lof} \qquad (12)$$

where the x-axis of the lof is aligned with the inertial satellite velocity vector, and the y-axis is aligned in the opposite direction of the inertial satellite angular momentum vector, and hence

$$\mathbf{R}_{eci-to-lof} = \begin{bmatrix} \vec{\mathbf{v}}_{eci} & -(\vec{\mathbf{v}}_{eci} \times \vec{\mathbf{r}}_{eci}) & \vec{\mathbf{v}}_{eci} \times -(\vec{\mathbf{v}}_{eci} \times \vec{\mathbf{r}}_{eci}) \end{bmatrix}^T . \qquad (13)$$

The resulting pitch, roll, and yaw angles for orbit 6985 are displayed in Figure 12.

5.4.3 MWI and ICI scanning

The scanning characteristic of MWI and ICI instrument are described in Sect. 3. The scanning rotation of MWI and ICI is clockwise and counterclockwise, respectively, when seen from zenith side of the platform. Elevation and azimuth offset angles between fixed on board angles are described in Table 4 and Table 5 for MWI and ICI, respectively.

The transformation of a direction vector pointing in the boresight direction (or z-direction) in the antenna reference frame (see Figure 2) to the s/c reference frame can be achieved by

$$\vec{\mathbf{r}}_{ref} = \mathbf{R}_{rfa-to-ref} \cdot \mathbf{R}_{ant-to-rfa} \cdot \begin{bmatrix} 0 \\ 0 \\ 1 \end{bmatrix} =$$

$$\begin{bmatrix} cos(\phi(t)) & -sin(\phi(t)) & 0 \\ sin(\phi(t)) & cos(\phi(t)) & 0 \\ 0 & 0 & 1 \end{bmatrix} \cdot \begin{bmatrix} cos(\theta_{ch}) & 0 & sin(\theta_{ch}) \\ 0 & 1 & 0 \\ -sin(\theta_{ch}) & 0 & cos(\theta_{ch}) \end{bmatrix} \cdot \begin{bmatrix} 0 \\ 0 \\ 1 \end{bmatrix}, \qquad (14)$$

where the $\mathbf{R}_{rfa-to-ref}$ describes the rotation part of the instrument (radio frequency assembly, see also Figure 1) relative to the s/c reference frame, and

$$\theta_{ch} = 180 - \theta_{OBA} + \Delta\theta_{ch}, \qquad (15)$$

and

$$\phi(t) = \phi_{start} \pm \omega t + \Delta\phi_{ch}, \qquad (16)$$

where $\Delta\theta_{ch}$ is a channel specific elevation offset, ω is scan rate (+ for MWI and - for ICI), t is time, and $\Delta\phi_{ch}$ is a channel specific azimuth offset. The transformation of $\vec{\mathbf{r}}_{s/c}$ to a viewing direction in the ECEF coordinate frame can then be obtained by using Eq. 8.

Figure 12 displays calculated viewing directions (geodetic zenith and azimuth angles) for ICI channel 4 and 10 and orbit 6985. Figure 12 also displays the geolocalisation of the observations.

5.4.4 Geolocation of observation and additional information

The location of an MWI and ICI observation on the geoid is found from finding the closest intersection point between the line of sight and an ellipsoid having WGS84 characteristic. The solar azimuth and zenith angle of this point and associated date, is calculated using pyephem (https://rhodesmill.org/pyephem/). Given a date and location on the Earth's surface, pyephem can compute the position of the Sun.
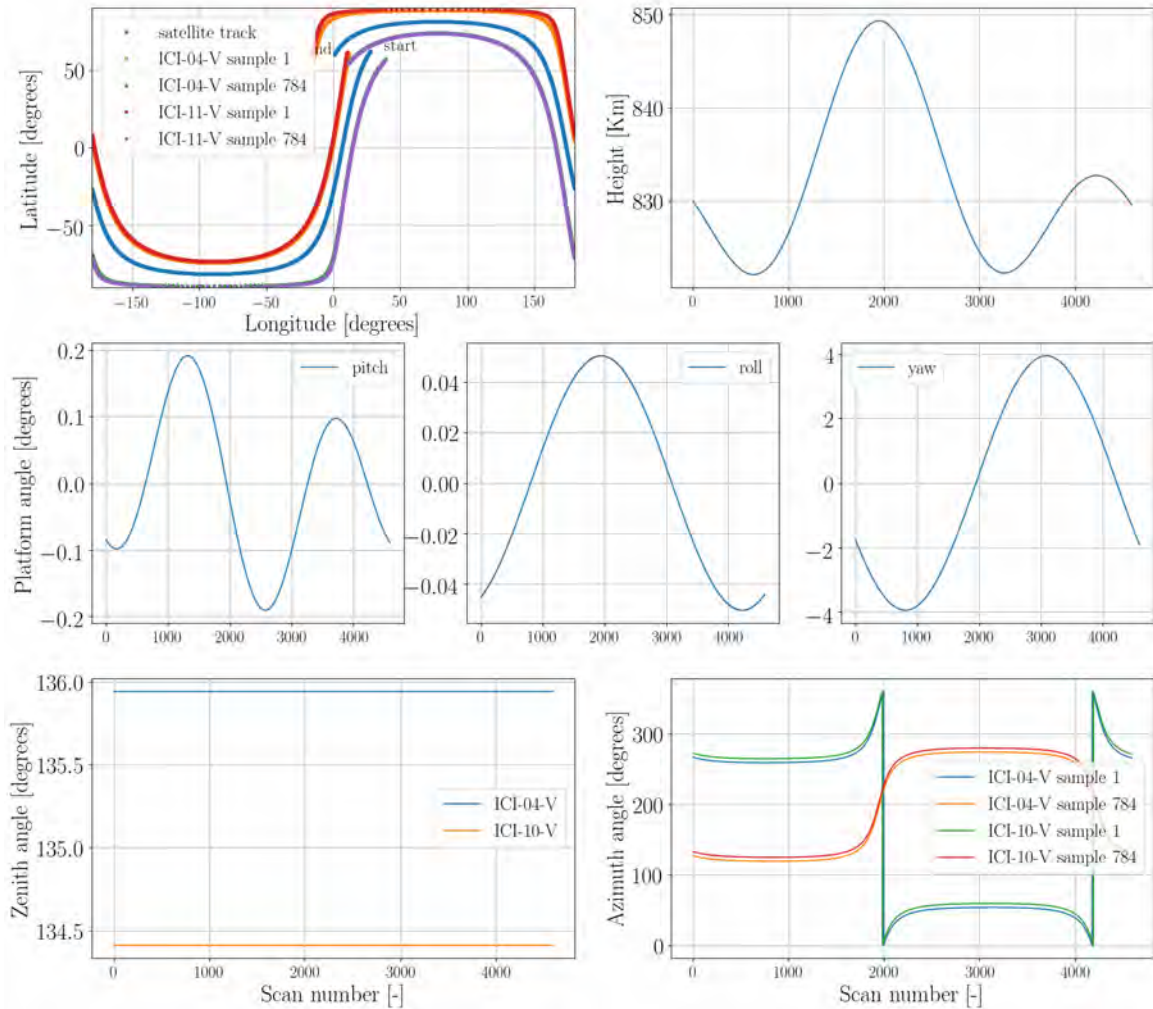
Figure 12: Results of scan simulations for ICI and orbit 6985. The upper left panel shows geodetic positions of satellite track and footprints on ground for the first and last sample of each scan ICI channel 4 and 10. The middle row panels shows resulting pitch, roll, and yaw angles related to the attitude steering. The lower panel shows (geodetic zenith and azimuth angles) for the ICI observations corresponding to the upper left panel.

	Backus-Gilbert footprint matching methodology applied on MWI and ICI observations	Code: TR/BG/MWI-ICI
		Issue: 1.0
		Date: June 5, 2019
		File: optimal-interpolation-applied.tex
		Page: 34 / 200

5.4.5 Antenna smoothing

The basic antenna response function used in this study only varies with angle from boresight for all MWI and ICI channels. However, the scanning motion of the instruments during the integration time will result in an antenna effective response function that varies with both zenith and azimuth angles. The antenna boresight will be rotated by an angle

$$\Delta\phi_{bs} = \Delta t / T_{scan} \cdot 360°, \tag{17}$$

where Δt and T_{scan} is the integration time and duration time of a complete scan, respectively, in the azimuthal direction during a given sample. These angles are 0.17847[degrees] and 0.10584[degrees] for ICI and MWI, respectively. The resulting antenna pattern smoothing effect is taken into account in the simulation.

Let us consider an antenna in space with the boresight directed towards Earth. The observed antenna temperature T_a can be described by

$$T_a = \int_\Omega G(\Omega) T_b(\Omega) d\Omega, \tag{18}$$

where G is the antenna response function or gain pattern, and is here normalised in such a way that

$$\int_\Omega G(\Omega) d\Omega = 1, \tag{19}$$

and Ω is the solid angle. Let us now consider an antenna that is moving during the integration time. If we let the antenna boresight direction be located in the xy-plane (see Figure 13), rotate an angle $\Delta\phi_{bs}$ around the z-axis, and point in the x-direction in the middle of the integration time (Δt), and furthermore assume that the beamwidth is narrow, we can rewrite Eq. 26 as

$$T_a = \int_{\theta=90-\Delta\theta}^{90+\Delta\theta} \int_{\phi=-\Delta\phi}^{\Delta\phi} \hat{G}(\theta,\phi) T_b(\theta,\phi) sin(\theta) d\theta' d\phi', \tag{20}$$

where $\hat{G}$ is an effective antenna response function that can be estimated as

$$\hat{G}(\theta,\phi) = \frac{1}{\Delta t} \int_{t=-\Delta t/2}^{\Delta t/2} G(\theta_{bs}(\theta,\phi,t)) dt', \tag{21}$$

where the angle relative to the boresight direction $\theta_{bs}(\theta,\phi,t)$, for a given point on the unit sphere is described by

$$\theta_{bs}(\theta,\phi,t) = \arccos\left([cos\left(\frac{\Delta\phi_{bs}t}{\Delta t}\right), sin\left(\frac{\Delta\phi_{bs}t}{\Delta t}\right), 0] \cdot [sin(\theta)cos(\phi), sin(\theta)sin(\phi), cos(\theta)] \right). \tag{22}$$

Example effective antenna response functions for MWI-1, MWI-18, ICI-1, and ICI-11 are shown in Figure 14, where it can be seen that the gain function is somewhat smoother along the direction aligned with the scanning motion (the effective gain function along the orthogonal direction is effectively identical to that of a non-rotating antenna). It can also be noted that

the smoothing effect is greater for the ICI channels than for the MWI channels, due to the ICI's longer integration time.

The effective antenna response function can further be discretized and normalized in such a way that

$$T_a = \sum_i^n \sum_j^m \hat{G}(\theta_i, \phi_j) T_b(\theta_i, \phi_j). \tag{23}$$
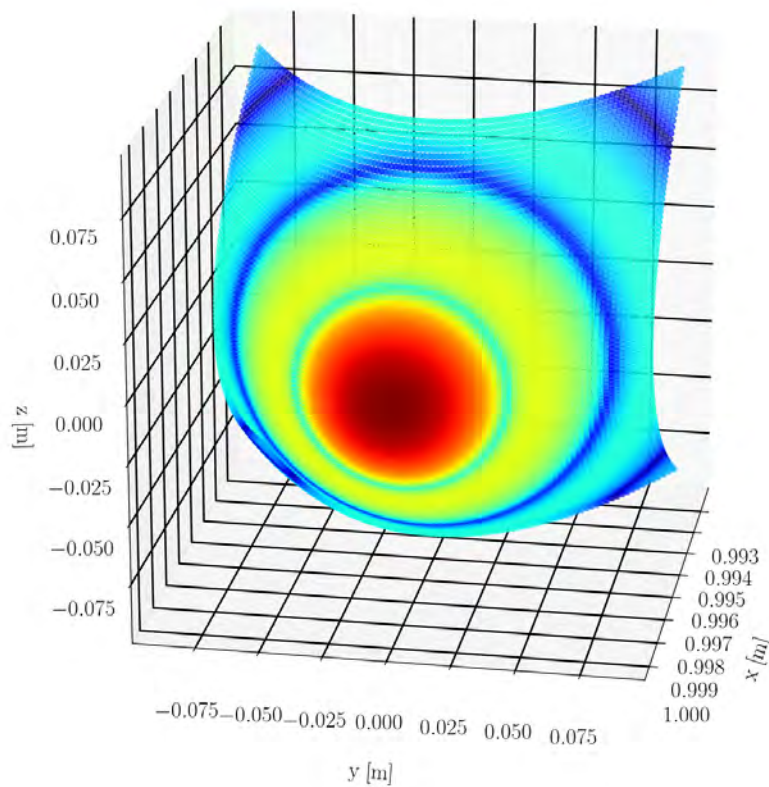
Figure 13: Schematic describing the geometry used when estimating effective antenna pattern, taking into account of a rotation (around z-axis in figure) during the integration time (see text for more details). The colorcoding corresponds to MWI-1 antenna pattern projected on a part of the unit sphere, centered around the boresight direction, which here points in the x-direction.

	Backus-Gilbert footprint matching methodology applied on MWI and ICI observations	Code: TR/BG/MWI-ICI
		Issue: 1.0
		Date: June 5, 2019
		File: optimal-interpolation-applied.tex
		Page: 37 / 200
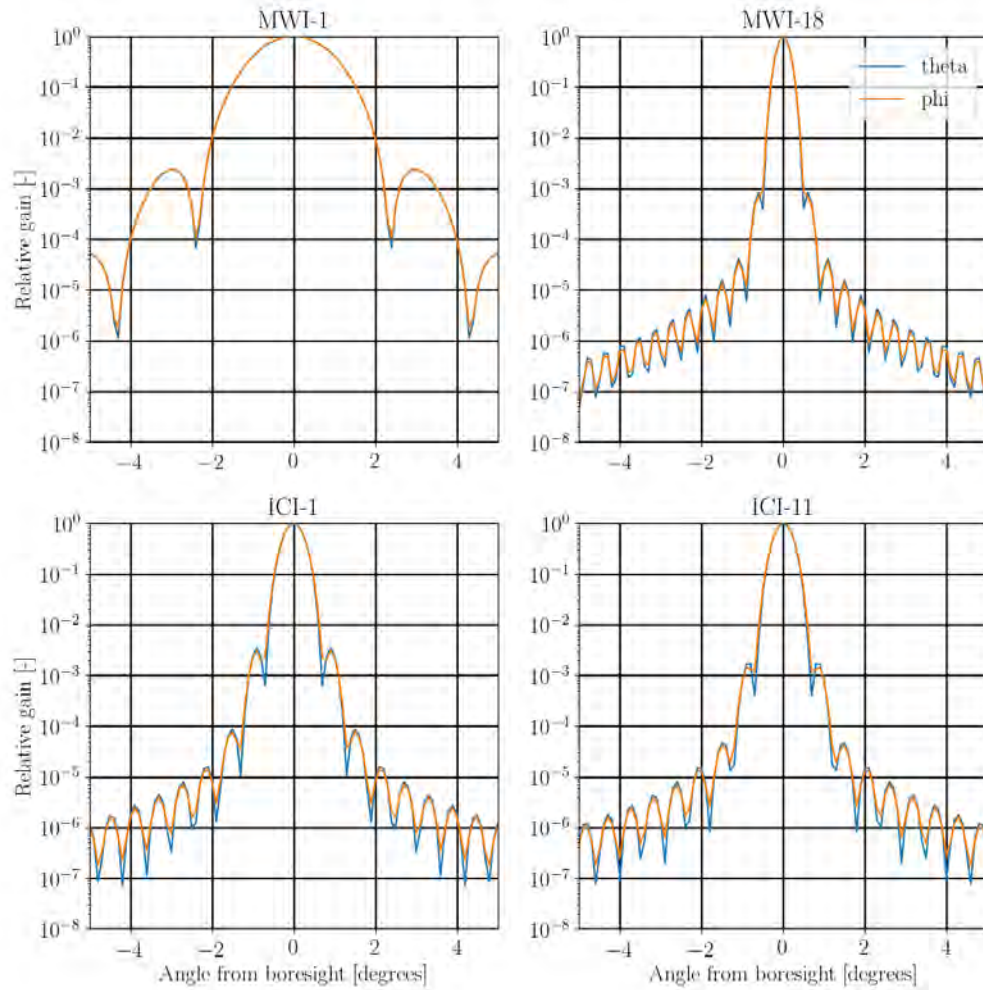
Figure 14: Effective relative gains for MWI-1, MWI-18, ICI-1, and ICI-11 as function of angle from boresight direction, along the directon of scan rotation (phi) and the orthogonal direction (theta).

	Backus-Gilbert footprint matching methodology applied on MWI and ICI observations	**Code:** TR/BG/MWI-ICI
		Issue: 1.0
		Date: June 5, 2019
		File: optimal-interpolation-applied.tex
		Page: 38 / 200

5.5 Generation of antenna temperatures

5.5.1 Representation of sensor characteristics

Antenna temperatures, T_a, are calculated as

$$T_a^V = \sum_{i=1}^{n} w^i (T_{b,I}^i + T_{b,Q}^i) \tag{24}$$

if the channel measures vertical polarisation and

$$T_a^H = \sum_{i=1}^{n} w^i (T_{b,I}^i - T_{b,Q}^i) \tag{25}$$

if the channel measures horizontal polarisation. Here, n is used for the number of directions, w^i is antenna weight for direction i and T_b^i is pencil beam Stokes vector derived for the direction. The set of antenna weights is always normalised to have a sum of 1. The Stokes vector T_b applied contains values converted to brightness temperatures, and the first element, representing the total intensity, is denoted as $T_{b,I}$ and the second element, representing the difference between V and H, is denoted as $T_{b,Q}$. See Eriksson et al. [2011] for further details.

How well the antenna pattern response gets represented depends on the number of direction considered and how they are distributed around the boresight direction. Some different approaches are discussed below. But as a general remark it is mentioned that it is not necessary to represent the antenna response over the full 10°x10° angle range provided. It was tested to extract centre regions with a width proportional to the HPBW. It was found that a (full) width of 5·HPBW throughout gives a coverage of 99.88% of the original response. This coverage should suffice, as a normalisation to 1 is applied. The normalisation ensures that a correct result is always obtained if T_b is totally constant. A worst case scenario is that the mean of T_b in the neglected region of the antenna pattern differs with 100 K to the mean inside the considered area. This scenario gives a maximum representation error of 0.12 K for a 99.88% coverage of the total response.

The equations above neglect a possible "leakage" between H and V of the sensor, but this should be a marginal effect and the polarisation of the sensor itself is well described. On the other hand, the radiative transfer simulations are not fully realistic with respect to polarisation. The main limitation is that only totally random orientation of hydrometeors is assumed.

It was decided to represent each instrument channel with a single (monochromatic frequency), to afford a more dense swath grid with the same simulation time. For channels around water vapour transitions, the centre frequency of the lower passband was selected. For all other channels, the mean frequency was applied. This is a simplification, but should be an acceptable one. The resulting error should mainly be of systematic character. Some test simulations gave that for clear-sky conditions the error is largest for 325.15 ±9.5 K. The difference for this channel between upper and lower passband was found to be 1.8 K for a tropical scenario, and smaller for other considered scenarios. Hydrometeor scattering will decrease the difference between the passbands. As the "true" value is the mean of the passbands, this means that error due to neglecting the second passband should stay below 1 K. It is not unlikely that the uncertainty in the water vapour absorption also corresponds to 1 K.

5.5.2 Approach to represent antenna pattern

The antenna pattern is given on a rectangular angular grid, centred around the boresight direction. A basic decision was to avoid doing any interpolation of the antenna response, as it varies with order of magnitudes and an interpolation easily can introduce large errors. That is, the summation in Eqs. 24 and 25 will follow the gridding of the antenna response and w^i are the antenna response values provided (after integration time smoothing).

The incoming radiances (T_b^i) are determined by projecting a number of antenna directions down to the reference ellipsoid and the Tb-data are interpolated to this point and incidence angle, as described below. Ideally, this projection and interpolation should be performed for all points of the antenna pattern considered, but this would lead to extensive calculations. This can be avoided by noting that the representation of the incoming radiance field is less critical away from the boresight direction, as the antenna response values are there orders of magnitude lower. For this reason, it was decided to determine T_b^i for a smaller set of directions and perform a second interpolation from these directions to all the antenna grid positions considered.

Several versions of this scheme was tested. In the end a scheme using nested rectangular grids was selected. The layout of these nested grids is described by Fig. 15. To summarise, there are two main steps

1 T_b^i is determined for each point on a nested grid. The nested grid is set according to the width of main lobe. Details are found below.

2 These data are interpolated to the full rectangular grid. With the settings suggested below, the points of the nested grid is a sub-set of the full grid, and around the boresight there is effectively no interpolation. That is, the interpolation only fills the "gaps" found away from the boresight direction.

The interpolation in step 2 is made by Delaunay triangulation, in a linear fashion. In practice this was achieved by Matlab's function `scatteredInterpolant`[9], with the option `method` set to "linear". Final data are exemplified in Figs. 9 and 16.

5.5.3 Nested grid settings

There are three settings in the generation of the nested grids applied: spacing of finest grid, minimum coverage of the finest grid, and minimum coverage of the full grid. The last two criteria are defined as a scaling factor with respect to HPBW, denoted as c and f, respectively. That is, the coverage shall be $\geq c{\cdot}$HPBW and $\geq f{\cdot}$HPBW, respectively.

A test area was simulated with different settings. It was found that the spacing of the finest grid preferably should be set to $0.1°$, to ensure that the nested grid and the antenna pattern grid overlap perfectly around the boresight direction. This is beneficial as then there is effectively no interpolation of the antenna pattern around the boresight direction. Compared to reference calculations with $0.05°$ spacing, a spacing of $0.08°$ of gave deviations up to $0.5\,\mathrm{K}$, while the deviations for $0.1°$ stayed below $0.01\,\mathrm{K}$. A spacing of $0.2°$ gives also a match between the antenna and nested grids, but was found to give errors up to $3\,\mathrm{K}$.

---

[9]mathworks.com/help/matlab/ref/scatteredinterpolant.html
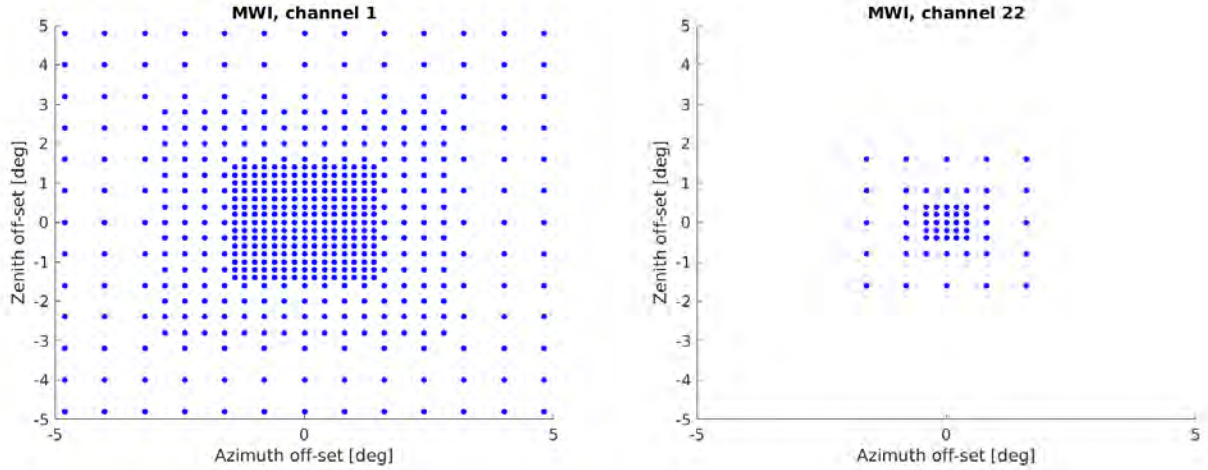
Figure 15: Examples on "nested grids" for MWI channel 1 (left) and channel 22 (right), representing most broad and most narrow antenna patterns to consider. The generation of a nested grid starts by laying out the innermost grid, defined to have a spacing and a width in terms of number of points. Layers are added until the target width is matched (probably with margin). For each new layer the spacing is doubled (number of points is not changed), and it is placed on top of the first one. The number of points must be an odd integer, and all layers obtain a point at (0,0). Duplicates of points are removed to form the full final nested grid. In these examples, the innermost layer has a spacing of 0.2°, the fine spacing covers $\geq 1.5\cdot$HPBW and the full width is $\geq 5\cdot$HPBW.

The value of c impacts strongly on the number of points of the nested grid. The factor f has less impact on the nested grid size, but a higher f results that data will be interpolated to more antenna directions (this number increases with f^2). That is, there is a considerable cost in increasing both c and f.

Various combinations of c and f were tested, and the combination of $c = 1$ and $f = 3.5$ was found to give a balance between accuracy and calculation time. Among the test simulations, the maximum deviation found, compared to test simulations using $c = 5$ and $f = 5.5$, was 0.5 K. No significant bias was found and the standard deviation of the deviations was only 0.03 K. The simulations indicated that the combination of $c = 2$ and $f = 4.5$ decreases the maximum deviations with one order of magnitude (but tested with less data), and this combination could be a candidate if very accurate simulations are required.

With $c = 1$ and $f = 3.5$, the number of points in the nested grid is $849/57/129$ and the processing time per Ta-value is $57/9/14$ ms (using one core) for MWI channel 1, MWI channel 15 and ICI channel 4, respectively. The processing for a complete orbit for these channels, using a single core, takes about 102, 16 and 14 hours, respectively.

5.5.4   Extraction of T_b^i

The scanning simulation gives the boresight direction for each antenna temperature value to derive. Each boresight direction is summed with the relative angles of the nested grid generated, to obtain the viewing directions for which T_b values shall be extracted. The viewing directions
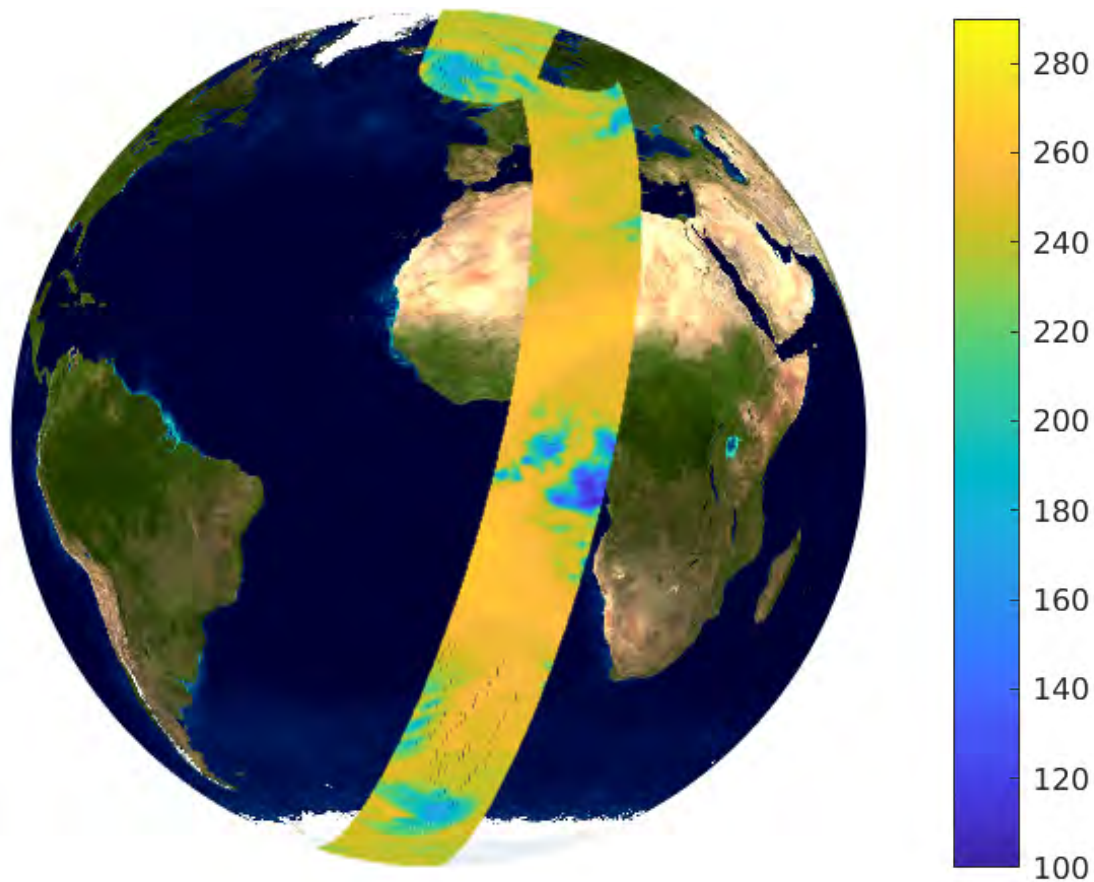
Figure 16: Example on simulated antenna temperatures. Data for ICI channel 12 and a part of orbit 6985 are shown.

are mapped to positions and zenith angles at the intersection with the reference ellipsoid. The found position and angle are used to interpolate the swath Tb-data. The most critical steps are commented below.

A possible pitfall is how boresight and antenna pattern angles are added. The angles can not simply be summed up. An obvious example is when the zenith angle of the boresight direction is 180°. The antenna pattern positions matching a positive shift in zenith angle of ±0.1° both ends up at a zenith angle of 179.9°, but at azimuth directions differing with 180°. In ARTS this handled by rotating unit vectors representing the antenna pattern angle off-sets from a proper reference direction, to the actual boresight direction. The ARTS approach was applied here.

As indicted above, for each pencil beam direction the intersection with the reference ellipsoid is determined (with a modified version of Matlab's `lookAtSpheroid`[10] function), that gives a geographical position. This position is related to the swath grid by another Delaunay-based interpolation (again using `scatteredInterpolant`). That is, the latitudes and longitudes of the swath grid are interpolated to the found intersection with ellipsoid in such way that the

---

[10]mathworks.com/help/map/ref/lookatspheroid.html

	Backus-Gilbert footprint matching methodology applied on MWI and ICI observations	Code:	TR/BG/MWI-ICI
		Issue:	1.0
		Date:	June 5, 2019
		File:	optimal-interpolation-applied.tex
		Page:	42 / 200

interpolation gives the "grid position". For example, a grid position of 8 means that a point is exactly on top of the 8th grid value, and a grid position of 8.5 means the point is at the middle point between grid value 8 and 9.

The along-track and across-track grid positions are converted to interpolation weights for the four grid values surrounding the intersection point. These weights are set to match a 2D linear interpolation. The two-step procedure of determining grid positions and applying interpolations weights follows how interpolation is done inside ARTS. In this way the interpolation can effectively be applied on multiple frequencies and all Stokes elements in parallel.

The last step is to interpolate the two Stokes elements at all frequencies of concern in (geocentric) zenith angle. A linear interpolation is applied. The zenith angle of the viewing direction (at the reference ellipsoid) is calculated by Atmlab's `cartposlos2geocentric`. This interpolation gives $T_{b,I}^i$ and $T_{b,Q}^i$.

No extrapolation is allowed in the Delaunay interpolation, which gives an automatic check that the swath Tb-data actually covers the antenna pattern. However, a small extrapolation must be allowed around the North and South poles. For example, the maximum latitude in the swath data can be $89.96°$, while a pencil beam direction can end up at latitude $89.98°$. This will appear as an extrapolation in latitude, even if the North pole is inside the swath grid. To handle this, nearest neighbour extrapolation is allowed of the absolute value of the latitude is above $88°$.

5.5.5 Simulations vs. observations

Figure 17 displays some observations and simulations for the part of orbit 6895 already considered in Fig. 9. The observations and simulations are not directly comparable. First of all, AMSU and MHS are across-track scanning instruments, while the simulated MWI is a conical scanning instrument. The effect of different incidence angles result in that MHS channel 5 has higher values than MWI channel 22 in the centre of the swath, while the agreement is much better at the edge of the MWI swath where the incidence angles roughly agree between the two instruments. For channels sensitive to the surface, the polarisation response must also be considered. At the edge of their swaths, AMSU and MHS has a polarisation response that approximately matches the mean of V and H. For this reason, the mean of MWI's V and H channels are shown in the top two rows of panels, corresponding to 31 and 89 GHz, respectively. Considering these aspects, there is no remarkable disagreement between observations and simulations.

Figure 18 shows the same selection of channels, but for a part of orbit 6895 covering an area with convective activity above the Pacific ocean. For this "scene" there are more clear differences. These differences should mainly have their origin in the ERA5 data. It shall here be remembered that forecast data have been applied, and not the analysis version that should be more accurate. The ICI simulations for this part of orbit 6895 are found in Figs. 19 and 20.
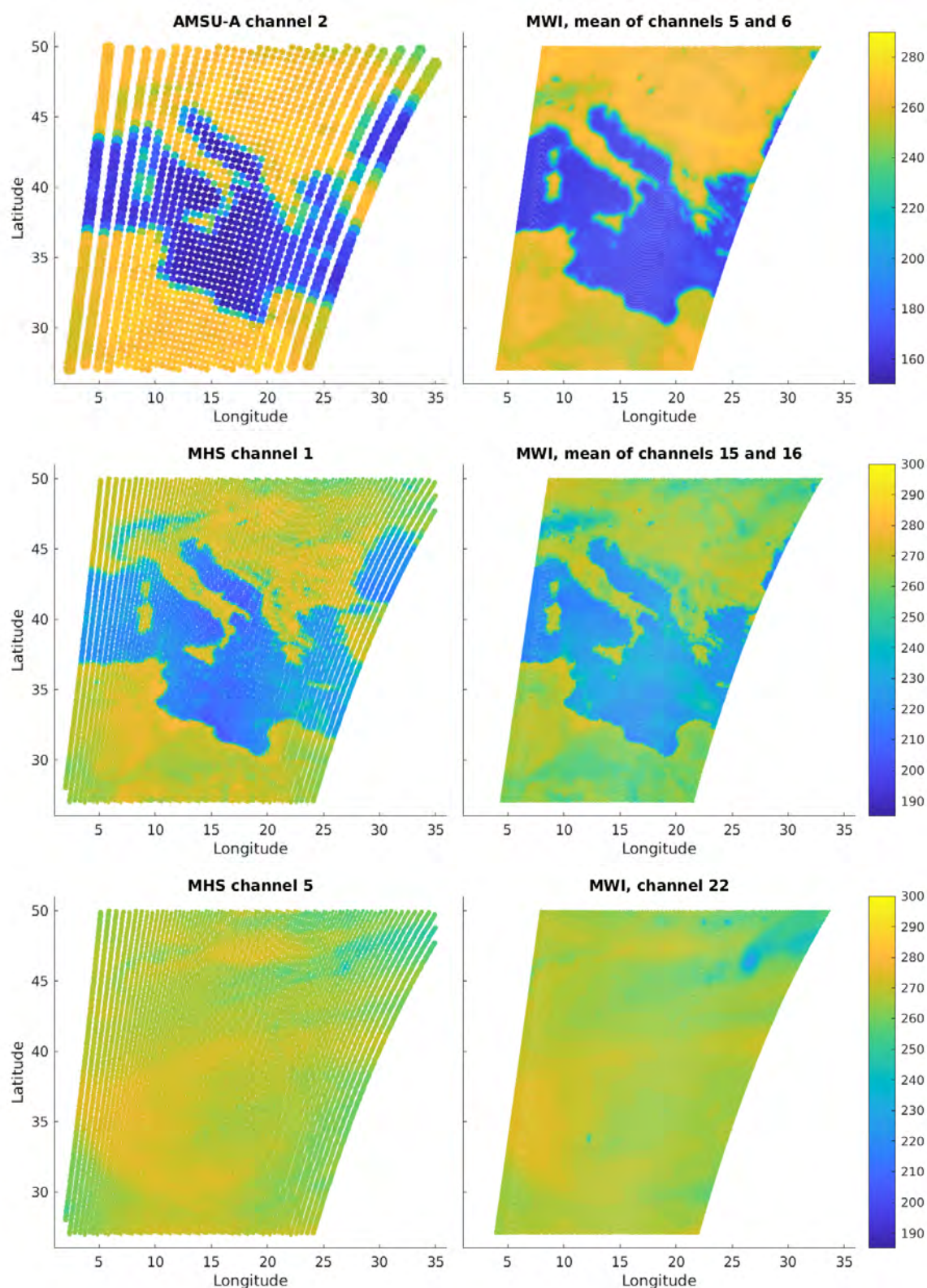
Figure 17: Observations by AMSU and MHS (left column) and MWI simulations (right column) for part of orbit 6895. The observation and simulations are not directly comparable, mainly due to different scanning patterns. See the text for details.

	Backus-Gilbert footprint matching methodology applied on MWI and ICI observations	Code:	TR/BG/MWI-ICI
		Issue:	1.0
		Date:	June 5, 2019
		File:	optimal-interpolation-applied.tex
		Page:	44 / 200
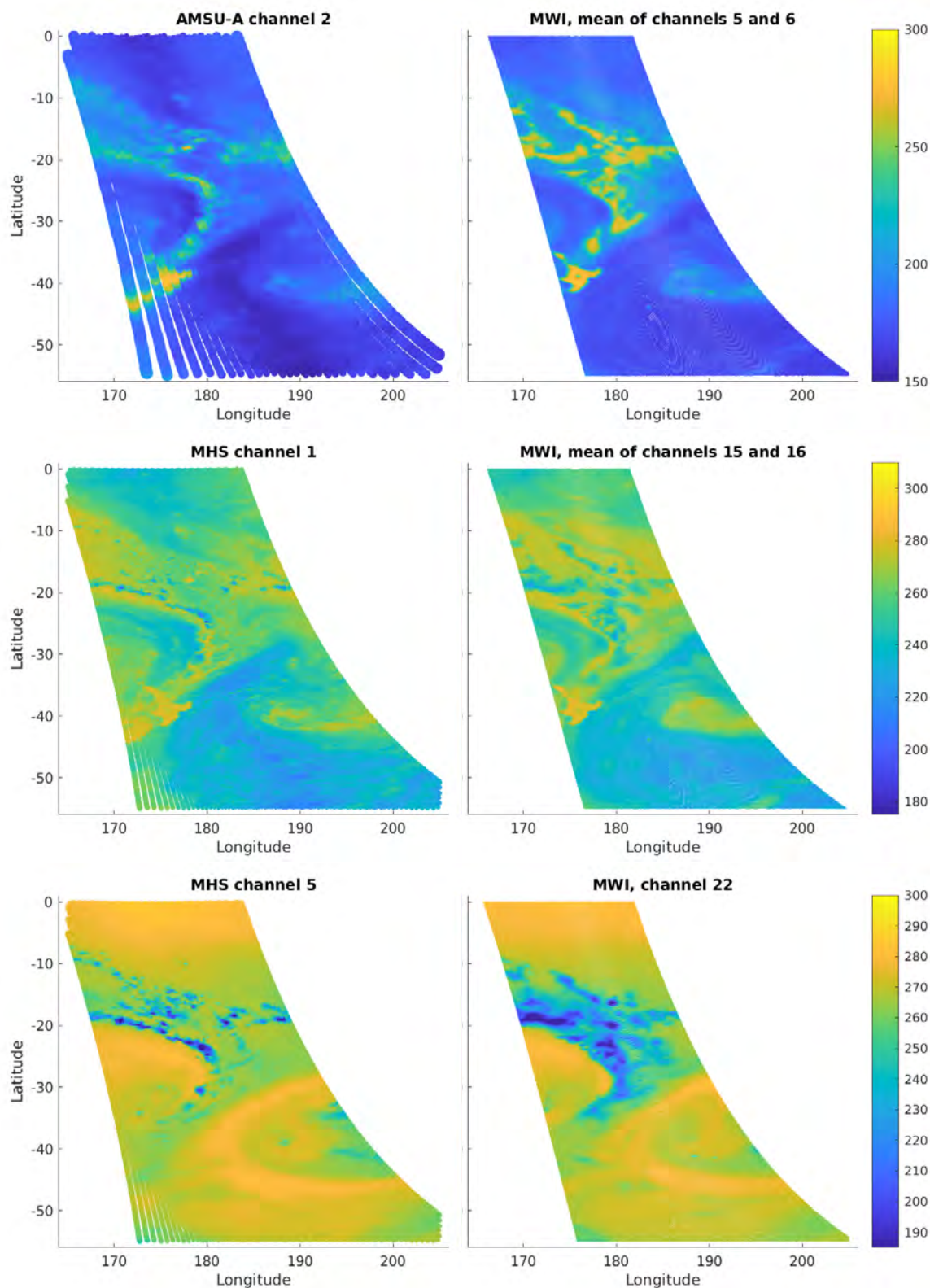
Figure 18: As previous figure, but for another part of orbit 6985.
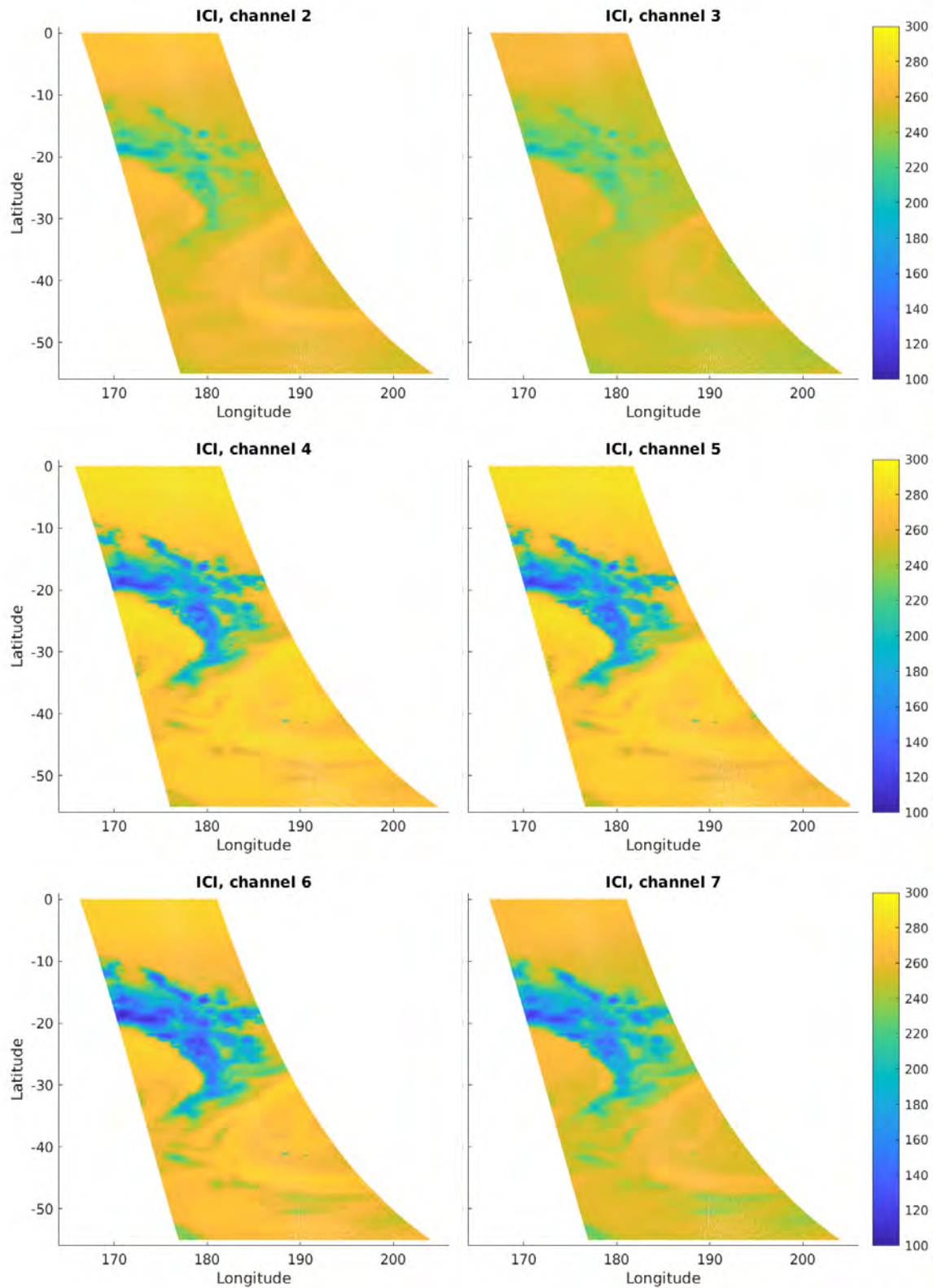
Figure 19: ICI simulations for channel 2-7 and same part of orbit 6895 as shown in previous figure. Results for ICI channel 1 are identical to the MWI channel 22 results (in the previous figure).

	Backus-Gilbert footprint matching methodology applied on MWI and ICI observations	Code: TR/BG/MWI-ICI
		Issue: 1.0
		Date: June 5, 2019
		File: optimal-interpolation-applied.tex
		Page: 46 / 200
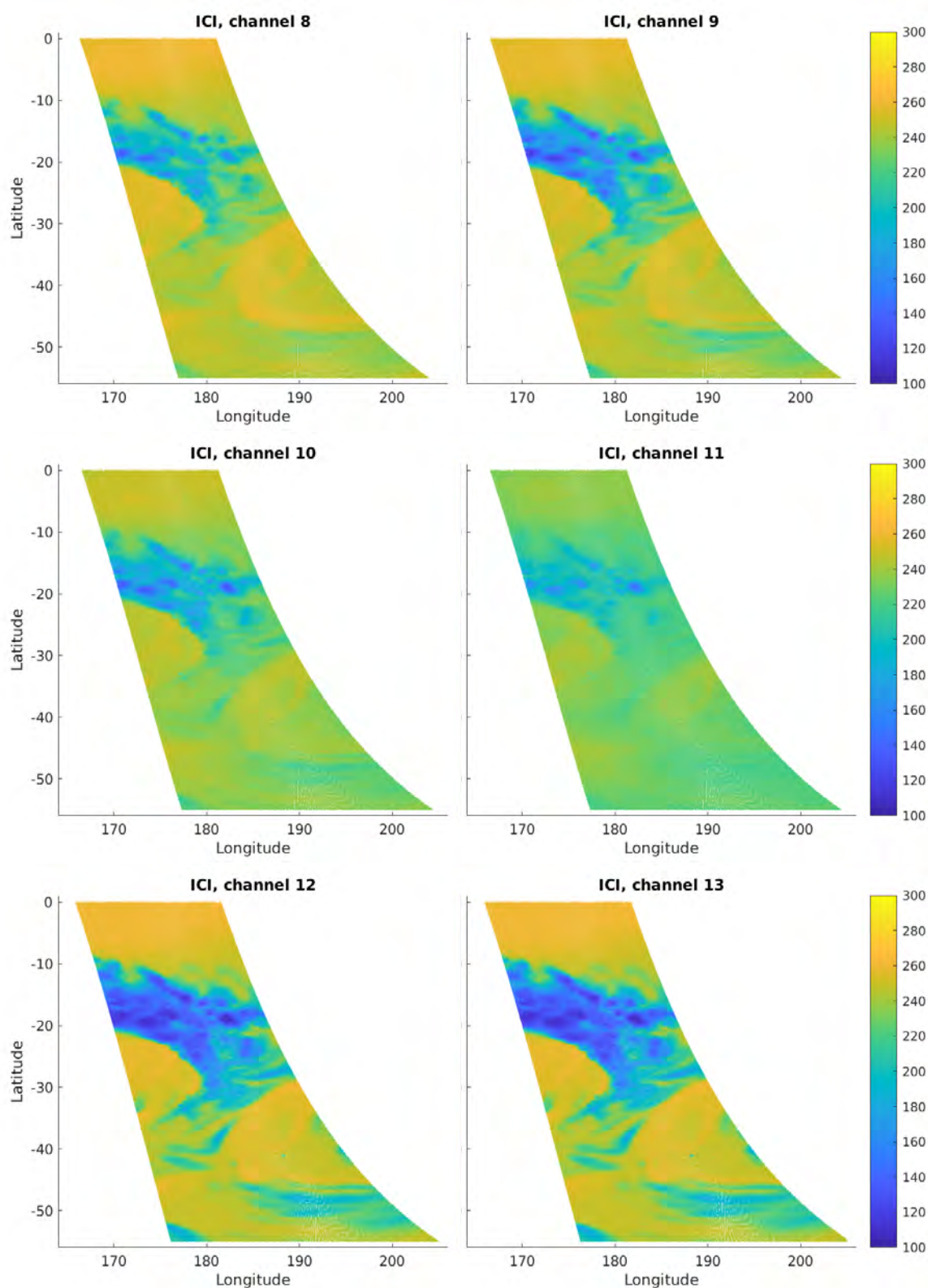
Figure 20: ICI simulations for channel 8-13 and same part of orbit 6895 as shown in two previous figures.

Part II

Backus-Gilbert footprint matching methodology:
Algorithm and toolbox description

6 Backus-Gilbert methodology

6.1 Basis for footprint matching

The Backus–Gilbert (BG) inversion method was first developed for the inversion of gross Earth data [Backus and Gilbert, 1970]. The BG methodology was then adapted by Stogryn [1978] for retrieving brightness temperatures fields from a set of radiometer measurements, and this methodology has successfully been applied for footprint matching between various satellite data channels (e.g Bennartz [2000] and Maeda and Imaoka [2016]). The basis of the BG methodology for footprint matching is described below.

Let us consider an antenna in space with the boresight directed towards Earth. The observed antenna temperature T_a can be described by

$$T_a = \int_\Omega G(\Omega)T_b(\Omega)d\Omega, \tag{26}$$

where G is the antenna gain function, and is here normalized in such a way that

$$\int_\Omega G(\Omega)d\Omega = 1, \tag{27}$$

and Ω is the solid angle. The solid angle is a measure of the amount of field of view from some particular point that a given object covers. One can approximate the solid angle subtended by a small facet having a flat surface area dA, orientation $\hat{n}$, and distance r from the antenna as

$$d\Omega = 4\pi \frac{dA}{A}(\hat{r} \cdot \hat{n}) = \frac{cos(\theta)dA}{r^2}, \tag{28}$$

where A=$4\pi r^2$ is the surface area of a sphere, and θ is the incidence angle. This gives that Eq. 26 can be rewritten as

$$T_a = \int_A \frac{G(\rho)T_b(\rho)cos(\theta)dA}{r(\rho)^2} = \int_A G_i(\rho)T_b(\rho)dA, \tag{29}$$

where ρ represents a position on Earth surface, and we also define the antenna gain pattern G_i. That is, each observation can be expressed as an integration over a surface area rather than an integration over a solid angle.

	Backus-Gilbert footprint matching methodology applied on MWI and ICI observations	Code: TR/BG/MWI-ICI
MᴏᴛᴀᴏW		Issue: 1.0
		Date: June 5, 2019
		File: optimal-interpolation-applied.tex
		Page: 48 / 200

Following the BG methodology [Stogryn, 1978], an estimate of a set of coefficients a_i can be derived, that allows one to make an estimate of the antenna temperature of a synthetic or target measurement,

$$T_a = \int_A T_b(\rho) F(\rho)(\rho) dA, \tag{30}$$

where F is the target antenna gain pattern, according to

$$\hat{T}_a = \sum_{i=1}^{n} a_i T_{a,i} = \int_A T_b(\rho) \sum_{i=1}^{n} a_i G_i(\rho) dA \tag{31}$$

where $T_{a,i}$ is a set of n actual observations with antenna gain pattern G_i. Ideally,

$$\sum_{i=1}^{n} a_i T_{a,i} - \int_A T_b(\rho) F(\rho)(\rho) dA = 0, \tag{32}$$

but it should be clear that the agreement is limited by the observation system.

The effective antenna gain pattern of $\hat{T}_a$ is

$$G_e = \sum_{i=1}^{n} a_i G_i, \tag{33}$$

and the error of the fit Q_0 to the target antenna pattern F is given by

$$Q_0 = \int_A \left(\sum_{i=1}^{n} a_i G_i(\rho) - F(\rho) \right)^2 dA, \tag{34}$$

and the error (variance) due to random measurement error is

$$\Delta T^2 = \mathbf{a^T E a} \tag{35}$$

where $\mathbf{E}$ is the measurement error covariance matrix.

The challenge is to find the set of coefficients a_i such that the reconstructed observation has desirable characteristics (low noise and good fit to the target antenna pattern). These two objectives are not directly comparable and not always obtainable, and may require some compromise. Anyhow, the BG method [Stogryn, 1978] provides a solution vector $\mathbf{a}$ of weights that minimize a sum of the integrated squared error in the fit, and variance due to noise amplification, i.e

$$Q = Q_0 + w\beta\Delta T^2, \tag{36}$$

where w and β is a scaling and smoothing parameter, respectively. For simplicity we set $w = 1$ and let β take the role as both a scaling and smoothing parameter. This has no effect on the range of possible solutions that can be obtained. The β parameter can also be seen as a trade off parameter, and is described more in details in Sect. 6.2. A normalization constraint while minimizing Q (Eq. 36) is

$$\int_S \sum_{i=1}^{n} a_i G_i dA = 1, \tag{37}$$

that will assure that Eq. 31 can be applied without introducing any bias if $T_b(\rho)$ is constant.

The vector of weighting coefficients can be obtained from

$$\mathbf{a} = \mathbf{V^{-1}} \left(\mathbf{v} + \frac{1 - \mathbf{u^T V^{-1} v}}{\mathbf{u^T V^{-1} u}} \mathbf{u} \right), \tag{38}$$

where

$$\mathbf{V} = \mathbf{G} + \mathbf{E}\beta, \tag{39}$$

$$u_i = \int_A G_i(\rho) dA, \tag{40}$$

$$v_i = \int_A G_i(\rho) F_i(\rho) dA, \tag{41}$$

and

$$G_{i,j} = \int_A G_i(\rho) G_j(\rho) dA. \tag{42}$$

It can be noted that $\mathbf{G}$ is a matrix of size $n \times n$ and element $G_{i,j}$ can be seen as description of the amount of antenna gain pattern overlap between sample i and j. The vector $\mathbf{v}$ has a length of n, and element v_i describes then the amount of overlap between sample i and the target antenna gain pattern. The vector $\mathbf{u}$ has also a length of n, and element u_i is a simple integration of the sample i antenna gain pattern over the surface, and can be seen to be included in order to obtain a correct normalization. It should be clear that the computational cost of solving Eq. 38 quickly grows with n.

6.2 Trade off between noise and fit error

The aim of the footprint remapping is that the reconstructed observations both have low noise and good fit to the target antenna gain pattern. These two objectives are not directly comparable and in general a trade off between the resulting noise and fit errors must be performed. That is, the smoothing parameter β to be applied should be selected in such a way that reconstructed observations have best possible characteristics.

The L-curve technique can here be used to allow for a trade-off analysis [Hansen and O'Leary, 1993]. The L-curve technique can be seen as a log-log plot of the obtained fit and noise errors, both functions of the smoothing parameter β. An example of such a plot is shown in Figure 21, which shows trade off analysis data for MWI-14 to MWI-3 remapping (details about how the data were obtained is described in Sect. 7). It can be seen that the shape of the curve is similar to the letter L, which explains the name of this technique. The general principle is that increased smoothing reduces the noise error while degrading the fit (the fit error is here defined as $\int_A \sqrt{\left(\sum_{i=1}^n a_i G_i(\rho) - F(\rho)\right)^2} dA$ and the noise error as $\sqrt{\mathbf{a}^T \mathbf{E} \mathbf{a}}$). Furthermore, it can be seen that the fit error is already relatively low for a β value around 10^{-6} and there is little reduction in fit error for lower β values. It is therefore reasonable to consider that a β value around 10^{-6} should be suitable to apply. The associated value of β of the point along the L-curve where the curvature, or κ, is as greatest, is an "optimal" value of β, according to the L-curve technique.

Calculation of κ for a point along the curve can be determined via numerical techniques, and is further described in Sect. 7.1.5.

A straight forward application of the L-curve technique to determine optimal value of β neglects that there might be additional constraints on the remapping, e.g. to keep the noise error below a given value. This is of particular importance for the remapping from a larger to smaller footprint which can result in high noise errors. An "optimal" value of β can then simply be obtained from the lowest value of β that results in an acceptable noise error.

Another consideration is that it is not meaningful to strive for fit errors that are smaller than uncertainties in the antenna patterns used in calculation. Additionally, it is preferable to apply as much smoothing as possible (given that fit-error is kept below an acceptable level) as increased smoothing produces the additional benefit of stabilizing the matrix inversions against round-off error without otherwise affecting the calculated weighting coefficients considerably. Thus, it is also meaningful to include a boundary condition around the smallest value of fit error that is of interest in the trade off analysis. Thus, if the "optimal" value of β as derived from L-curve technique results in a fit error that is lower than a specified limit, one can simply chose a higher value of β with a corresponding fit error that match the specified limit. Trade off analysis for MWI and ICI remapping is further described in Sect.7.1.5.
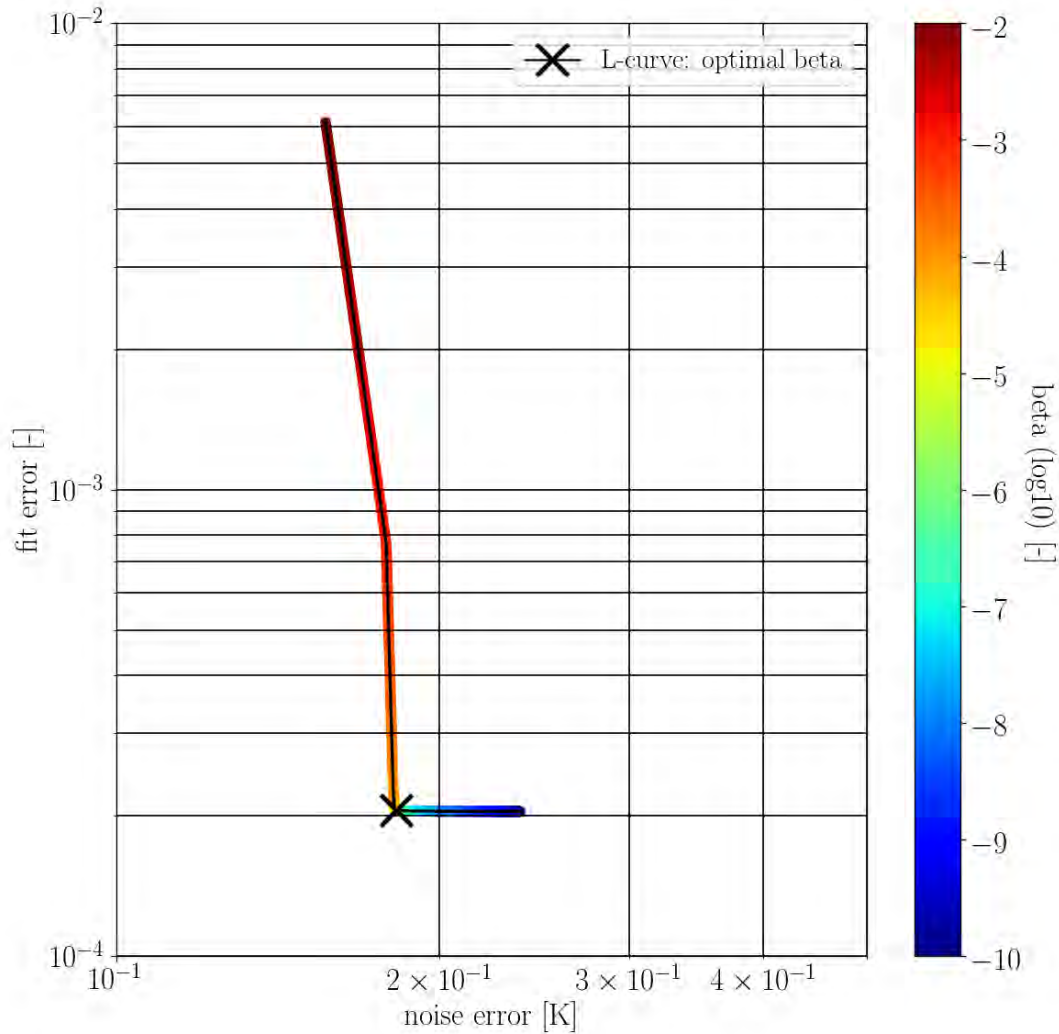
Figure 21: Trade off analysis data: log of noise and fit error as function of smoothing parameter beta, for MWI-14 to MWI-3 remapping. This curve is referred to as the L-curve due to its shape, and can be used to derive an optimal value of beta, and the optimal beta derived from the L-curve technique is also indicated in plot (see text for more details).

	Backus-Gilbert footprint matching methodology applied on MWI and ICI observations	**Code:** TR/BG/MWI-ICI
		Issue: 1.0
		Date: June 5, 2019
		File: optimal-interpolation-applied.tex
		Page: 52 / 200

7 Footprint remapping applied on MWI and ICI

7.1 Deriving weighting coefficients for remapping

The algorithm applied to derive optimal weights for footprint remapping of MWI and ICI observations is here described. It is stressed that, in general, it is not sufficient to derive a single set of weighting coefficients for the channel remapping, as, for example, optimal weighting coefficients will be different for observations in the center and outer part of a given scan. This is further discussed in Sect. 7.3, and we here focus on the basic task of the estimation of optimal weighting coefficients for a given observation. The flow scheme of the calculation can be described by:

- calculate the position on the geoid for the "target" observation (see Figure 22). Scan and channel characteristics of MWI and ICI observations, and how to model the scanning and determine the geolocation of a given observation, are described in Sect. 3 and Sect. 5.4

- generate a rectangular grid on geoid surface centered around the geolocation, and with an orientation that is aligned with the line of sight to the sensor (see Figure 22)

- identify all samples (from the channel that is to be remapped) that have a geolocation closer than a distance r_{max} from the target geolocation (see Figure 22 and Sect. 7.1.4). Only these samples will be included in the calculation.

- construct 2-dimensional smoothed antenna gain functions (from basic 1-dimensional antenna gain function data) that takes into account of the movement of the antenna boresight during the integration time (see 7.1.2)

- calculate the projection of the antenna gain pattern on the rectangular grid for the target observation (see Sect. 7.1.3 and Fig. 24) and all identified samples

- apply the Backus-Gilbert methodology (Sect. 6) and make a trade off analysis (Sect. 7.1.5) in order to derive best possible characteristic of the reconstructed observation (Sect. 7.2).
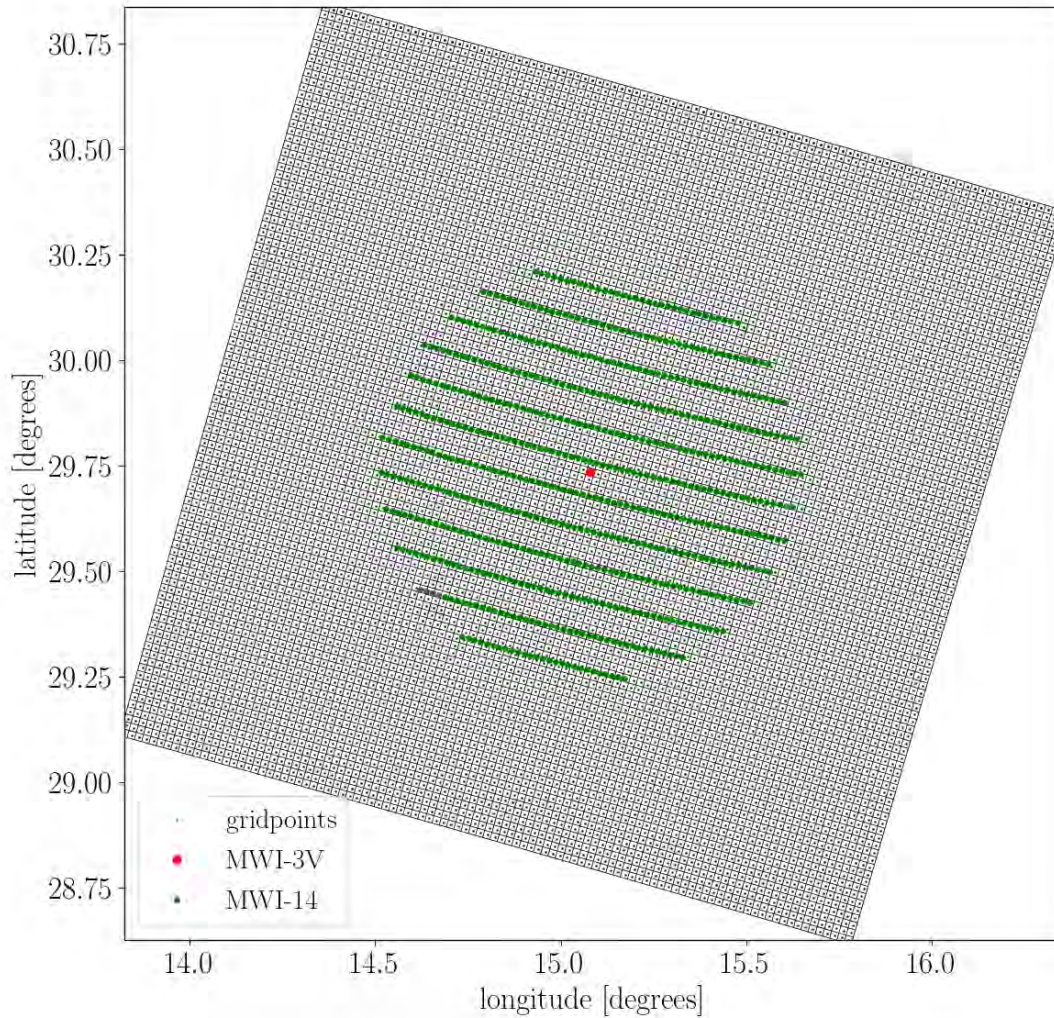
Figure 22: Schematic showing the applied rectangular grid and selection of samples to be included in the calculation for deriving weighting coefficients, using the the resampling of MWI-14 (10[km] footprint size) samples to the target MWI-3 resolution (30[km] footprint size). The rectangular grid on geoid surface is centered around the geolocation of the "target" observation (in this case MWI-3) and with an orientation that is aligned with the line of sight to the sensor. The figure also displays the geolocation of all MWI-14 samples within a radius of 55[Km] from the MWI-3 observation, and only these samples are considered for further calculation (A 55[Km] radius is appropriate to use for the MWI-14 to MWI-3 remapping, but should not be seen as a general value for all MWI and ICI remappings and this is further discussed in the text).

7.1.1 Grid for remapping

A rectangular grid on geoid surface centered around the geolocation of the target observation is used for the footprint remapping. Each point on the grid is responsible for covering a surface area element dA as shown in Figure 22. The orientation of the grid is dependent (or aligned) with the line of sight (LOS) to the sensor, and the dimensions of the grid can be seen as along-track (or along-LOS) and across-track (or across-LOS). The grid is generated in the following way:

- first a suitable size and resolution of the grid is determined (e.g. a 160[Km] x 160[Km] wide grid with a resolution of 1[Km]). Suitable width and resolution of the grid depends on which type of remapping that is of interest, and is described in more detail in Sect. 7.1.4

- then the positions on geoid for an equally distance spaced array (e.g. [-80, -79.5, ..., 80] [Km]) centered on the geolocation of the target, and with a heading towards the sensor, is calculated. This is the "center line" of the grid. Note that the resolution of the array is 0.5[Km] as positions for the corners of each surface element also needs to be calculated

- then, grid positions, along the across-track direction for each point along the "center line" are calculated. The distance vector described above is deployed also here.

The distances to neighboring gridpoints will be close to identical for all gridpoints, following this method to generate the grid. This gives that each gridpoint "covers" identical surface area dA (e.g.1[Km] x 1[Km] following the example described).

7.1.2 Target antenna gain functions

The target antenna patterns for remapping MWI and ICI channels are that of MWI-3V and ICI-1, respectively. However, the target antenna pattern should not match the effective one from a single sample, but the effective antenna pattern from a number of samples where the integration time is long enough to meet required NEΔT for the target channel. This integration time corresponds to 5.200[ms] and 2.532[ms] for MWI-3V and ICI-1, respectively. During this time the antenna boresight will be rotated by an angle

$$\Delta\phi_{bs} = \Delta t/T_{scan} \cdot 360°, \tag{43}$$

where Δt and T_{scan} is the integration time and duration time of a complete scan, respectively, in the azimuth direction during a given sample. These angles are 1.404[degrees] and 0.68364[degrees] for MWI and ICI, respectively. The resulting smoothing effect on the effective antenna gain function is taken into account in the simulation as described in Sect. 5.4, and Figure 23 shows effective antenna gain functions for MWI-3V and ICI-1 that is used as target antenna gain functions. The half power beam-width is approximately 1 and 1.5[degrees] in the along track and across track direction, respectively, for MWI-3V, and 0.5 and 0.75[degrees] for ICI-1.

	Backus-Gilbert footprint matching methodology applied on MWI and ICI observations	Code: TR/BG/MWI-ICI
		Issue: 1.0
		Date: June 5, 2019
		File: optimal-interpolation-applied.tex
		Page: 55 / 200
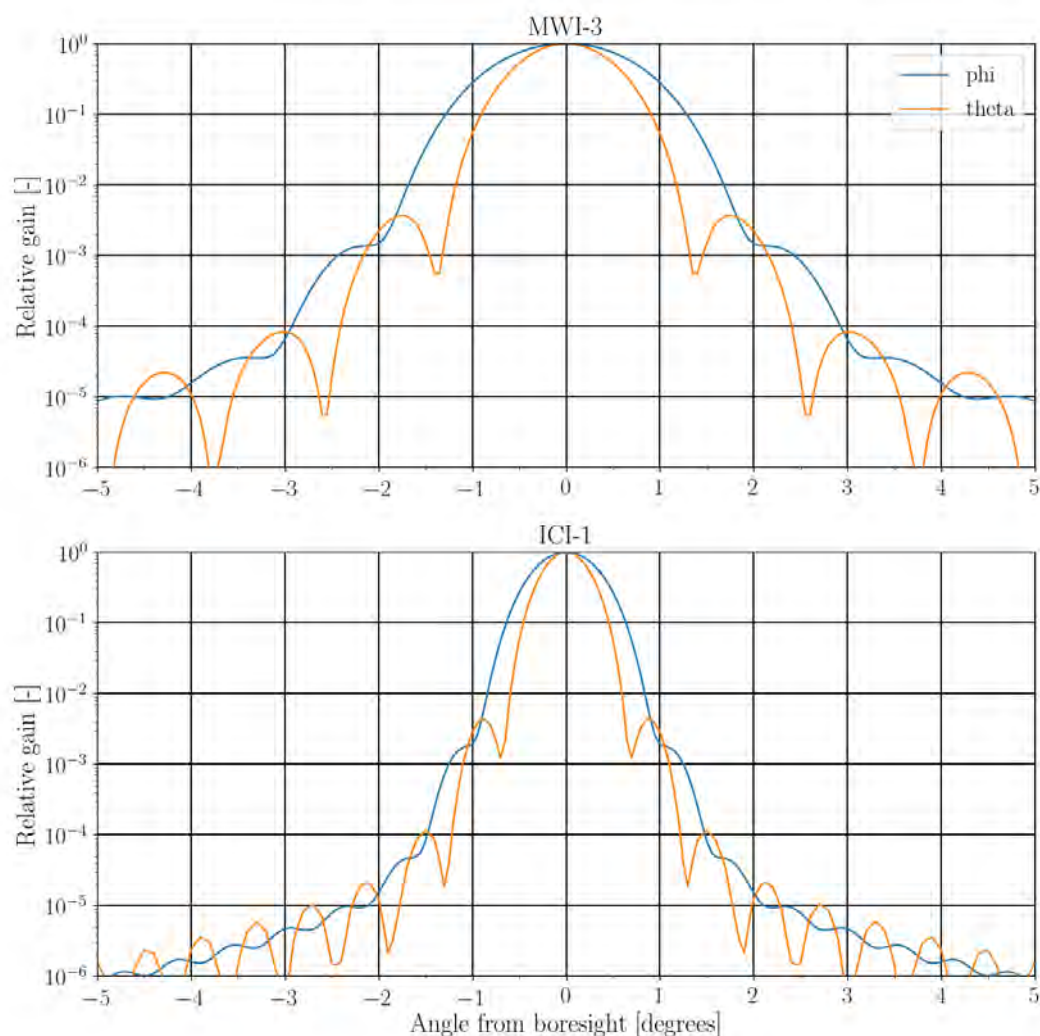
Figure 23: Effective antenna pattern as function of angle from boresight (phi is an angle in the scanning direction and theta in elevation) for MWI-3V and ICI-1. These antenna patterns are used as target antenna gain functions for footprint remapping.

7.1.3 Calculation of antenna pattern on grid

The projections of the target antenna gain pattern on a surface grid for MWI-3V and ICI-1 are shown in Figure 24 and Figure 25, respectively. The projection of the antenna gain pattern (F) on a surface facet around grid point (i, j) of the applied rectangular grid (see Figure. 22) is described by

$$F_{i,j} = \frac{cos(\theta_{inc,i,j})}{r_{i,j}^2} \sum_{i=0}^{1} \sum_{j=0}^{1} \frac{F(\theta_{i-1/2,j-1/2}, \phi_{i-1/2,j-1/2})}{4} \tag{44}$$

where $\theta_{inc,i,j}$ is the incidence angle, $r_{i,j}$ is the distance to the sensor, and the angles $\theta_{i-1/2,j-1/2}$ and $\phi_{i-1/2,j-1/2}$ describe the angles relative to the boresight direction that a grid point is observed by, and the summation is performed over the four corners of the surface facet corresponding to grid point (i, j).

The incidence angle is calculated as

$$\theta_{inc,i,j} = arccos(\vec{r}_{zenith,i,j} \cdot \vec{r}_{sensor,i,j}) \tag{45}$$

where $\vec{r}_{zenith,i,j}$ is a unit vector pointing towards the geodetic zenith (i.e taking the WGS84 geoid into account) at grid position (i, j) and $\vec{r}_{sensor,i,j}$ is a unit vector directed towards the sensor. A unit vector pointing towards the geodetic zenith can be obtained using coordinate transformation (between geodetic and x, y, z coordinates in earth centered earth fixed (ECEF) frame as

$$\vec{r}_{zenith,i,j} = geodetic2ecef('WGS84', latitude_{i,j}, longitude_{i,j}, altitude = 1m) - [x_{i,j}, y_{i,j}, z_{i,z}], \tag{46}$$

where $(latitude_{i,j}, longitude_{i,j})$ and $(x_{i,j}, y_{i,j}, z_{i,z})$ is the geodetic and ECEF coordinates of grid position (i, j), respectively, and geodetic2ecef represents a function that makes a conversion between geodetic to ECEF coordinate systems (taking WGS84 geoid into account).

A position within the 2-dimensional antenna diagram is described by spherical coordinates ($\theta_{i-1/2,j-1/2}$ and $\phi_{i-1/2,j-1/2}$). For some application it is more convenient to let the antenna boresight be directed towards the pole of the coordinate system, while for other application it is more useful to let the boresight points towards the equator of the coordinate system. This is mentioned, as both these approaches are used here and can easily cause confusion. We first describe how the $\theta_{i-1/2,j-1/2}$ and $\phi_{i-1/2,j-1/2}$ angles can be obtained following the "boresight towards pole definition".

The angle relative to the boresight direction can be obtained by

$$\theta_{i-1/2,j-1/2} = arccos(\vec{r}_{i-1/2,j-1/2} \cdot \vec{r}_{bs}), \tag{47}$$

where $\vec{r}_{i-1/2,j-1/2}$ is a unit vector pointing towards grid point $(i - 1/2, j - 1/2)$ from the sensor and $\vec{r}_{bs}$ is the boresight pointing unit vector.

In order to calculate $\phi_{i-1/2,j-1/2}$ we must define a coordinate system where the z-axis points in the boresight direction, and the x-axis ($\vec{u}_x$) is orthogonal to the z-axis and aligned with the scanning direction and the y-axis is orthogonal to both the x and z-axis. A vector that is aligned with the scanning direction can be obtained from

$$\vec{u}_x = \frac{\vec{r}_{nadir} \times \vec{r}_{bs}}{||\vec{r}_{nadir} \times \vec{r}_{bs}||}, \tag{48}$$

	Backus-Gilbert footprint matching methodology applied on MWI and ICI observations	Code:	TR/BG/MWI-ICI
MoHoW		Issue:	1.0
		Date:	June 5, 2019
		File:	optimal-interpolation-applied.tex
		Page:	57 / 200

where $\vec{\mathbf{r}}_{nadir}$ is a unit vector pointing in the nadir direction, and then

$$\vec{\mathbf{u}}_y = \vec{\mathbf{r}}_{bs} \times \vec{\mathbf{u}}_x. \tag{49}$$

$\phi_{i-1/2,j-1/2}$ can then be obtained from

$$\phi_{i-1/2,j-1/2} = arctan2(\vec{\mathbf{u}}_y \cdot \vec{\mathbf{r}}_{i-1/2,j-1/2}, \vec{\mathbf{u}}_x \cdot \vec{\mathbf{r}}_{i-1/2,j-1/2}). \tag{50}$$

Eq. 50 results in angles that lie in the interval $[0, 360]$[degrees] for the grid point positions, and hence these angles can only directly be used for "antenna data interpolation" if the antenna pattern is specified using the "boresight towards pole definition". This is currently not the case here, as the effective antenna pattern is calculated using a "boresight towards eauator definition" (see e.g. Figure 23).

Theerfore, the obtained $\theta_{i-1/2,j-1/2}$ and $\phi_{i-1/2,j-1/2}$ angles must be transformed to corresponding angles in a spherical coordinate system where the boresight is directed towards the equator. This gives that the $\theta_{i-1/2,j-1/2}$ and $\phi_{i-1/2,j-1/2}$ angles must be rotated 90[degrees] around the y-axis, and that can be obtained by

$$\begin{bmatrix} x_{rotated} \\ y_{rotated} \\ z_{rotated} \end{bmatrix} = \begin{bmatrix} 0 & 0 & 1 \\ 0 & 1 & 0 \\ -1 & 0 & 0 \end{bmatrix} \cdot \begin{bmatrix} sin(\theta_{i-1/2,j-1/2})cos(\phi_{i-1/2,j-1/2}) \\ sin(\theta_{i-1/2,j-1/2})sin(\phi_{i-1/2,j-1/2}) \\ cos(\theta_{i-1/2,j-1/2}) \end{bmatrix} \tag{51}$$

and

$$\theta'_{i-1/2,j-1/2} = \pi/2 - arccos(z_{rotated}) \tag{52}$$

and

$$\phi'_{i-1/2,j-1/2} = arctan2(y_{rotated}, x_{rotated}) \tag{53}$$

$F(\theta'_{i-1/2,j-1/2}, \phi'_{i-1/2,j-1/2})$ is then calculated by interpolating the 2-dimensional varying antenna gain function data, having a 0.1[degree] resolution, using a bivariate spline method.
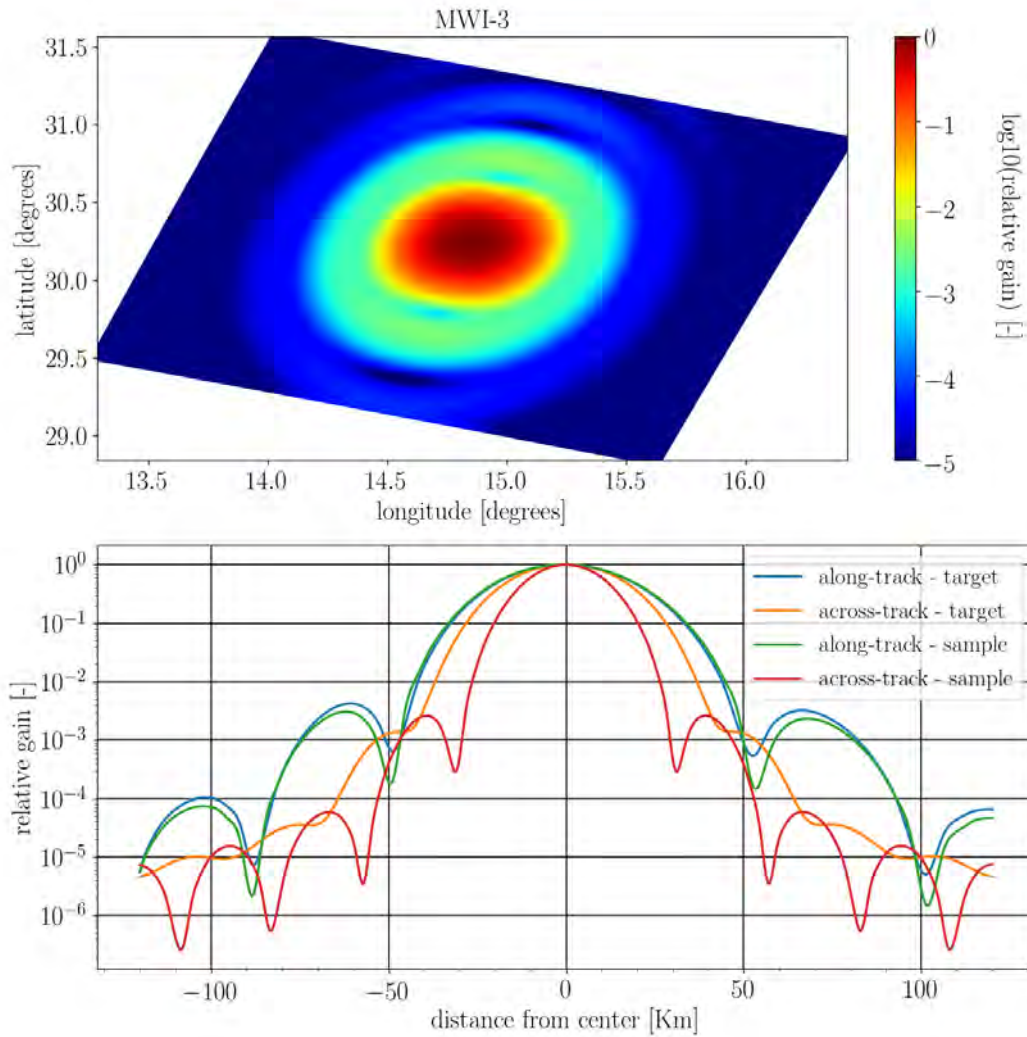
Figure 24: Target effective antenna pattern of MWI-3V projected on the grid on geoid surface (or projected on the surface facet of each grid point as displayed in Figure 22). The lower panel shows the variation of the antenna pattern in the along and across track direction (around the center of the footprint). The effective antenna pattern of that of a single sample of MWI-3V is also displayed, as a reference.

	Backus-Gilbert footprint matching methodology applied on MWI and ICI observations	Code:	TR/BG/MWI-ICI
		Issue:	1.0
		Date:	June 5, 2019
		File:	optimal-interpolation-applied.tex
		Page:	59 / 200
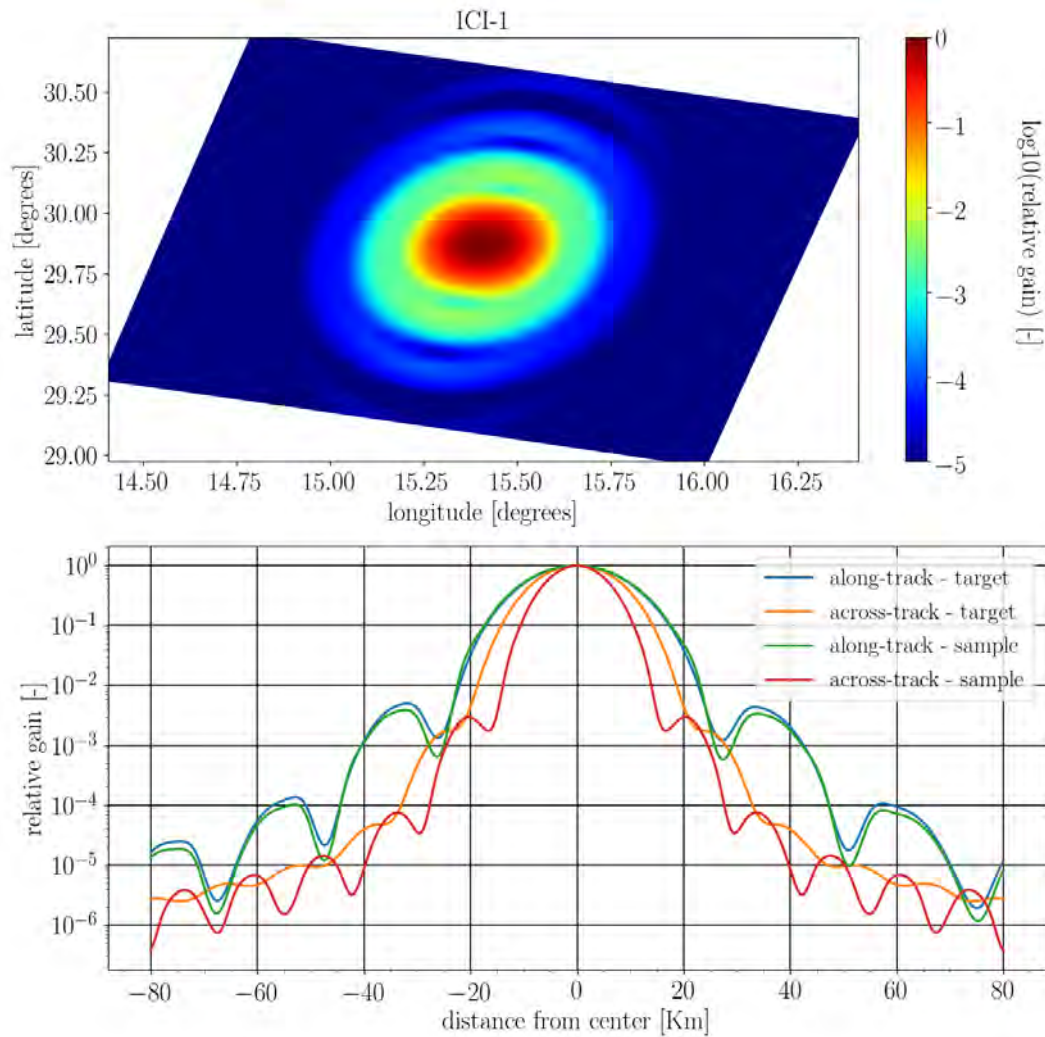
Figure 25: As Figure 24 but for the target effective antenna pattern of ICI-1.

7.1.4 Selection of samples to include in remapping

The remapping requires that one select which samples to include in the calculation (see e.g. Fig. 26). It is preferable to only include samples that have a significant impact on the derived weights, since the computational cost rapidly increases with number of samples included. How many samples to include in the remapping is further discussed in Sect. 9, but below is given a few guidelines.

All observations that have a geolocation closer than a distance r_{max} from the target geolocation is included in the calculation. A good choice of r_{max} depends on both the size of the target and sample footprint, as described below.

When remapping between two channels with similar footprint sizes or from smaller to a larger, a reasonable choice of r_{max} is about the half width of the target -30[dB] footprint size, given that it is of interest to match the target pattern at the -30[dB] level. This corresponds to about 50[Km] and 30[Km] for MWI and ICI, respectively (see Figure 24 and Figure 25).

The remapping from a larger to a smaller footprint (i.e MWI-1 and MWI-2 to MWI-3) is more challenging, due to the fact that some of the weights must be negative to allow for an increase in resolution, and r_{max} must be greater than for the case described above, This gives that a good value of r_{max} should at least be about the sum of the half width of the sample and target -30[dB] footprint size, and that corresponds to about 80[Km] for the MWI-1 and MWI-2 to MWI-3 remapping.

The selected value of r_{max} will effect how wide the grid for remapping (Sect. 7.1.1) must be. The important consideration is that the grid is wide enough to allow for a projection of the antenna gain patterns (for both the target and all included samples) onto grid points (i.e. contribution outside the grid must be negligible small). This gives that the width of the grid should not be smaller than about 4 times the size of r_{max}, in order "cover" the main beam of all involved observation.

The spacing between grid points should be small enough to not significantly effect the result. That is, resolution must be fine enough to capture the details of the structure in antenna pattern (basic antenna gain function data used here has a resolution of 0.1[degrees]), and this results in a required resolution in the order of 1[Km] to 2[Km].

| | Backus-Gilbert footprint matching methodology applied on MWI and ICI observations | Code: TR/BG/MWI-ICI
Issue: 1.0
Date: June 5, 2019
File: optimal-interpolation-applied.tex
Page: 61 / 200 |

7.1.5 Trade-off analysis

The ultimate aim of the trade off analysis is to determine an optimal set of weighting coefficients to be applied in the remapping. This requires that a trade off between fit and noise errors is performed, in such a way that the amount of smoothing applied, results in an optimal compromise. The trade off analysis is done in the following way:

- vector of weighting coefficients, and resulting fit and noise errors, are calculated for a range of values (typically between 10^{-3} to 10^{-9}) of the smoothing parameter β (apply Eq. 38, Eq. 34, and Eq. 35)

- the L-curve technique (see Sect. 6.2 and Fig. 21) is applied to identify an optimal value of β. That is, the point along the L-curve (log-log noise and fit error space) having the greatest curvature is determined. The curvature is calculated from the radius of curvature $(R = 1/\kappa)$ of a circle that connects three closely spaced points $(\beta - \Delta\beta, \beta, \beta + \Delta\beta)$ along the L-curve

- the resulting noise error (of the L-curve determined β) is compared to a defined acceptable noise error $(\text{NE}\Delta\text{T}_{max})$, and if the resulting noise error is to high, the optimal β value is adjusted. The β value associated with greatest acceptable noise error is then considered to be optimal.

- to avoid over fitting, the obtained fit error is compared to a minimum fit error value, and the β value is adjusted if the obtained fit error is lower than this value. The β value associated with smallest acceptable fit error is then considered to be optimal.

Results from trade off analysis for a number of remappings between MWI and ICI channels are presented in the following section.

	Backus-Gilbert footprint matching methodology applied on MWI and ICI observations	Code: TR/BG/MWI-ICI
		Issue: 1.0
		Date: June 5, 2019
		File: optimal-interpolation-applied.tex
		Page: 62 / 200

7.2 Example remappings

In this section we present characteristics from example remapping of MWI samples from three selected channels to MWI-3V footprint, and ICI samples to ICI-1 footprint. Here we only presents results from remappings around the center scan position, while results from the complete scan is presented in Sect. 9. The half power beam-widths of all ICI channels are similar to each other, whereas the half power beam-widths of the MWI channels are 1.67, 1.0, 0.33[degrees] for the lowest, middle, and highest frequency channels, respectively (see e.g. Sect. 3). We therefore can identify three types of remappings between MWI channels in terms of sample footprint sizes

- remapping to a larger sized footprint (e.g MWI-14 to MWI-3V)

- remapping to a smaller size footprint (e.g MWI-1V to MWI-3V)

- remapping to a similar sized footprint (e.g MWI-4V to MWI-3V)

but only one for ICI (remapping to a similar sized footprint).

In the following subsections we present example results of remapping between the channels described above, with the aim to identify how the characteristic of remapped samples compare to channel specific requirement (see Table 1 and Table 1) for channel specific requirement on NEΔT). We here only consider remappings close to the center of the scan (in the very edges of the scan the remapping is more challenging and less accurate and this is more described in Sect. 9).

7.2.1 Trade off criteria and assumptions

No requirement on fit-error is available for the MWI and ICI footprint remapping. We here primarily focus on obtaining a reasonable match with the main beam. Generally, it is possible to also match sidelobes, but that requires that more samples are included in the calculation than applied here. Defined channel specific requirement on NEΔT is described in Table 1 and Table 2 and also found below. It is stressed that these requirements do not strictly apply on remapped observations, but on footprint sizes as described in the tables. This gives that these numbers are more or less valid for the remapping between channels having similar footprint sizes, whereas the numbers are invalid for MWI-1V to MWI-3V and MWI-14 to MWI-3V remapping. It will be very challenging to achieve the "required" NEΔT value for the MWI-1V to MWI-3V remapping, whereas a much lower NEΔT value than "required" is expected to be obtained for the MWI-14 to MWI-3V remapping.

It was already shown in Sect. 6.2 that the L-curve technique can be used as a tool for the trade-off analysis. If the trade off analysis results in an L-curve that actually resemble the letter L, and the noise error corresponding to the the "L-curve optimal β" is sufficiently low, than it is very natural to accept this β as an optimal choice. This is also done here.

For the situation where the L-curve has a less characteristic shape (which is shown to be the case for the MWI-1V to MWI-3V remapping) the trade off becomes more complicated. The L-curve technique will clearly result in a suggested value of the smoothing, but both the fit and noise-error can potentially be high. The trade-off criteria applied here is then simple: do

	Backus-Gilbert footprint matching methodology applied on MWI and ICI observations	**Code:** TR/BG/MWI-ICI
		Issue: 1.0
		Date: June 5, 2019
		File: optimal-interpolation-applied.tex
		Page: 63 / 200

not accept a value of the smoothing parameter that results in a noise-error that is higher than 2[K].

In all examples, we assume that the noise (NEΔT) is uncorrelated between all samples (i.e. we apply a diagonal measurement error covariance matrix). We furthermore make some assumption on NEΔT values for individual samples, based on our best guess of the anticipated performance and requirements of the channels, which can be summarized as:

- MWI-1V, NEΔT (individual sample): 3.72[K]

  - required NEΔT: ≤ 0.8[K]
  - needed integration time (to obtain required NEΔT): 8.480[ms]
  - equivalent number of samples (to obtain required NEΔT): 21.6

- MWI-4V, NEΔT (individual sample): 3.59[K]

  - required NEΔT: ≤ 1.1[K]
  - needed integration time: 4.175[ms]
  - equivalent number of samples: 10.7

- MWI-14, NEΔT (individual sample): 2.25[K]

  - required NEΔT: ≤ 1.3[K]
  - needed integration time: 1.178[ms]
  - equivalent number of samples: 3.0

- ICI-5, NEΔT (individual sample): 2.20[K]

  - required NEΔT: ≤ 1.2[K]
  - needed integration time: 2.212[ms]
  - equivalent number of samples: 3.3

- ICI-10, NEΔT (individual sample): 3.51[K]

  - required NEΔT: ≤ 2.0[K]
  - needed integration time: 2.038[ms]
  - equivalent number of samples: 3.1

- ICI-11V, NEΔT (individual sample): 3.4[K]

  - required NEΔT: ≤ 1.6[K]
  - needed integration time: 2.990[ms]
  - equivalent number of samples: 4.5

7.2.2 MWI-14 to MWI-3V

Results of the MWI-14 to MWI-3V remapping are presented in Figure 26 and 27. The remapping calculation was performed using a 200[Km] x 200[Km] wide grid having a 2[Km] spacing between grid points. All MWI-14 samples (630) within a radius of 55[Km] from the geolocation (boresight intersection with geoid) of the MWI-3V target footprint were included in the calculation.

Trade off analysis data were already shown in Figure 21, and a β value around 10^{-6} was found to be ideal to apply. Estimated noise on the resampled observation is lower than 0.2[K]. This is considerable lower than the requirement of NEΔT lower than 1.3[K]. A basic reason for this great difference is that the requirement apply to a smaller footprint (the MWI-14 footprint), whereas the estimate of 0.2[K] apply to the MWI-3V footprint. It is only needed to average three samples to obtain a NEΔT that fulfills the requirement, whereas it can be seen in Figure 26 that much more samples contribute to remapped observation, which is favorable in terms of reducing the noise. However, the simulation assumed that noise is uncorrelated between samples, that might be a bit optimistic.

Obtained weights for the individual samples, target antenna pattern, and obtained antenna pattern are shown in Figure 26. MWI-14 to MWI-3V remapping is a remapping from a small to large footprint and the obtained weights resemble the shape of the target antenna pattern, as expected. Highest weights are given to samples close to the geolocation of the MWI-3V observation, and the weight for an individual sample decrease with distance from the geolocation.

The fit of the obtained to the target antenna pattern is described in more details in Figure 27. The agreement between the two is high within the main lobe down to about -23[dB]. The sidelobe of the target antenna pattern found about 60[Km] from the center of the footprint in the along track direction is not captured by the the remapped footprint, and can be explained by the fact that this sidelobe is located outside the radius from which observations was included.

The agreement between the obtained and target antenna pattern is higher along the across-track than the along-track direction. The reason for this is related to both the fact that the target antenna pattern is more smooth in the across-track direction and to the observation geometry. The distance between two neighboring samples are much smaller in the across-track direction than in the along-track direction, since neighboring pixels in the across-track direction belongs to the same scan, and neighboring samples in the along-track direction belongs to two different scans. This gives that it is less challenging to obtain a good fit to the target antenna pattern in the across-track direction than in the along-track direction.

	Backus-Gilbert footprint matching methodology applied on MWI and ICI observations	Code: TR/BG/MWI-ICI
		Issue: 1.0
		Date: June 5, 2019
		File: optimal-interpolation-applied.tex
		Page: 65 / 200

Figure 26: Footprint remapping of MWI-14 samples to MWI-3V target footprint or FOV. 630 samples (green) within a radius of 55[Km] from the MWI-3V (red) geolocation is used (upper left panel). Lower left and right panel shows relative gain of target and obtained antenna pattern on the (surface) grid points, respectively. Upper right panel shows derived "optimal" weights (a coefficients) and the "+" marker shows the geolocation of the center of the target FOV.

	Backus-Gilbert footprint matching methodology applied on MWI and ICI observations	Code:	TR/BG/MWI-ICI
		Issue:	1.0
		Date:	June 5, 2019
		File:	optimal-interpolation-applied.tex
		Page:	66 / 200
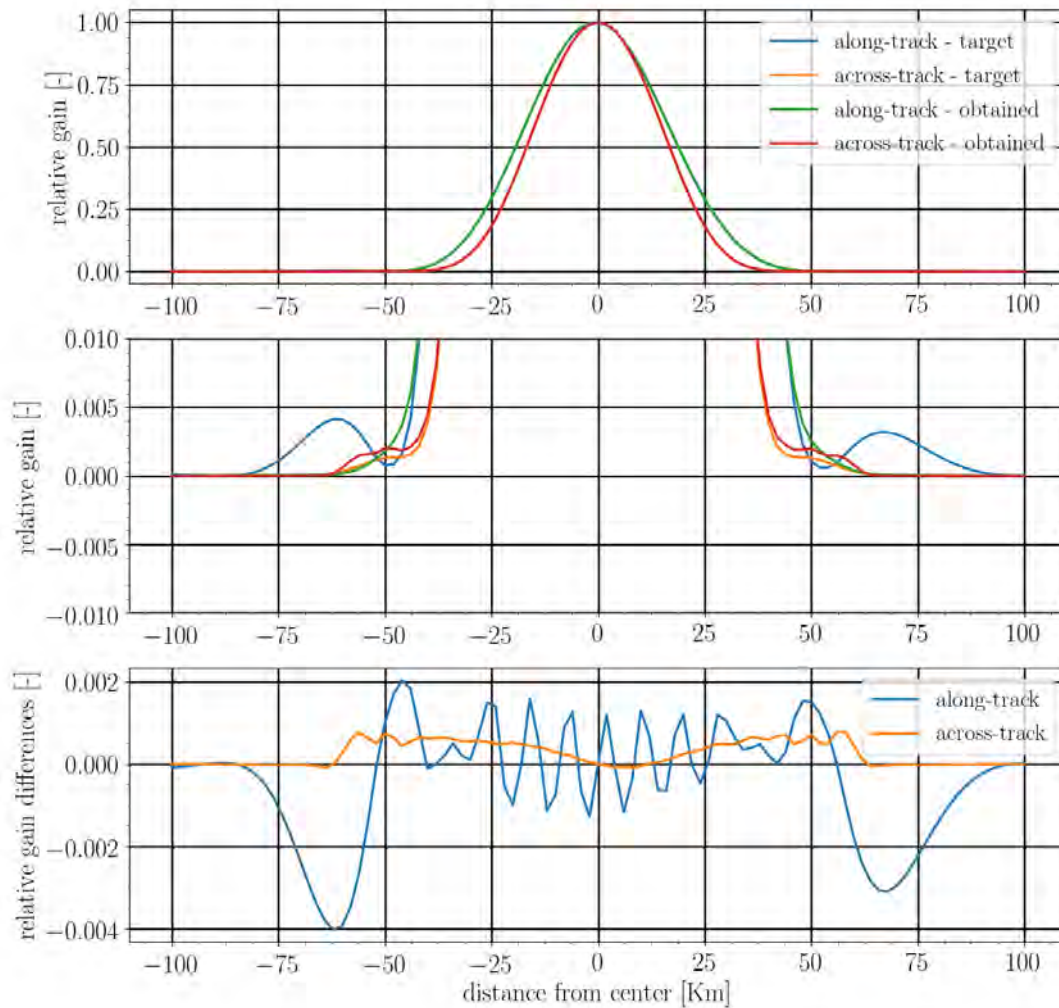
Figure 27: MWI-14 to MWI-3V. Upper and middle panel show target and obtained antenna pattern in the along- track and across-track directions. The middle panel is zoomed in on small values. The lower panel shows the difference between obtained and target gain function in the along-track and across-track directions.

Figure 28: Trade off noise and fit-error (in log space) as function of smoothing parameter (β), for MWI-4V to MWI-3V remapping. See text for more details.

7.2.3 MWI-4V to MWI-3V

Result of the MWI-4V to MWI-3V remapping is presented in Figures 28 to 30. The remapping calculation was performed using a 240[Km] x 240[Km] wide grid having a 2[Km] spacing between grid points. All MWI-14 samples (654) within a radius of 55[Km] from the geolocation (boresight intersection with geoid) of the MWI-3V target footprint were included in the calculation.

Obtained weights for the individual samples, target antenna pattern, and obtained antenna pattern are shown in Figure 29. MWI-4 to MWI-3V remapping is a remapping between similar sized footprints. This gives that most weights are given to samples along the scan closest to the MWI-3V target observation, and hence the distribution of weights among the samples do not resemble the shape of the target antenna pattern as was the case for the MWI-14 to MWI-3V

remapping.

Estimated noise on the resampled observation is 0.95[K]. This is considerable lower than the requirement of NEΔT lower than 1.3[K]. The reason for this great difference is that it is only needed to average 11 samples to obtain a NEΔT that fulfills the requirement, whereas it can be seen in Figure 29 that more samples than that contribute to remapped observation (e.g the highest weight for a sample is just above 0.03 which approximately means that at least 30 samples have significant contribution to the remapping), which is favorable in terms of reducing the noise. However, the simulation assumed that noise is uncorrelated between samples, that might be to optimistic.

The fit of the obtained to the target antenna pattern is described in more details in Figure 30. The agreement between the two is high, both within the main lobe and the first side lobe. Differences are here typically less than -30[dB]. The reason to the fact that the first sidelobe could be reconstructed for the MWI-4V to MWI-3V remapping but not for the MWI-14 to MWI-3V remapping, even though to the same radius was deployed to include samples, can be related to two facts. First, the MWI-3V target antenna pattern differ less to the MWI-4V than to the MWI-14 effective antenna pattern for individual samples. Secondly, the footprint size of individual samples is greater for MWI-4V than that of MWI-14, which effectively gives that the possibility to reconstruct antenna pattern features outside the 55[Km] radius is greater for MWI-4V than for MWI-14.

	Backus-Gilbert footprint matching methodology applied on MWI and ICI observations	Code:	TR/BG/MWI-ICI
		Issue:	1.0
		Date:	June 5, 2019
		File:	optimal-interpolation-applied.tex
		Page:	69 / 200

Figure 29: Footprint remapping of MWI-4V samples to MWI-3V target footprint. 654 samples within a radius of 55[Km] from the MWI-3V geolocation is used. Otherwise as Figure 26.

	Backus-Gilbert footprint matching methodology applied on MWI and ICI observations	Code:	TR/BG/MWI-ICI
		Issue:	1.0
		Date:	June 5, 2019
		File:	optimal-interpolation-applied.tex
		Page:	70 / 200

Figure 30: As Figure 27 but for MWI-4V to MWI-3V remapping.

7.2.4   MWI-1V to MWI-3V

Result of the MWI-1V to MWI-3V remapping is presented in Figures 31, 32, and and 33. The remapping calculation was performed using a 400[Km] x 400[Km] wide grid having a 3[Km] spacing between grid points. All MWI-1 samples (3111) within a radius of 120[Km] from the geolocation (boresight intersection with geoid) of the MWI-3V target footprint were included in the calculation.

The remapping from MWI-1V to MWI-3V is the most challenging case, due to the fact the remapping must enhance the resolution of MWI-1V samples. This means that some of the weight coefficients must be negative (as is clearly seen in Figure 31), and this can severely amplify the noise. Figure 33 show trade-off noise and fit-error for the remapping, and this data look significantly different for the MWI-1V to MWI-3V remapping compared to all other cases considered here. For small values of β the noise of the remapped measurement can be above 100[K]. A β value of 0.0001 was used here, which gives that the noise is about 1[K]. This is above the "required" NEΔT, but this requirement does not apply here as described in Sect. 7.2. It should be clear that a lower value of β than used here gives significantly better fit to the target, but the trade off is not trivial in this case.

Already from Figure 31 one can see that the match between obtained and target antenna pattern is lower as compared to all other remappings. The fit of the obtained to the target antenna pattern is described in more details in Figure 32. The agreement is fair in the across-track direction, but the main issue is in the along-track direction where significant differences are found even in the main lobe. The FWHM footprint size is more than 10[Km] wider than that of the target, and sidelobes (both positive and negative) above -20[dB] extends out to 150[Km].

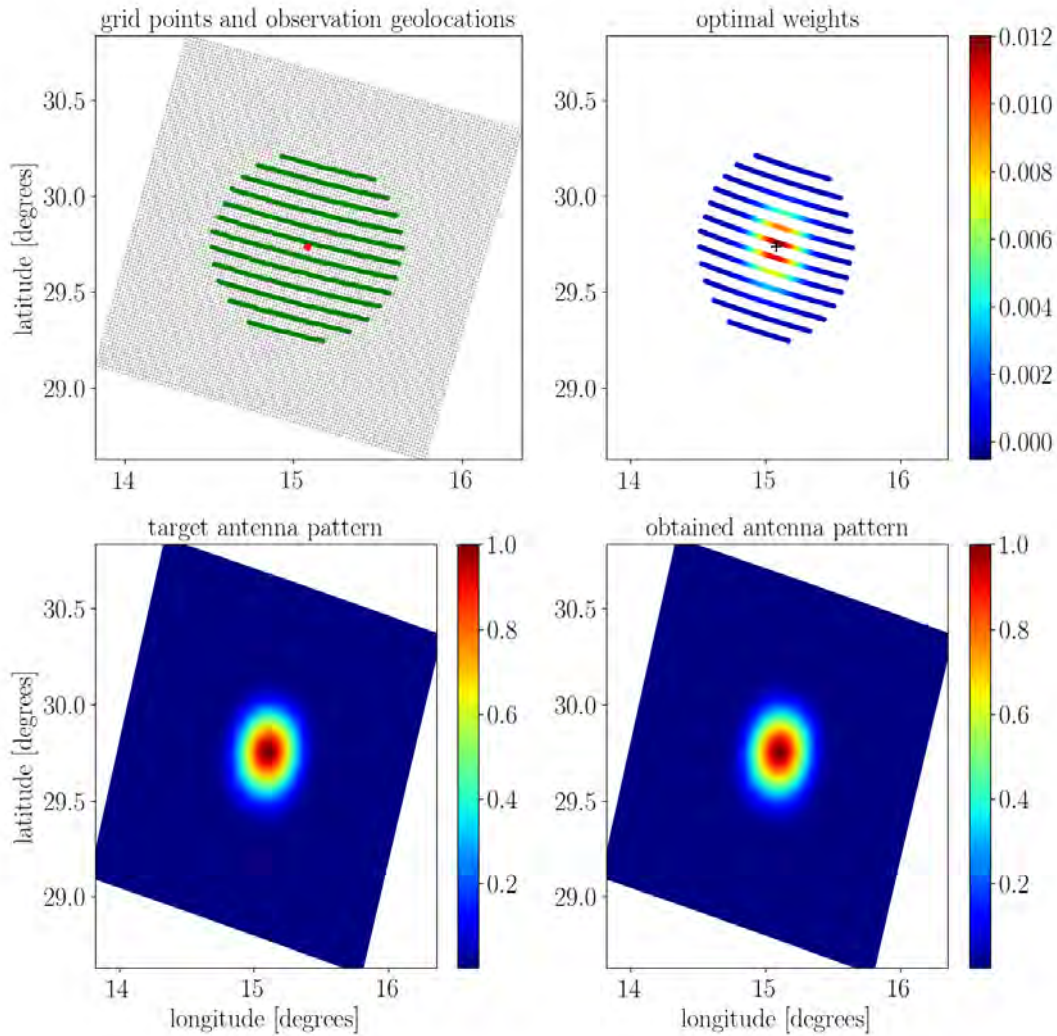Figure 31: Footprint remapping of MWI-1V samples to MW3-1V target footprint. 3111 samples within a radius of 120[Km] from the MWI-3V geolocation is used. Otherwise as Figure 26.
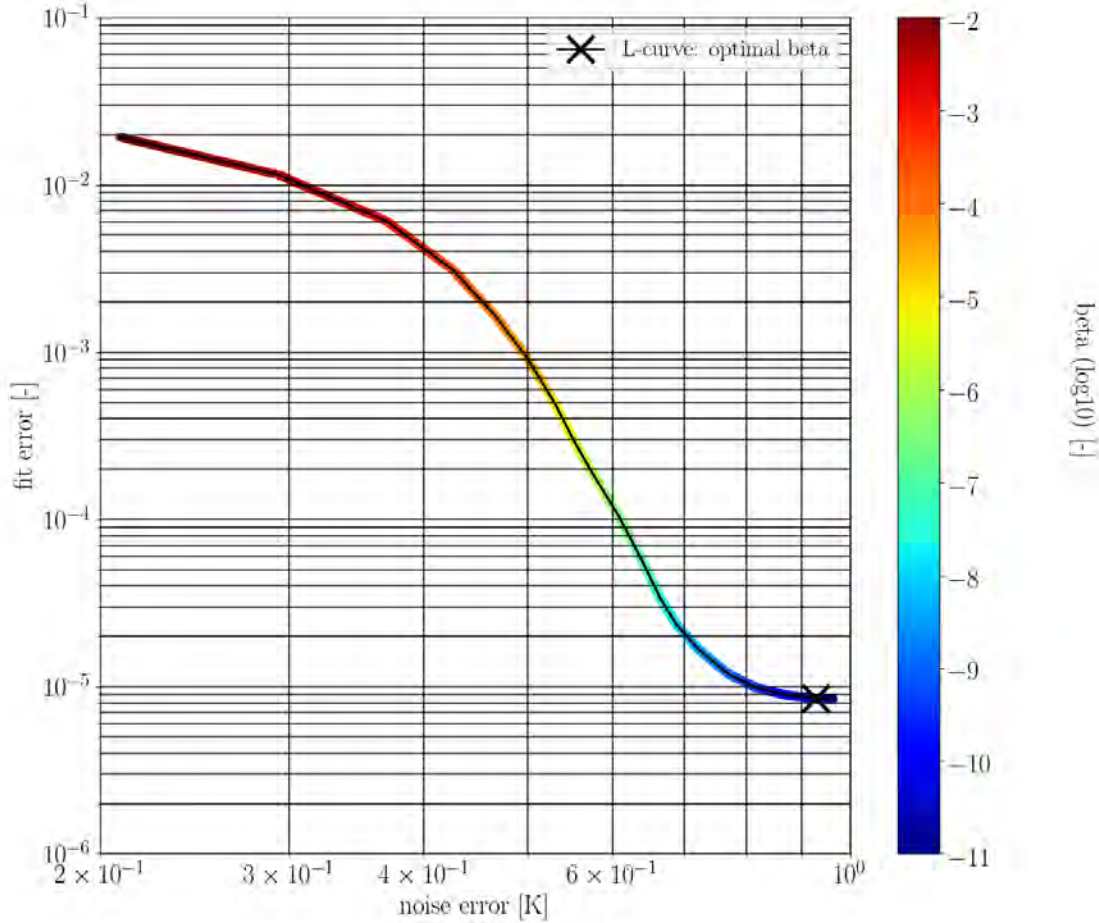
Figure 32: As Figure 27 but for MWI-1V to MWI-3V remapping.
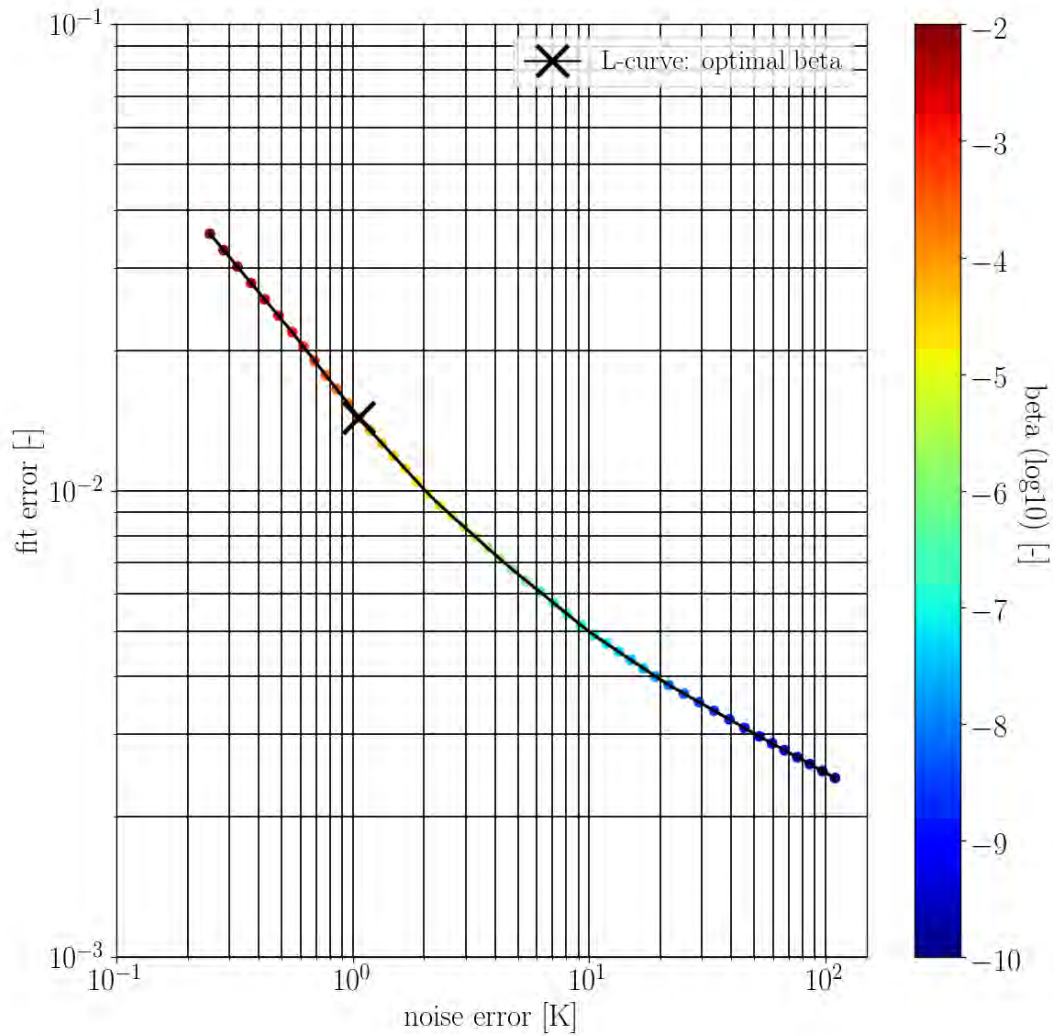
Figure 33: Trade off noise and fit error as function of smoothing parameter (β) for MWI-1V to MWI-3V remapping. See text for more details.

7.2.5 ICI-5 to ICI-1

Result of the ICI-5 to ICI-1 remapping is presented in Figures 34 and 35. The remapping calculation was performed using a 160[Km] x 160[Km] wide grid having a 1[Km] spacing between grid points. All ICI-5 samples (116) within a radius of 30[Km] from the geolocation (boresight intersection with geoid) of the ICI-1 target footprint were included in the calculation.

Obtained weights for the individual samples, target antenna pattern, and obtained antenna pattern are shown in Figure 34. ICI-5 to ICI-1 remapping is a remapping between similar sized footprints. This gives that most weights are given to samples along the scan closest to the ICI-1 target observation. It can be seen that the four closest samples are given a considerably greater weight than the other samples.

Estimated noise on the resampled observation is 0.7[K]. This is considerable lower than the requirement of NEΔT lower than 1.2[K]. The reason for this great difference is that it is only needed to average 3.3 samples to obtain a NEΔT that fulfills the requirement, whereas it can be seen in Figure 34 that more samples than that contribute to remapped observation (e.g the highest weight for a sample is just above 0.125 which approximately means that at least 8 samples have significant contribution to the remapping), which is favorable in terms of reducing the noise. However, the simulation assumed that noise is uncorrelated between samples, that might be to optimistic.

The fit of the obtained to the target antenna pattern is described in more details in Figure 35. The agreement between the two, within the mainlobe, is high down to -23[dB], both in the along-track and across-track direction. The agreement along the across-track direction is excellent even further away from the center. Deviations between the target and obtained antenna pattern sidelobes in the along-track direction can clearly be seen, and in particular towards the direction towards the sensor (-35[Km]). It can even be seen that the obtained antenna pattern is negative between the main and first sidelobe. This should not be possible for a physical antenna, but can clearly be the case for a reconstructed antenna pattern. This minimum between the main and first sidelobe in the along-track direction is probably the most difficult feature to reconstruct, but this minimum "covers" a quite limited area as can be seen in Figure 25.

	Backus-Gilbert footprint matching methodology applied on MWI and ICI observations	Code:	TR/BG/MWI-ICI
		Issue:	1.0
		Date:	June 5, 2019
		File:	optimal-interpolation-applied.tex
		Page:	76 / 200

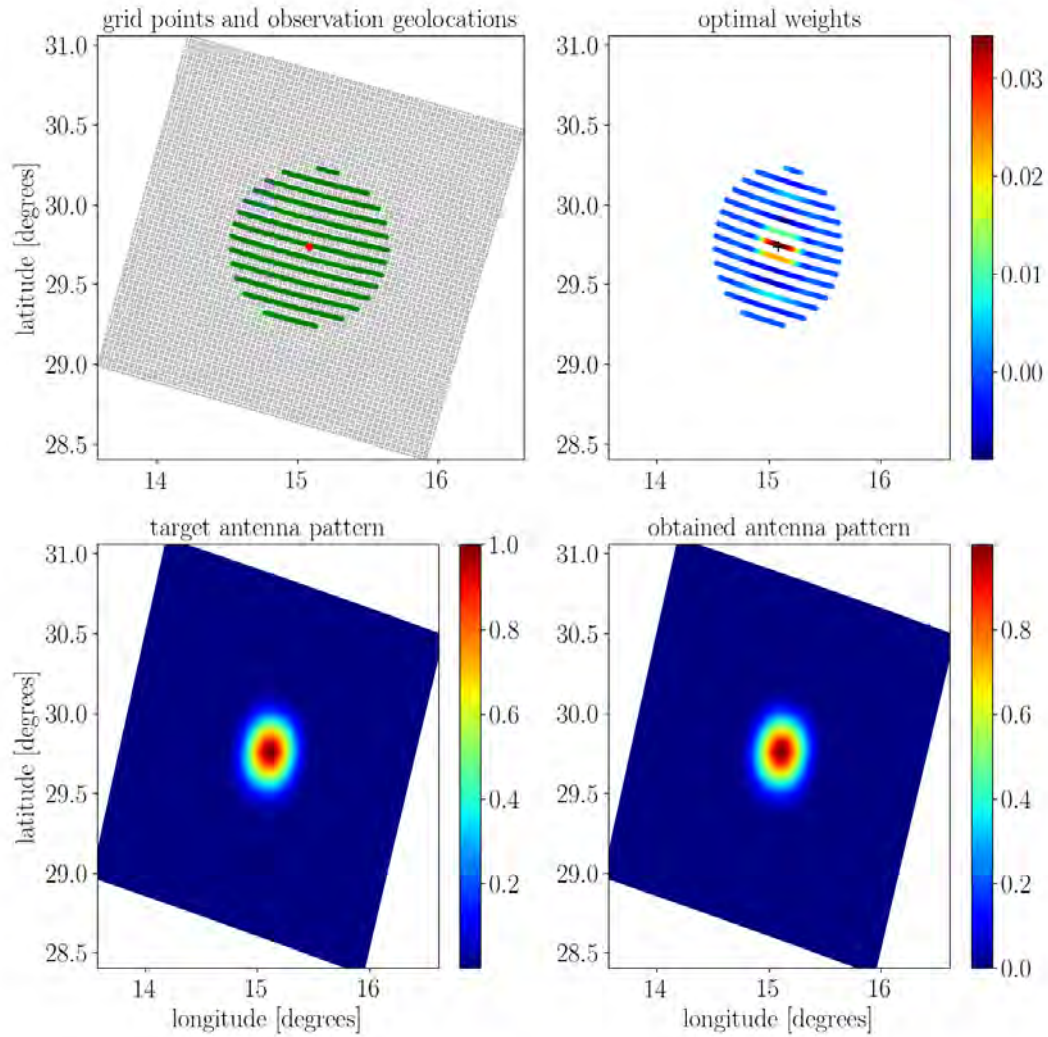Figure 34: Footprint remapping of ICI-5 samples to ICI-1 target footprint. 116 samples within a radius of 30[Km] from the ICI-1 geolocation is used. Otherwise as Figure 26.
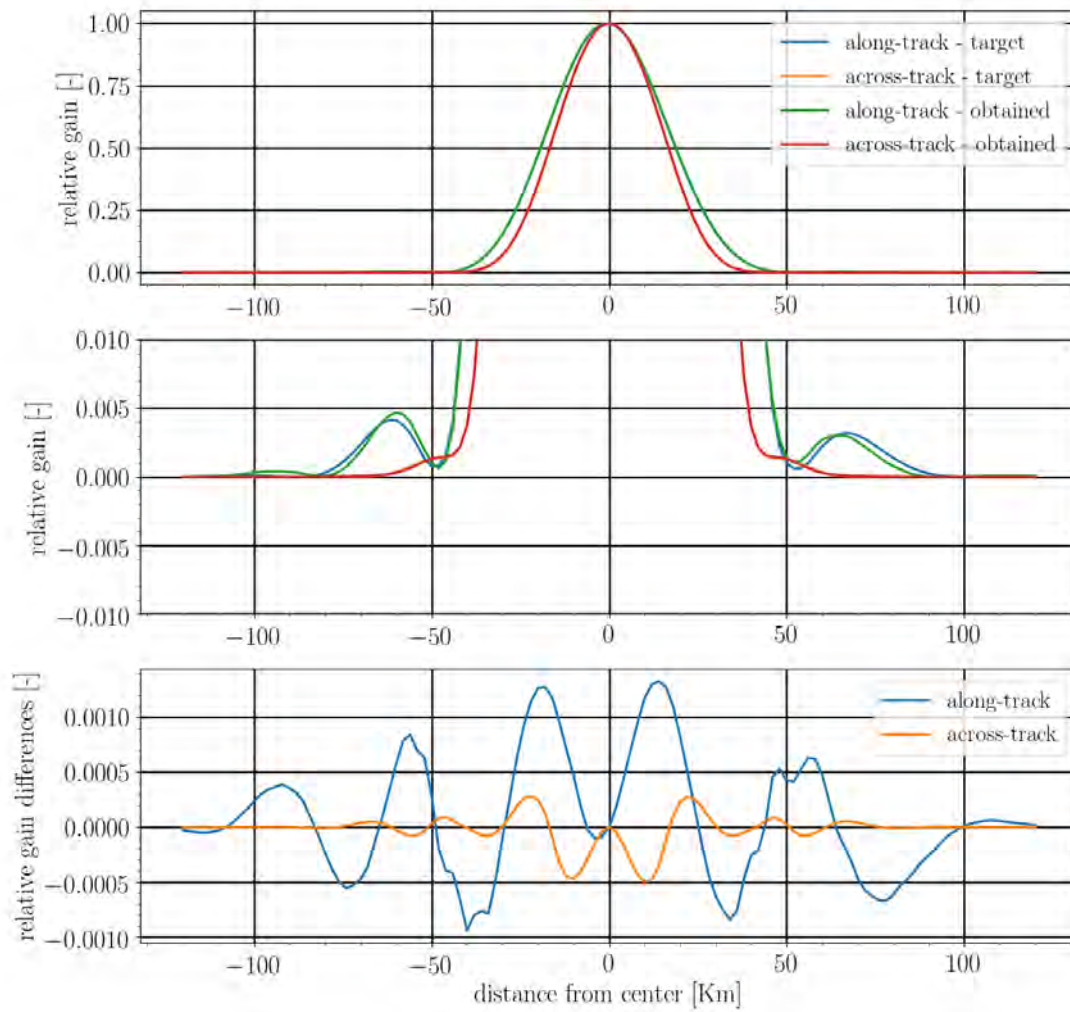
Figure 35: As Figure 27 but for ICI-5 to ICI-1 remapping.

7.2.6   ICI-10 to ICI-1

Results of the ICI-10 to ICI-1 remapping is presented in Figures 36 to 38. The remapping calculation was performed using a 160[Km] x 160[Km] wide grid having a 1[Km] spacing between grid points. All ICI-11V samples (115) within a radius of 30[Km] from the geolocation (boresight intersection with geoid) of the ICI-1 target footprint were included in the calculation.

Trade off data are shown in Figure 36, and the shape of the "L-curve" is similar for all considered ICI remappings, but only shown for this case. The optimal β according to the L-curve technique gives an acceptable noise error, and the fit error will practically not be reduced using less smoothing.

The result of the ICI-10 to ICI-1 remapping is very similar to the characteristic of the ICI-5 to ICI-1 remapping. The main difference is that the estimated noise of the resampled observation is 1.15[K], which is higher than for the ICI-5 case, but is explained by the fact the noise of individual samples is higher for ICI-10 than for ICI-5.

	Backus-Gilbert footprint matching methodology applied on MWI and ICI observations	Code: TR/BG/MWI-ICI
		Issue: 1.0
		Date: June 5, 2019
		File: optimal-interpolation-applied.tex
		Page: 79 / 200
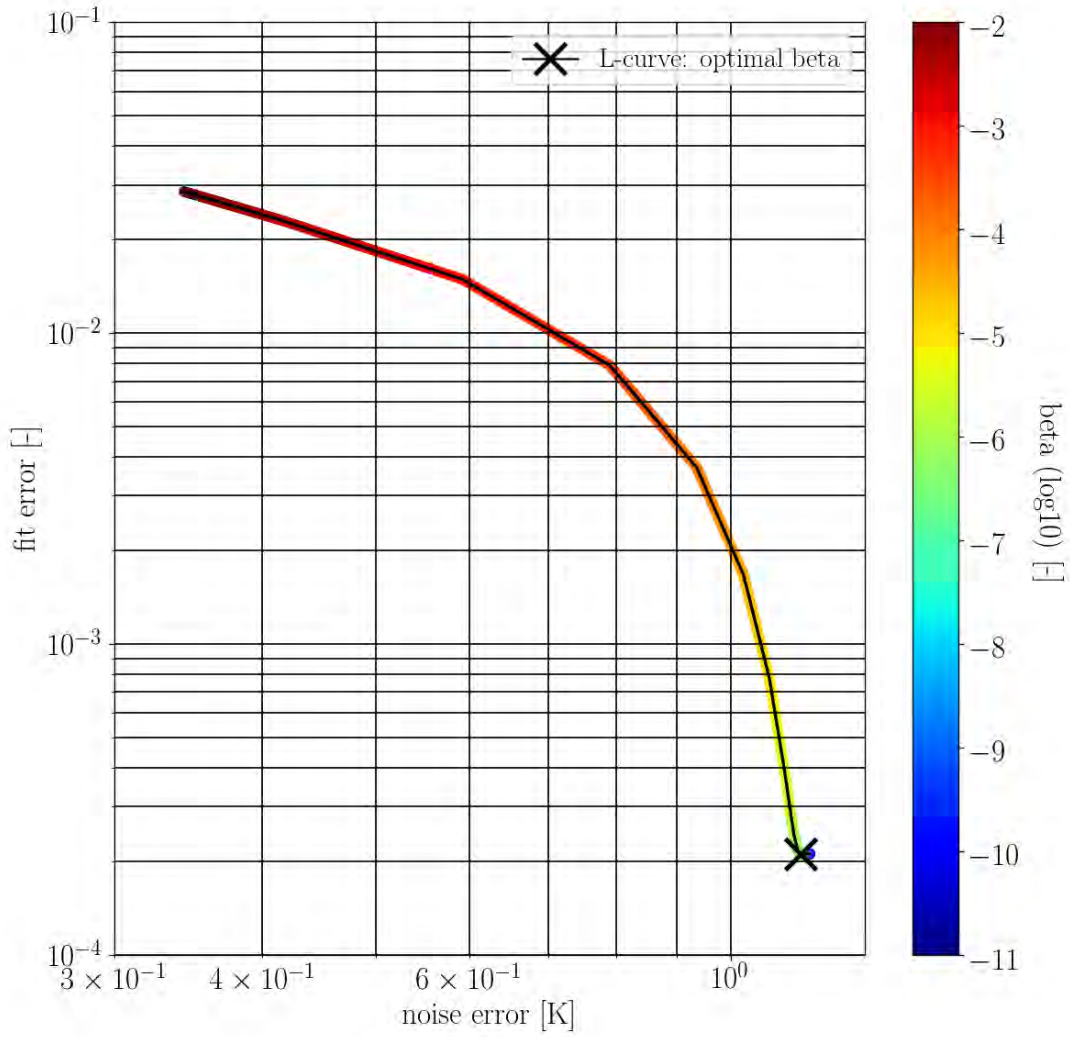
Figure 36: Trade off noise and fit-error (in log space) as function of smoothing parameter (β), for ICI-10 to ICI-1 remapping. See text for more details.

	Backus-Gilbert footprint matching methodology applied on MWI and ICI observations	Code: TR/BG/MWI-ICI
		Issue: 1.0
		Date: June 5, 2019
		File: optimal-interpolation-applied.tex
		Page: 80 / 200
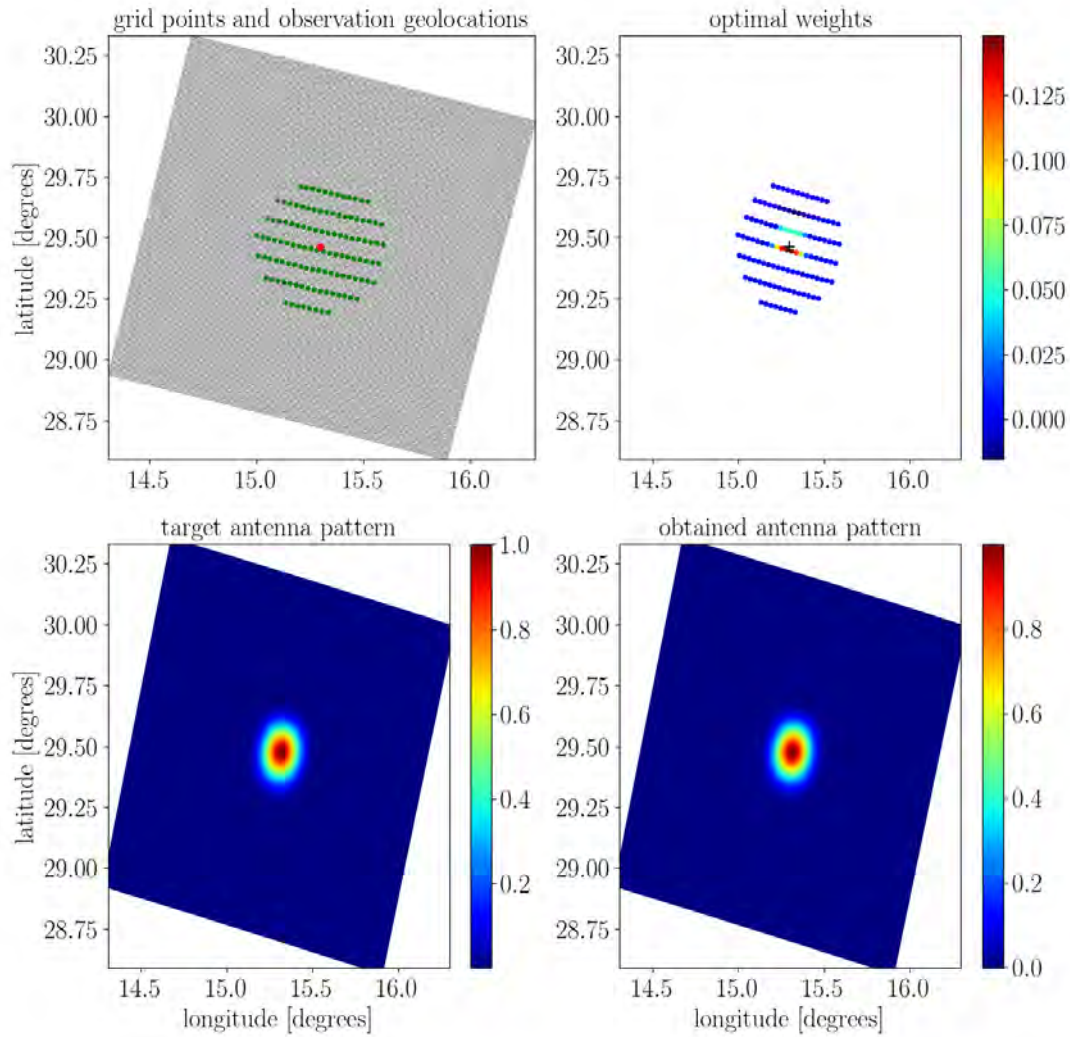
Figure 37: Footprint remapping of ICI-10 samples to ICI-1 target footprint. 115 samples within a radius of 30[Km] from the ICI-1 geolocation is used. Otherwise as Figure 26.

	Backus-Gilbert footprint matching methodology applied on MWI and ICI observations	Code:	TR/BG/MWI-ICI
		Issue:	1.0
		Date:	June 5, 2019
		File:	optimal-interpolation-applied.tex
		Page:	81 / 200
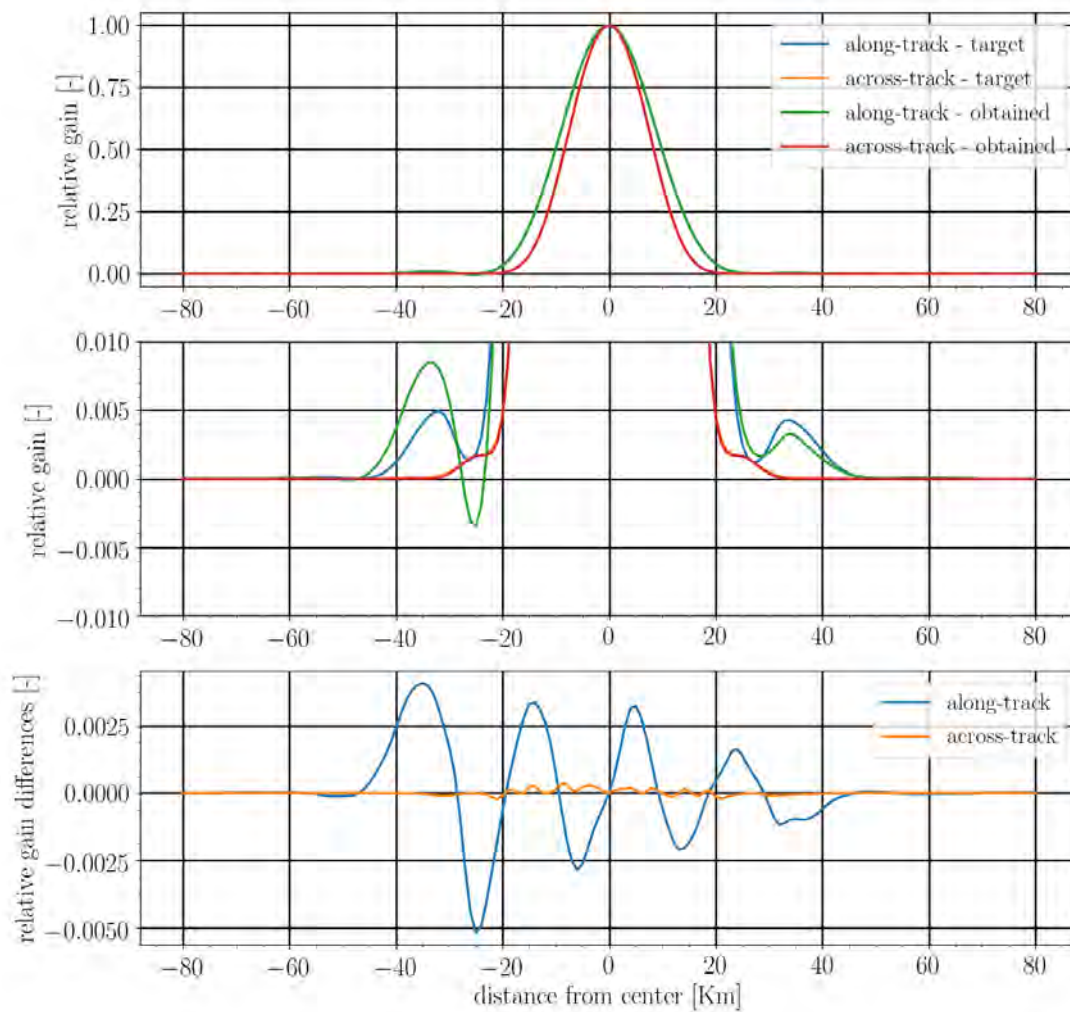
Figure 38: As Figure 27 but for ICI-10 to ICI-1 remapping.

	Backus-Gilbert footprint matching methodology applied on MWI and ICI observations	Code: TR/BG/MWI-ICI
		Issue: 1.0
		Date: June 5, 2019
		File: optimal-interpolation-applied.tex
		Page: 82 / 200

7.2.7 ICI-11V to ICI-1

Results of the ICI-11V to ICI-1 remapping is presented in Figures 39 and 40. The remapping calculation was performed using a 160[Km] x 160[Km] wide grid having a 1[Km] spacing between grid points. All ICI-11V samples (122) within a radius of 30[Km] from the geolocation (boresight intersection with geoid) of the ICI-1 target footprint were included in the calculation.

The result of the ICI-11V to ICI-1 remapping is very similar to the characteristic of the ICI-5 to ICI-1 remapping. The main difference is that the estimated noise of the resampled observation is 0.95[K], which is higher than for the ICI-5 case, but is explained by the fact the noise of individual samples is higher for ICI-11V than for ICI-5. Another small difference is that the fit to the target is slightly better for ICI-11V than for ICI-5.
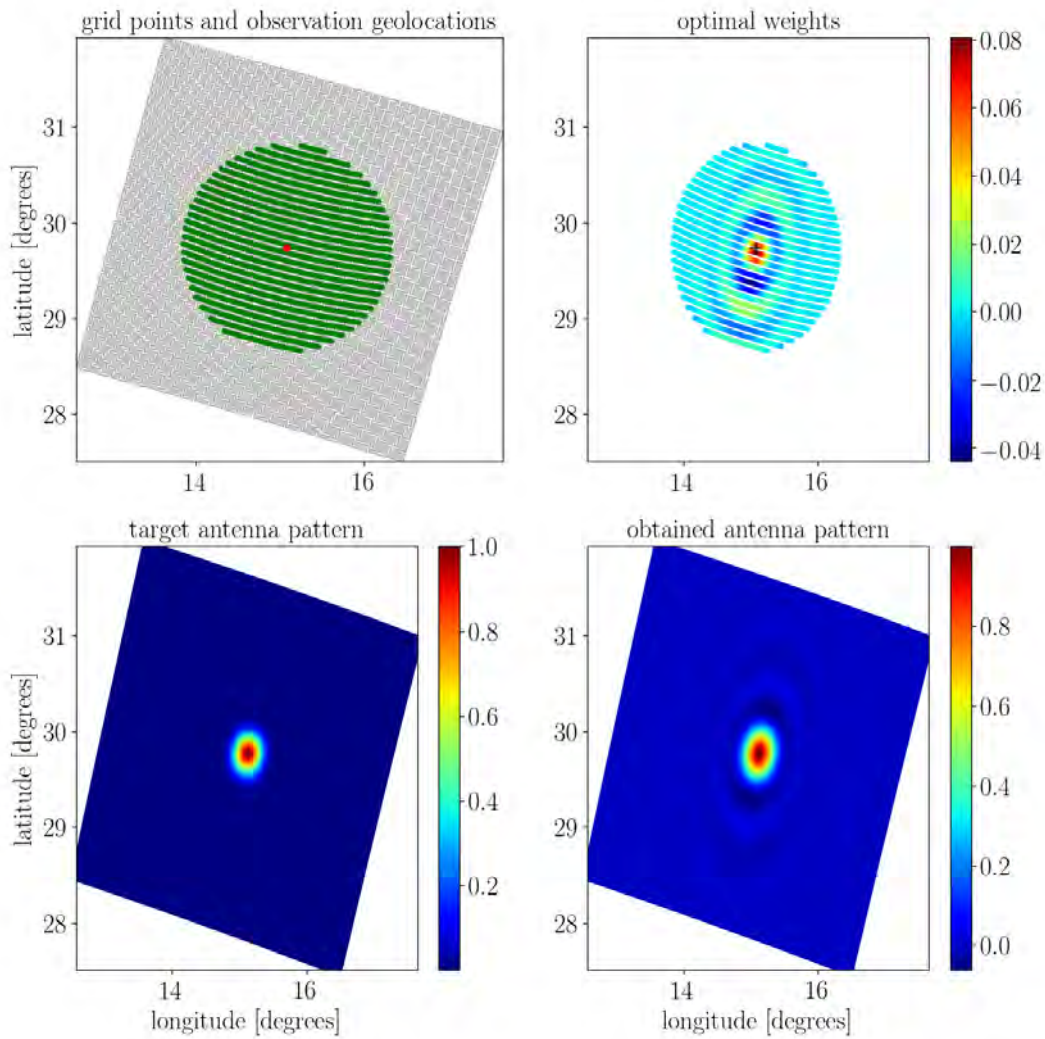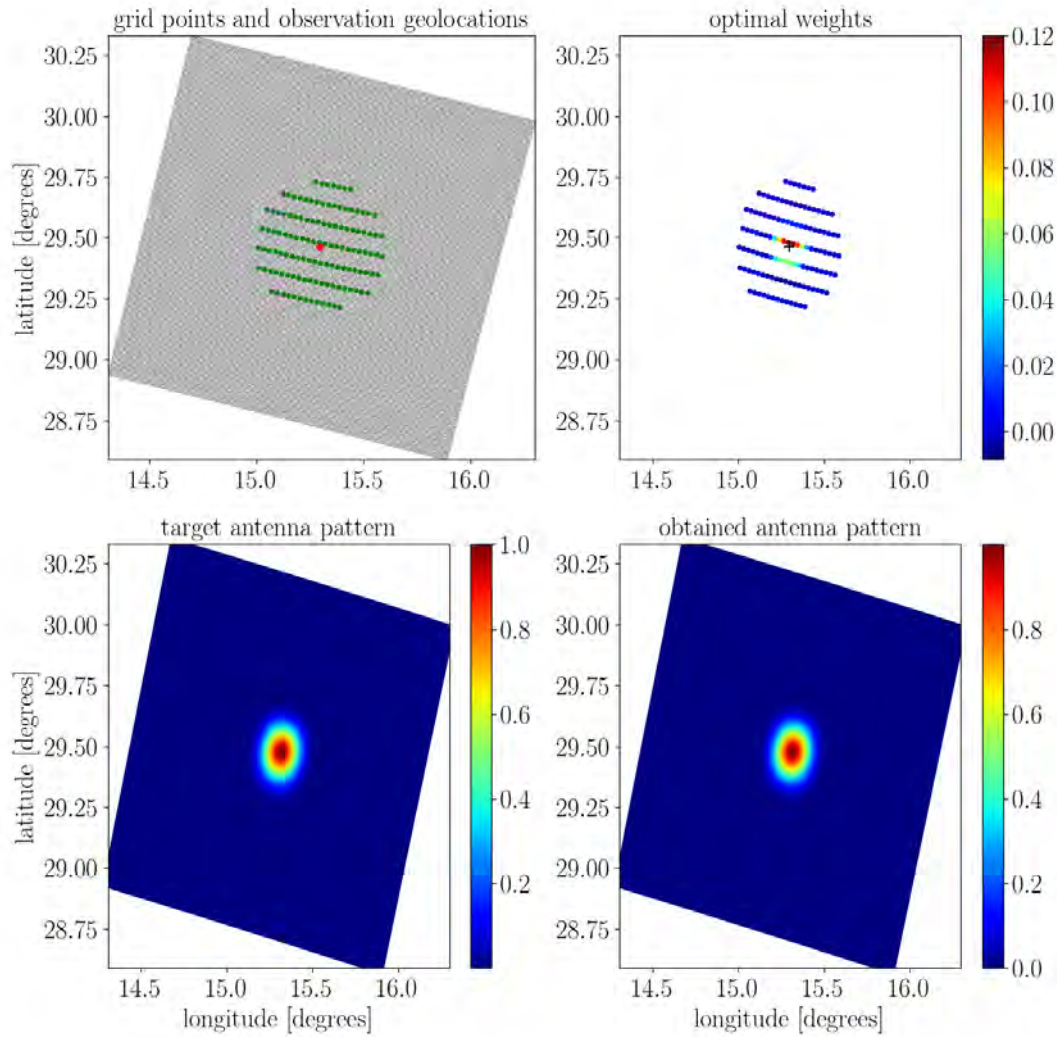
Figure 39: Footprint remapping of ICI-11V samples to ICI-1 target footprint. 122 samples within a radius of 30[Km] from the ICI-1 geolocation is used. Otherwise as Figure 26.
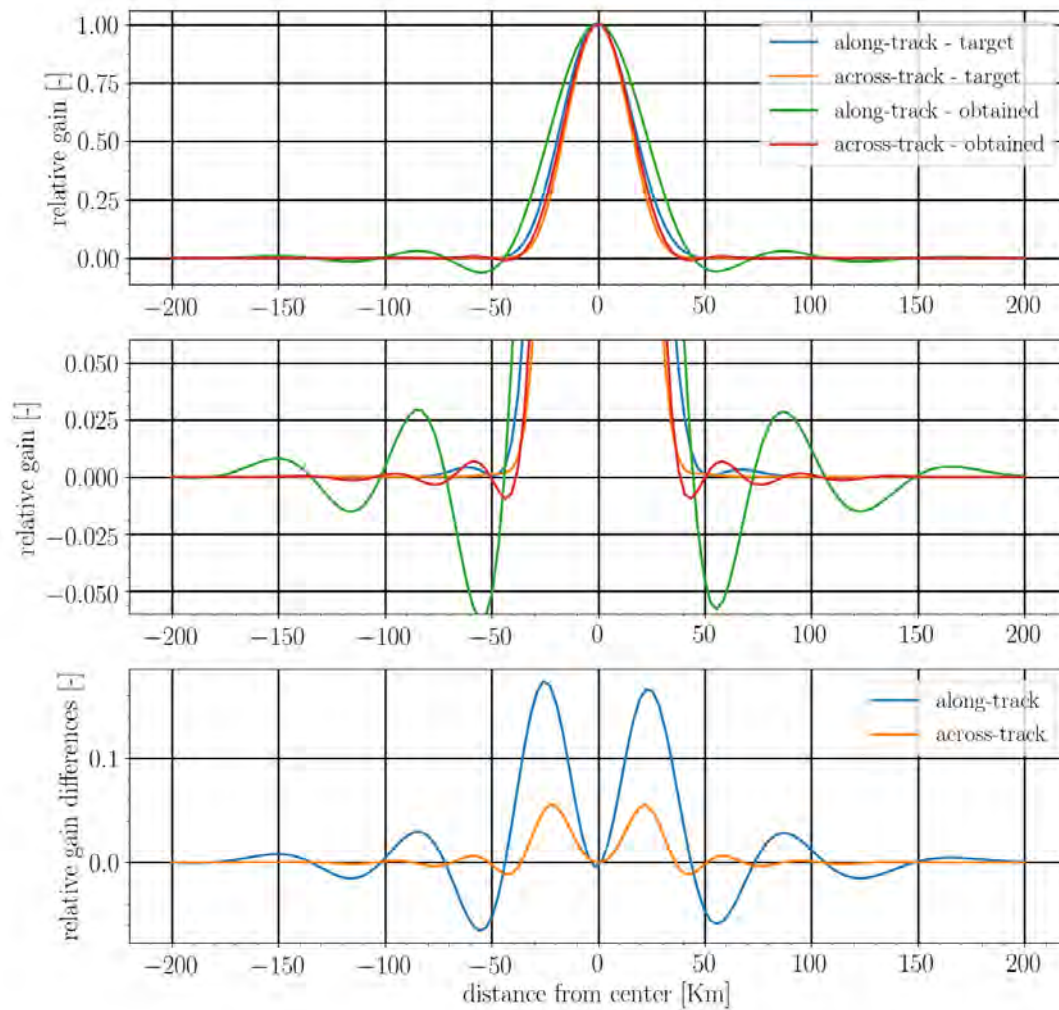
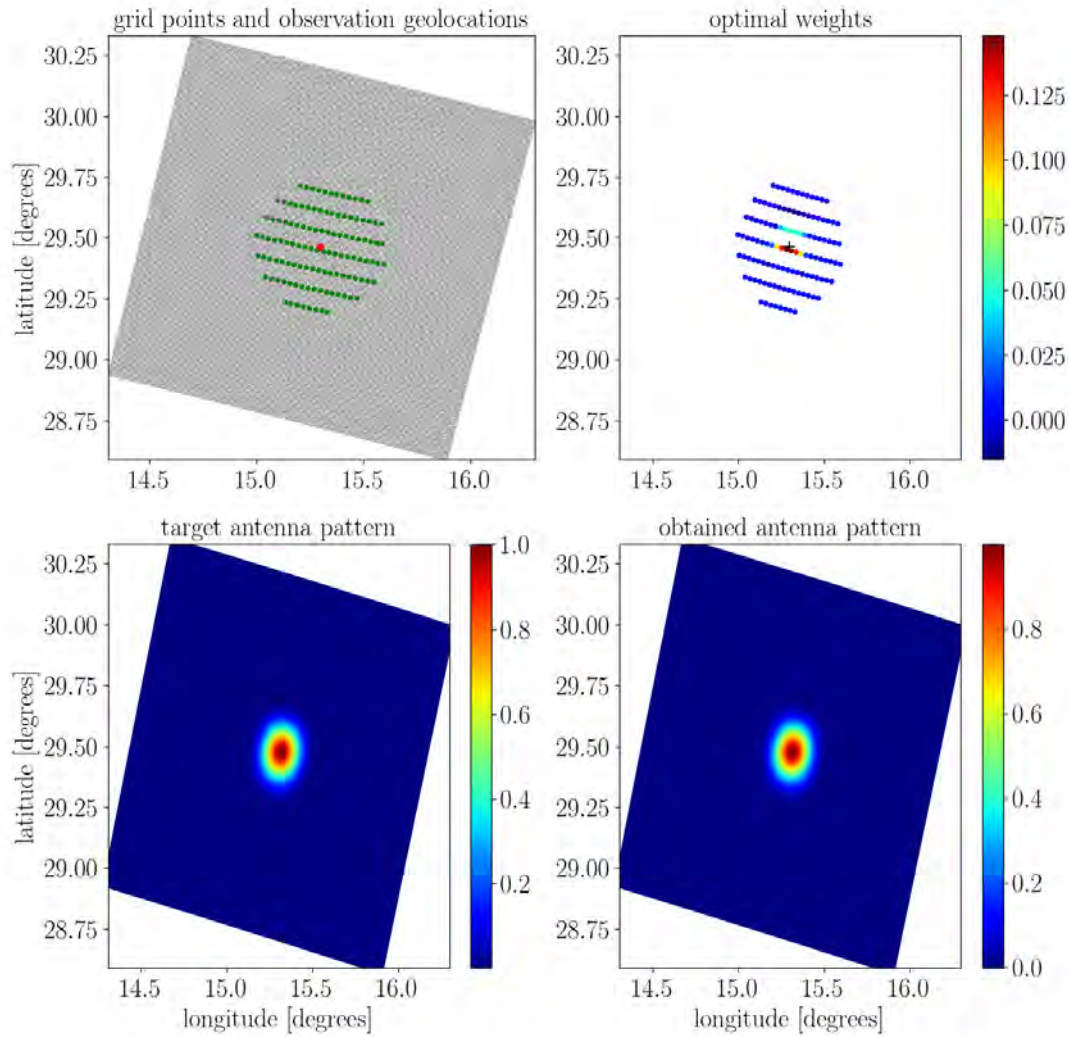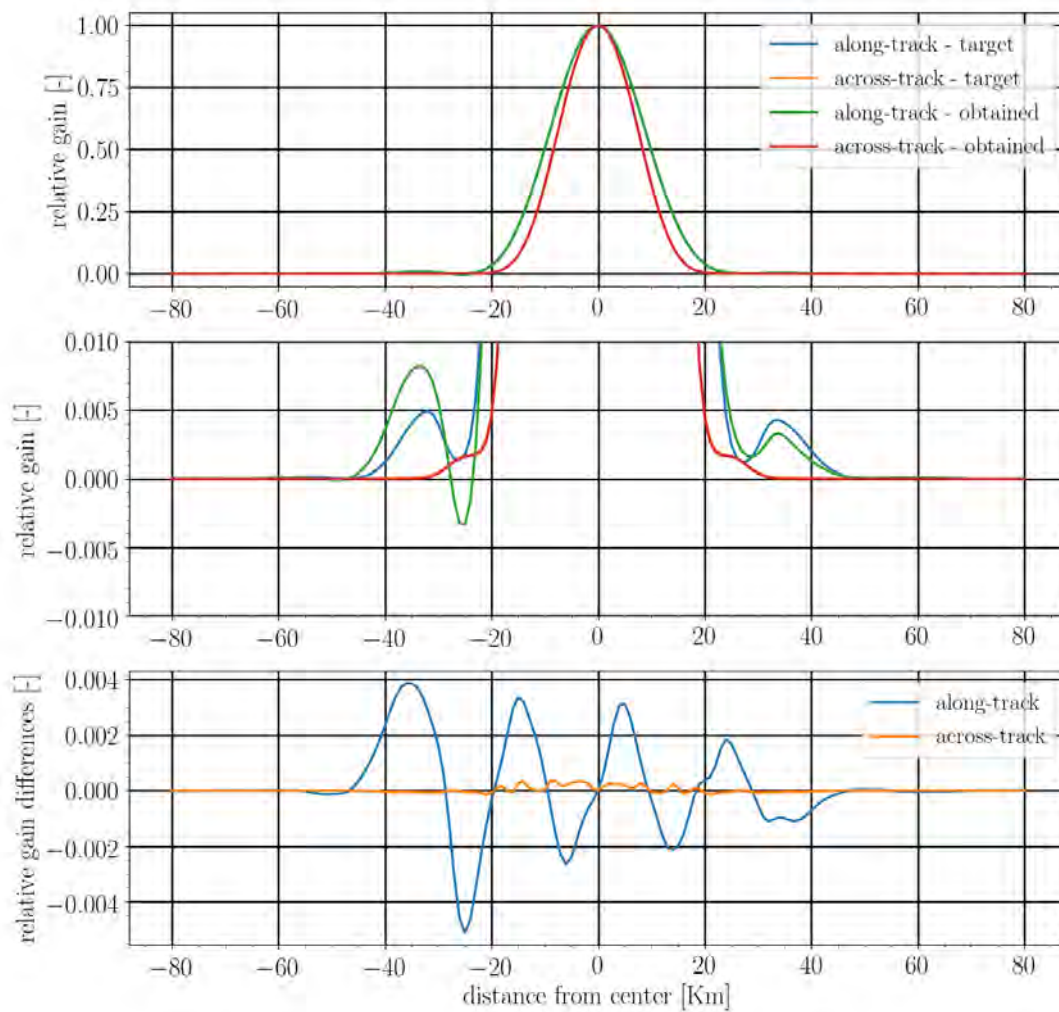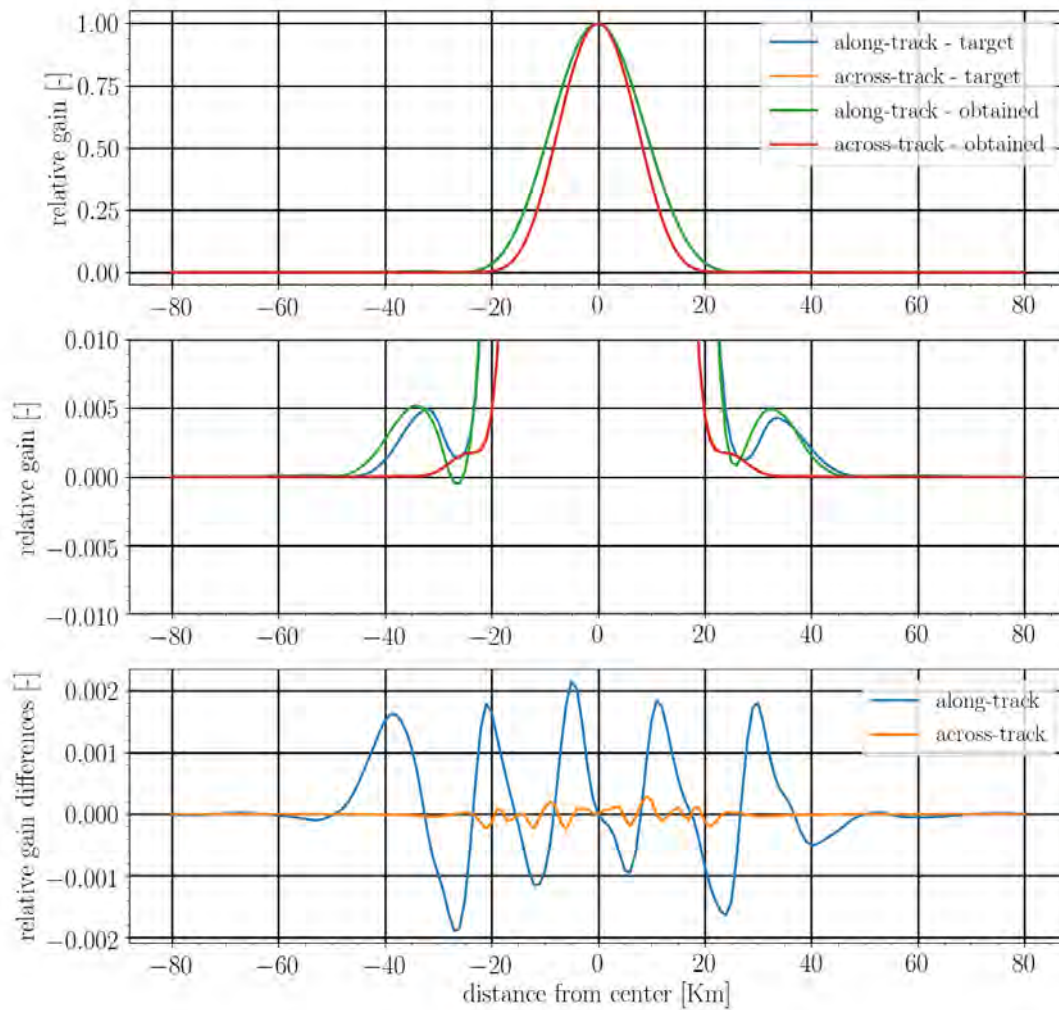Figure 40: As Figure 27 but for ICI-11V to ICI-1 remapping.

	Backus-Gilbert footprint matching methodology applied on MWI and ICI observations	**Code:** TR/BG/MWI-ICI
		Issue: 1.0
		Date: June 5, 2019
		File: optimal-interpolation-applied.tex
		Page: 85 / 200

7.3 "Operational" footprint remapping

A gain of the BG footprint matching technique is that it is a rather computational inexpensive and non-complex algorithm to apply operationally. This is because it is possible to use a set of precalculated weighting coefficients for the remapping between channel footprints, and hence, only the calculation of a weighted sum of the involved samples is needed (see Eq. 31).

However, it is in general not sufficient to only use one set of weighting coefficients for the remapping between two channel footprints, as the optimal set of weighting coefficients depends on both

1. the position of the target footprint within the scan (i.e. sample number). At the edges of the scan a proper remapping can even be impossible to perform. This is the case as some of the channels do not have equally wide "swath width" as the target channel, and this is described in more details in Sect. 9, and consequently less overlapping samples are available for the remapping at the very edges of the scan.

   The best situation for the remapping is in general for samples numbers a bit away from both the very edge of the scan and middle of the scan. In the outer part of the scan the distance between the geolocations of samples of two consecutive scans are shorter than in the center part of the scan, due to the satellite propagation direction. Thus, more and better overlapping samples are available for the remapping a bit away from the center samples of the scan.

2. the distance from the sensor to Earth surface or r (see Eq. 29 and Eq. 31 and r will not be constant, as the platform altitude will vary between 820[km] and 850[km] for a given orbit). However, it is not obvious that the weighting coefficients dependency on r is great enough to be needed to be taken into account of. This is studied in more details in Sect. 9.

This gives that a dataset of weighting coefficients for various sample positions and sensor altitudes of the target observation must be created to allow for an "operational" remapping. The deployed format for storing the weighting coefficient dataset is described in List. 3.

Given that such a dataset is available, the estimation of antenna temperature $T_{a,remapped}$ of a target FOV centered around a given scan and sample number (s and t) can be described by

$$T_{a,remapped}[s,t] = \sum_{i=1}^{n} a_{t,z}[i] T_{a,sample}[s + \Delta s[i], t + \Delta t[i]], \tag{54}$$

where $a_{t,z}[i]$ denotes the sample number and sensor altitude specific weighting coefficients, and $\Delta s[i]$ and $\Delta t[i]$ describes the scan and sample number offsets (relative to the target scan and sample number) of the observations to be remapped, respectively, and $T_{a,sample}$ denotes the antenna temperature of these. The dataset of weighting coefficients has an altitude dimension, and the weighting coefficients valid for the closest altitude to the sensor altitude of the observation is used.

	Backus-Gilbert footprint matching methodology applied on MWI and ICI observations	Code: TR/BG/MWI-ICI
		Issue: 1.0
		Date: June 5, 2019
		File: optimal-interpolation-applied.tex
		Page: 86 / 200

8 Optimal interpolation software package

8.1 Introduction

The *optimal-interpolation* (OI) is a Python[11] package developed in order to study and apply the Backus-Gilbert footprint matching methodology on MWI and ICI observations. It contains modules and scripts that deploy the algorithms for footprint remapping described in Sect. 7. That is, it contains modules/functions and scripts for:

- basic geometry calculation

- MWI and ICI scanning

- antenna gain function manipulation

- Backus-Gilbert formalism and trade off analysis

- remapping of MWI and ICI samples using precalculated weights

The package also contains relevant data files (e.g. antenna gain functions for the MWI and ICI channels and orbit state vector data covering some reference orbits).

8.2 Installation

The OI package is build around a number of other Python packages:

- pymap3d[12]: pure Python coordinate conversions

- numpy[13]: is the fundamental package for scientific computing with Python.

- netcdf4[14]: is a Python interface to the netCDF C library

- pyproj[15]: Performs cartographic transformations and geodetic computations.

- scipy[16]:a collection of numerical algorithms and domain-specific toolboxes

- matplotlib[17]: is a Python plotting library.

These packages can be obtained from Python Package Index (PyPI[18]), but *wheels*[19] for these packages are included in the OI package, instead of depending on PyPI or some other network

---

[11]https://www.python.org/

[12]https://pypi.org/project/pymap3d/

[13]http://www.numpy.org/

[14]http://unidata.github.io/netcdf4-python/

[15]https://pypi.org/project/pyproj/

[16]https://www.scipy.org/

[17]https://matplotlib.org/

[18]https://pypi.org/

[19]https://pythonwheels.com/

location. These wheels are Python3.6 and linux dependent, and Python3.6 is the newest major release of the Python language.

Python packages should almost never be installed on the host Python environment, and the OI package is preferably installed in a *virtualenv*[20]. A suitable virtualenv for the OI package can be created by first installing the package *virtualenvwrapper*[21]:

```
sudo pip install virtualenvwrapper
```

on the host (so check that you are not in a virutalenv before installing). Also add this to your shell startup file:

```
export WORKON_HOME=$HOME/.virtualenvs # The virtualenvs are stored here.
export PROJECT_HOME=$HOME/Devel # Location of your development project directories
source /usr/local/bin/virtualenvwrapper.sh
```

Then you can create a virtualenv by:

```
mkvirtualenv −−python=/usr/bin/python3.6 optimal−interpolation
```

and change to this environment by:

```
workon optimal−interpolation
```

and if you want to change back:

```
deactivate
```

The OI package can then be installed in two ways, either by using the included wheels (Python3.6 and linux dependent)

```
pip install −r requirements/requirements.txt −−no−index −−find−links requirements/wheelhouse
python3 setup.py build
python3 setup.py install
```

or, alternatively by (collecting dependencies from PyPI, and can also be done using a virtualenv for Python3.7 if that is preferable)

```
pip install −r requirements/requirements.txt
python3 setup.py build
python3 setup.py install
```

For developers

The requirements.txt file can be updated, if necessary, by:

```
pip install pip−tools
pip−compile requirements/requirements.in
```

and the package can then be re-installed by:

---

[20] https://virtualenv.pypa.io/en/latest/
[21] https://virtualenvwrapper.readthedocs.io/en/latest/install.html

	Backus-Gilbert footprint matching methodology applied on MWI and ICI observations	Code: TR/BG/MWI-ICI
		Issue: 1.0
		Date: June 5, 2019
		File: optimal-interpolation-applied.tex
		Page: 88 / 200

```
pip install −r requirements/requirements.txt
python3 setup.py install
```

There is no promise that everything will work after this, but there is a number of unittests that can be run using tox[22]. The tests can be run in two ways, either using the included wheels, by:

```
pip install tox
tox −py3wheel
```

or not, by:

```
pip install tox
tox −py3
```

8.3 Usage

In this section, example usage of the most important executable programs and module functions of the package is demonstrated. The OI package contains four main executable programs (Fig. 41):

- *trade_off_analysis*, that runs the algorithm for deriving a set of optimal weights (described in Sect. 7) for a specified remapping (e.g. the remapping of ICI-11 samples into ICI-1 FOV for sample number 392) and saves the result into a file

- *repeated_trade_off_calculation*, that primarily is a wrapper around *trade_off_analysis* and derive optimal weighting coefficients for e.g. all samples/FOVs of a given scan or many scans

- *create_weighting_coefficients_file*, that collects weighting coefficients file for individual FOVs and stores the results into a single weighting coefficients file, that can be used as input for the program *weighting_calculation* described below

- *weighting_calculation*, that applies the remapping between channel footprints using pre-calculated weights (defined by an input weighting coefficients file)

Basic usage, including input and output file formats, of these programs are shown in this section. The basic modules of the package can also be used interactively, and example usage is provided within this section (and a more detailed API is described in Sect. 8.4).

Remapping model parameter file

The input JSON[23] formatted remapping model parameter file (that is input to the *trade_off_analysis*, *repeated_trade_off_calculation*, and *create_weighting_coefficients_file*) is described below.

---

[22]https://tox.readthedocs.io/en/latest/
[23]https://www.json.org/
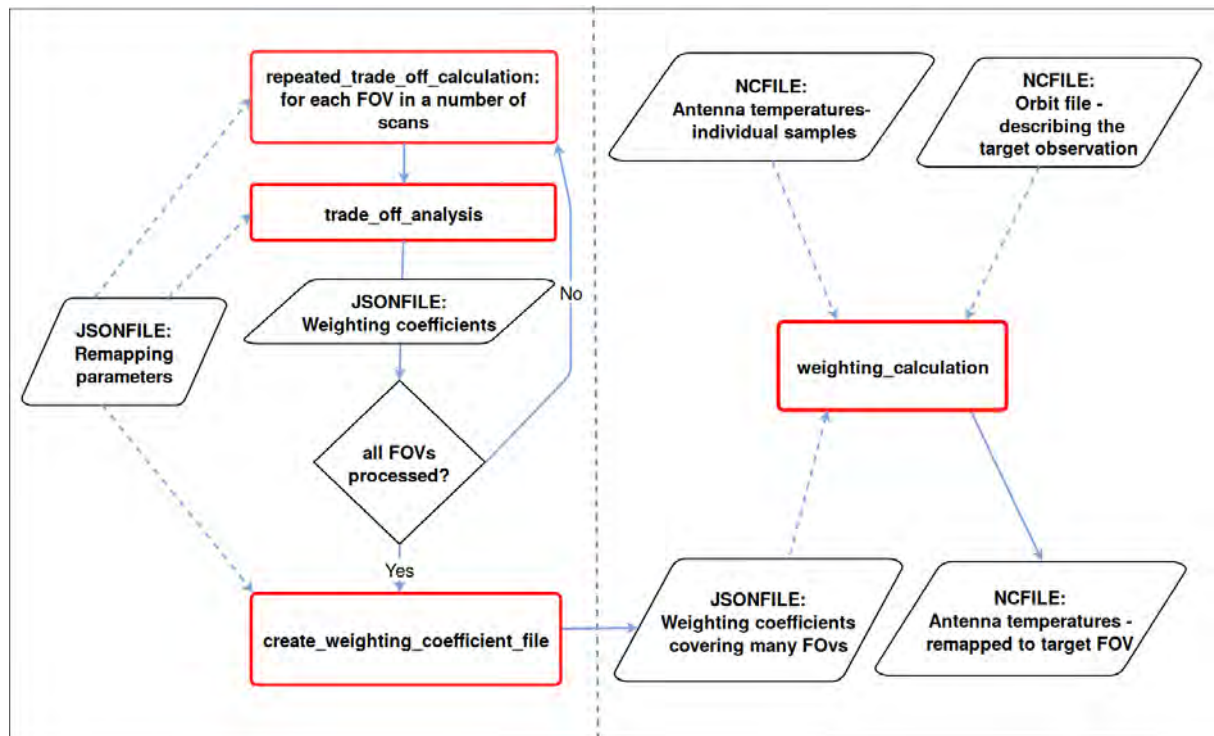
Figure 41: Schematic describing the dependencies between the four main executable programs (red boxes) of the packake, and to input/output files. The three program in the left part of the graph shares a common "remapping parameters" input file. The *repeated_trade_off_calculation* program is simply a wrapper around the *trade_off_analysis* program, that outputs a "weighting coefficients file" for each analysed FOV. The program *create_weighting_coefficients_file* collects the generated weighting coefficients files for individual FOVs and stores the results into a single weighting coefficients file. The program *weighting_calculation* outputs a NetCDF file containing remapped observations, and require three types of input files.

Code Listing 1: Description of the JSON formatted remapping model parameter file (input file to the programs *trade_off_analysis*, *repeated_trade_off_calculation*, and *create_weighting_coefficients_file*) and example usage of how to generate one.

```python
import json


remapping_model_parameter = {
    "targetInstrument": "ICI",
    "targetChannel": 1,
    "targetIntegrationTime": 2.532e-3,
    "nativeInstrument": "ICI",
    "nativeChannel": 11,
    "nativeStartTimeFirstScanOffset": 0,
    "nativeIntegrationTime": 0.661e-3,
    "nativeNoise": 3.51,
    "maxRadius": 30e3,
```

	Backus-Gilbert footprint matching methodology applied on MWI and ICI observations	**Code:** TR/BG/MWI-ICI
		Issue: 1.0
		Date: June 5, 2019
		File: optimal-interpolation-applied.tex
		Page: 90 / 200

```
    "halfWidthOfGrid": 80e3,
    "approximateResolution": 1e3,
    "betaMin": 1e-9,
    "betaMax": 1e-3,
    "betaNpoints": 100,
    "maxNoiseError": 2.0,
    "minFitError": 1e-5,
}
remapping_model_filename = "/data/remapping_ICI11_to_ICI1.json"

with open(remapping_model_filename, 'w') as outfile:
    json.dump(remapping_model_parameter, outfile)
```

- "targetInstrument": (str), target instrument ("MWI" or "ICI")

- "targetChannel": (int), target channel number (1-13 for ICI and 1-26 for MWI is possible, although 1 and 5 corresponds to ICI-1 and MWI-3V, respectively, and these channels are the channels that are planned to be used as target channels "operationally")

- "targetIntegrationTime": (float) integration time [s] of the target observation

- "nativeInstrument": (str), instrument of the samples to be remapped ("MWI" or "ICI")

- "nativeChannel": (int), channel number of the samples to be remapped (1-13 for ICI and 1-26 for MWI)

- "nativeStartTimeFirstScanOffset": (int), offset in time $[\mu s]$ between the first scan of the target and native instrument (this parameter allows to study remappings between ICI and MWI observations where the scan starts may not be synchronized)

- "nativeIntegrationTime": (float), integration time [s] of the samples to be remapped

- "nativeNoise": (float), noise [K] of the individual samples

- "maxRadius": (float), max distance [m] from target geolocation from where to include samples in the calculation

- "halfWidthOfGrid": (float), half width [m] of the grid used for remapping

- "approximateResolution": (float), resolution [m] of the grid used for remapping. The actual resolution of the grid will be the specified one if 2 x "halfWidthOfGrid" / approximateResolution is an integer, otherwise the resolution differs slightly from the specied one, which explains the name "approximateResolution"

- "betaMin": (float), min value of smoothing parameter

- "betaMax": (float), max value of smoothing parameter

- "betaNpoints": (int), number of smoothing paramers

- "maxNoiseError": (float), maximum acceptable noise error in trade off analysis

- "minFitError": (float), minimum acceptable fit error in trade off analysis

The package comes with a set of model parameter files (located in scripts/jsonfiles). These were generated by running the script:

```
./create_remapping_parameter_file.py −q /datadir−for−save
```

and this script should be uncomplicated to modify in order to create files with updated values.

	Backus-Gilbert footprint matching methodology applied on MWI and ICI observations	Code:	TR/BG/MWI-ICI
		Issue:	1.0
		Date:	June 5, 2019
		File:	optimal-interpolation-applied.tex
		Page:	92 / 200

Program for deriving optimal weighting coefficients for a specific remapping

The usage of the program *trade_off_analysis* is described below:

```
usage: trade_off_analysis [-h] [-o NCFILE] [-s START_TIME_OF_FIRST_SCAN]
                          [-p PLOT_DATA] [-r SAVE_DATA]
                          [-q DATADIR_FOR_SAVE]
                          JSONFILE scan-number sample-number


positional arguments:
  JSONFILE remapping model parameter file
  scan-number scan number of target observation
  sample-number sample number of target observation

optional arguments:
  -h, --help show this help message and exit
  -o NCFILE, --orbit-file NCFILE
                      orbit state vector file (metop_a_orbit_4655.nc is
                      default)
  -s START_TIME_OF_FIRST_SCAN, --start-time-of-first-scan START_TIME_OF_FIRST_SCAN
                      start time (YYYY-mm-ddTHH:MM:SS) of the first scan of
                      the target instrument, default is 2007-09-12T08:43:03
  -p PLOT_DATA, --plot-results PLOT_DATA
                      plot data (0 or 1) default is 1 (True)
  -r SAVE_DATA, --save-results SAVE_DATA
                      save generated data (0 or 1) default is 0 (False)
  -q DATADIR_FOR_SAVE, --datadir-for-save DATADIR_FOR_SAVE
                      data directory for saving output default is /tmp
```

The program can for instance be invoked by:

```
trade_off_analysis /full-path-to-file/remapping_ICI11_to_ICI1.json 205 392 -r 1
```

and than optimal weighting coefficients for the remapping from ICI-11 samples into the ICI-1 field of view for scan number 205 and sample number 392 will be calculated. The calculation uses precaclulated orbit state vector data contained in the default orbit file, but an orbit file can also be given as input. If the "SAVE_DATA" option is turned on, key parameters from the calculation is saved into a JSON format output file, as described below:

	Backus-Gilbert footprint matching methodology applied on MWI and ICI observations	Code:	TR/BG/MWI-ICI
MoHoW		Issue:	1.0
		Date:	June 5, 2019
		File:	optimal-interpolation-applied.tex
		Page:	93 / 200

Code Listing 2: Description of the JSON formatted output file of the program *trade_off_analysis*

```json
{
    "targetInstrument": str,
    "targetChannel": int,
    "nativeInstrument": str,
    "nativeChannel": int,
    "remappingData": {
        "sensorAltitude": float,
        "targetScanNumber": int,
        "targetSampleNumber": int,
        "weights": array(float),
        "scanNumberOffsets": array(int),
        "sampleNumberOffsets": array(int),
        "optimalBeta": float,
        "noiseError": float,
        "fitError": float
    }
}
```

where

- "sensorAltitude": altitude [m] of the sensor at the aqusition time of the target observation

- "weights": derived weighting coefficients (array of floats)

- "scanNumberOffsets": the weights corresponding scan number offsets (relative to scan number of target observation)

- "sampleNumberOffsets": the weights corresponding sample number offsets (relative to scan number of target observation)

- "optimalBeta": the obtained optimal value of the smoothing parameter beta

- "noiseError": the obtained noise error [K] of the remapping

- "fitError": the obtained fit error [-] of the remapping

Program for running trade off analysis for many FOVs

The usage of the program *repeated_trade_off_calculation*, that is a wrapper around the program *trade_off_analysis*, is described below:

```
usage: repeated_trade_off_calculation [-h] [-o NCFILE]
                                      [-s START_TIME_OF_FIRST_SCAN]
                                      [-q DATADIR_FOR_SAVE]
                                      JSONFILE scan-number [scan-number ...]
                                      sample_number_start sample_number_end
                                      sample_number_step


positional arguments:
  JSONFILE remapping model parameter file
  scan-number scan number(s) of target observation
  sample_number_start first sample number to process
  sample_number_end last sample number to process
  sample_number_step step between sample numbers to process

optional arguments:
  -h, --help show this help message and exit
  -o NCFILE, --orbit-file NCFILE
                      orbit state vector file (metop_a_orbit_4655.nc is
                      default)
  -s START_TIME_OF_FIRST_SCAN, --start-time-of-first-scan START_TIME_OF_FIRST_SCAN
                      start time (YYYY-mm-ddTHH:MM:SS) of the first scan of
                      the target instrument, default is 2007-09-12T08:43:03
  -q DATADIR_FOR_SAVE, --datadir-for-save DATADIR_FOR_SAVE
                      data directory for saving output default is /tmp
```

The program can for instance be invoked by:

```
repeated_trade_off_calculation /full−path−to−file/remapping_ICI11_to_ICI1.json 205 1000 1 784 3
```

and in that case a trade of analysis of ICI11 samples to ICI1 field of view (FOV) will be performed, for scan number 205 and 1000 and for ICI1 sample numbers 1, 4, ..., 784. A file, as generated by the program *trade_off_analysis*, will be created, for each successful analysed FOV. In the outer part of the scan it might be impossible to perform a remapping, as the various channels have slightly different swath width (as decribed in e.g. Sect. 9.2 and Sect. 9.3), and that will effectively result in that no samples located close enough to the geolocation of the target footprint are available, and in that case no output file is generated.

	Backus-Gilbert footprint matching methodology applied on MWI and ICI observations	**Code:** TR/BG/MWI-ICI
		Issue: 1.0
		Date: June 5, 2019
		File: optimal-interpolation-applied.tex
		Page: 95 / 200

Creating a weighting coefficients file covering many scans FOVs

The usage of the program *create_weighting_coefficients_file* is described below (it is dependent on that the program *repeated_trade_off_calculation* has been executed and generated weighting coefficients files for individual FOVs):

```
usage: create_weighting_coefficients_file [-h]
                                [-q DATADIR_FOR_SAVE]
                                JSONFILE
                                [scan-number ...]
                                sample_number_start
                                sample_number_end
                                sample_number_step
                                datadir_preprocessed_files

positional arguments:
  JSONFILE remapping model parameter file
  scan-number scan number(s) of target observation
  sample_number_start first sample number to process
  sample_number_end last sample number to process
  sample_number_step step between sample numbers to process
  datadir_preprocessed_files data directory of the preprocessed weighting
                          coefficients file for individual FOVs

optional arguments:
  -h, --help show this help message and exit
  -q DATADIR_FOR_SAVE, --datadir-for-save DATADIR_FOR_SAVE
                    data directory for saving output default is /tmp
```

The program can for instance be invoked by:

```
remapping_file="/full-path-to-file/remapping_ICI11_to_ICI1.json"
create_weighting_coefficients_file $remapping_file 205 1000 1 784 3 /data
```

and in that case the program will try to collect all individual preprocessed weighting coefficients file for individual FOVs for scan number 205 and 1000 and for ICI1 sample numbers 1, 4, ..., 784, and these files are assumed to be located in directory /data. A single weighting coefficients file having a format described in Listing 3 will be generated. This file can be used as input to the program for remapping using precalculated weights.

Code Listing 3: Description of the JSON formatted weighting coefficient file, generated by the program *create_weighting_coefficients_file* and used as input to the program *weighting_calculation* (with fake data in order to give a better view of the structure).

```json
{
    "targetInstrument": "ICI",
    "targetChannel": 1,
    "nativeInstrument": "ICI",
    "nativeChannel": 11,
    "remappingData": [
        {
            "sensorAltitude": 830e3,
            "applicableSampleNumbers": [1, 2],
            "weights": [0.25, 0.25, 0.25, 0.25],
            "scanNumberOffsets": [0, 0, 0, 0],
            "sampleNumberOffsets": [13, 14, 15, 16],
        },
        {
            "sensorAltitude": 830e3,
            "applicableSampleNumbers": [3, 4, 5],
            "weights": [0.2, 0.2, 0.2, 0.2, 0.2],
            "scanNumberOffsets": [0, 0, 0, 0, 0],
            "sampleNumberOffsets": [12, 13, 14, 15, 16],
        },
        ...
        ,
        {
            "sensorAltitude": 820e3,
            "applicableSampleNumbers": [1, 2],
            "weights": [0.2, 0.3, 0.3, 0.2],
            "scanNumberOffsets": [0, 0, 0, 0],
            "sampleNumberOffsets": [13, 14, 15, 16],
        },
        ...

    ]
}
```

where

- "sensorAltitude": altitude [m] of the sensor around which the weights are valid (float)

- "applicableSampleNumbers": the target sample numbers where the weights are considered to better to use than any other available data (array of ints). That is, if this file was created based on trade off analysis calculations of ICI1 sample numbers 1, 4, ..., 784, it is assumed that the set of weighting coefficients derived for e.g. sample number 4 is the best one to apply for sample numbers 3, 4, and 5, and so on. In general, it is most safe to derive weighting coefficients for all scan positions of interest, but having it in this way we allow for a simplification.

- "weights": derived weighting coefficients (array of floats)

	Backus-Gilbert footprint matching methodology applied on MWI and ICI observations	Code: TR/BG/MWI-ICI
		Issue: 1.0
		Date: June 5, 2019
		File: optimal-interpolation-applied.tex
		Page: 97 / 200

- "scanNumberOffsets": the weights corresponding scan number offsets (relative to scan number of target observation) (array of ints)

- "sampleNumberOffsets": the weights corresponding sample number offsets (relative to scan number of target observation) (array of ints)

Program for remapping using precalculated weights

The usage of the program *weighting_calculation* is described below:

```
usage: weighting_calculation [-h] [-c CHANNEL_NUMBER] [-p PLOT_DATA]
                             [-r SAVE_DATA] [-q DATADIR_FOR_SAVE]
                             JSONFILE NCFILE NCFILE scan_number_start
                             scan_number_end sample_number_start
                             sample_number_end sample_number_step


positional arguments:
  JSONFILE weighting coefficient file to apply for remapping
  NCFILE orbit file describing the target observations
  NCFILE file containing antenna temperatures for individual
                     samples
  scan_number_start first scan number to process
  scan_number_end last scan number to process
  sample_number_start first sample number to process
  sample_number_end last sample number to process
  sample_number_step step between sample numbers to process


optional arguments:
  -h, --help show this help message and exit
  -c CHANNEL_NUMBER, --channel-number CHANNEL_NUMBER
                     channel number, this option allows to apply weights
                     derived from one channel to another channel
  -p PLOT_DATA, --plot-results PLOT_DATA
                     plot data (0 or 1) default is 0 (False)
  -r SAVE_DATA, --save-results SAVE_DATA
                     save generated data (0 or 1) default is 1 (True)
  -q DATADIR_FOR_SAVE, --datadir-for-save DATADIR_FOR_SAVE
                     data directory for saving output default is /tmp
```

The program can for instance be invoked by:

```
weighting_coefficient_file="/full-path-to-file/weighting_coefficients_ICI11_to_ICI1.json"
orbit_file="/full-path-to-file/metop_a_orbit_4655_ICI_line_of_sight.nc"
ta_file="/full-path-to-file/ta_orbit4655_ici_ch11.nc"

weighting_calculation $weighting_coefficient_file $orbit_file $ta_file 1 4455 1 784 3
```

and in that case a remapping of ICI11 samples to ICI1 field of view (FOV) will be performed, for scan numbers between 1 and 4456 and for ICI1 sample numbers 1, 4, ..., 784, as defined by the *metop_a_orbit_4655_ICI_line_of_sight.nc* file. The data will be stored in a netCDF file as described below. The required orbit and antenna temperature file formats are described in Appendix A. The input weighting coefficients file is described in Listing 3. The optional argument *CHANNEL_NUMBER* can be set, and this option allows to apply weights derived from one channel for samples from another channel (see Sect. 9 for a description of which channels this can be used for).

It is stressed that the item *remappingData*, of the weighting coefficient file (described in Listing 3) is a list of "dictionaries" and the items *sensorAltitude* and *applicableSampleNumbers* describes the condition on where the weights are valid. These "dictionaries" must be specified for at least one *sensorAltitude* and all target sample numbers of interest and with no ambiguity. If such data are specified for several values of *sensorAltitude*, weights for the "dictionary" with the closest *sensorAltitude* to the sensor altitude of target observation will be used in the remapping calculation.

The items *scanNumberOffsets* (Δs) and *sampleNumberOffsets* (Δt) describes offsets relative to the target scan number (s) and sample number (t), in such a way that the remapping of sample antenna temperature data $T_{a,sample}$ into the target FOV can be achived by:

$$T_{a,remapped} = \sum_{i=1}^{n} w[i] T_{a,sample}[s + \Delta s[i], t + \Delta t[i]], \tag{55}$$

where w is the weight.

If the "SAVE_DATA" option is turned on, remapped antenna temperatures from the calculation is saved into a netCDF format output file, as described below:

```
netcdf ta_remapped_orbit4655_ICI_ch11_on_ICI_ch1_fov {
dimensions:
        scan = 4455 ;
        sample = 262 ;
variables:
        int scan_number(scan) ;
                scan_number:description = "scan number" ;
                scan_number:actual_range = 1LL, 4455LL ;
        int sample_number(sample) ;
                sample_number:description = "sample number" ;
                sample_number:actual_range = 1LL, 784LL ;
                sample_number:valid_range = 4, 784 ;
        float TA(scan, sample) ;
                TA:least_significant_digit = 3LL ;
                TA:description = "Remapped Antenna Brightness Temperature [K]" ;
                TA:actual_range = 149.047631669692, 247.013230894616 ;

// global attributes:
                :orbit = "4655" ;
                :instrument = "ICI" ;
                :channel = "11" ;
}
```

	Backus-Gilbert footprint matching methodology applied on MWI and ICI observations	**Code:** TR/BG/MWI-ICI
		Issue: 1.0
		Date: June 5, 2019
		File: optimal-interpolation-applied.tex
		Page: 100 / 200

Calculation of geolocation of a given sample

The example below shows how to calculate the geolocation of a given sample and orbit for MWI. The package comes with precalculated orbit state vector data, and orbit state vector data is interpolated to the corresponding time of the measurement.

```python
# example how to calculate geolocation of a given sample
import os
import numpy as np
from netCDF4 import Dataset
from optimal_interpolation.mwi_and_ici_scanning import (
    ScanSampleGeolocator,
    get_orbit_data
)
from optimal_interpolation.observation_geometry import (
    get_geolocation
)


orbit_file = os.path.join(DATADIR, "orbit", "metop_a_orbit_4655.nc")
orbit_data = get_orbit_data(Dataset(orbit_file, 'r'))
start_time_of_first_scan = np.datetime64("2007-09-12T08:43:03")
target_instrument = "MWI"
target_channel = 5
target_scan_number = 205
target_sample_number = 680

scan_geolocator = ScanSampleGeolocator(
    target_instrument,
    orbit_data,
    start_time_of_first_scan
)

sample_data = scan_geolocator.get_orbit_state_and_viewing_direction_ecef(
    target_channel,
    target_scan_number,
    target_sample_number
)

(latitude, longitude) = get_geolocation(
    sample_data["orbit_state"].position[0],
    sample_data["orbit_state"].position[1],
    sample_data["orbit_state"].position[2],
    sample_data["viewing_direction_ecef"][0],
    sample_data["viewing_direction_ecef"][1],
    sample_data["viewing_direction_ecef"][2]
)

print(latitude, longitude, sample_data["azimuth_angle"])
29.735355163740667 15.080342075619788 195.9035317648112
```

Generate a grid to be used for resampling

The example below shows how to calculate a rectangular grid around a given location for the remapping remapping calculation (described in Sect. 7.1.1 and Fig. 22).

```python
import matplotlib.pyplot as plt
from optimal_interpolation.antenna_pattern_projection import (
    get_grid_for_resampling,
)


latitude = 29.73
longitude = 15.08
half_width = 100e3   # m
approximate_resolution = 2e3   # m
azimuth_angle_sensor_to_grid_center = 195.90 # degrees

grid_for_resampling = get_grid_for_resampling(
    latitude,
    longitude,
    azimuth_angle_sensor_to_grid_center,
    half_width,
    approximate_resolution
)

plt.plot(
    grid_for_resampling["longitudes"],
    grid_for_resampling["latitudes"],
    'k.',
    markersize=1.0
)
plt.show()
```

	Backus-Gilbert footprint matching methodology applied on MWI and ICI observations	**Code:** TR/BG/MWI-ICI
		Issue: 1.0
		Date: June 5, 2019
		File: optimal-interpolation-applied.tex
		Page: 102 / 200

Get all MWI/ICI samples within a radius from a given point

The example below shows how to get all MWI/ICI samples within a radius from a given point or the geolocation of the target (described in Sect. 7.1.4 and Fig. 26). This is done by searching in a range of scans and samples around the target scan and sample number:

```python
from optimal_interpolation.antenna_pattern_projection import (
    get_native_scan_samples_within_radius
)

target_scan_number = 205
target_sample_number = 680
latitude = 29.73
longitude = 15.08

native_instrument = "MWI"
native_channel = 22
scan_number_offset = 25
sample_number_offset = 100
scan_number_range = np.arange(
    target_scan_number - scan_number_offset,
    target_scan_number + scan_number_offset
)
sample_number_range = np.arange(
    target_sample_number - sample_number_offset,
    target_sample_number + sample_number_offset
)
radius = 55e3   # m

samples_within_radius = get_native_scan_samples_within_radius(
    orbit_data,
    start_time_of_first_scan,
    native_instrument,
    native_channel,
    scan_number_range,
    sample_number_range,
    latitude,
    longitude,
    radius
)

# plot geolocation of all samples within specified radius
plt.plot(
    [sample["longitude_geolocation"] for sample in samples_within_radius],
    [sample["latitude_geolocation"] for sample in samples_within_radius],
    'g.',
    markersize=2.0
)
plt.show()
```

	Backus-Gilbert footprint matching methodology applied on MWI and ICI observations	Code: TR/BG/MWI-ICI
		Issue: 1.0
		Date: June 5, 2019
		File: optimal-interpolation-applied.tex
		Page: 103 / 200

Calculation of a smoothed antenna pattern

The example below shows how to calculate a smoothed 2-d antenna gain pattern (taking into account of the rotation during the integration time) from a 1-d antenna diagram (described in Sect. 7.1.2 and Figure 23).

```python
from optimal_interpolation.antenna_pattern_projection import (
    get_antenna_power,
    get_smoothed_antenna_pattern
)

antenna_datadir = os.path.join(DATADIR, "antenna-pattern")

target_instrument = "MWI"
target_channel = 5
scan_duration = 1.3333   # s
target_integration_time = 5.200e-3   # s

antenna_data_1d_target = get_antenna_power(
    antenna_datadir,
    target_instrument,
    target_channel,
    'best'
)

antenna_data_2d_target = get_smoothed_antenna_pattern(
    antenna_data_1d_target,
    target_integration_time,
    scan_duration,
    dx=10, #  width in degrees
    n=201 #  number of points in each dimension
)

plt.pcolor(
    antenna_data_2d_target["theta"],
    antenna_data_2d_target["phi"],
    np.log10(antenna_data_2d_target["data"])
)
plt.show()
```

	Backus-Gilbert footprint matching methodology applied on MWI and ICI observations	**Code:**	TR/BG/MWI-ICI
		Issue:	1.0
		Date:	June 5, 2019
		File:	optimal-interpolation-applied.tex
		Page:	104 / 200

Projection of an antenna pattern on grid

Example below shows how to calculate the projection of an antenna pattern on the grid used for resampling (desribed in Sect. 7.1.3 and Fig. 24 and 25).

```python
import matplotlib.pyplot as plt
from optimal_interpolation.antenna_pattern_projection import (
    get_antenna_pattern_interpolator,
    get_projected_antenna_pattern
)


antenna_datadir = os.path.join(DATADIR, "antenna-pattern")
target_instrument = "MWI"
target_channel = 5
target_integration_time = 5.200e-3  # s
scan_duration = 1.3333  # s

antenna_target_interpolator = get_antenna_pattern_interpolator(
    antenna_datadir,
    target_instrument,
    target_channel,
    target_integration_time,
    scan_duration
)

target_antenna_pattern = get_projected_antenna_pattern(
    antenna_target_interpolator,
    grid_for_resampling,
    sample_data["orbit_state"].position,
    sample_data["viewing_direction_ecef"],
    normalize=True
)

# plot antenna pattern on grid positions
plt.scatter(
    grid_for_resampling["longitudes"].flatten(),
    grid_for_resampling["latitudes"].flatten(),
    c=np.log10(target_antenna_pattern.flatten()),
    s=5,
    cmap='jet',
)
plt.show()
```

	Backus-Gilbert footprint matching methodology applied on MWI and ICI observations	Code:	TR/BG/MWI-ICI
		Issue:	1.0
		Date:	June 5, 2019
		File:	optimal-interpolation-applied.tex
		Page:	105 / 200

8.4 API

MWI and ICI scanning

Module for handling the scanning of MWI and ICI.

class optimal_interpolation.mwi_and_ici_scanning.**ScanSampleGeolocator**(
        instrument, orbit_data, start_time_of_first_scan)
        Class for handling the scanning of MWI and ICI

        get_number_of_scans_covered_by_orbit_data()
        Returns the number of scans covered by the orbit data

        get_orbit_state(*acquisition_time)*
        Returns orbit state vector data (in ECEF coordinates) for the given input time

        get_antenna_tilt_angle(*channel_number)*
        Returns the channel specific antenna tilt angle [degrees]

        get_elevation_offset_angle(*channel_number)*
        Returns the channel specific elevation offset angle [degrees]

        get_azimuth_offset_angle(*channel_number)*
        Returns the channel specific azimuth offset angle [degrees]

        get_integration_time()
        Returns the integration time [s]

        get_scan_speed()
        Returns the scan speed [rpm]

        get_scan_duration()
        Returns the scan duration time [s]

        get_phi_start_window_angle()
        Returns the start window angle [degrees]

        get_phi_start()
        Returns the scan start angle [degrees]

        get_number_of_channels()
        Returns the number of channels of the instrument

        get_start_time_of_sample(*scan_number, sample_number)*
        Returns the start time of the integration for a specific scan and sample

        get_start_time_of_scan(*scan_number)*
        Returns the start time of a scan

        get_acquisition_time(*channel_number, scan_number, sample_number)*
        Returns the acquisition time

        get_phi_rotating_angle(*channel_number, sample_number)*
        Returns the value scanning rotation angle [degrees]

	Backus-Gilbert footprint matching methodology applied on MWI and ICI observations	**Code:** TR/BG/MWI-ICI
		Issue: 1.0
		Date: June 5, 2019
		File: optimal-interpolation-applied.tex
		Page: 106 / 200

get_viewing_direction_sc(*channel_number, sample_number*)
Returns the viewing direction in the satellite coordinate frame

get_orbit_state_and_viewing_direction_ecef(*channel_number, scan_number, sample_number*)
Returns orbit state vector and viewing direction (in ECEF coordinate frame)

function optimal_interpolation.mwi_and_ici_scanning.**get_orbit_data**(*dataset*)
Imports and returns orbit state vector data from a given netCDF orbit dataset

The following exceptions can be raised if an input parameter, to function above, has an invalid value:
exception optimal_interpolation.mwi_and_ici_scanning.**ChannelNumberOutOfRange**

exception optimal_interpolation.mwi_and_ici_scanning.**SampleNumberOutOfRange**

exception optimal_interpolation.mwi_and_ici_scanning.**StartTimeOutsideOrbitDataCoverage**

exception optimal_interpolation.mwi_and_ici_scanning.**AcquisitionTimeOutsideOrbitDataCoverage**

Observation geometry

Module for handling geometry calculation.

function optimal_interpolation.observation_geometry.**get_geolocation**(*x, y, z, dx, dy, dz*)
x, y, z and dx, dy, dz [m] describe a position and viewing direction (in ECEF coordinates) and the function returns the geodetic latitude and longitude of the intersection of this line of sight and the geoid (WGS84)

function optimal_interpolation.observation_geometry.**get_distance_on_surface**(
latitude1, longitude1, latitude2, longitude2)
Returns the distance (on geoid surface) between two positions

function optimal_interpolation.observation_geometry.**get_distance_to_sensor**(
sensor_position, latitude_surface, longitue_surface)
Returns the distance [m] bewteen the sensor position (ECEF coordinates) and a position on the geoid

function optimal_interpolation.observation_geometry.**get_incidence_angle**(
sensor_position, latitudes_surface, longitudes_surface)
Returns the angles (incidence angles [degree]) between the geodetic zenith direction and the vector pointing towards the sensor position for a set of positions on geoid

function optimal_interpolation.observation_geometry.**get_geodetic_nadir_direction**(*sensor_position*)
Returns the direction (in ECEF) towards the geodetic nadir direction

Antenna pattern handling

Module for handling antenna pattern calculations.

function optimal_interpolation.antenna_pattern_projection.**get_grid_for_resampling**(
latitude, longitude, azimuth_angle, half_width, resolution)
Returns a grid used for the footprint remapping

function optimal_interpolation.antenna_pattern_projection.**get_antenna_power**(

	Backus-Gilbert footprint matching methodology applied on MWI and ICI observations	**Code:** TR/BG/MWI-ICI
		Issue: 1.0
		Date: June 5, 2019
		File: optimal-interpolation-applied.tex
		Page: 107 / 200

ANTENNA_DATADIR, instrument, channel, type)
Returns 1-dimensional varying antenna gain function data imported from file

function optimal_interpolation.antenna_pattern_projection.**get_smoothed_antenna_pattern(**
antenna_data, integration_time, scan_duration, dx=5, n=201)
Returns 2-dimensional varying antenna gain function data taking into account of the scanning rotation during the integration time

function optimal_interpolation.antenna_pattern_projection.**get_antenna_pattern_interpolator(**
antenna_datadir, instrument, channel, integration_time, scan_duration)
Returns an antenna gain function (2-dimensional) interpolation object

function optimal_interpolation.antenna_pattern_projection.**get_incidence_angle(**
sensor_position, grid)
Returns the angles (incidence angles [degree]) between the geodetic zenith direction and the vector pointing towards the sensor position for all grid point positions

function optimal_interpolation.antenna_pattern_projection.**get_boresight_offset_angles(**
x, y, z, sensor_position, sensor_viewing_direction)
Returns the angles (angles to boresight and azimuth angle) relative to the sensor viewing direction for a set of positions specfied by x, y, z coordinates in ECEF

function optimal_interpolation.antenna_pattern_projection.**get_projected_antenna_pattern(**
antenna_data, grid, sensor_position, sensor_direction, normalize=False)
Returns the antenna pattern integrated over each surface element corresponding to a grid point position

function optimal_interpolation.antenna_pattern_projection.**get_native_scan_samples_within_radius(**
orbit_data, start_time_of_first_scan, native_instrument, native_channel, scan_numbers, sample_numbers, latitude, longitue, radius)
Returns sensor positions and viewing directions for all samples within a given radius [m] from a given position

Backus-Gilbert formalism

Module for handling of Backus-Gilbert formalism:

function optimal_interpolation.interpolation.**get_weights_for_various_level_of_smoothing(**
grid_for_resampling, target_antenna_pattern, native_antenna_patterns, measurement_noise, betas)
Returns weighting coefficients and corresponding noise and fit errors by applying the Backus-Gilbert methodolgy for a range of values of smooting parameter

function optimal_interpolation.interpolation.**get_lcurve_beta(**
betas, noise_errors, fit_errors, max_noise_error, min_fit_error)(
Returns optimal value of the smoothing parameter beta according to the L-curve methodology, but also takes into account of that noise and fit errors are within acceptable levels

	Backus-Gilbert footprint matching methodology applied on MWI and ICI observations	**Code:** TR/BG/MWI-ICI
		Issue: 1.0
		Date: June 5, 2019
		File: optimal-interpolation-applied.tex
		Page: 108 / 200

Part III
Application on MWI and ICI data

9 Footprint matching applied on MWI and ICI

9.1 Overview

To prepare MWI and ICI data for Cal/Val activities and Level2 processing it is relevant to remap samples from all channels to the FOV of a target channel. The target channel is MWI-3V (30[km] FWHM) and ICI-1 (16[km] FWHM) for MWI and ICI, respectively (see Sect. 7.1.2 and Sect. 7.1.3 for a more detailed description of the target channels and their antenna functions and FOV).

In this section we present results from the Backus-Gilbert footprint matching methodology applied on:

- remapping of MWI samples onto the MWI-3V FOV (Sect. 9.2)

- remapping of ICI samples onto the ICI-1 FOV (Sect. 9.3)

- remapping of MWI samples onto the ICI-1 FOV (Sect. 9.4).

We assess each type of remapping in terms of

- how many scans / samples to use when deriving optimal remapping coefficients

- obtained noise and fit-errors

- treatment around swath edges

- sensitivity to orbital variation.

The sensitivity to scan synchronization is also studied for the remapping of MWI samples onto the ICI-1 FOV.
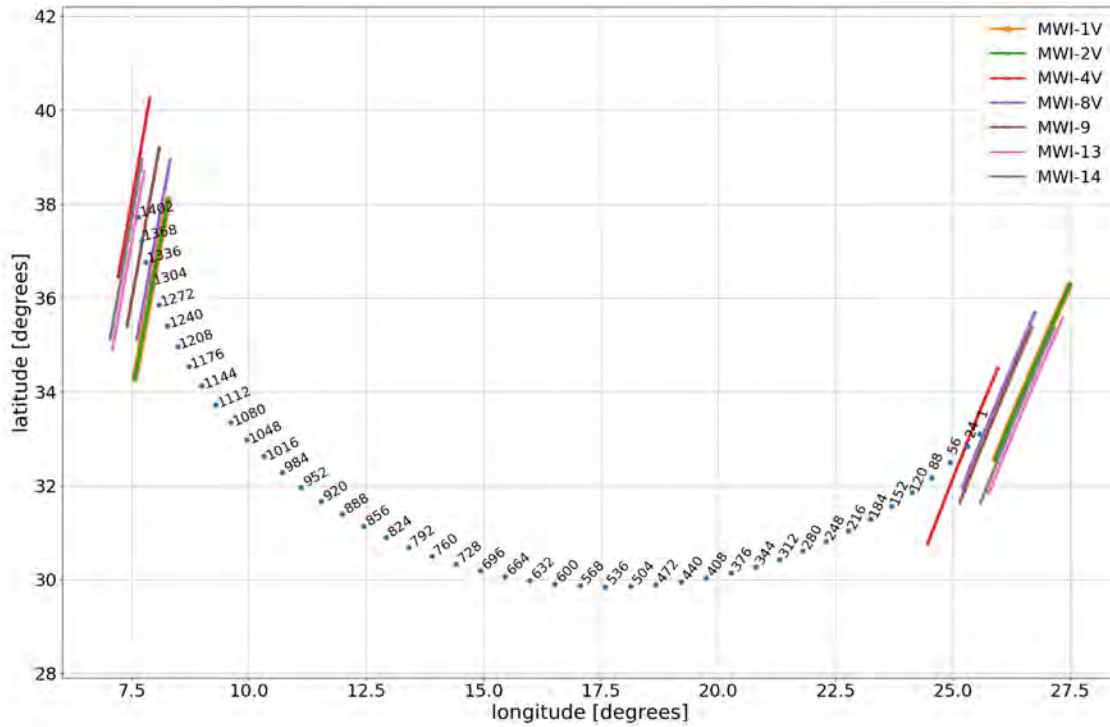
Figure 42: Geolocation on geoid of different sample positions for MWI-3V (target channel) within a given scan. Geolocation of outer sample positions for neighboring scans and for some other MWI channels are also displayed. The figure indicate that it should be possible to remap observations for all channels for sample numbers between about 30 to 1300 (see Table 8 for actual range and corresponding scan angles).

9.2 MWI

MWI provides 1402 samples / scan for each of its 26 channels (see Sect. 3). The time integration for each sample is 0.392[ms], and the scan duration time is 4/3[s]. The time integration for a FOV varies between channels and is 5.2[ms] (i.e. about 13.3 times greater than for each individual sample) for MWI-3V (target channel). The target FOV is described in more details in Sect. 7.1.2 and Sect. 7.1.3.

Figure 42 shows the geolocation of MWI-3V (target) samples on geoid for some positions within a given scan. The figure also displays geolocations of samples from the outer scan positions for neighboring scans and for some other MWI channels. At a given moment all MWI channels do not exactly view towards the same direction and Figure 42 shows that all MWI channels do not cover the complete swath of MWI-3V.

9.2.1 Number of scans / samples to include in the calculation

The details of the remapping algorithm are described in Sect. 7. An important consideration when applying the remapping algorithm is to decide how many samples to include in the remapping calculation. In the current algorithm this is determined by the parameter "maxRadius". All samples from the "native" channel where the distance to the geolocation (on geoid surface) of the target channel is less than "maxRadius" are included in the calculation. Figure 43 shows remapping characteristic data for the center scan position for some MWI channels, having a similar or smaller footprint size than MWI-3, as function of "maxRadius".

In general, it is not obvious to identify an optimal "maxRadius" to use in the remapping calculation from Figure 43. One reason for this is that a small fit-error (see Sect. 6 for a definition) is not always an advantage. The fit-error describes the disagreement between the target antenna pattern (on the geoid) and that of the remapped observation. Trying to obtain a fit-error that is smaller than uncertainties in the antenna pattern is not useful, as this only adds computational cost and complexity. Additionally, even a fit-error of 0 does not necessarily means that there is a perfect match between the two observations, because the scene can be viewed from slightly different angles, meaning that the observations can be sensitive to slightly different parts of the atmosphere, but still have the same projected antenna pattern on the geoid. This implies that it can possibly be better to accept a relative high fit-error (as obtained from adding samples from a decent amount of scans) than strive for a low fit-error (as obtained from adding samples from a huge amount of scans).

Anyhow, Figure 43 is still interesting to analyze in order to obtain, at least, a "sub-optimal" "maxRadius" to use in the calculation. MWI-8V, MWI-9, MWI-13, and MWI-14 all have a footprint size of around 10[km] and have similar characteristics in Figure 43. The noise error decreases with "maxRadius" until about 30[km], where it saturates around $0.2 - 0.25$[K]. The fit-error, on the other hand, continues to decrease until a "maxRadius" of about 65[km]. This is not a true saturation, as the setup of the trade off calculation was such that no fit error lower than 1e-4 was allowed. Any "maxRadius" between about $40 - 70$[km] can be argued to be a best compromise in terms of noise and fit-error and complexity (number of samples). Therefore, a "maxRadius" in the middle of this range, i.e. 55[km] was chosen for further calculation.

The characteristic of MWI-4V (footprint size of around 30[km]) is significantly different from the MWI channels described above. Already at a low "maxRadius" (20[km]) a good fit to the target FOV is obtained. However, by selecting a greater "maxRadius" the noise error can be reduced significantly. For symmetric reason a "maxRadius" of 55[km] was applied also for MWI-4V, although the gain in noise error compared to e.g. 45[km] is low (about 0.05[K]).

Thus, a "maxRadius" of 55[km] is applied for MWI-3 to MWI-18, and this gives that for the center scan position samples from around 12 to 13 scans or around 650 samples are used in the remapping calculation. In the outer part of the scan these numbers are greater, as shown in Figure 47, and this is due to the fact that the distance between two scan lines is greater in the center part of the scan. By design, a "maxRadius" was chosen as a parameter to describe how many samples to include in the remapping calculation, and the aim is to include samples that effectively cover the main beam of the FOV. A drawback, in terms of computational cost, with this parameter is that it results in that a large number of samples are used in the outer part of the scan. That is, a large number of overlapping samples, probably more than necessary, is available at the scan edges. A naive approach would also be to directly limit the number

	Backus-Gilbert footprint matching methodology applied on MWI and ICI observations	Code:	TR/BG/MWI-ICI
		Issue:	1.0
		Date:	June 5, 2019
		File:	optimal-interpolation-applied.tex
		Page:	111 / 200

of scan lines to include in the calculation. In practice, this is quite complex, due to the fact that the swath width, and hence the distance between scanlines, varies in the outer part of the swath between the various MWI channels. The "problem" is in principle that the overlap between available samples are high in the along-track direction, and not that samples from too many scan lines are included. A possible solution will be to make a thinning of the samples to apply in the calculation, but that was considered as more complex than useful.

The MWI-1 and MWI-2 channels have a greater footprint size than that of MWI-3V, and the remapping is hence more complicated than for the other channels. It was found that the L-curve technique (described in Sect. 6.2) used for the trade off between fit and noise error is not suited for MWI-1 and MWI-2 deconvolution onto MWI-3V FOV. The L-curve technique works well when the curve of a log-log plot of noise and fit-errors resembles the letter L, but that is not the case for MWI-1 and MWI-2. Applying the L-curve technique for MWI-1 and MWI-2 results in an unstable solution, and is therefore not applied. Instead a constant value of the smoothing parameter is applied for MWI-1 and MWI-2.

A reasonable value of "maxRadius" and smoothing parameter to apply for MWI-1 and MWI-2 was obtained in an iterative way. Figure 44 shows noise and fit-error as function of smoothing parameter β for MWI-1V and MWI-2V, for the center position of a scan, applying a "maxRadius" of 90[km] (see Figure 45 for a justification of the "maxRadius" value). It can be seen that applying a low value of the smoothing parameter can results in relatively low fit-error (below 0.003) but in that case the resulting noise is unacceptable high (40[K]). Furthermore, setting β to 10^{-4} gives low noise (below 1[K]), but high fit-error. It was judged that applying a β value of 10^{-5} is a reasonable compromise between noise and fit-error. A β value of 10^{-5} will result in a noise that is roughly two times greater than desired noise for MWI-1 and MWI-2, as described in Table 8. The fit-error is not intuitively easy to understand, but for MWI-1V and MWI-2V the fit-error is relatively low in the across-track direction and high in the along-track direction (see Sect. 7.2).

Figure 45 shows remapping characteristic data for MWI-1V and MWI-2V as function of "maxRadius", where a fixed value ($\beta = 10^{-5}$) is applied. It can be seen that the fit-error decreases with increasing "maxRadius" until about 90[km], while the noise is fairly constant. Applying a "maxRadius" of 90[km] gives that samples from around 20 scans or around 1800 samples are used in the remapping calculation for the center scan position, and in the outer part of the scan these numbers are greater as shown in Figure 48. Including data from 20 scans gives that the acquisition time can differ by about 30[s] between the included samples. This can potentially be a problem for some situations where the state varies in a non negligible manner w.r.t. time (e.g. due to strong winds), but this level of detail is not covered by simulations within this study.
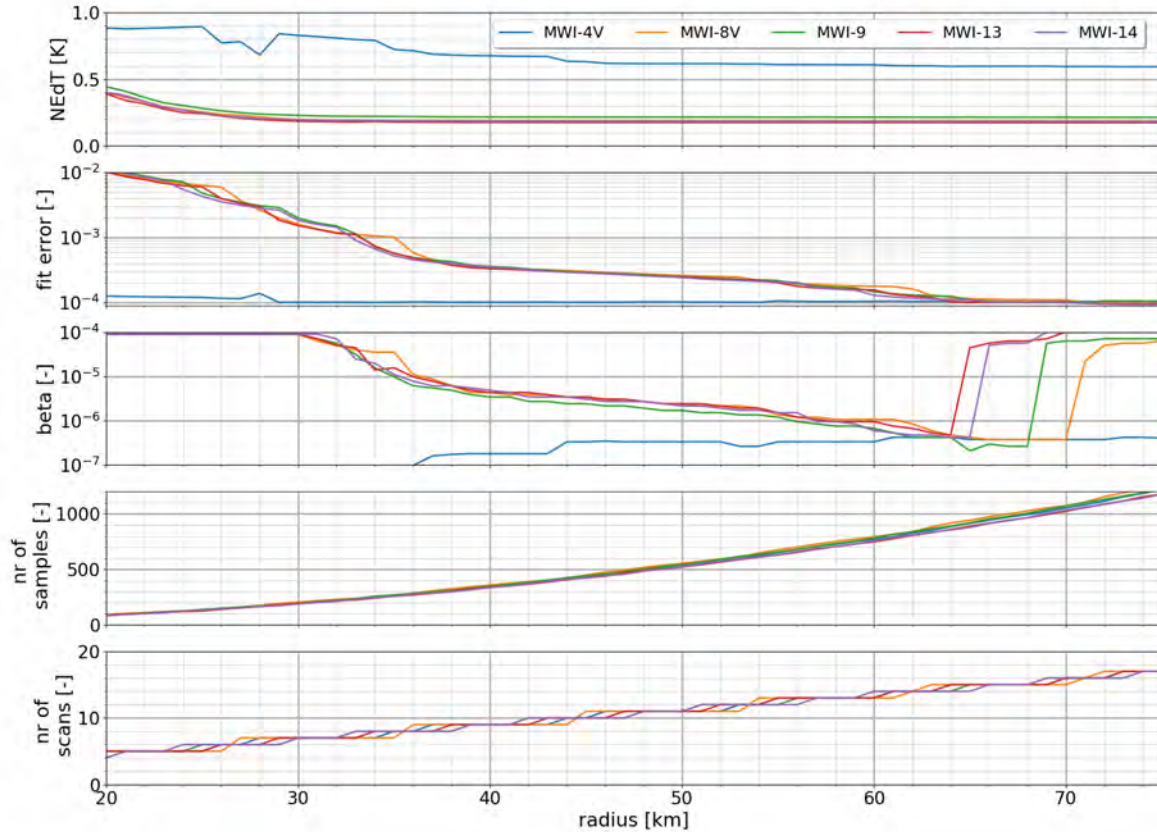
Figure 43: MWI-3V remapping characteristic data for some MWI channels, having a similar or smaller footprint size than MWI-3V, as function radius. Data are representative for the center position of the scan (i.e. scan position 662, see Figure 47). The upper panel shows noise of the remapped sample, second panel fit-error, and the third panel shows the optimal value of the smoothing parameter from the trade off analysis. The fourth panel shows how many samples that were included in the calculation, and the bottom panel shows the number of scan lines that these samples origin from.

	Backus-Gilbert footprint matching methodology applied on MWI and ICI observations	Code: TR/BG/MWI-ICI
		Issue: 1.0
		Date: June 5, 2019
		File: optimal-interpolation-applied.tex
		Page: 113 / 200
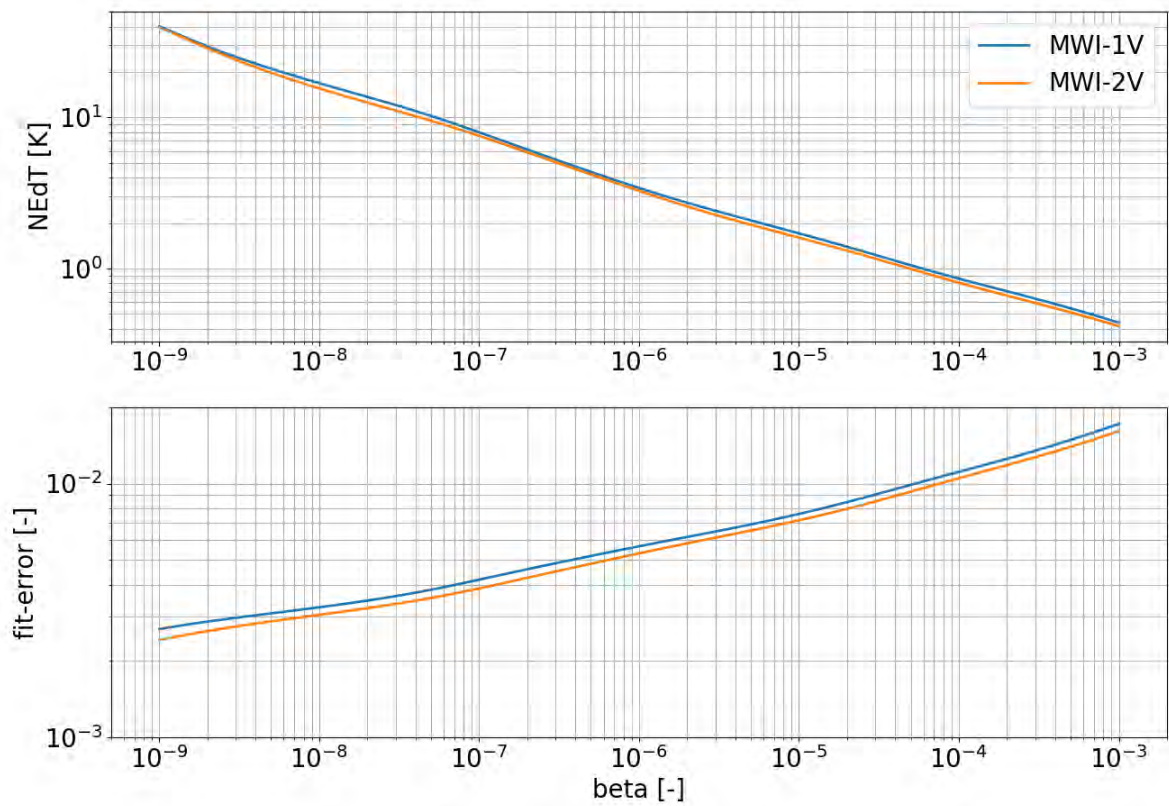
Figure 44: Noise and fit-error as function of smoothing parameter β for MWI-1V and MWI-2V for the center position of a scan and using a "maxRadius" of 90[km].

Backus-Gilbert footprint matching methodology applied on MWI and ICI observations

Code: TR/BG/MWI-ICI
Issue: 1.0
Date: June 5, 2019
File: optimal-interpolation-applied.tex
Page: 114 / 200
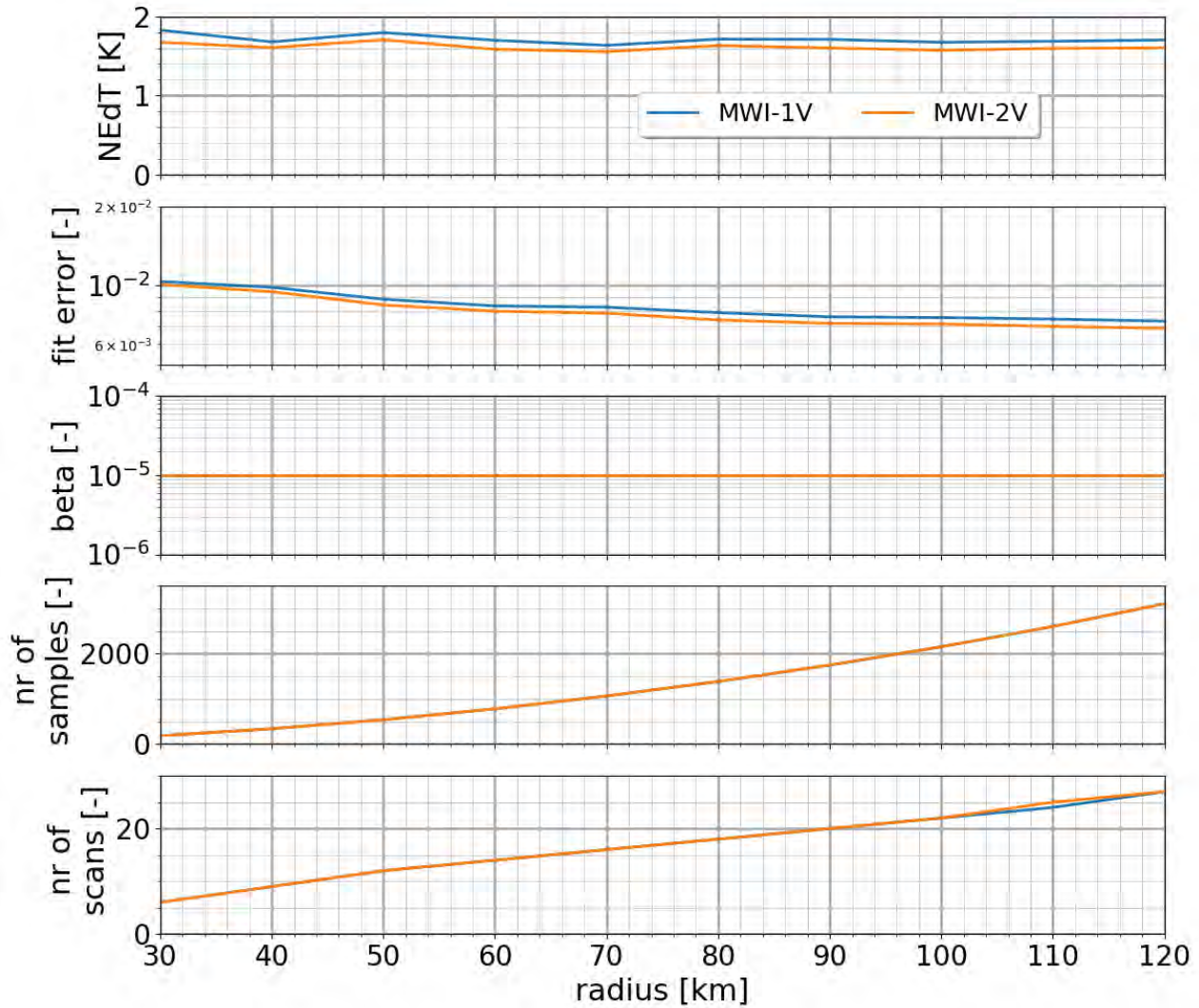
Figure 45: As Figure 43 but for MWI-1V and MWI-2V. See text for more details.

	Backus-Gilbert footprint matching methodology applied on MWI and ICI observations	**Code:** TR/BG/MWI-ICI
		Issue: 1.0
		Date: June 5, 2019
		File: optimal-interpolation-applied.tex
		Page: 115 / 200
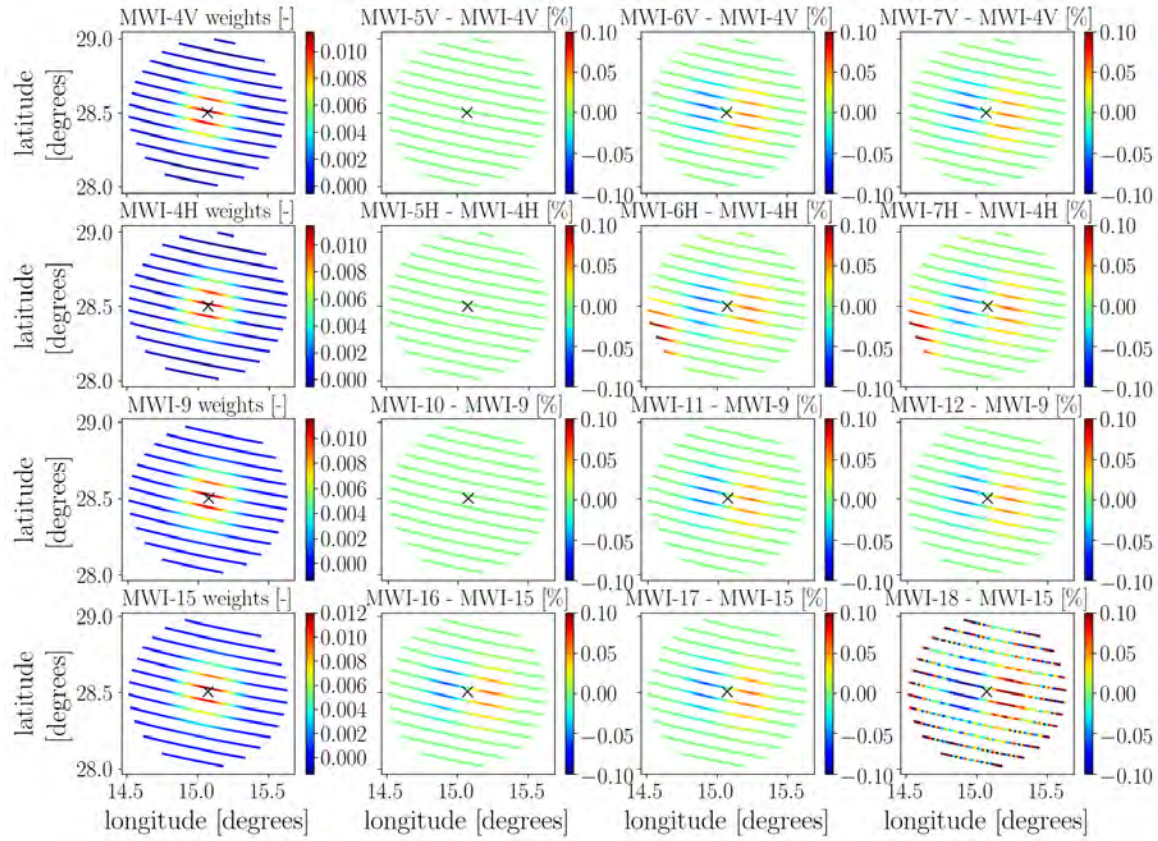
Figure 46: Difference in weighting coefficients for channels with similar characteristic. The left column show derived weighting coefficients for samples within 55[km] from the geolocation of the target footprint (marked with x) for MWI-4V, MWI-4H, MWI-9 and MWI-15 for the center scan position of a given scan. The second, third, and right panel in upper row show difference of derived weighting coefficients for MWI-5V, MWI-6V, MWI-7V, respectively, relative to the max value of the weighting coefficients for MWI-4V. The second, third, and lowest row show corresponding data for MWI-5H/MWI-6H/MWI-7H, MWI-10/MWI-11/MWI-12, and MWI-16/MWI-17/MWI-18.

9.2.2 Channels with similar characteristic

Samples from some of the MWI channels share similar viewing angles and have effectively identical antenna patterns, and the possibility to simplify the remapping calculation for these channels is here assessed. The channels of concern are:

- MWI-4V, MWI-5V, MWI-6V, and MWI-7V

- MWI-4H, MWI-5H, MWI-6H, and MWI-7H

- MWI-9, MWI-10, MWI-11, and MWI-12

- MWI-14, MWI-15, MWI-16, MWI-17, and MWI-18.

	Backus-Gilbert footprint matching methodology applied on MWI and ICI observations	Code:	TR/BG/MWI-ICI
		Issue:	1.0
		Date:	June 5, 2019
		File:	optimal-interpolation-applied.tex
		Page:	116 / 200

Derived weighting coefficients for these channels will be be similar as can be seen from Figure 46, that shows weighting coefficients derived for MWI-4V, MWI-4H, MWI-9 and MWI-15 for the center scan position, and relative difference to weighting coefficients for the channels with similar characteristic. The differences that can be seen are primarily due to a small shift in acquisition time between samples from two channels and a given scan position.

Applying weighting coefficients derived for e.g. MWI-4V for MWI-6V will have the effect that MWI-6V samples remapped to MWI-3V FOV will have a slight offset in the across-track direction. However, the sum of the absolute differences of the n weighting coefficients (w_i) (e.g. $\sum_{i=1}^{n} |w_{mwi6v,i} - w_{mwi4v,i}|$) is smaller than 0.001 for all channels except for MWI-18/MWI-15 where this measure is 0.005. The sum of absolute differences corresponds to a worst case error if there is a 1[K] variation between all samples of the scene. Thus, even if the variation is much greater than 1[K] this effect is negligible small (e.g. a 20[K] variation gives a maximum error of 0.01[K]), and this should allow for a simplification in an operational processing for the considered channels.

Table 8: MWI remapping characteristic for remapping into MWI-3V FOV. NEΔT and fit-error are described as median values for the scan.

Channel	Frequency [GHz]	NEΔT (sample / required / remapped) [K]	Fit-Error [-]	Sample Number (min/max) [-]	Scan Angle (min/max) [degrees]
MWI-1V	18.7	3.72 / 0.8 / 1.6	7.4e-3	1 / 1249	-69.99 / 62.10
MWI-1H	18.7	3.72 / 0.8 / 1.6	7.4e-3	1 / 1249	-69.99 / 62.10
MWI-2V	23.8	3.19 / 0.7 / 1.5	7.0e-3	1 / 1265	-69.99 / 63.79
MWI-2H	23.8	3.19 / 0.7 / 1.5	7.0e-3	1 / 1265	-69.99 / 63.79
MWI-3V	31.4	3.28 / 0.9 / 0.45	1.0e-4	9 / 1393	-69.14 / 77.34
MWI-3H	31.4	3.28 / 0.9 / 0.45	1.0e-4	9 / 1393	-69.14 / 77.34
MWI-4V	50.3	3.59 / 1.1 / 0.56	1.0e-4	37 / 1401	-66.18 / 78.19
MWI-4H	50.3	3.59 / 1.1 / 0.56	1.0e-4	37 / 1401	-66.18 / 78.19
MWI-5V	52.610	3.59 / 1.1 / 0.56	1.0e-4	37 / 1401	-66.18 / 78.19
MWI-5H	52.610	3.59 / 1.1 / 0.56	1.0e-4	37 / 1401	-66.18 / 78.19
MWI-6V	53.24	3.59 / 1.1 / 0.56	1.0e-4	37 / 1401	-66.18 / 78.19
MWI-6H	53.24	3.59 / 1.1 / 0.56	1.0e-4	37 / 1401	-66.18 / 78.19
MWI-7V	53.750	3.59 / 1.1 / 0.56	1.0e-4	37 / 1401	-66.18 / 78.19
MWI-7H	53.750	3.59 / 1.1 / 0.56	1.0e-4	37 / 1401	-66.18 / 78.19
MWI-8V	89	2.38 / 1.1 / 0.16	2.0e-4	37 / 1273	-66.18 / 64.64
MWI-8H	89	2.38 / 1.1 / 0.16	2.0e-4	37 / 1273	-66.18 / 64.64
MWI-9	118.7503 ± 3.2	2.71 / 1.3 / 0.19	1.8e-4	25 / 1309	-67.45 / 68.45
MWI-10	118.7503 ± 2.1	2.71 / 1.3 / 0.19	1.8e-4	25 / 1309	-67.45 / 68.45
MWI-11	118.7503 ± 1.4	2.71 / 1.3 / 0.19	1.8e-4	25 / 1309	-67.45 / 68.45
MWI-12	118.7503 ± 1.2	2.71 / 1.3 / 0.19	1.8e-4	25 / 1309	-67.45 / 68.45
MWI-13	165.5 ± 0.75	2.14 / 1.2 / 0.15	1.8e-4	1 / 1349	-69.99 / 72.68
MWI-14	183.31 ± 7.0	2.25 / 1.3 / 0.16	1.8e-4	1 / 1365	-69.99 / 74.38
MWI-15	183.31 ± 6.1	2.08 / 1.2 / 0.15	1.8e-4	1 / 1365	-69.99 / 74.38
MWI-16	183.31 ± 4.9	2.08 / 1.2 / 0.15	1.8e-4	1 / 1365	-69.99 / 74.38
MWI-17	183.31 ± 3.4	2.08 / 1.2 / 0.15	1.8e-4	1 / 1365	-69.99 / 74.38
MWI-18	183.31 ± 1.3	2.25 / 1.3 / 0.16	1.8e-4	1 / 1365	-69.99 / 74.38

9.2.3 Remapping characteristic / treatment of swath edges

Figure 42 shows geolocation of MWI-3V samples on the geoid for a given scan, together with the geolocation of samples from other channels for neighboring scans and outermost scan positions. From Figure 42 it is evident that the remapping of samples to MWI-3V FOV depends on scan position as the various channels have effectively different swath widths. In general, optimal set of weighting coefficients depends on both

- *scan position*: the position of the target footprint within the scan (i.e. sample number). At the edges of the scan a proper remapping can even be impossible to perform. This is the case as some of the channels do not have equally wide "swath width" as the target channel. The best situation for the remapping is in general for samples numbers a bit away from both the very edge of the scan and middle of the scan. In the outer part of the scan the distance between the geolocations of samples of two consecutive scans are shorter than in the center part of the scan, due to the satellite propagation direction. Thus, more and better overlapping samples are available for the remapping a bit away from the center samples of the scan.

- *sensor altitude*: or actually the square of the distance to the surface where the footprint is matched. This is further discussed in Sect. 9.2.4.

Figure 47 shows remapping characteristic as function of scan position for some MWI channels, having a similar or smaller footprint size than MWI-3V, for a given scan, and the result

	Backus-Gilbert footprint matching methodology applied on MWI and ICI observations	Code: TR/BG/MWI-ICI
		Issue: 1.0
		Date: June 5, 2019
		File: optimal-interpolation-applied.tex
		Page: 118 / 200

is summarized in Table 8. The remapping characteristic is fairly symmetric around MWI-3V scanning angle of 0[°] (sample number 661) for all channels. The fit and noise errors decreases with increasing scan angle. A degradation in remapping performance (high noise and fit errors) are seen at the swath edges for some channels and scanning angles above 65[°]. MWI-3V and MWI-4V data stands out (greater noise and lower fit-errors than for the other channels) which is due to the fact that the sample footprint size (30[km]) is similar to that of the target MWI-3V (note that we here also remap MWI-3V samples to the MWI-3V FOV), while the other channels have a finer resolution (around 10[km]). The remapping noise is low (below 0.2[K]) for MWI-8V, MWI-9, MWI-13, and MWI-14. This noise is much lower than the required noise described in Table 8. However, the noise described in Table 8 apply to Level1B data, and not on remapped data.

Figure 47 shows that the remapping works poorly in the scan edges for some channels (explained by Figure 42), e.g. MWI-8V and high sample numbers / scan angles. When the fit error and / or noise is high enough the remapped observation becomes useless. The exact boundary is application specific, but Table 8 describes the scan range where the remapping noise is within requirements and fit error below 5e-4, and this gives that "high quality" remappings for all channels can be obtained for scan angles between about -66 to 65[°].

Figure 48 shows data for MWI-1V and MWI-2V. Noise and fit-errors for these channels are in general much greater than for the other MWI channels, and that is basically due to the larger footprint size of these channels, as discussed in Sect. 9.2.1. A fixed value of the smoothing parameter was deployed, and that was also discussed in Sect. 9.2.1. A degradation in the remapping performance is found for scan angles above 62[°]. Even though, many samples are available (geolocation within 90[km]) for the remapping above 62[°] the remapping performance is limited, as these samples are primarily geolocated on one side (in the along track-direction) relative to the target footprint geolocation, and this does not allow for a proper fit.

Thus, samples from most MWI channels can be remapped to the MWI-3V FOV between scan position 37 and 1273. However, there is a great footprint overlap of MWI-3V FOVs from two consecutive scan positions, as the center positions only differs by about 1.6[km] (in the across-track direction) on ground and the footprint size is about 30[km]. Therefore, it might not be very meaningful to remap data for all scan positions. A remapping to every sixth scan position results in that the separation between two FOVs approximately match the along-track separation of two scan lines that is about 9[km], but it also results in a large overlap between two FOVs (about 65 %). A remapping to every eighth scan position gives that the distance (center to center) and overlap between two such samples is about 10.8[km] and 55[%], respectively. This remapping frequency (every 8th scan position between scan position 37 and 1273) results in 155 different FOVs per scan.
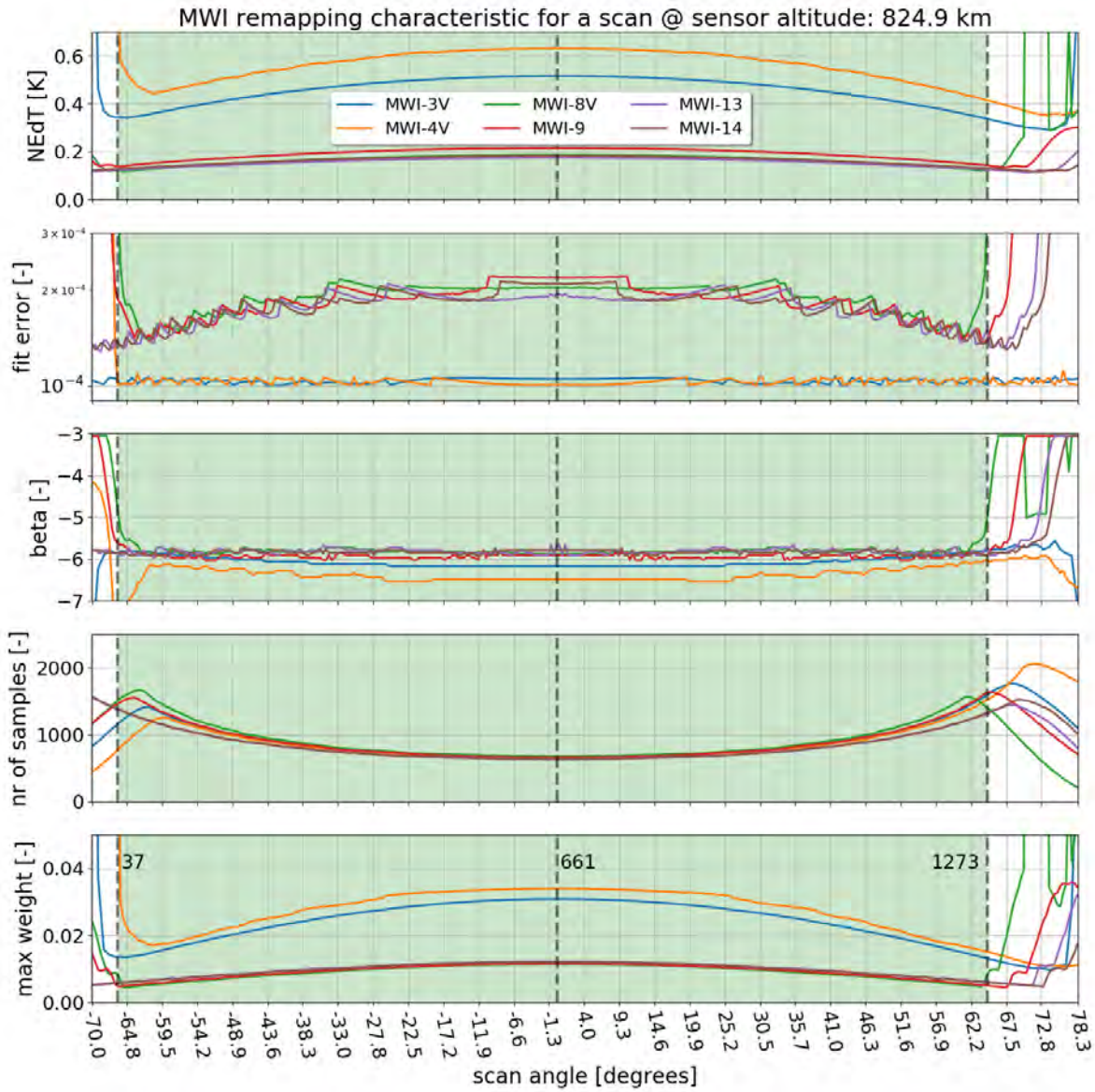
Figure 47: Trade off analysis data as function of scan angle / scan position for MWI channels, having a similar or smaller footprint size than MWI-3V. The two upper panels show the obtained noise error and fit error. The middle panel shows the optimal value of the smoothing parameter deployed in the BG methodology. The fourth panel shows the number of samples that are found within 55[km] from the geolocation of the center of the target footprint, and used in the remapping calculation. The bottom panel shows the maximum weight given to a single sample.

	Backus-Gilbert footprint matching methodology applied on MWI and ICI observations	Code:	TR/BG/MWI-ICI
		Issue:	1.0
		Date:	June 5, 2019
		File:	optimal-interpolation-applied.tex
		Page:	120 / 200

Figure 48: As Figure 47 but for MWI-1V and MWI-2V, except that the fourth panel shows the number of samples that are found within 90[km] from the geolocation of the center of the target footprint.

9.2.4 Remapping sensitivity to orbital variations

The altitude of Metop varies between about 820 to 850[km], and the platform attitude will follow the local normal pointing law and the swath will be centered around the sub-nadir orbit track. The derived weights, for the footprint remapping, do not directly depend on the altitude or attitude of the platform, but, in general, on the distance from the platform to geoid surface where the footprint is matched (see e.g. Sect. 6).

The altitude dependency is important to study for an "operational" remapping processing purpose. An "operational" remapping processing can be setup to deploy a set of precalculated weighting coefficients, derived from a single scan, or from many scans, depending on how strong the altitude dependency is.

The possible altitude dependency can be understood as the optimal weights derived around a given altitude of the sensor and for a specific remapping results in that the target FOV is matched at the surface (that is located a distance r from the sensor). Now, if these weights are applied at a different sensor location, e.g. at a position where the sensor altitude is greater, than the target footprint is still matched at a distance r from the sensor, but that is now not on the surface, but a bit above the surface. This has practically no impact if the "native" and target channels viewing angles are more or less identical (as e.g for MWI-3H and MWI-3V). However, if there is an offset between the effective viewing angles between the two channels, the result is that the footprint on ground is not necessarily matched, i.e. it will be an offset between the geolocation of the "center" of the two footprints. This can potentially result in a deviation in antenna temperatures between the two observations, if there is a contrast in the "surface brightness temperature field".

Figure 49 shows remapping data for MWI-4V and MWI-14 derived from three different orbital positions. The fit error can be seen to vary slightly with sensor altitude, although these variations are smaller than the variations between scan positions for a given scan.

Variations with sensor altitude seen in Figure 49 indicates that it might not be optimal to use weighting coefficients derived from a single scan for MWI-14 in an "operational" processing. This is further studied in a test, as described below: an optimal set of weighting coefficients were derived for a number of MWI channels and for positions throughout th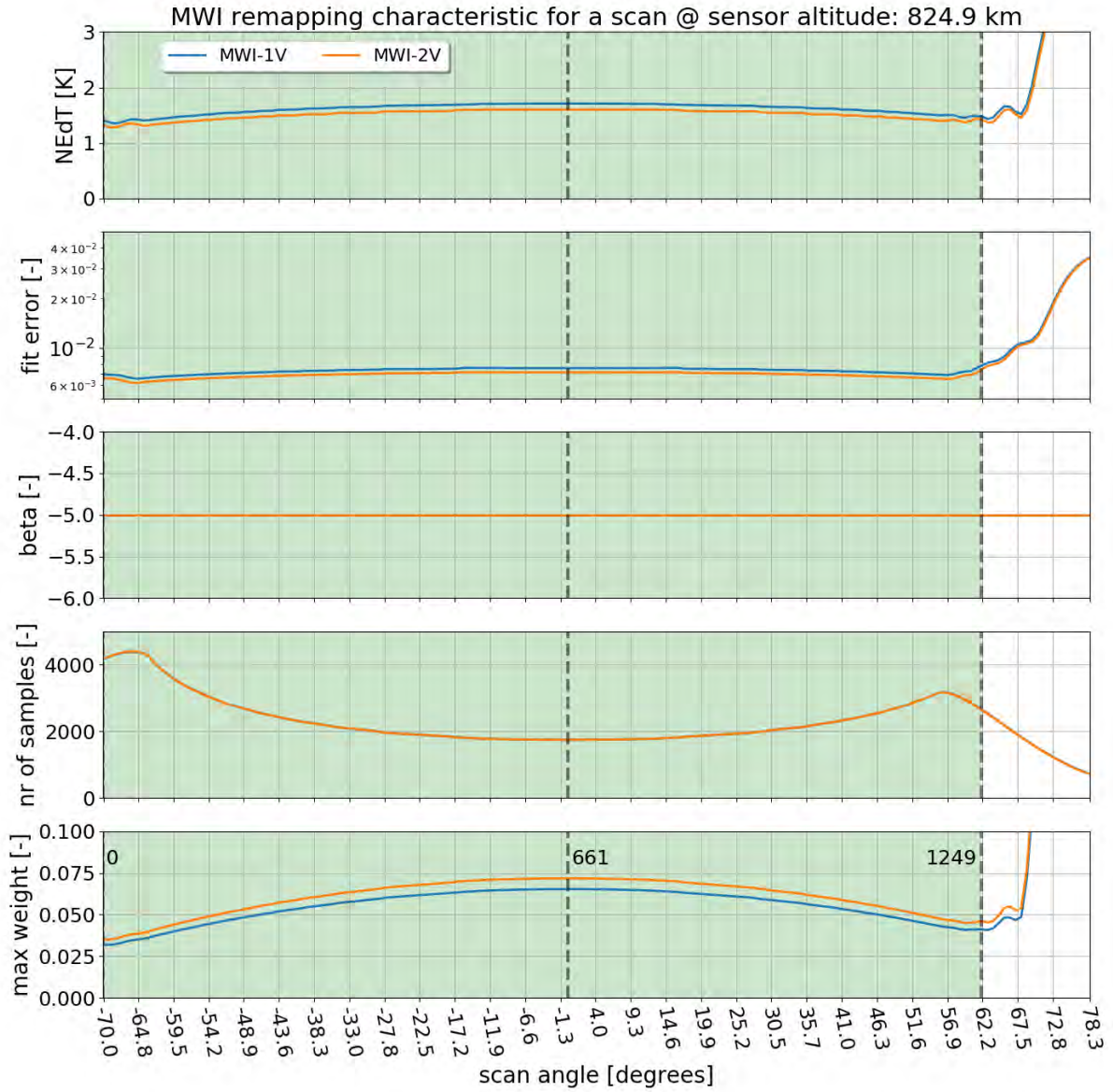e scan from three different positions within an orbit (effectively at three different sensor altitudes: at low (822.9 km), intermediate (836.1 km), and high (848.1 km) altitude. Then a remapping from samples into the MWI-3V FOV was done for a Metop-A reference orbit for each of the set of weighting coefficients, resulting in three different versions of remapped observations. Then we study differences between the three sets of remapped observations for each channel. The derived weighting coefficients have no critical dependency on orbit altitude, if no differences are seen between the remapped observations. If clear differences are seen, orbital variations must be taken into account of in "operational" footprint remapping. That is, weighting coefficients from a number of orbit positions must be generated and used.

The result is summarized in Table 9, where it can be seen that the $\pm 1\,\sigma$ of the resulting error is very low for the channels with the best match in incidence angle to the target (i.e. MWI-3V, MWI-4V, and MWI-9). The error is higher (0.02[K]) for MWI-8V, MWI-13, and MWI-14, but still low compared to e.g. $NE\Delta T$.

The error introduced by simplifying the remapping calculation should be uncorrelated to $NE\Delta T$, and hence more or less negligible. However, for situations where there is a large

	Backus-Gilbert footprint matching methodology applied on MWI and ICI observations	Code:	TR/BG/MWI-ICI
		Issue:	1.0
		Date:	June 5, 2019
		File:	optimal-interpolation-applied.tex
		Page:	122 / 200

contrast in the "surface brightness temperature field", such as for a cloudy scene, the error can be considerable higher than described in Table 9. But, for such situations there is an additional "noise term" arising from observing a cloudy scene from different viewing angles, as described in Sect. 10.2.2.

In summary, the error introduced by simplify the remapping calculation should be more or less negligible compared to other error sources.

Table 9: MWI remapping sensitivity to orbital variations. The error represents an estimate of the error (1 standard deviation) that will be introduced if only weighting coefficients derived from a single scan are used for operational remapping (see text for more details). The incidence angle is described for one particular condition, it varies both during a scan and throughout the orbit.

Channel	Frequency [GHz]	Incidence angle [degrees]	Error [K]
MWI-1V	18.7	53.0611	0.02
MWI-2V	23.8	53.0685	0.02
MWI-3V	31.4	52.8759	0
MWI-4V	50.3	53.1537	0.005
MWI-8V	89	52.2042	0.02
MWI-9	118.7503 ± 3.2	52.7802	0.002
MWI-13	165.5 ± 0.75	54.0936	0.02
MWI-14	183.31 ± 7.0	54.0539	0.02
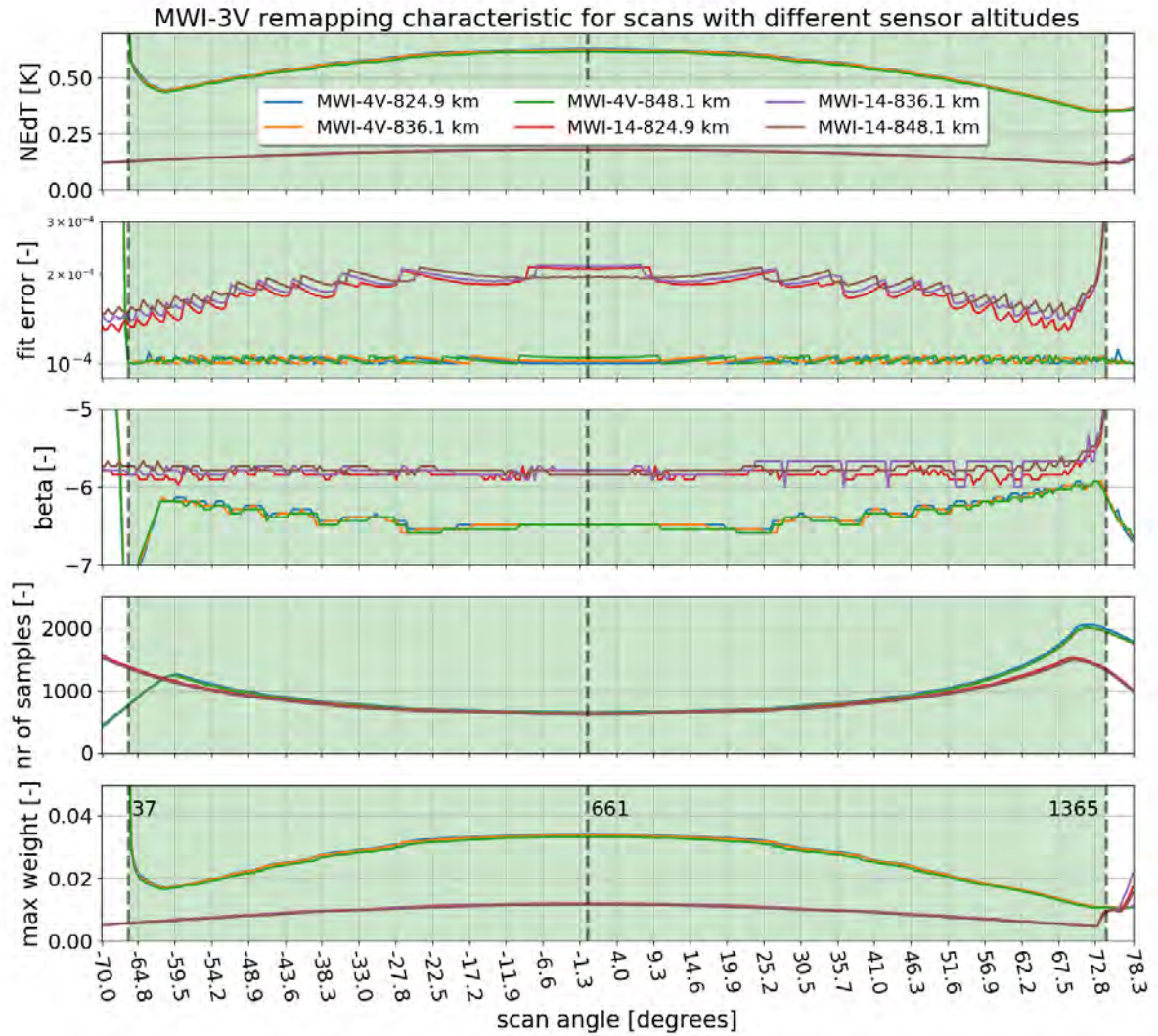
Figure 49: Trade off analysis data as function of scan angle / scan position for MWI-4V and MWI-14 derived from three different sensor positions, otherwise as Figure 47.
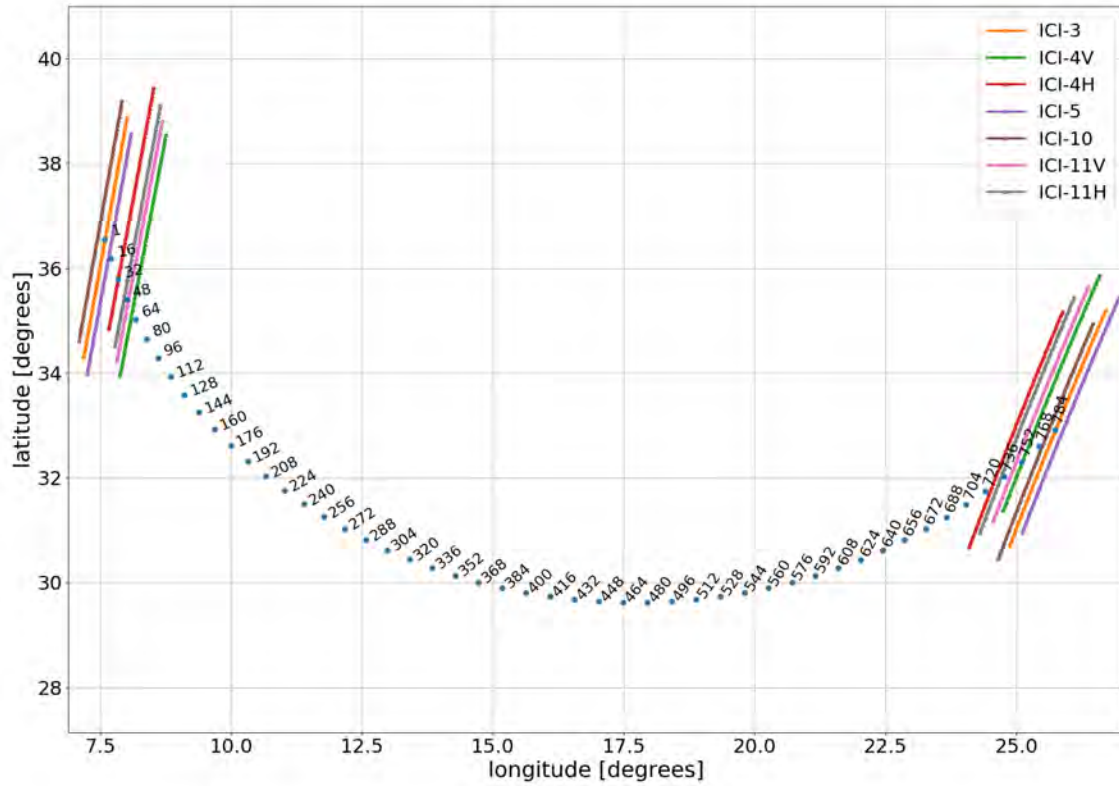
Figure 50: Geolocation on geoid of different sample positions for ICI-1 (target channel) within a given scan. Geolocation of outer sample positions for neighboring scans and for some other ICI channels are also displayed. The figure indicate that it should be possible to remap observations for all channels for sample numbers between about 60 to 720 (see Table 10 for actual range and corresponding scan angles).

9.3   ICI

ICI provides 784 samples / scan for each of its 13 channels (see Sect. 3). The time integration for each sample is 0.661[ms], and the scan duration time is 4/3[s]. The time integration for the ICI-1 target FOV is 2.532[ms] (i.e. about 3.8 times greater than for each individual sample). The target FOV is described in more details in Sect. 7.1.2 and Sect. 7.1.3.

Figure 50 shows the geolocation of ICI-1 samples on geoid for some positions within a given scan. The figure also displays geolocations of scan end positions for neighboring scans for samples from some other ICI channels. At a given moment all ICI channels do not exactly view towards the same direction and Figure 50 shows that all ICI channels do not cover the complete swath of ICI-1.

9.3.1 Number of scans / samples to include in the calculation

An important consideration when applying the remapping algorithm is to decide how many samples to include in the remapping calculation, as discussed in more details in Sect. 9.2.1 and for MWI. Remapping (from ICI channels to ICI-1 FOV) characteristic is shown in Figure 51. All ICI channels have a footprint size similar to that of the target ICI-1, and the remapping characteristic (Figure 51) of all channels are similar (ICI-3 has a smaller fit error than the other channels, as ICI-3 viewing direction is aligned with ICI-1). The noise error saturates for all channels around a "maxRadius" of 11[km] but the fit error continues to decrease. A "maxRadius" of 30[km] is applied for all ICI channels. This gives that samples from 7 scans or around 125 samples are used in the remapping calculation for the center position of the ICI scan. In the outer part of the scan these numbers are greater as shown in Figure 53. Somewhat smaller fit errors can be obtained by using a greater "maxRadius" than applied here, but that is on the cost of adding complexity.

	Backus-Gilbert footprint matching methodology applied on MWI and ICI observations	Code:	TR/BG/MWI-ICI
		Issue:	1.0
		Date:	June 5, 2019
		File:	optimal-interpolation-applied.tex
		Page:	126 / 200
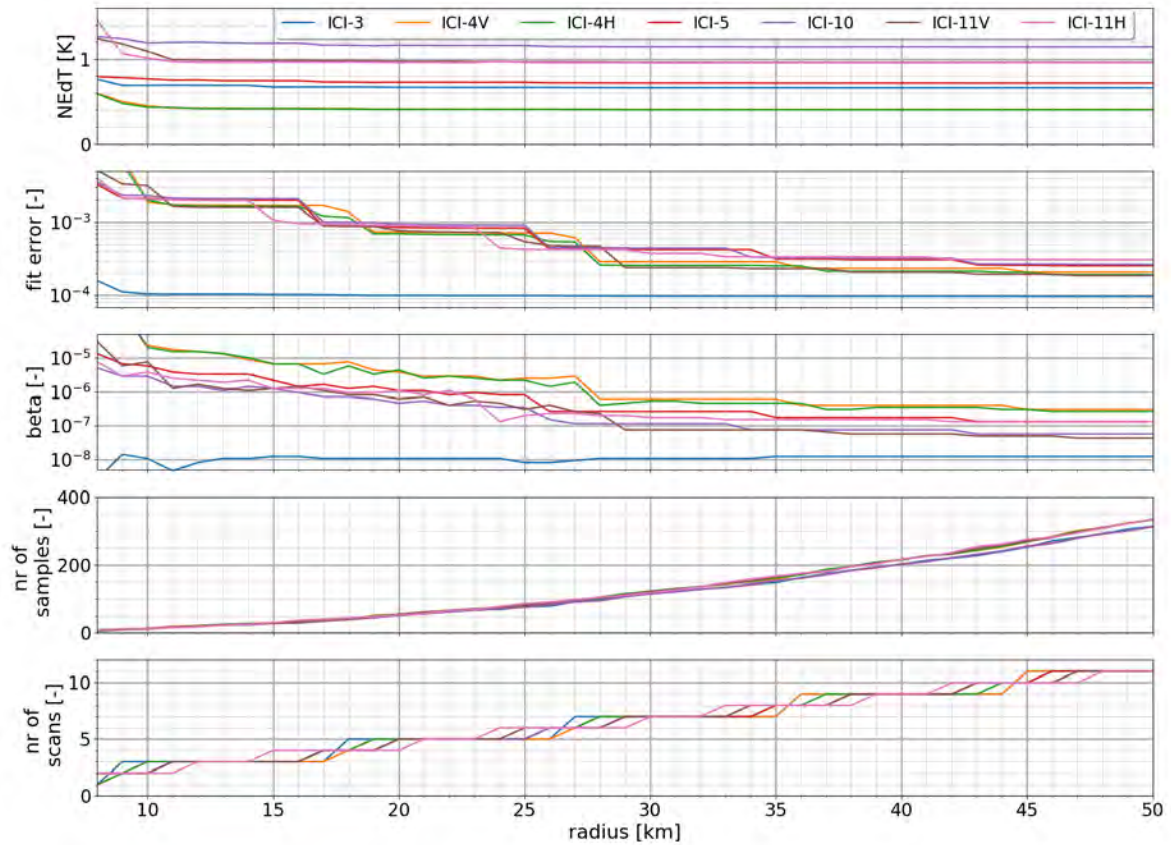
Figure 51: ICI-1 remapping characteristic data for some ICI channels as function radius. Data are representative for the center position of the scan (i.e. scan position 392, see Figure 53). The upper panel shows noise of the remapped sample, second panel fit-error, and the third panel shows the optimal value of the smoothing parameter from the trade off analysis. The fourth panel shows how many samples that were included in the calculation, and the bottom panel shows the number of scan lines that these samples origin from.

	Backus-Gilbert footprint matching methodology applied on MWI and ICI observations	**Code:** TR/BG/MWI-ICI
MoHHoW		**Issue:** 1.0
		Date: June 5, 2019
		File: optimal-interpolation-applied.tex
		Page: 127 / 200

9.3.2   Channels with similar characteristic

Samples from some of the ICI channels share similar viewing angles and have effectively identical antenna patterns, and these are

- ICI-1, ICI-2, and ICI-3 (channels around 183.31[GHz])

- ICI-5, ICI-6, and ICI-7 (channels around 325.15[GHz])

- ICI-8, ICI-9, and ICI-10 (channels around 448.0[GHz])

Derived weighting coefficients for these channels will be be similar as can be seen from Figure 52, that shows weighting coefficients derived for ICI-2, ICI-6, and ICI-9 for the center scan position, and relative difference to weighting coefficients for the channels with similar characteristic. The differences that can be seen are primarily due to a small shift in acquisition time between e.g. ICI-1, ICI-2, and ICI-3 samples.

Applying weighting coefficients derived for e.g. ICI-2 for ICI-1 and ICI-3 will have the effect that ICI-1 and ICI-3 will have a slight offset (in the across-track direction) in sensitivity relative to ICI-2. The sum of the absolute differences of weighting coefficients (corresponds to a worst case error if there is a 1[K] variation between all samples of the scene) is around 0.018 for ICI-1/ICI-3 and ICI-2 and around 0.010 for for ICI-5/ICI-7 and ICI-8/ICI-10 relative to ICI-6 and ICI-9, respectively. This gives that for cloud free observations, where differences in antenna temperature between neighboring samples are relatively small, this effect is negligible, as the resulting error in antenna temperature will typically be smaller than 0.01[K]. For cloudy condition, and if the cloud structure varies significantly in the across-track direction, this effect can give rise to greater differences. To study the actual effect in more details will require more detailed cloud simulation, with a finer spatial resolution, than available in this study.

The main conclusion is anyhow, that for cloud free condition, and for cloudy condition with small variation inside the footprint the described simplification only give rise to negligible errors.
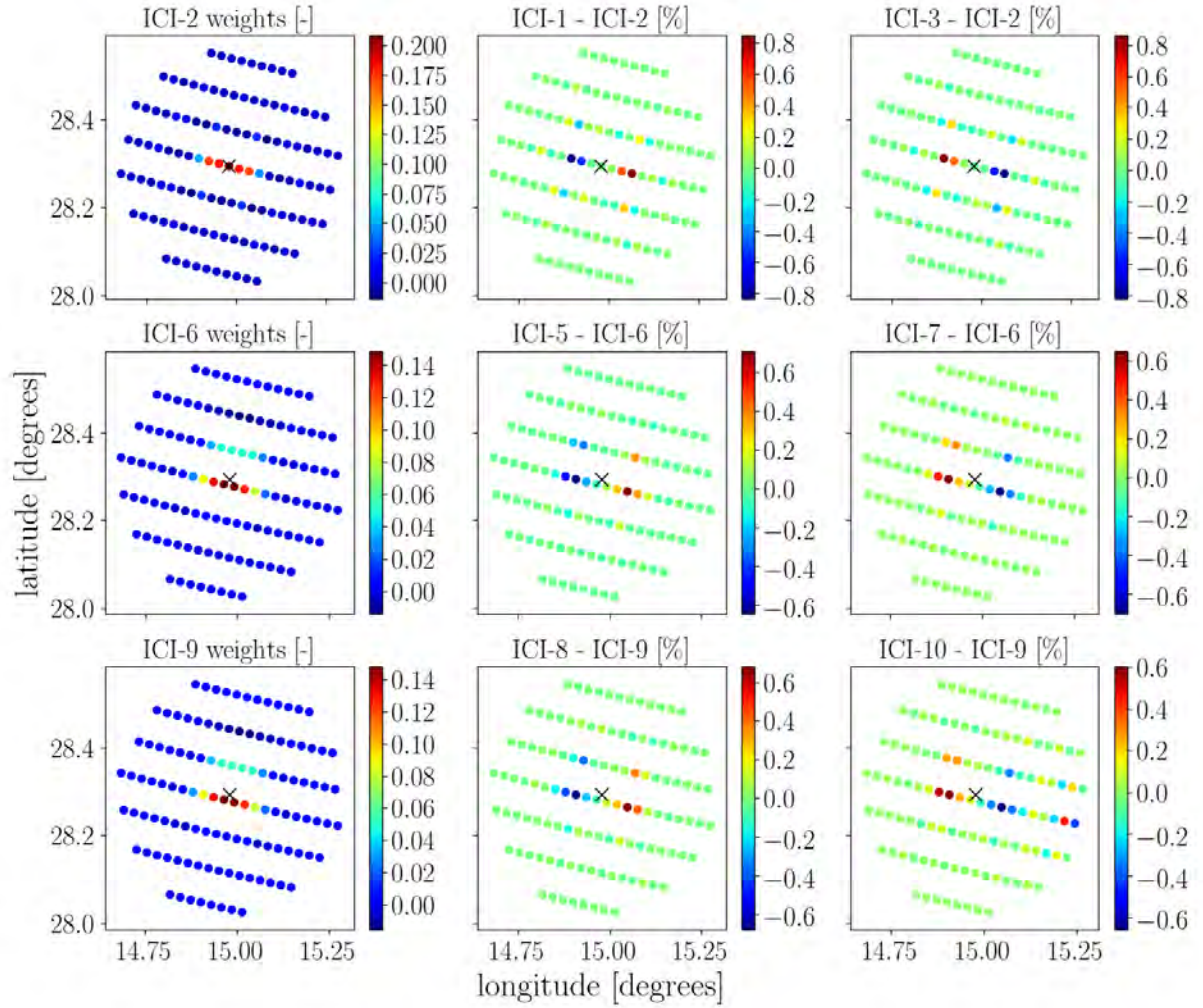
Figure 52: Difference in weighting coefficients for channels with similar characteristic. The left column show derived weighting coefficients for samples within 30[km] from the geolocation of the target footprint (marked with x) for ICI-2, ICI-6, and ICI-9. The middle and right panel in upper row show difference of derived weighting coefficients for ICI-1 and ICI-3, respectively, relative to that of the max value of weighting coefficients for ICI-2. The middle and lower row show corresponding data for ICI-5/ICI-7 and ICI-8/ICI-10.

	Backus-Gilbert footprint matching methodology applied on MWI and ICI observations	Code: TR/BG/MWI-ICI
		Issue: 1.0
		Date: June 5, 2019
		File: optimal-interpolation-applied.tex
		Page: 129 / 200

Table 10: ICI remapping characteristic for remapping into ICI-1 FOV. NEΔT and fit-error are described as median values for the scan.

Channel	Frequency [GHz]	NEΔT (sample / required / remapped) [K]	Fit Error [-]	Sample Number (min/max) [-]	Scan Angle (min/max) [degrees]
ICI-1	183.31 ± 7.0	1.57 / 0.8 / 0.6	0.75e-4	4 / 781	69.36 / -69.32
ICI-2	183.31 ± 3.4	1.56 / 0.8 / 0.6	0.75e-4	4 / 781	69.36 / -69.32
ICI-3	183.31 ± 2.0	1.56 / 0.8 / 0.6	0.75e-4	4 / 781	69.36 / -69.32
ICI-4V	243.2 ± 2.5	1.42 / 0.7 / 0.4	0.98e-4	64 / 748	58.65 / -63.43
ICI-4H	243.2 ± 2.5	1.41 / 0.7 / 0.4	1.0e-4	37 / 721	63.47 / -58.61
ICI-5	325.15 ± 9.5	2.20 / 1.2 / 0.65	1.0e-4	16 / 784	67.21 / -69.85
ICI-6	325.15 ± 3.5	2.38 / 1.3 / 0.7	1.0e-4	16 / 784	67.21 / -69.85
ICI-7	325.15 ± 1.5	2.75 / 1.5 / 0.8	1.0e-4	16 / 784	67.21 / -69.85
ICI-8	448.0 ± 7.2	2.47 / 1.4 / 0.7	0.96e-4	1 / 769	69.89 / -67.17
ICI-9	448.0 ± 3.0	2.80 / 1.6 / 0.8	0.96e-4	1 / 769	69.89 / -67.17
ICI-10	448.0 ± 1.4	3.51 / 2.0 / 1.0	0.96e-4	1 / 769	69.89 / -67.17
ICI-11V	664.0 ± 4.2	3.40 / 1.6 / 0.9	1.0e-4	31 / 766	64.54 / -66.64
ICI-11H	664.0 ± 4.2	3.43 / 1.6 / 0.9	0.90e-4	25 / 751	65.61 / -63.96

9.3.3 Remapping characteristic / treatment of swath edges

Figure 53 shows remapping characteristic as function of scan position for some ICI channels for a given scan, and the result is summarized in Table 10. The remapping characteristic is fairly symmetric around the center scan position for all channels, and the fit and noise errors decreases with increasing scan angle. A degradation in remapping performance (high noise and fit errors) are seen at the swath edges for some channels (e.g. for ICI-4V and sample numbers below 60). The reason for this is explained by Figure 50, that shows that the ICI-4V effective swath width is smaller than that of ICI-1, and the ICI-4V observation does not cover the ICI-1 FOV at low sample numbers. A further comparison of Figure 50 and Figure 53 gives that the footprint matching works well for the overlapping part of the swath, and all channels can remapped (without too high errors) for scanning angles between about 59 to -59[°] (or sample numbers between about 64 and 721). The noise of the remapped observations are here well below the required Level1B noise levels (Table 10) for all channels.

Thus, samples from all ICI channels can be remapped to the ICI-1 FOV between scan position 64 and 721. However, there is a great footprint overlap of ICI-1 FOVs from two consecutive scan positions, as the center positions only differs by about 2.7[km] (in the across-track direction) on ground and the footprint size is about 16[km]. Therefore, it might not be very meaningful to remap data for all scan positions. A remapping to every third scan position gives that the distance (center to center) and overlap between two such samples is about 8.1[km] and 40[%], respectively. This approximately match the along-track characteristic (the distance between two scan lines is about 9[km]). This remapping frequency (every third scan position between scan position 64 and 721) results in 220 different FOVs per scan.

	Backus-Gilbert footprint matching methodology applied on MWI and ICI observations	**Code:** TR/BG/MWI-ICI
		Issue: 1.0
		Date: June 5, 2019
		File: optimal-interpolation-applied.tex
		Page: 130 / 200
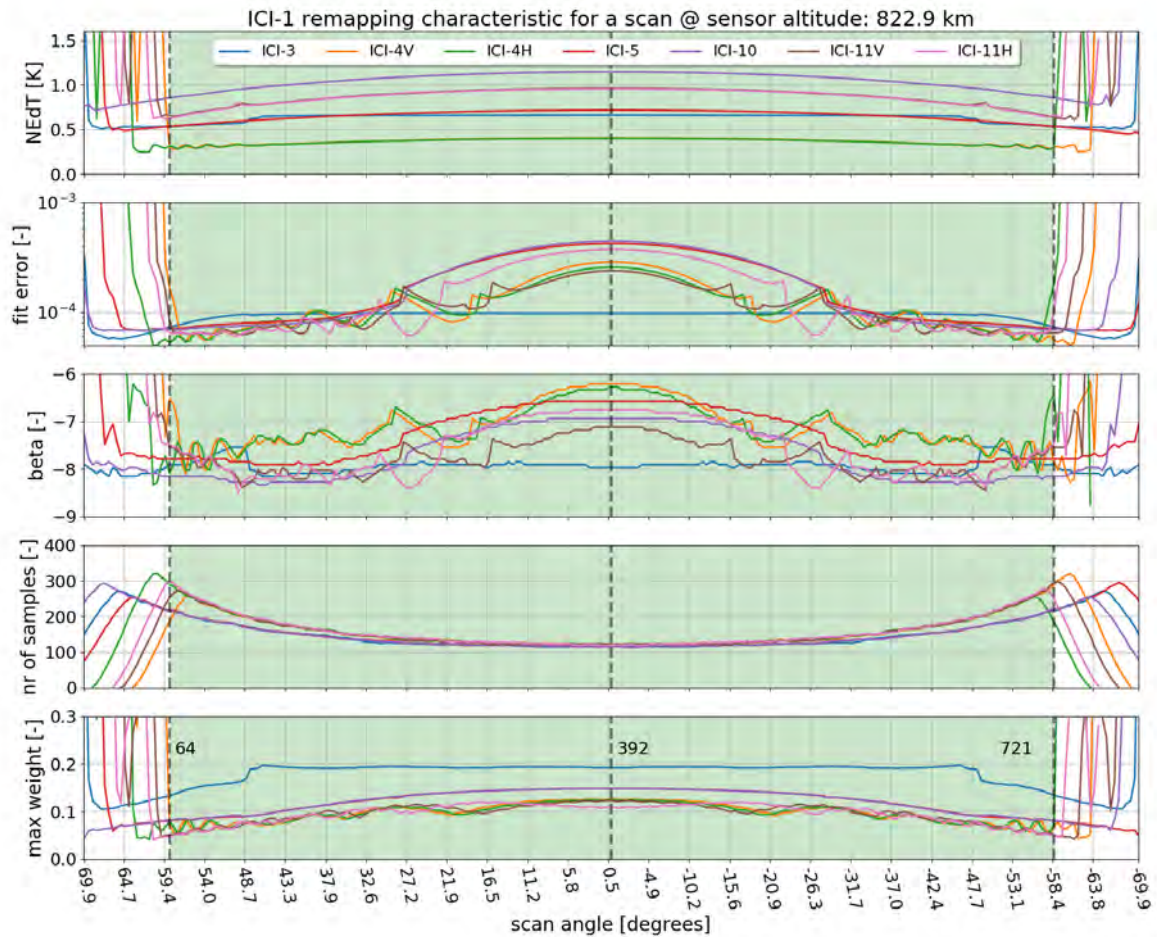
Figure 53: Trade off analysis data as function of scan angle / scan position for ICI channels. The two upper panels show the obtained noise error and fit error. The middle panel shows the optimal value of the smoothing parameter deployed in the BG methodology. The fourth panel shows the number of samples that are found within 30[km] from the geolocation of the center of the target footprint, and used in the remapping calculation. The bottom panel shows the maximum weight given to a single sample.

	Backus-Gilbert footprint matching methodology applied on MWI and ICI observations	Code: TR/BG/MWI-ICI
		Issue: 1.0
		Date: June 5, 2019
		File: optimal-interpolation-applied.tex
		Page: 131 / 200

9.3.4 Remapping sensitivity to orbital variations

The importance of studying the sensitivity to orbital variations was described in Sect. 9.2.4. Figure 54 shows remapping characteristic data for ICI-3 and ICI-4V and for three different scans (different sensor altitudes). It can be seen that the ICI-4V data have a stronger variation with altitude as compared to ICI-3 data, that only varies marginally. A main difference between ICI-3 and ICI-4V is that ICI-3 views in a direction that is aligned to the target channel ICI-1, whereas ICI-4V is not (the incidence angle of ICI-4V samples is about $2[°]$ smaller than ICI-1 as described in Table 11).

The result from a sensitivity test (described in Sect. 9.2.4 but applied on MWI data) is summarized in Table 11. It can be seen the for the ICI-3 to ICI-1 remapping, there is basically no difference at all between remapped observations (based on different set of weighting coefficients), and the ICI-3 to ICI-1 remapping is not dependent on sensor altitude, which can be explained by the fact that the viewing angles between ICI-3 and ICI-1 is aligned. In practise, these also applies to ICI-5 to ICI-10 as well.

Greatest errors are found for the ICI-4 and ICI-11 channels $(0.03[K])$, but the error is low compared to $NE\Delta T$, and on top of that uncorrelated, which gives that this error should be negligible, at least, for cloud free condition. For cloudy condition the error can be considerable greater than described in Table 11. However, for cloudy condition there is an additional "noise term" arising from observing a cloudy scene from different viewing angles, as described in Sect. 10.2.2. This "noise term" is generally greater than the error due to the simplification described here.

In summary, the remapping of ICI-4 and ICI-11 samples are clearly more sensitive to orbital variations than the other channels, and errors for ICI-4 and ICI-11 can be reduced if multiple set of weighting coefficients are applied.

Table 11: ICI remapping sensitivity to orbital variations. The error represents an estimate of the error (1 standard deviation) that will be introduced if only weighting coefficients derived from a single scan are used for operational remapping (see text for more details).

Channel	Frequency [GHz]	Incidence angle [degrees]	Error [K]
ICI-1	183.31 ± 7.0	53.7453	0
ICI-2	183.31 ± 3.4	53.7453	0
ICI-3	183.31 ± 2.0	53.7453	0
ICI-4V	243.2 ± 2.5	51.7720	0.03
ICI-4H	243.2 ± 2.5	51.7427	0.03
ICI-5	325.15 ± 9.5	53.8021	0.001
ICI-6	325.15 ± 3.5	53.8021	0.001
ICI-7	325.15 ± 1.5	53.8021	0.001
ICI-8	448.0 ± 7.2	53.8006	0.001
ICI-9	448.0 ± 3.0	53.8006	0.001
ICI-10	448.0 ± 1.4	53.8006	0.001
ICI-11V	664.0 ± 4.2	51.7166	0.03
ICI-11H	664.0 ± 4.2	51.5542	0.03

	Backus-Gilbert footprint matching methodology applied on MWI and ICI observations	Code:	TR/BG/MWI-ICI
		Issue:	1.0
		Date:	June 5, 2019
		File:	optimal-interpolation-applied.tex
		Page:	133 / 200
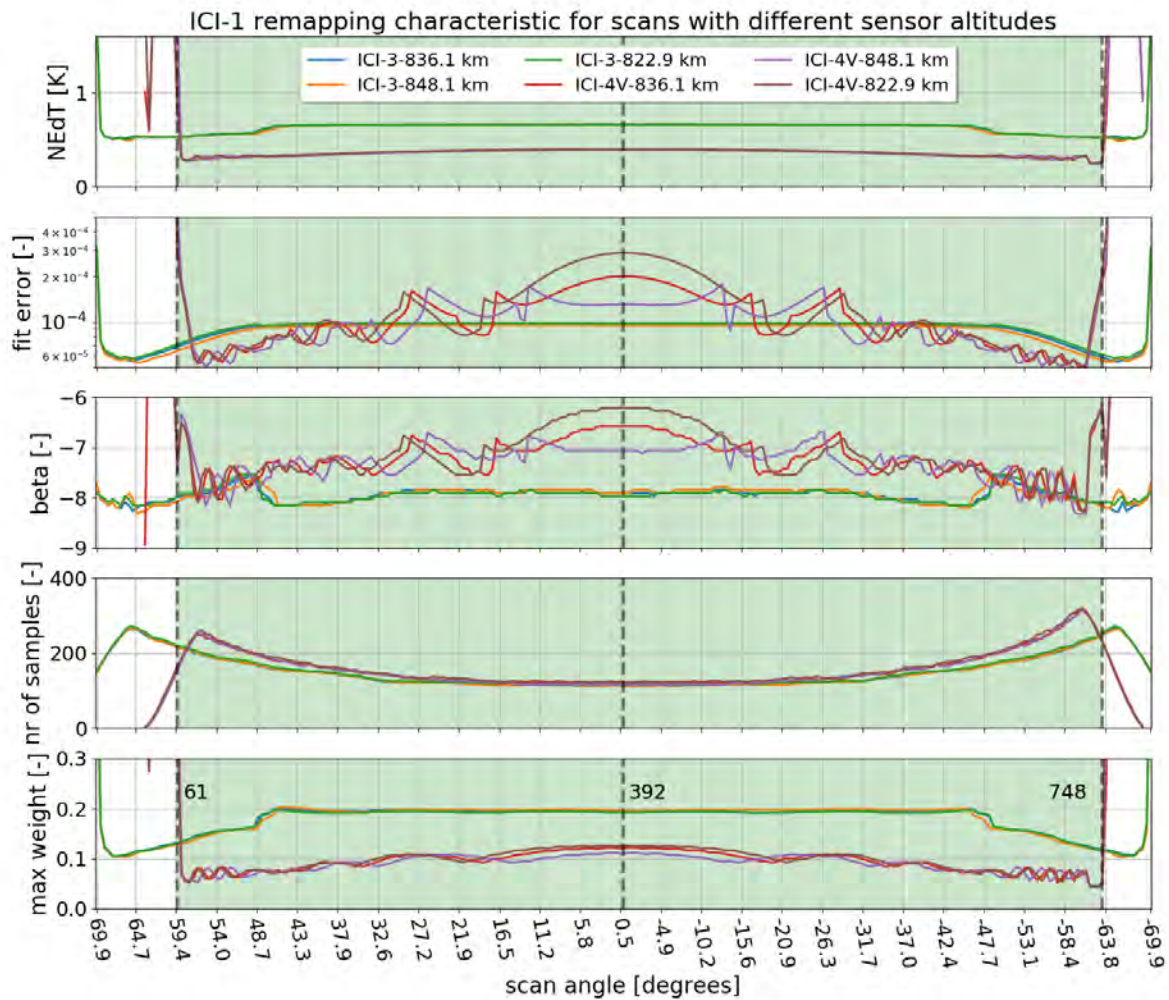
Figure 54: Trade off analysis data as function of scan angle / scan position for ICI-3 and ICI-4V derived from three different sensor positions, otherwise as Figure 53.
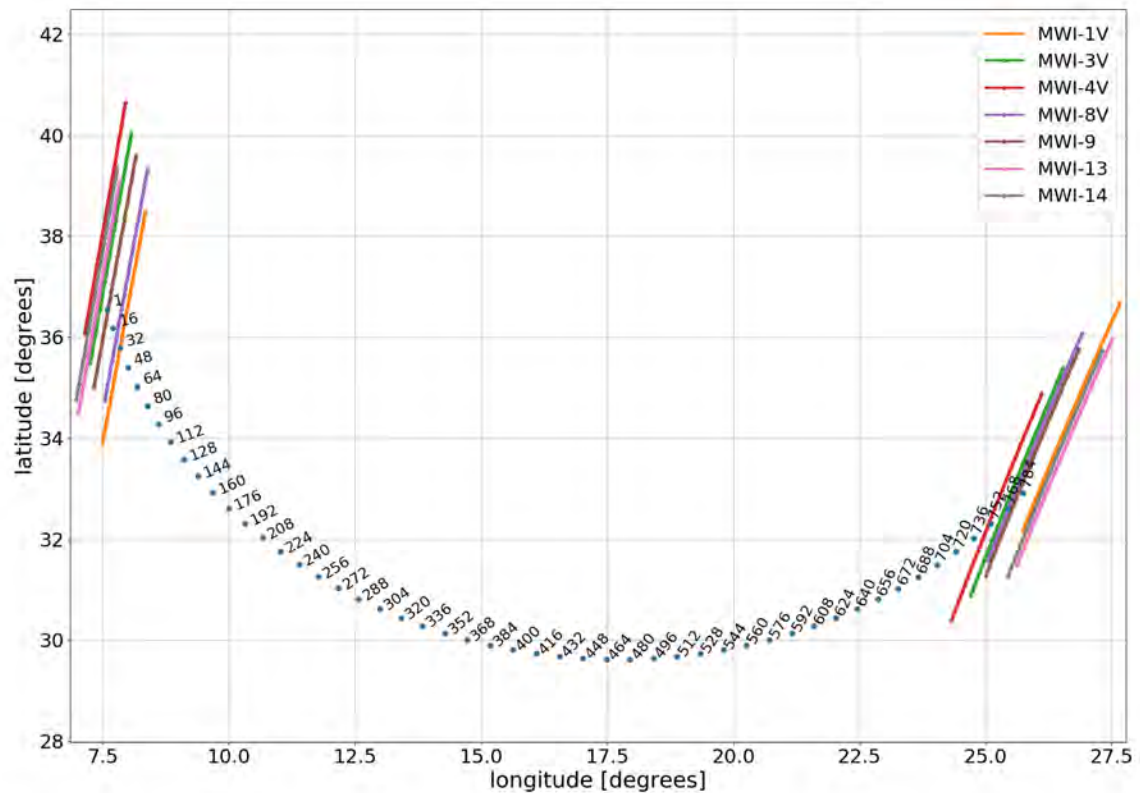
Figure 55: Geolocation on geoid of different sample positions for ICI-1 (target channel) within a given scan. Geolocation of outer sample positions for neighboring scans and for some MWI channels are also displayed. The figure indicate that it should be possible to remap observations for all channels for sample numbers between about 32 to 752 (see Table 12 for actual range and corresponding scan angles).

9.4   MWI and ICI

Remapping of MWI channels to ICI-1 FOV is of interest for several reasons. For example, MWI-14, MWI-17, and MWI-18 overlap ICI-1, ICI-2, and ICI-3, respectively, in terms of frequency coverage. Thus, comparison between remapped observations from these channels is of interest for a CAL/VAL purpose. Remapping of MWI channels to ICI-1 FOV is also of interest for a Level2 processing purpose, as it will allow for retrieval of geophysical products from a combination of MWI and ICI observations. For example, MWI has more channels than ICI around the 183[GHz] water vapor line, and ICI lacks channels around the 118[GHz] oxygen line. The MWI window channels around 89[GHz] and 165[GHz] can potentially also be of interest to use in a joint MWI and ICI retrieval. Individual samples for the MWI channels mentioned above have a finer footprint size than that of ICI-1, and this is preferable, as compared to the other way around, in terms of errors generated by the remapping procedure. The focus in this

Table 12: MWI remapping characteristic for remapping into ICI-1 FOV. NEΔT and fit-error are described as median values for the scan.

Channel	Frequency [GHz]	NEΔT (sample / required / remapped) [K]	Fit Error [-]	Sample Number (min/max) [-]	Scan Angle (min/max) [degrees]
MWI-8V	89	2.38 / 1.1 / 0.36	1.6e-4	31 / 760	64.54 / -65.57
MWI-8H	89	2.38 / 1.1 / 0.36	1.6e-4	31 / 760	64.54 / -65.57
MWI-9	118.7503 ± 3.2	2.71 / 1.3 / 0.42	1.4e-4	13 / 766	67.75 / -66.64
MWI-10	118.7503 ± 2.1	2.71 / 1.3 / 0.42	1.4e-4	13 / 766	67.75 / -66.64
MWI-11	118.7503 ± 1.4	2.71 / 1.3 / 0.42	1.4e-4	13 / 766	67.75 / -66.64
MWI-12	118.7503 ± 1.2	2.71 / 1.3 / 0.42	1.4e-4	13 / 766	67.75 / -66.64
MWI-13	165.5 ± 0.75	2.14 / 1.2 / 0.35	1.2e-4	1 / 784	69.89 / -69.85
MWI-14	183.31 ± 7.0	2.25 / 1.3 / 0.36	1.4e-4	1 / 784	69.89 / -69.85
MWI-15	183.31 ± 6.1	2.08 / 1.2 / 0.33	1.4e-4	1 / 784	69.89 / -69.85
MWI-16	183.31 ± 4.9	2.08 / 1.2 / 0.33	1.4e-4	1 / 784	69.89 / -69.85
MWI-17	183.31 ± 3.4	2.08 / 1.2 / 0.33	1.4e-4	1 / 784	69.89 / -69.85
MWI-18	183.31 ± 1.3	2.25 / 1.3 / 0.36	1.4e-4	1 / 784	69.89 / -69.85

section is therefore on the remapping of MWI-8 - MWI-18 onto ICI-1 FOV.

Figure 55 shows the geolocation of ICI-1 samples on geoid for some positions within a given scan. The figure also displays geolocations of scan end positions for neighboring scans for samples from some MWI channels. Most of the ICI-1 swath is covered by the MWI channels, although the coverage is not complete for all MWI channels.

9.4.1 Number of scans / samples to include in the calculation

An important consideration when applying the remapping algorithm is to decide how many samples to include in the remapping calculation, as discussed in more details in Sect. 9.2.1 and for MWI. Remapping (from MWI channels to ICI-1 FOV) characteristic is shown in Figure 56. The noise error saturates around a "maxRadius" of 15[km] and the fit error around a "maxRadius" of 30[km]. Therefore, a "maxRadius" of 30[km] is applied for all MWI channels. This gives that samples from 7 scans or around 200 samples are used in the remapping calculation for the center position of the ICI scan. In the outer part of the scan these numbers are greater as shown in Figure 57.

9.4.2 Remapping characteristic / treatment of swath edges

Figure 57 shows remapping characteristic as function of scan position for some MWI channels for a given scan, and the result is summarized in Table 12. The fit-error is less symmetric around the center scan position than for the "pure" MWI and ICI remapping (Figure 47 and Figure 53), but a non-symmetry is to be expected due to the difference in scan rotation directions between MWI and ICI. Anyhow, the fit-error is at a maximum around the center scan position for all channels, and decreases with increasing scan angle, until the edges of scan where the performance degrade. Figure 57 shows that the main part of ICI-1 swath is covered by the MWI channels, and some of the MWI channels (MWI-13 and MWI-14 or actually MWI-13 to MWI-18) even covers the complete swath. All MWI channels considered here covers at least ICI-1 scanning angles between about 65 and -65[°] and that is greater range than was covered by all ICI channels (59 and -59[°] as described in Sect. 9.3). The noise on the remapped observations are in general low (between 0.25 and 0.5[K] in the ±65[°] window), and this is in

	Backus-Gilbert footprint matching methodology applied on MWI and ICI observations	**Code:** TR/BG/MWI-ICI
		Issue: 1.0
		Date: June 5, 2019
		File: optimal-interpolation-applied.tex
		Page: 136 / 200

general lower than the noise of remapped ICI samples. The fit-error, on the other hand, is slightly higher for MWI than for the remapped ICI observations.

	Backus-Gilbert footprint matching methodology applied on MWI and ICI observations	Code: TR/BG/MWI-ICI
		Issue: 1.0
		Date: June 5, 2019
		File: optimal-interpolation-applied.tex
		Page: 137 / 200
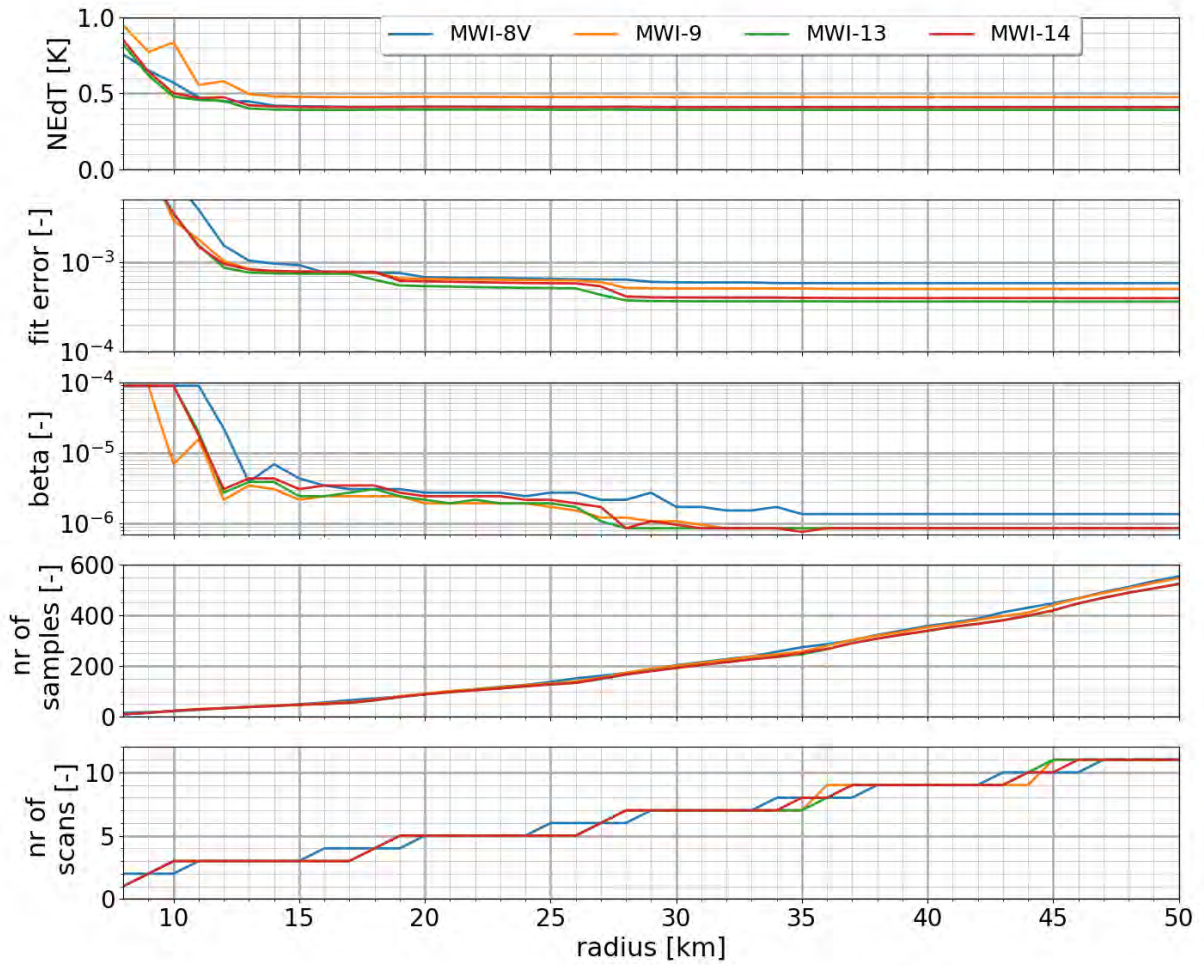
Figure 56: ICI-1 remapping characteristic data for some MWI channels as function radius. Data are representative for the center position of the scan (i.e. scan position 392, see Figure 57). The upper panel shows noise of the remapped sample, second panel fit-error, and the third panel shows the optimal value of the smoothing parameter from the trade off analysis. The fourth panel shows how many samples that were included in the calculation, and the bottom panel shows the number of scan lines that these samples origin from.
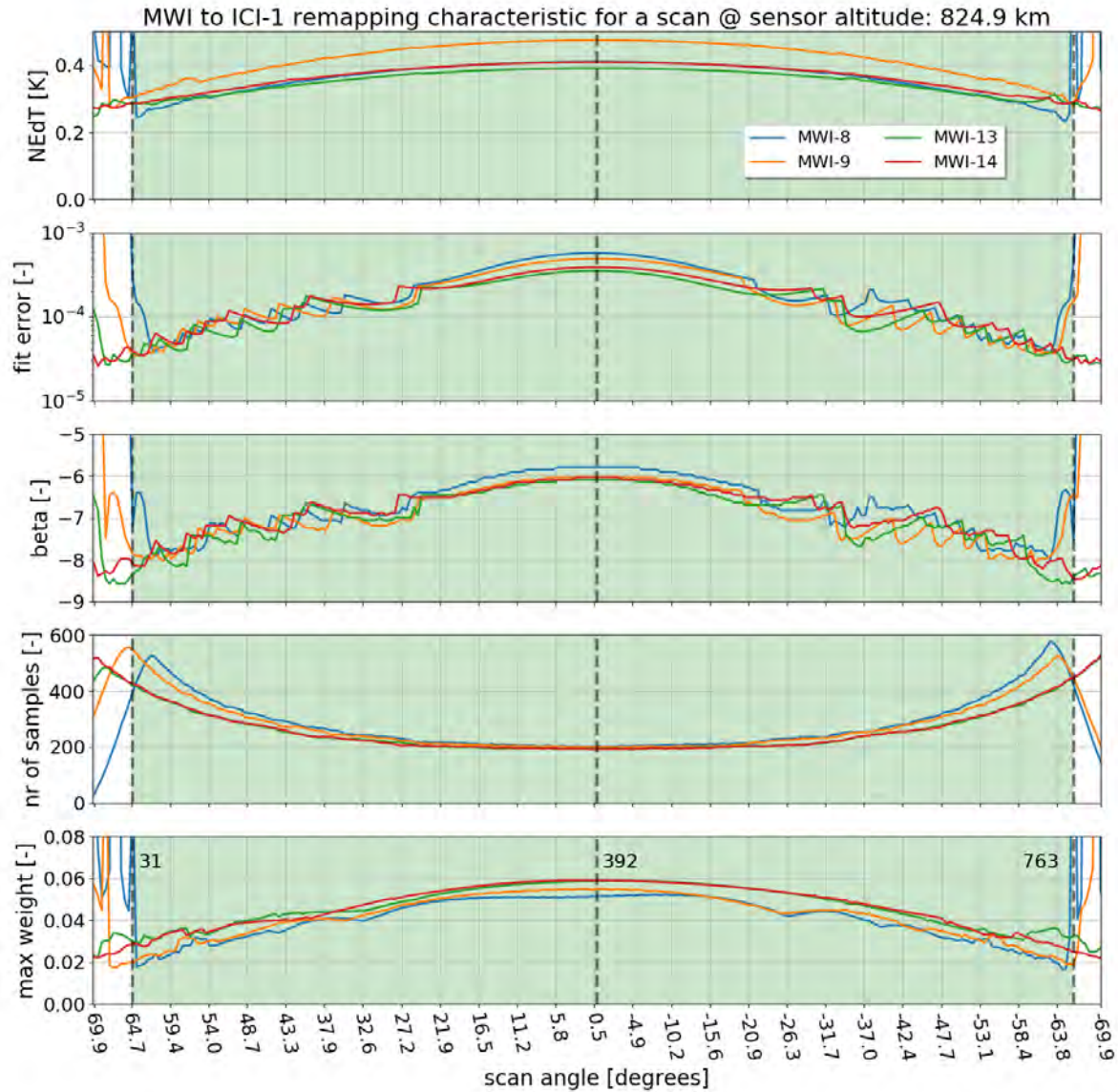
Figure 57: Trade off analysis data as function of scan angle / scan position for MWI to ICI-1 remapping. The two upper panels show the obtained noise error and fit error. The middle panel shows the optimal value of the smoothing parameter deployed in the BG methodology. The fourth panel shows the number of samples that are found within 30[km] from the geolocation of the center of the target footprint, and used in the remapping calculation. The bottom panel shows the maximum weight given to a single sample.

	Backus-Gilbert footprint matching methodology applied on MWI and ICI observations	Code: TR/BG/MWI-ICI
		Issue: 1.0
		Date: June 5, 2019
		File: optimal-interpolation-applied.tex
		Page: 139 / 200

Table 13: MWI to ICI-1 remapping sensitivity to orbital variations.

Channel	Frequency [GHz]	Incidence angle [degrees]	Error [K]
MWI-8V	89	52.2042	0.05
MWI-9	118.7503 ± 3.2	52.7802	0.01
MWI-13	165.5 ± 0.75	54.0936	0.008
MWI-14	183.31 ± 7.0	54.0539	0.005

9.4.3 Remapping sensitivity to orbital variations.

The importance of studying the sensitivity to orbital variations was described in Sect. 9.2.4. Figure 58 shows remapping data for MWI-8V and MWI-14 derived from three different orbital positions.

The result from a sensitivity test (described in Sect. 9.2.4 but applied on relevant MWI and ICI data) is summarized in Table 13. Table 13 describes estimated noise that will be induced if only weighting coefficients from only one scan (around a sensor altitude of 836.1[km]) is used in operational processing. This noise is low compared to other noise sources, and on top of that uncorrelated to most other error sources, and consequently more or less negligible.

| | Backus-Gilbert footprint matching methodology applied on MWI and ICI observations | Code: TR/BG/MWI-ICI
Issue: 1.0
Date: June 5, 2019
File: optimal-interpolation-applied.tex
Page: 140 / 200 |
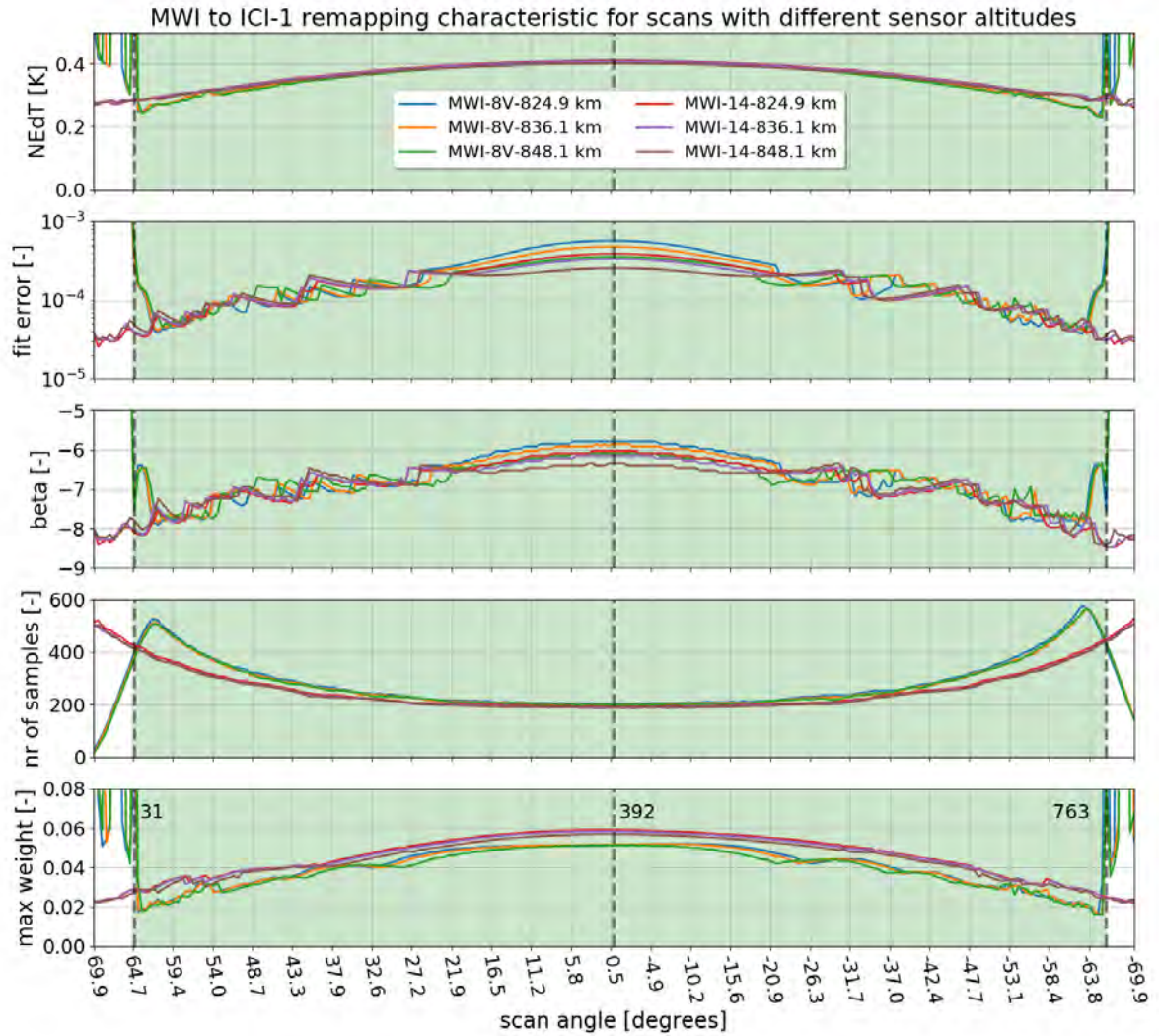
Figure 58: Trade off analysis data as function of scan angle / scan position for MWI-8V and MWI-14 derived from three different sensor positions, otherwise as Figure 57.
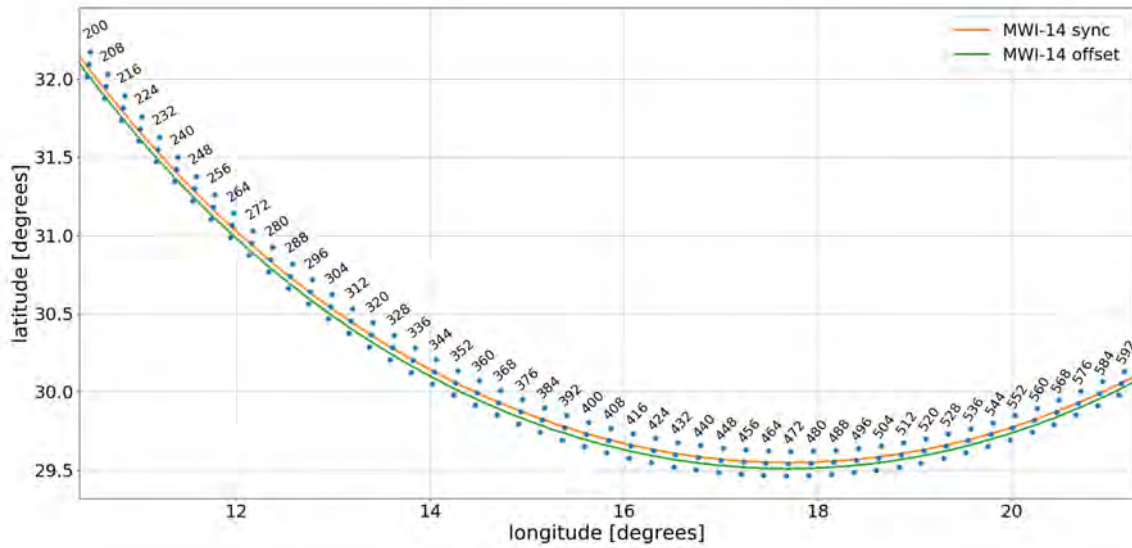
Figure 59: Gelocations of sample positions in the center part of three consecutive scans for ICI-1 samples (blue dots), and for sample positions of a "single" scan for MWI-14. Two versions of the this "single" scan are displayed, one where the start time of the MWI-14 and the center ICI scan is synchronized, and one where the MWI-14 scan is delayed by half the scan duration time.

9.4.4 Remapping sensitivity to scan synchronization

MWI and ICI scan rotation is clockwise and counterclockwise, respectively, as seen from zenith side of the platform. We here analyze the sensitivity to the synchronization of the MWI and ICI scan, by comparing remappings from MWI channels onto ICI-1 FOV for two special case:

1. Start time of the MWI and ICI scan is coincident

2. Start time of the MWI scan is delayed by 2/3[s] (i.e. half scan duration time) compared to the ICI scan.

Figure 59 shows the corresponding effect on the positions of the geolocations on the geoid of ICI-1 and MWI-14 samples, due to the synchronization of the start time of the MWI and ICI scan. Data are shown for the center part of the scan, where the along-track distance between two consecutive scans is relatively large compared to the outer part of the scan. Consequently, the remapping can possibly be most sensitive to scan synchronization in the center part of the scan. It can be seen that MWI-14 collocation to ICI-1 scan line is better if the start time of the scan is synchronized than delayed. In the latter case, the MWI-14 samples are located more or less right between two ICI-1 scan lines.

Figure 60 shows remapping characteristics obtained from three different sensor positions at different altitudes, and two sets of weighting coefficients were derived for each altitude, one where the start time of the MWI and ICI scan is coincident, and one where the start time of

	Backus-Gilbert footprint matching methodology applied on MWI and ICI observations	**Code:** TR/BG/MWI-ICI
		Issue: 1.0
		Date: June 5, 2019
		File: optimal-interpolation-applied.tex
		Page: 142 / 200

MWI scan is delayed by 2/3[s] compared to the ICI scan. Figure 60 shows that the obtained noise of the remapping has no strong dependency on the scan synchronization. The fit-error, on the other hand, can be seen to be dependent on scan synchronization. In the center part of the scan, where in general the fit-error is at a maximum, the remapping error is somewhat lower if the start time of the scan is synchronized. In the outer part of the scan, the fit-error "oscillates" and at some scan positions the error is lower for the synchronized scan, and vice versa for some scan positions. A likely explanation for the lower fit-error in the center part of the scan for the synchronized scan is probably related to the fact that the distance difference (in the along-track direction) between the geolocation of MWI and ICI samples is smaller if the scan is synchronized, than out of sync, and that should allow for a better FOV fit (see Figure 60).

However, the slight increase in fit-error in the center part of the scan for a non coincident scan start time of MWI and ICI scan must be considered to be a minor issue, as the extra error has a similar magnitude as the variation in fit-error w.r.t sensor altitude. Thus, it appears that a synchronization of the start time of the MWI and ICI is not a critical issue, as long as there is no drift between the start times of the two scans. In principal, it should be possible to remap MWI samples onto ICI-1 FOVs even if there is a drift, but then this drift must be taken into account to avoid geolocation errors. For example, geolocation errors of several kilometers will be introduced, if the remapping of MWI samples onto ICI-1 FOV is done using a precalculated set of weighting coefficients based on a specific scan start time difference, but the actual start time difference is more than 0.392[ms] (corresponding to MWI sample integration time) different from this.
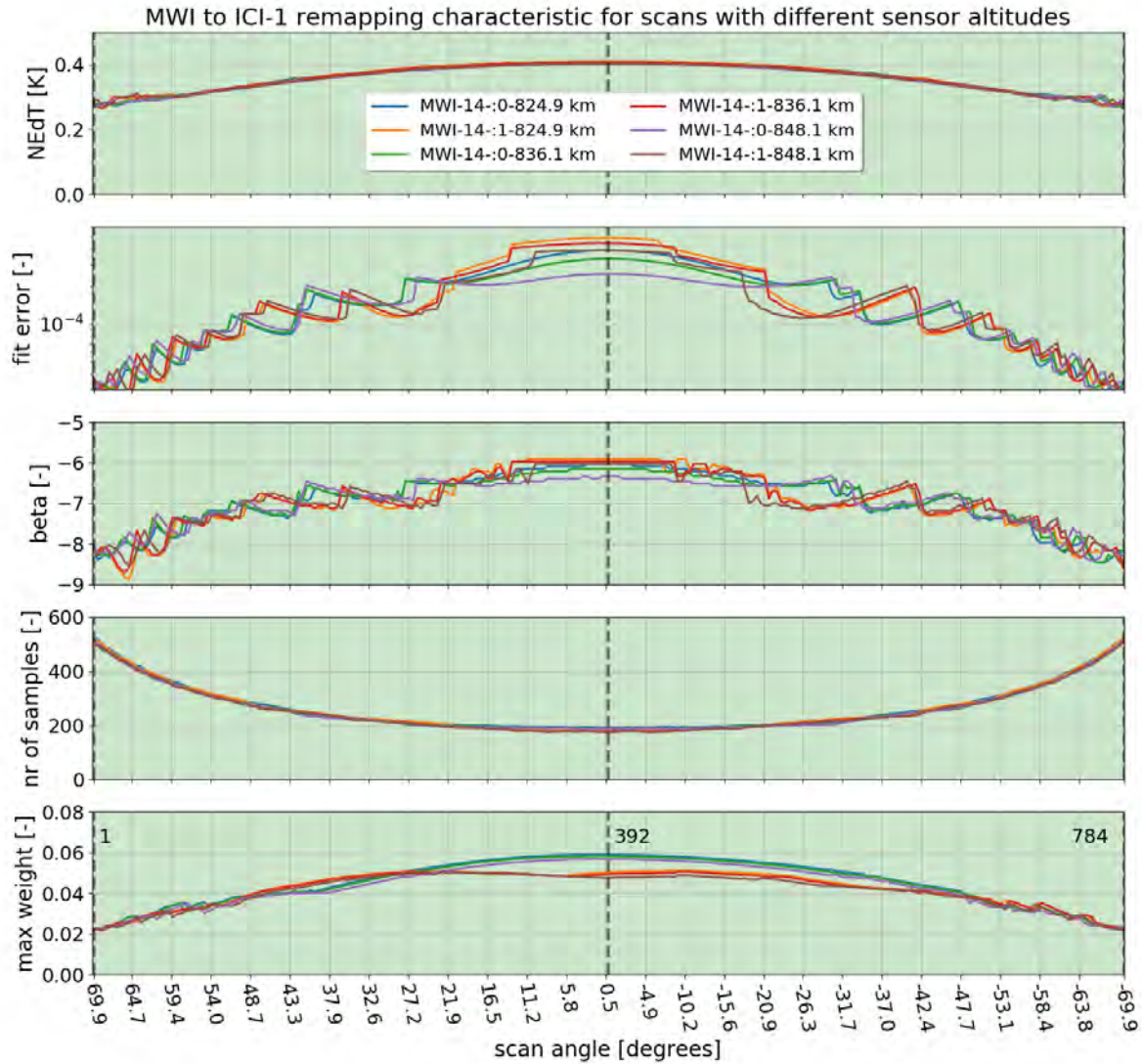
Figure 60: Trade off analysis data as function of scan angle / scan position for MWI-14 to ICI-1 remapping, for scans with synchronized and delayed scan start (described 0 and 1 in legend, respectively), see text for more details. The two upper panels show the obtained noise error and fit error for three different sensor positions. The middle panel shows the optimal value of the smoothing parameter deployed in the BG methodology. The fourth panel shows the number of samples that are found within 30 km from the geolocation of the center of the target footprint, and used in the remapping calculation. The second bottom panel shows the maximum weights given to a single sample.

10 Bias assessment

10.1 Overview

In this section we assess biases related to the remapping of MWI and ICI samples. The remapping of samples from a given channel to a target FOV results in that the antenna pattern on the geoid is approximately matched. In general, a remapped MWI / ICI observation can be seen as an estimate of the antenna temperature of the channel of concern, as "measured" from the MWI-3V / ICI-1 viewing angle and antenna pattern. However, the various channels of MWI and ICI have slightly different viewing angles, and that results in that a given scene is seen with varying incidence angles. Both surface emissivity / reflectively and atmospheric transmission varies with incidence angle (and with surface type and atmospheric condition). The consequence is that there can be a bias between a remapped observation compared to the "true" antenna temperature.

A dataset consisting of detailed MWI and ICI simulations (described in Rydberg and Eriksson [2018]), for four complete reference Metop orbits is used for the bias assessment. The simulation takes into account of the scanning and antenna patterns of MWI and ICI and its channels, surface emission and reflectivity, atmospheric emission and transmission, and clouds (both liquid and snow/ice clouds are included).

The dataset of detailed MWI and ICI simulations is used to estimate both "true" and remapped antenna temperatures, and that allows for inter-channel and inter-fov bias assessments. The main focus is here for cloud-free conditions, both over ocean and land, but also the impact of clouds on biases is assessed. The surface emissivity / reflectivity depends on surface types, and can vary quite dramatically between ocean and land for some of the MWI channels, and hence, "incidence angle" biases can potentially vary significantly between ocean and land, and estimates of biases for MWI and ICI channels are presented in Sect. 10.2.1 and Sect. 10.3.1, respectively.

Additionally, MWI and ICI, both have a number of channels around 183.31[GHz] and ICI-1 / MWI-14, ICI-2 / MWI-17, and ICI-3 / MWI-18 overlaps in frequency coverage. Therefore, biases between samples, convolved to the ICI-1 FOV, from these channels will be of particular interest in a Cal / Val activity, and a bias assessment is presented in Sect. 10.4.

	Backus-Gilbert footprint matching methodology applied on MWI and ICI observations	Code: TR/BG/MWI-ICI
		Issue: 1.0
		Date: June 5, 2019
		File: optimal-interpolation-applied.tex
		Page: 145 / 200

Table 14: MWI remapping bias for clear sky condition over ocean and land surface. Note that the bias is state dependent and applies to the data described in this section, and it is described by the 16th and 84th percentile. Incidence angle is varying with sensor altitude and is given for a height of 822.14[km].

Channel	Frequency [GHz]	Incidence angle [degrees]	Target channel	Bias (ocean) [K]	Bias (land) [K]
MWI-3V	31.4	52.8759	MWI-3V	[-0.006, -0.004]	[-0.002, -0.004]
MWI-4V	50.3	53.1537	MWI-3V	[0.17, 0.21]	[-0.10, -0.08]
MWI-8V	89	52.2042	MWI-3V	[-0.77, -0.69]	[0.05, 0.08]
MWI-9	118.7503 ± 3.2	52.7802	MWI-3V	[0.06, 0.07]	[0.12, 0.13]
MWI-13	165.5 ± 0.75	54.0936	MWI-3V	[-0.10, 0.29]	[-0.45, -0.36]
MWI-14	183.31 ± 7.0	54.0539	MWI-3V	[-0.30, -0.18]	[-0.39, -0.33]
MWI-1V	18.7	53.0611	MWI-1V	[-0.015, 0.012]	[-0.002, 0.005]
MWI-2V	23.8	53.0685	MWI-1V	[-0.001, 0.003]	[-0.001, 0.006]
MWI-3V	31.4	52.8759	MWI-1V	[-0.45, -0.37]	[-0.006, -0.04]
MWI-4V	50.3	53.1537	MWI-1V	[0.13, 0.15]	[0.03, 0.05]
MWI-8V	89	52.2042	MWI-1V	[-0.97, -0.86]	[0.08, 0.15]
MWI-9	118.7503 ± 3.2	52.7802	MWI-1V	[0.16, 0.19]	[0.30, 0.33]
MWI-13	165.5 ± 0.75	54.0936	MWI-1V	[-0.05, 0.28]	[-0.35, -0.27]
MWI-14	183.31 ± 7.0	54.0539	MWI-1V	[-0.23, -0.13]	[-0.30, -0.25]

10.2 MWI

10.2.1 Cloud free condition

Biases of samples remapped onto MWI-3V and MWI-1V FOVs for cloud free condition are here assessed, and the main aim of this section is to assess if any inter-FOV bias (scan position varying bias) can be seen in simulated data. A given scene is observed with slightly different incidence angles (up to about $\sim$1.2[°], see Table 14) by the various channels of MWI. These incidence angles varies somewhat with orbit and scan positions. The incidence angle varies by about $\sim$0.2[°] for the center scan position for each given channel throughout an orbit, but the relative variation w.r.t. the target channel is less than $\sim$0.012[°]. The variation in incidence angle with scan position is $\sim$0.03[°], but the relative variation w.r.t. the target channel is less than $\sim$0.01[°]. Thus, variations in incidence angles throughout the orbit and scan positions are generally much smaller than the "main" offset, and hence inter-FOV biases, for a given channel, are expected to be lower than the "main" bias.

In general the remapping rule should be that the channel with higher resolution is remapped onto the channel with lower resolution, for an inter-channel (or inter-FOV) bias assessment. For this purpose, two types of remappings are here considered, i.e.:

- MWI samples, from channels having a similar or smaller footprint size than MWI-3V, were remapped onto the FOV of MWI-3V for sample positions $1, 9, ..., 1401$ using weighting coefficients with characteristic described in Sect.9.2. The "true" FOV value, for each channel and FOV, was simulated using the MWI-3V target antenna pattern and viewing

	Backus-Gilbert footprint matching methodology applied on MWI and ICI observations	Code: TR/BG/MWI-ICI
		Issue: 1.0
		Date: June 5, 2019
		File: optimal-interpolation-applied.tex
		Page: 146 / 200

angle, and biases for this dataset are discussed relative to this simulation.

- MWI samples from various channels were also remapped onto the FOV of MWI-1V for sample positions $1, 9, ..., 1401$ and using a FOV integration time of 8.480[ms] (i.e. about 21.6 times greater than for each individual sample), in order to allow to study inter-channel and inter-FOV biases considering the MWI-1 and MWI-2 channels. The "true" FOV value, for each channel and FOV, was simulated using the MWI-1V target antenna pattern and viewing angle, and biases for this dataset are discussed relative to this simulation. Figure 61 show characteristics for the remapping onto the MWI-1V FOV, and it can be seen that a proper (low noise and fit-error) remapping can be performed for MWI-1V scan angles within about $\pm 61[°]$ for all channels, and even in a wider range for some channels (e.g. MWI-2V).

Figure 62 to 67 show comparisons between samples from MWI channels remapped onto the MWI-1V and MWI-3V FOVs and the "true" FOVs value for two sections of orbit 4655 (2007-09-12), one section over ocean (Figure 62 to 64) and one section over land (Figure 65 to 67), with relatively low cloud coverage, although cloud features can surly be seen in simulated antenna temperatures. These sections of the orbit were selected for this study because they contains at least some part where the state variation across the scene is limited. The swath width of MWI is around 1500[km], and it is in general not easy to find sections with low state variability.

A number of interesting features can be observed from Figure 62 to 71:

- the bias is different for the various channels (see Table 14), and in general also differ between ocean and land. The bias tends to be relatively low (below about 0.2[K] and with low variation) for the channels that have a similar incidence angle as the target channel (i.e. for the remapping of MWI-3V, MWI-4V, and MWI-9 channels onto the MWI-3V FOV, and for the remapping of MWI-1V, MWI-2V, and MWI-4V onto the MWI-1 FOV), and relatively high (above 0.2[K]) for the channels where the incidence angles differ by more than a few tenth of a degree compared to that of the target.

- the bias is, in general, state dependent. This is probably most clear for MWI-13 and MWI-14 observations over ocean (see Figure 64). The brightness temperature of a cloud free scene is strongly related to the total column water vapor for MWI-13 and MWI-14. The total column water vapor can vary strongly, making these channels more or less sensitive to surface emissivity/reflectivity. When the total column water vapor is high the atmosphere transmission becomes low, and the surface impact become low. The brightness temperature of the scene will then decrease with increasing incident angle (see e.g. Figure 85, although the figure shows data for an ICI related frequency), and this will give rise to a negative bias for MWI-13 and MWI-14. However, when the total column water vapor is low, the surface emissivity/reflectivity variation with incidence angle will have an impact on the bias, and this can even make the bias to become positive (as can be seen for MWI-13 in Figure 64)

- A clear scan position dependent bias, for low sample numbers (below 150), can be seen for the MWI-3V, MWI-4V, MWI-8V, and MWI-9V remappings onto MWI-1V FOVs (see

	Backus-Gilbert footprint matching methodology applied on MWI and ICI observations	Code: TR/BG/MWI-ICI
		Issue: 1.0
		Date: June 5, 2019
		File: optimal-interpolation-applied.tex
		Page: 147 / 200

e.g. Figure 70). However, the quality of remappings onto FOVs for sample positions below 150 is expected to be low, due to difference in swath coverage, and as can be seen from Figure 61. No significant inter-FOV bias is seen for any of these channel for sample positions above 150. A similar feature can also be seen for high sample numbers (above 1300) and for MWI-8V and MWI-9 remappings onto MWI-3V FOVs (see e.g. Figure 68). In Sect. 9.2 it is described that the performance of the remapping of these channels and for sample numbers above 1300 is limited. No significant inter-FOV bias is seen for these channels and for sample positions below 1300.

- the state dependency gives that it is not trivial to assess inter-FOV biases for MWI-13 and MWI-14, as the state dependent variation is greater than any expected inter-FOV biases. The scatter and slope seen in the data (see e.g. Figure 68 and Figure 69) for MWI-13 and MWI-14 are more related to state variation within the scene than to inter-FOV biases. For example, data for MWI-13 and for the ocean scene indicates that the bias varies by about 0.2[K] across the scene, while this is not seen for data over land. The conclusion is therefore that no inter-FOV bias can be seen in the data, and if it exists it should be small compared to other uncertainties.

- the remapping onto the MWI-1 FOV(s) is probably most interesting for inter-channel and inter-FOV bias assessments for the channels with a native footprint size of around 30 or 50[km] (here MWI-1V, MWI-2V, MWI-3V, and MWI-4V). These channels have a strong sensitivity to surface emissivity/reflectivity. Surface reflectivity is in general complicated to model, in particular for land surfaces. The surface emissivity tool TELSEM was deployed in the simulation for generating the dataset, and the bias over land presented here depends, clearly, on how accurate the incidence angle dependency in TELSEM is. Anyhow, the bias for MWI-2V is in the mK order of magnitude and hence negligible small. Biases for MWI-3V are MWI-4V are also found to be low for the land scene. The greatest bias, around 0.4[K], is here found for MWI-3V and for the ocean scene. Figure 70 and Figure 71 show that the bias, as function of scan position, is more or less constant for MWI-1V, MWI-2V, MWI-3V, and MWI-4V. The exception is for MWI-3V and MWI-4V and for sample number below 150, and the reason is described above.

- low bias variation is seen for the MWI-3V, MWI-4V, and MWI-9 remappings onto the MWI-3V FOVs, both over ocean and land surface, although the bias differs between ocean and land for MWI-4V and MWI-9. Effectively, no inter-FOV biases are found. The exception is for MWI-9 and sample numbers above 1300 (see e.g. the most westerly part of the scene in Figure 64) where the remapping works poorly, and this is outside the range where the MWI-9 to MWI-3V remapping works properly, as described above.

- MWI-8V has a relatively large difference between land and water bias, compared to other channels, and that is due to the fact to that the incidence angle "mismatch" to the target channel is greater than for other channels that have a strong sensitivity to the surface.

- the bias variation of MWI-13 and MWI-14 is comparable to estimated effective NEΔT values presented in Table 8.

	Backus-Gilbert footprint matching methodology applied on MWI and ICI observations	**Code:**	TR/BG/MWI-ICI
		Issue:	1.0
		Date:	June 5, 2019
		File:	optimal-interpolation-applied.tex
		Page:	148 / 200

- clouds within the FOV will have an impact on biases (on top of the cloud free bias, and this id further described in Sect. 10.2.2)

The main conclusion from here is that there will be non negligible inter-channel biases for samples remapped onto MWI-1V and MWI-3V FOVs, related to the variation in scene viewing incidence angle among channels. However, no significant scan position dependent biases were found within the MWI-3V scan angle range of -66° to 65° where the remapping is anticipated to work well (Sect. 9.2).

	Backus-Gilbert footprint matching methodology applied on MWI and ICI observations	Code:	TR/BG/MWI-ICI
		Issue:	1.0
		Date:	June 5, 2019
		File:	optimal-interpolation-applied.tex
		Page:	149 / 200
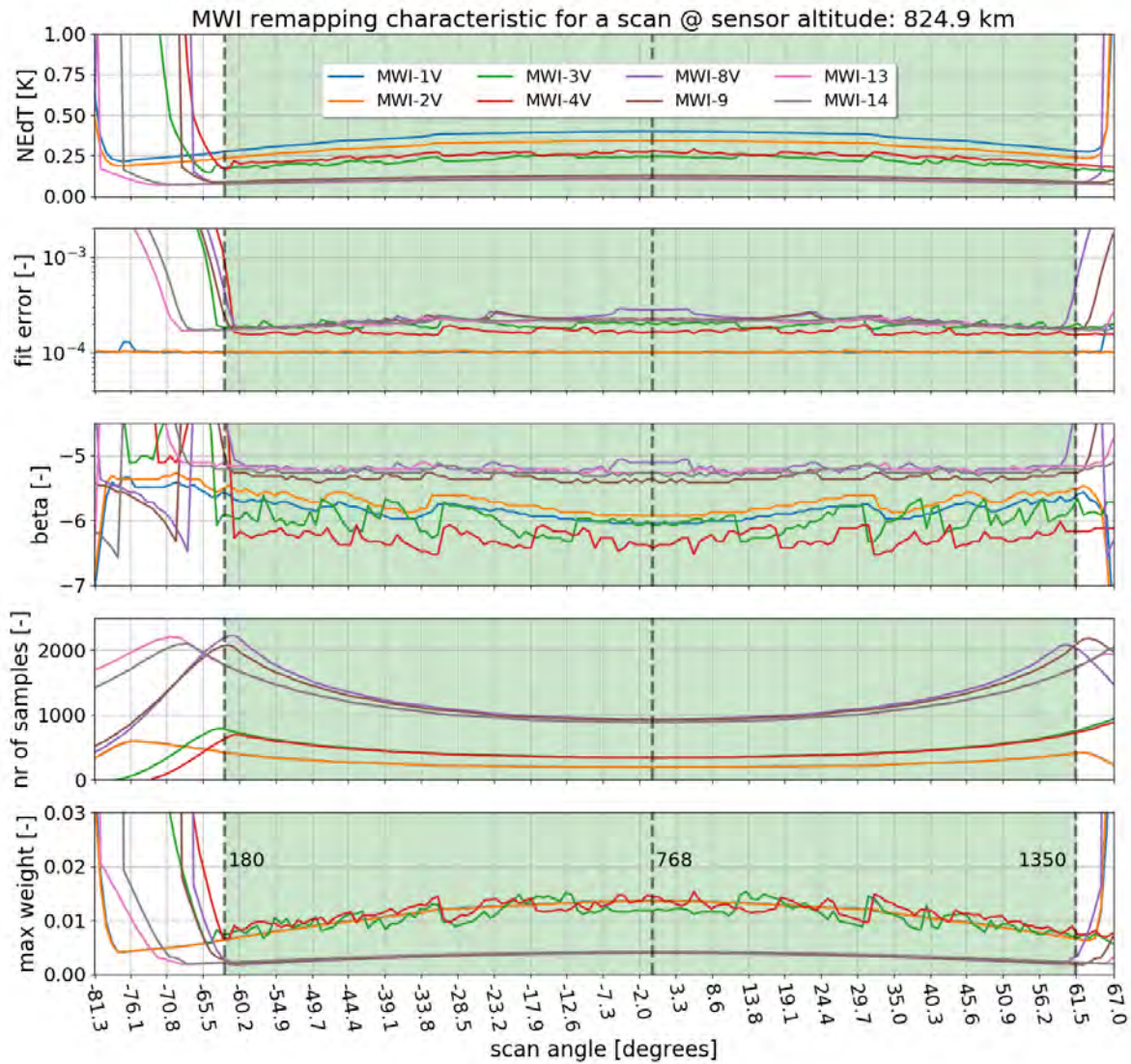
Figure 61: As Figure 47 but showing characteristic for remapping onto the MWI-1V FOV(s). The "maxRadius" parameter used is 30, 40, and 65[km] for the channels having a native footprint size of around 50 (MWI-1V and MWI-2V), 30 (MWI-3V and MWI-4V), and 10[km] (MWI-8V, MWI-9, MWI-13, and MWI-14), respectively.
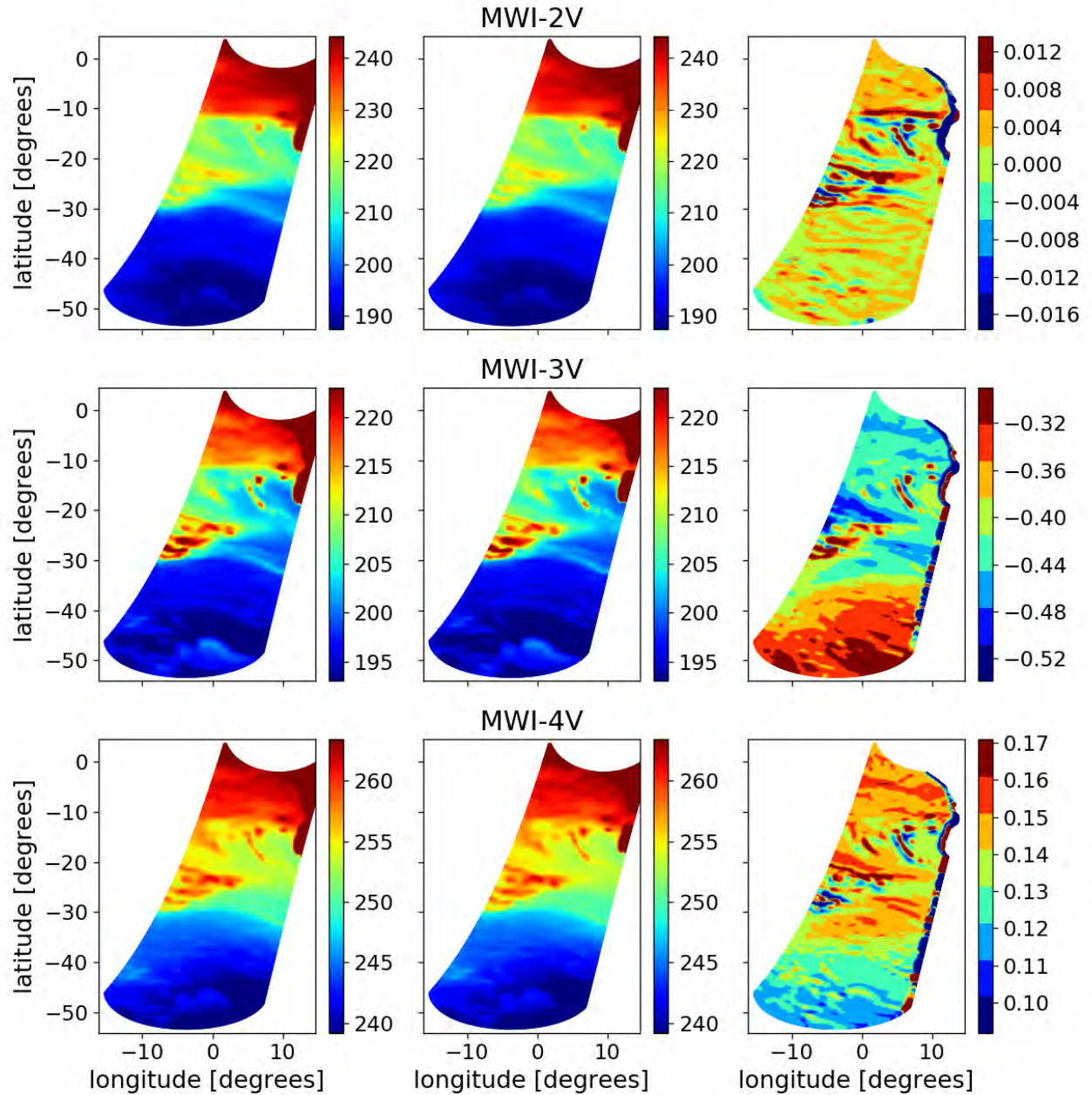
Figure 62: Bias between samples from MWI-2V, MWI-3V, and MWI-4V remapped onto MWI-1V FOVs and the "true" antenna temperature, based on simulation of a section of Metop-A orbit 4655 (2007-09-12) over southern part of Atlantic Ocean Left and middle column show "true" and remapped antenna temperature (described in text), respectively, and the right column shows the difference (remapped - "true"), where the northeastern part of the scene is screened for land. The unit associated to the colorbars is K.

	Backus-Gilbert footprint matching methodology applied on MWI and ICI observations	Code:	TR/BG/MWI-ICI
		Issue:	1.0
		Date:	June 5, 2019
		File:	optimal-interpolation-applied.tex
		Page:	151 / 200
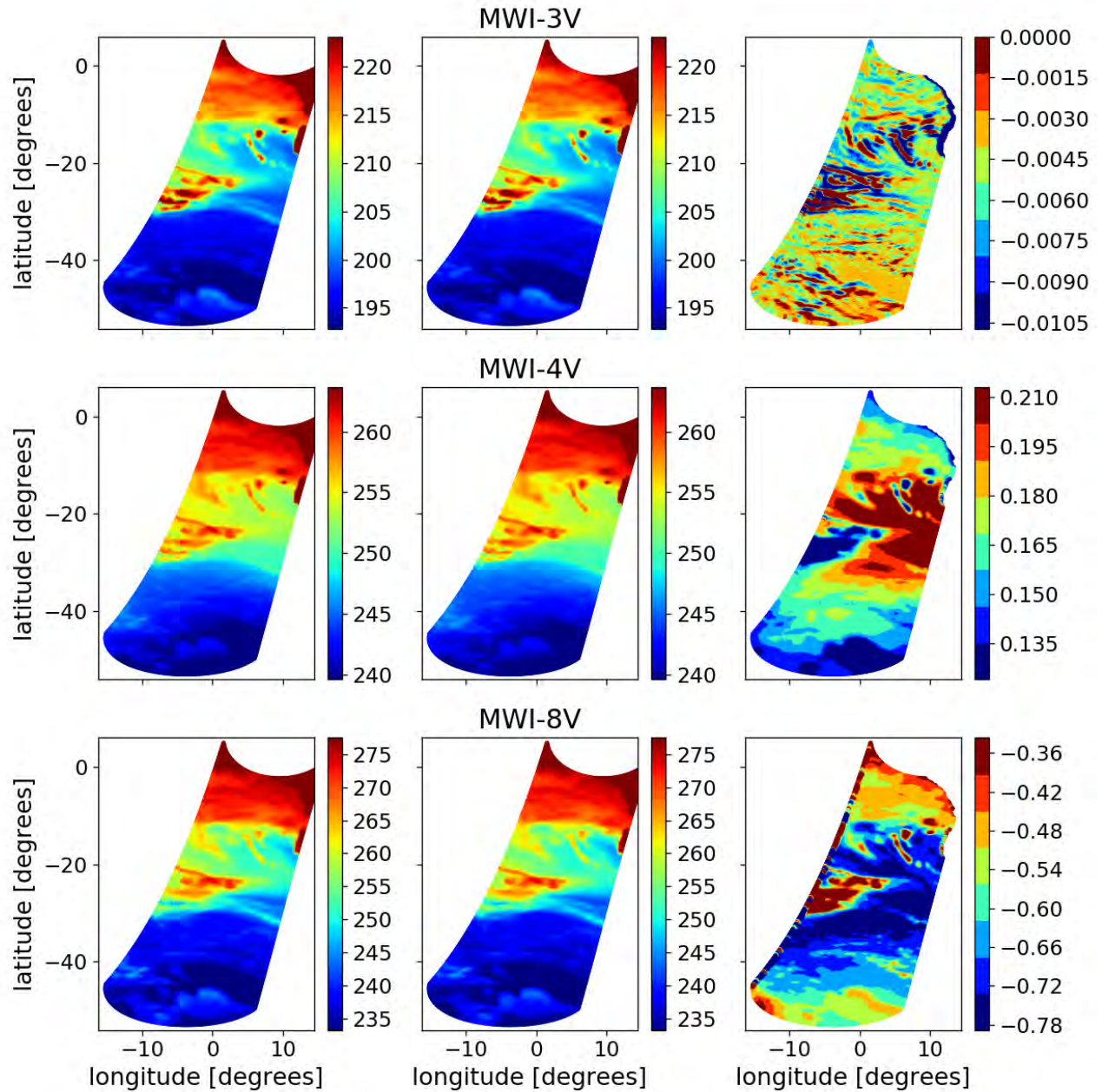
Figure 63: As Figure 62 but showing data for MWI-3V, MWI-4V, and MWI-8V remapped onto MWI-3V FOVs.

	Backus-Gilbert footprint matching methodology applied on MWI and ICI observations	Code:	TR/BG/MWI-ICI
		Issue:	1.0
		Date:	June 5, 2019
		File:	optimal-interpolation-applied.tex
		Page:	152 / 200
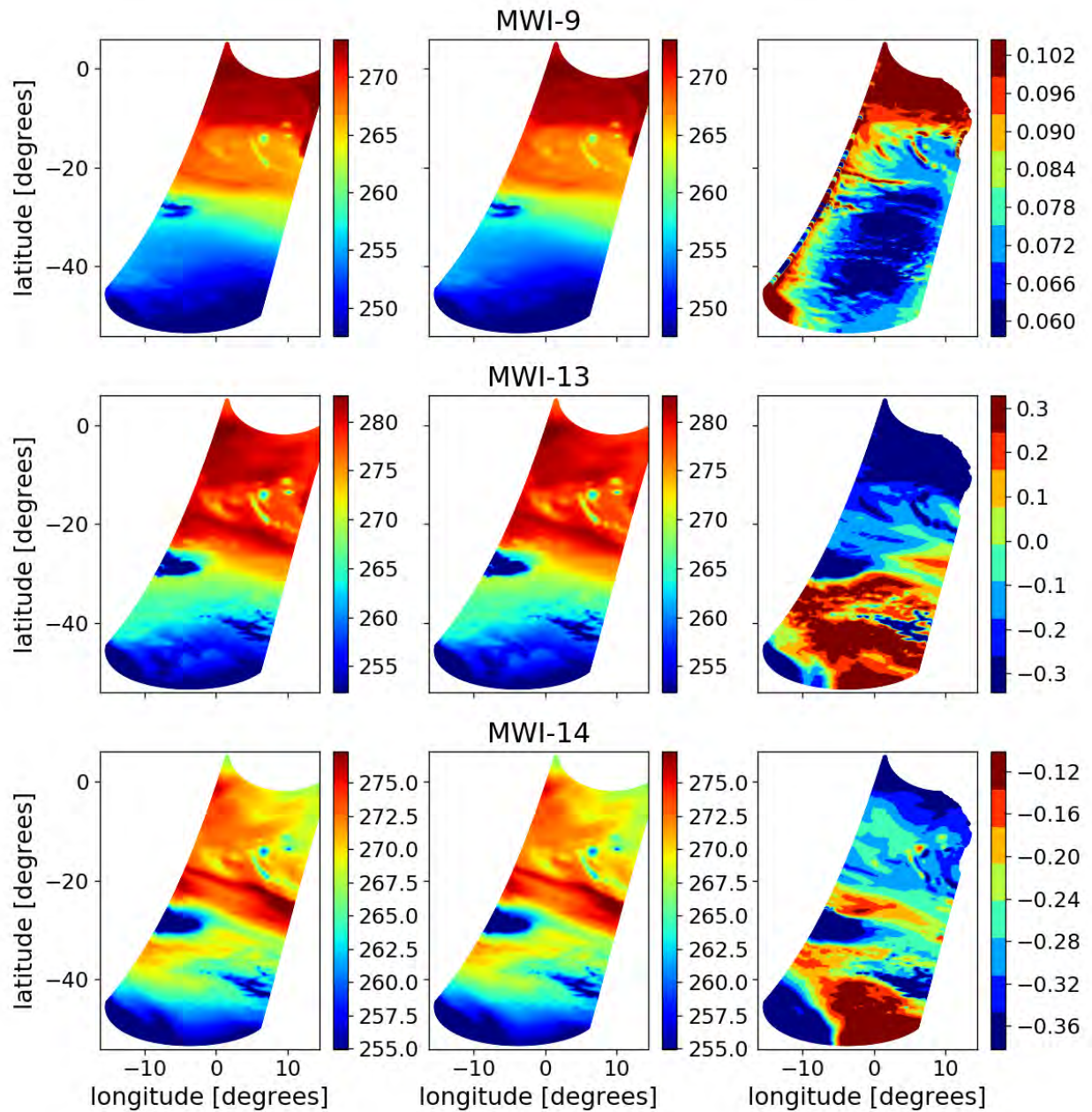
Figure 64: As Figure 62 but showing data for MWI-9, MWI-13, and MWI-14 remapped onto MWI-3V FOVs.
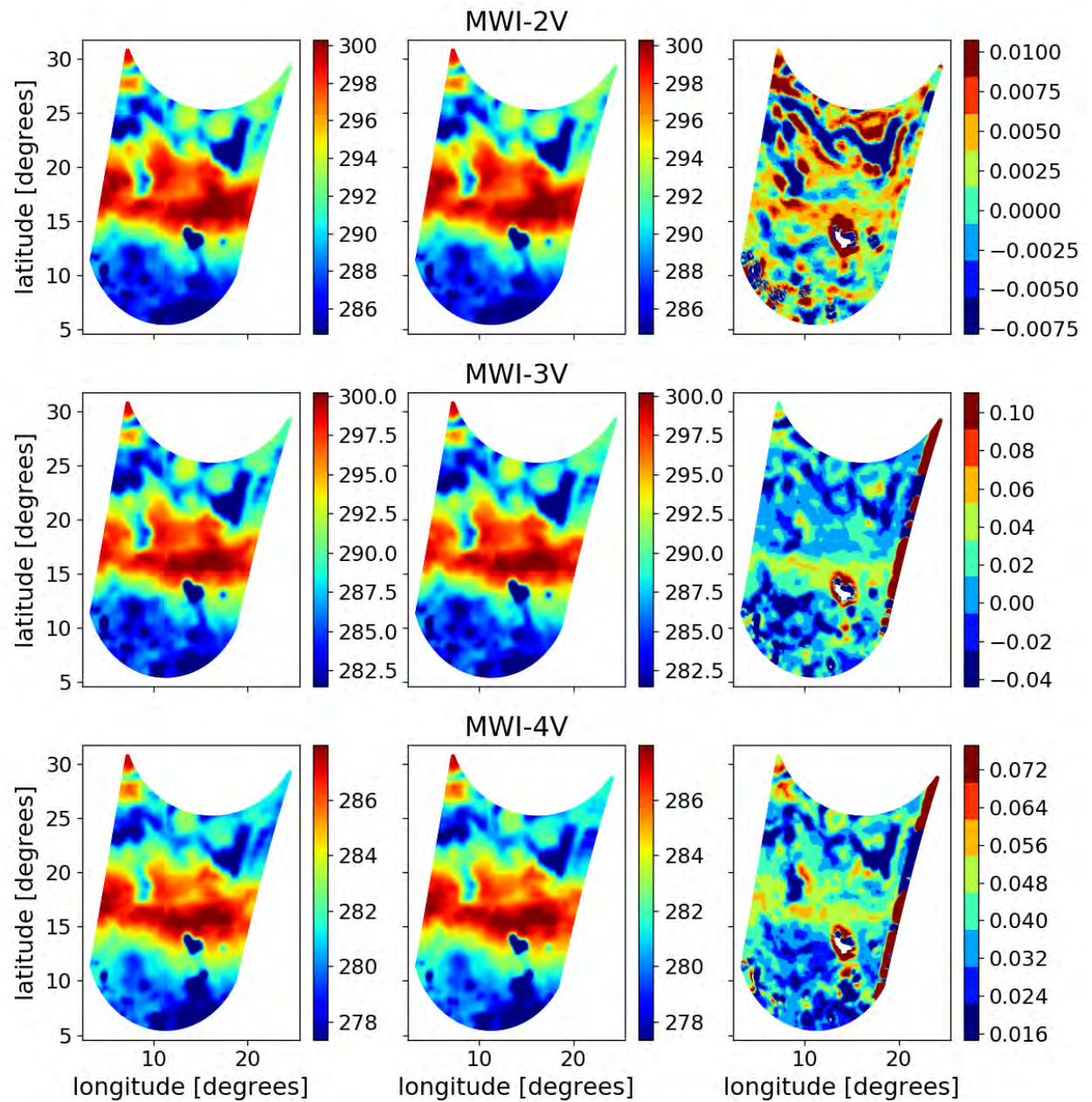
Figure 65: As Figure 62 but showing data for a scene over Africa.
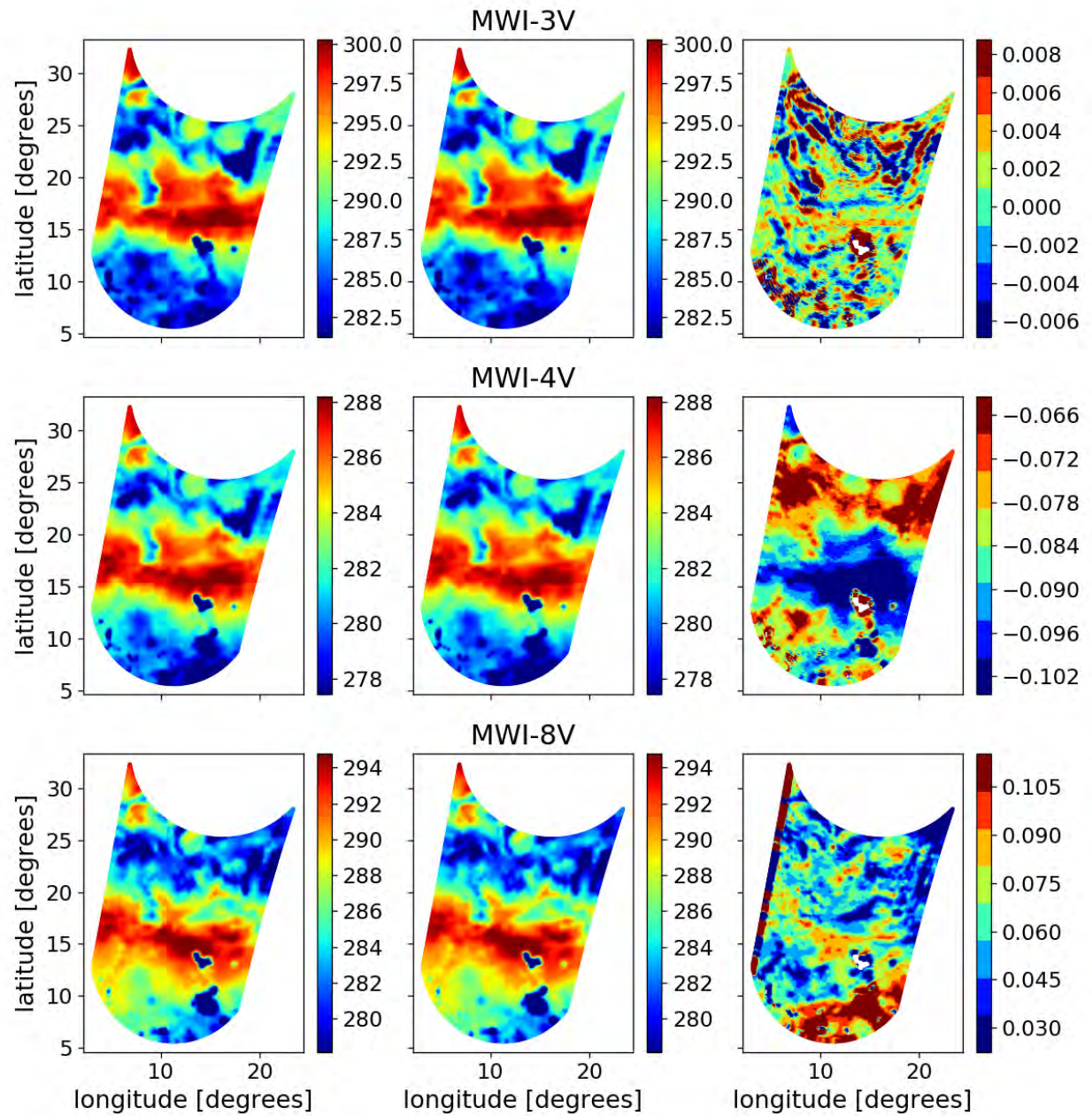
Figure 66: As Figure 62 but showing data for a scene over Africa for MWI-3V, MWI-4V, and MWI-8V remapped onto MWI-3V FOVs.

	Backus-Gilbert footprint matching methodology applied on MWI and ICI observations	**Code:** TR/BG/MWI-ICI
		Issue: 1.0
		Date: June 5, 2019
		File: optimal-interpolation-applied.tex
		Page: 155 / 200
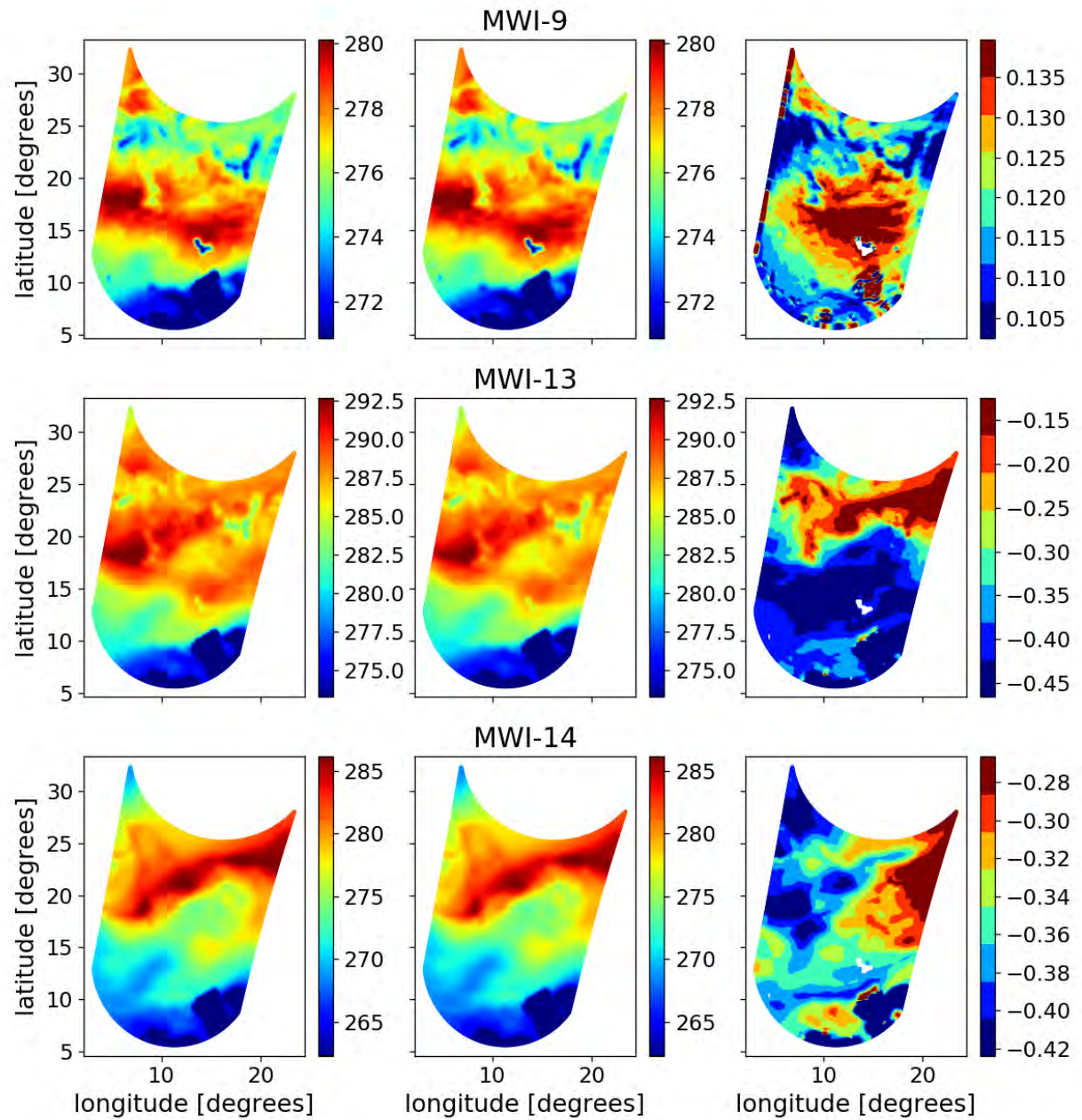
Figure 67: As Figure 62 but showing data for a scene over Africa for MWI-9, MWI-13, and MWI-14 remapped onto MWI-3V FOVs.

	Backus-Gilbert footprint matching methodology applied on MWI and ICI observations	Code: TR/BG/MWI-ICI
		Issue: 1.0
		Date: June 5, 2019
		File: optimal-interpolation-applied.tex
		Page: 156 / 200
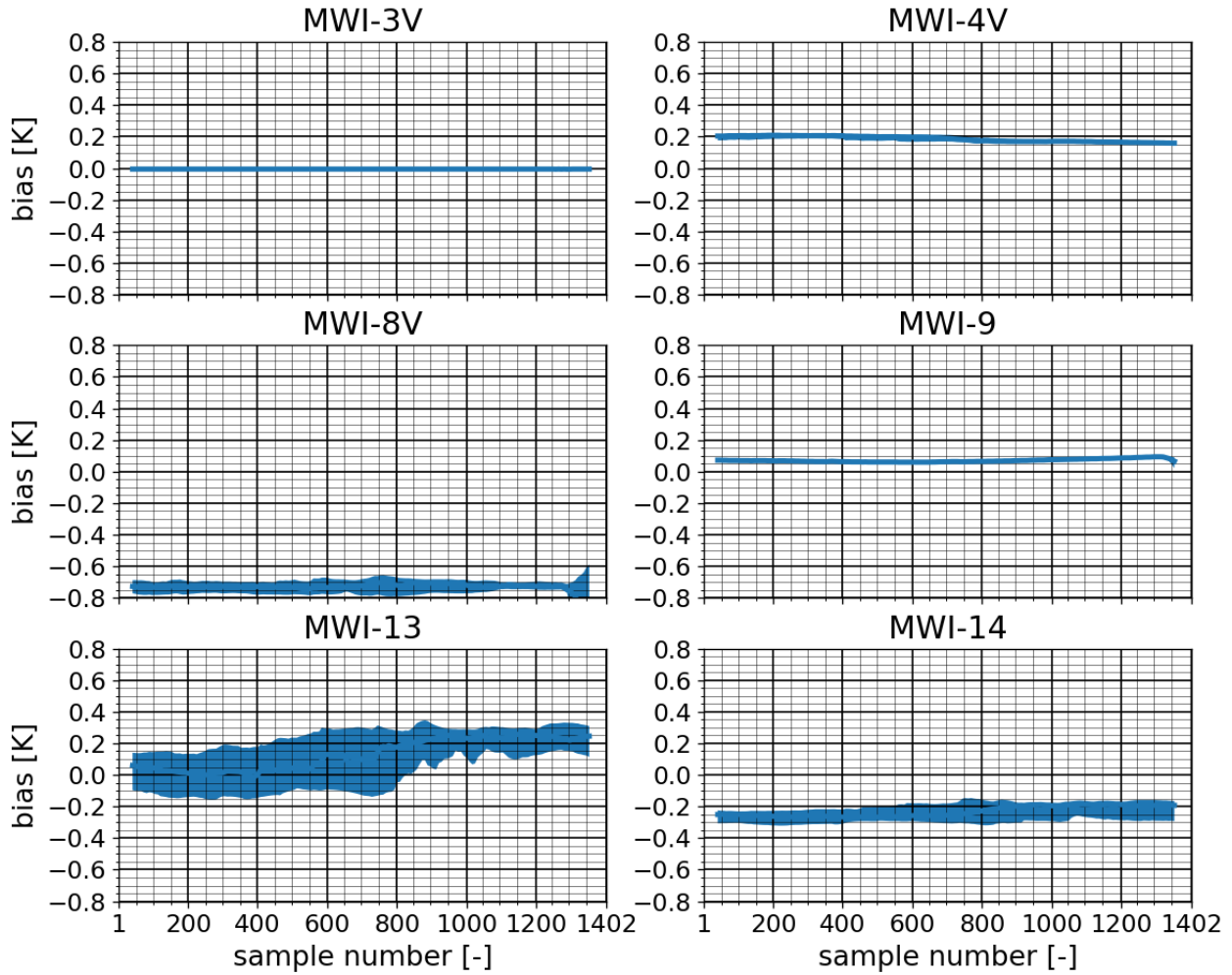
Figure 68: Bias between samples from MWI channels remapped onto MWI-3V FOV and the "true" antenna temperature as function of scan position for simulated observation over southern part of Atlantic Ocean (see Figure 63 to 64). The lower and upper bounds of the shaded area corresponds to the 16th to 84th percentile of the data points, respectively (corresponding to $\pm 1\sigma$).

	Backus-Gilbert footprint matching methodology applied on MWI and ICI observations	Code:	TR/BG/MWI-ICI
		Issue:	1.0
		Date:	June 5, 2019
		File:	optimal-interpolation-applied.tex
		Page:	157 / 200

Figure 69: As Figure 68 but showing data for a scene over Africa (see Figure 65 to 67).

Figure 70: As Figure 68 but showing data MWI channels remapped onto MWI-1V FOV. (see Figure 62).

Figure 71: As Figure 68 but showing data MWI channels remapped onto MWI-1V FOV and for a scene over Africa (see Figure 65).

	Backus-Gilbert footprint matching methodology applied on MWI and ICI observations	Code: TR/BG/MWI-ICI
		Issue: 1.0
		Date: June 5, 2019
		File: optimal-interpolation-applied.tex
		Page: 160 / 200

10.2.2 Impact of cloud on biases

Figure 72 and Figure 73 show comparisons between "true" and remapped samples for a cloudy scene (over the Atlantic Ocean) for MWI-2V and MWI-3V samples remapped onto MWI-1V FOVs. Figure 74 to Figure 78 show similar data, but for MWI-4V, MWI-8V, MWI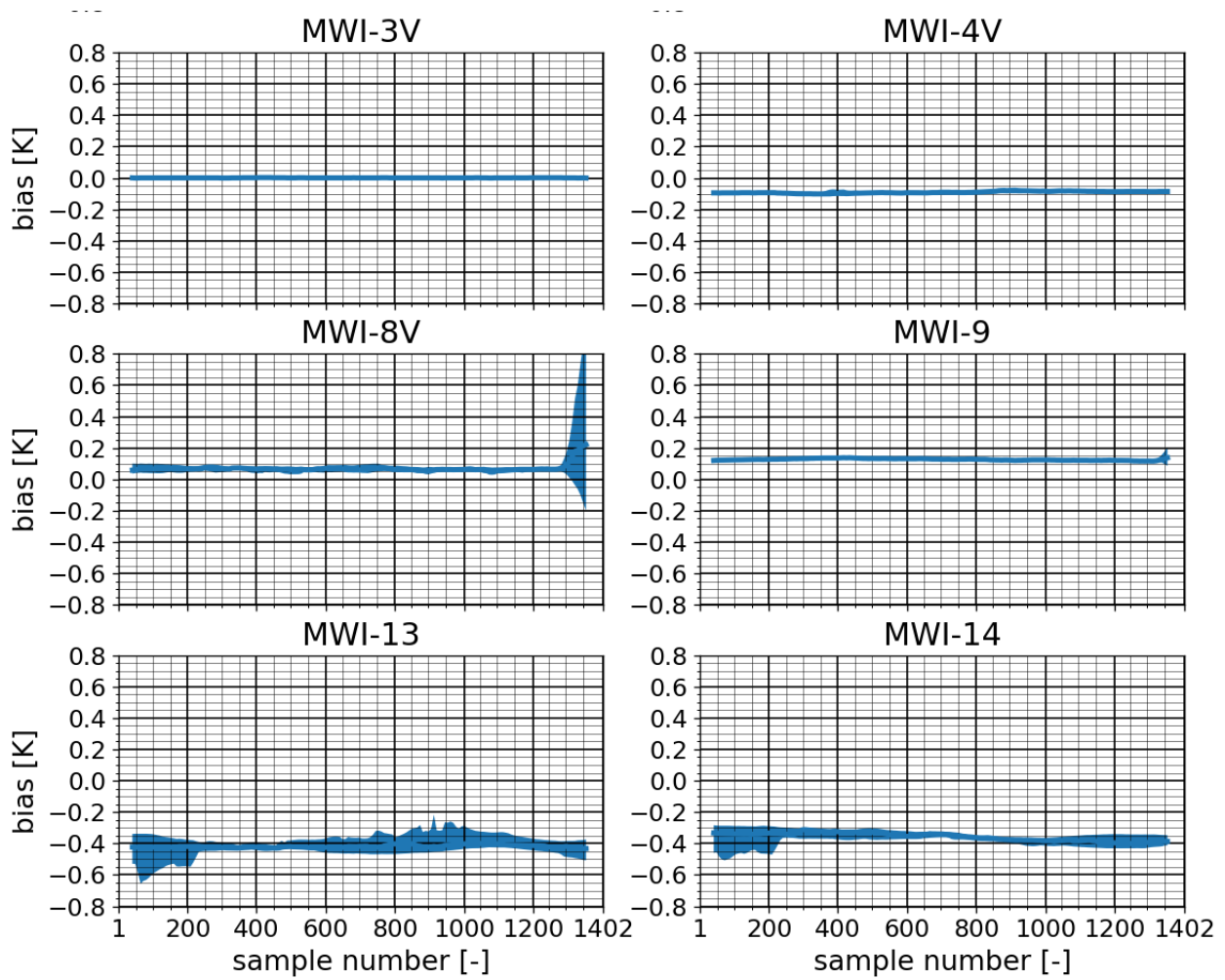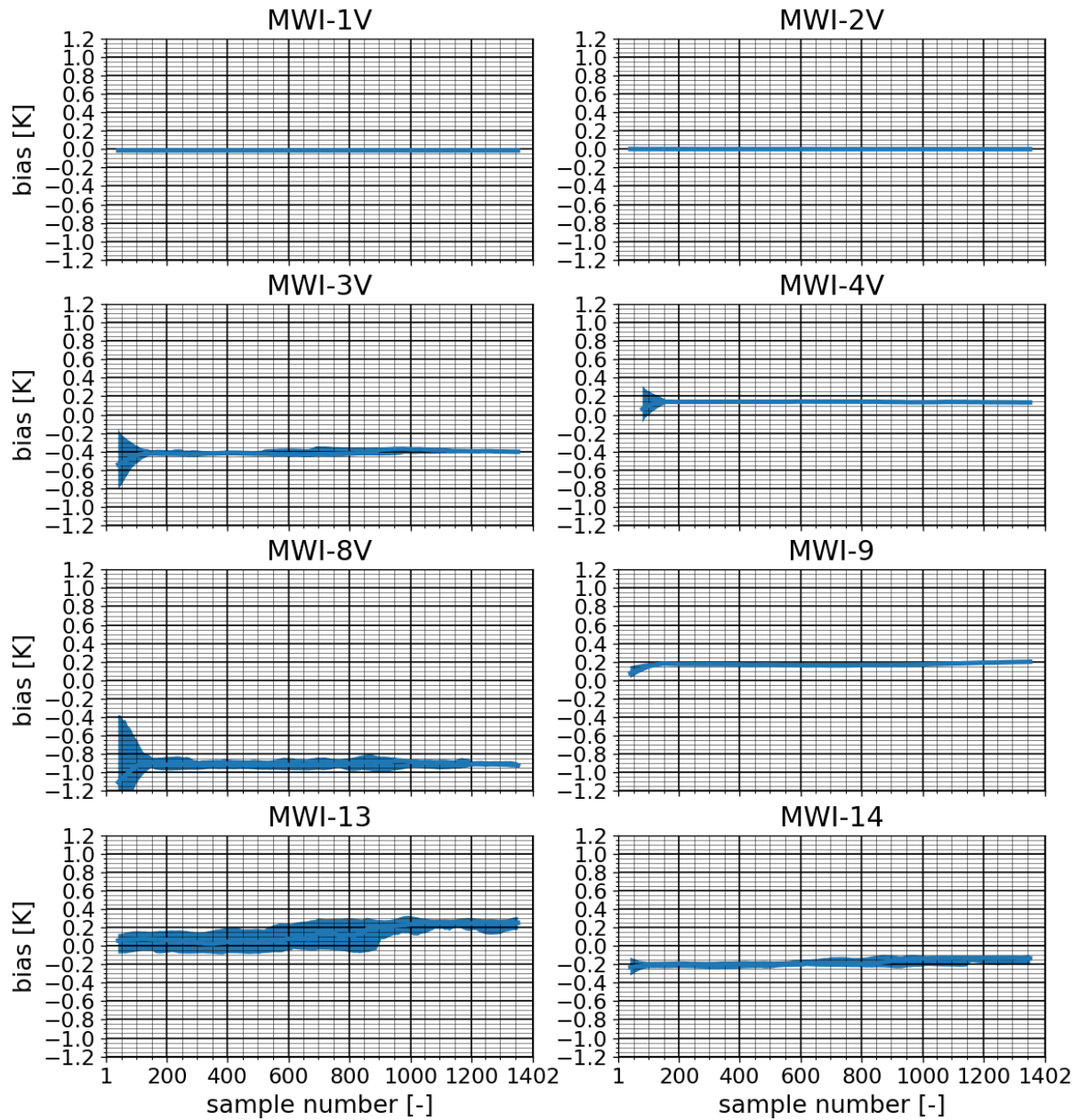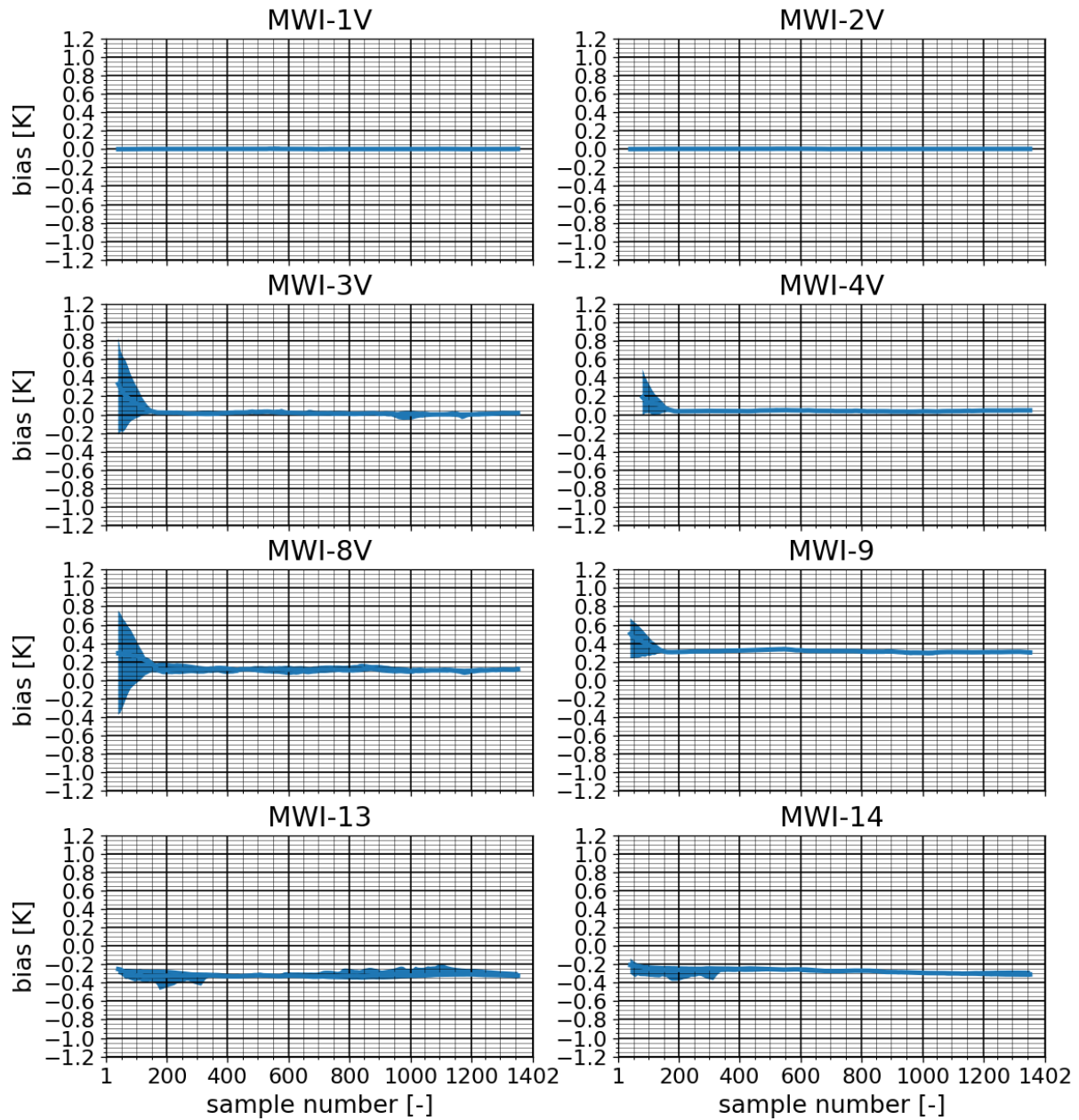-9, MWI-13, and MWI-14 samples remapped onto MWI-3V FOVs. The scene is fairly complex in terms of cloud coverage, and includes clouds containing both liquid and snow/ice particles, and liquid and ice water path data from the ERA5 dataset used in the simulation are shown in the figures. It can be seen that clouds, within the FOV can have a non negligible influence, on top of the cloud free bias, discussed in the previous section, and the impact varies between channels and phase of cloud.

The MWI channels have varying sensitivity to various types of clouds. For example, MWI-4V and MWI-14 is primarily sensitive to liquid and ice phase cloud, respectively, while MWI-13 is clearly sensitive to both. Liquid phase clouds, effectively, interacts with radiation through emission and absorption effects at MWI frequencies, while ice phase clouds, effectively, interacts through absorption and scattering effects. This difference gives that liquid and ice phase clouds have different impact on the "cloud free" bias, as described below.

Ocean surface emissivity is low, and "cloud free" atmospheric transmission is high, for MWI-2V, MWI-3V, MWI-4V and MWI-8V. This gives that thermal emission from liquid phase clouds will increase the radiant emission, compared to a cloud free scene over an ocean surface, and liquid phase clouds appear as hot objects in Figure 72 to Figure 75. On the same time, liquid phase clouds will decrease the atmospheric transmission, giving that the contribution from the surface emissivity/reflectivity decreases, and hence, decrease biases related to surface contribution. This effect can be seen to occur for MWI-4V samples remapped onto MWI-3V FOVs (see Figure 74). Samples of MWI-4V have a $\sim$0.28[°] greater incidence angle than that of the target and a $\sim$0.2[K] "cloud free" bias, but for samples effected by clouds the bias is closer to $\sim$0[K].

The impact of liquid clouds can also be to reduce a negative bias. The "cloud free" bias is negative for both MWI-3V samples remapped onto MWI-1V FOVs and MWI-8V samples remapped onto MWI-3V FOVs, and the impact of liquid phase clouds is to make these biases to become less negative. It can even be seen that for some MWI-8V samples the bias is positive, but this is not due to liquid phase cloud, but to ice phase cloud.

MWI-2 and MWI-9 are the channel with the closest match in incidence angle to their respective targets, and the cloud induced bias is in principle negligible small for those channels.

MWI-13 is probably the most complicated channel, in terms of of impact of cloud on "cloud free" bias. The observed antenna temperature will be governed by the total column water vapor, for "cloud free" condition. Now, the column water vapor can vary considerably. It can be seen from Figure 77, that at low and high latitude the antenna temperature is around $\sim$280[K] and $\sim$250[K] for cloud free samples. This is the case as column water vapor is greater at low latitudes for this scene. The impact of liquid phase clouds on the observation depends the temperature of the cloud relative to the background brightness temperature, and liquid phase clouds occur both as relative cold objects (in the upper part of Figure 77) and as warm objects (in the lower part of Figure 77). At low latitudes, the "cloud free" bias is $\sim$-0.15[K]. Here the impact of liquid phase clouds is to amplify this bias somewhat(MWI-13 has a $\sim$0.28[°] higher incidence angle than target). At high latitude the cloud free bias is governed by surface

emissivity/reflectivity effects and is around ($\sim0.25[K]$). Here, the impact of liquid phase clouds is to reduce the bias.

The impact of cloud ice on the "cloud free" bias is more straight forward, than that of liquid clouds. A negative bias, up to about $\sim$-1[K] are found for MWI-14 and MWI-13 and "observations" effected by high altitude cloud ice. Cloud ice primarily interact with radiation through scattering and absorption effects, and both these effects increases with incidence angle. The impact of cloud ice on bias is discussed in more details for ICI.

In summary, both liquid and ice phase clouds can have an impact, on top of the "cloud free" bias. The cloud induced bias is clearly state dependent, and the effect can be correlated/anti-correlated between channels. The impact of liquid phase clouds tend to decrease the bias related to surface emissivity / reflectivity variation with incidence angle, as the observation becomes less sensitive to the surface contribution. Greatest impact on bias for liquid phase cloud is found for MWI-8V. Additionally, cloud induced "bias" can be strong relative to the "cloud free" bias, and greatest impacts are found for MWI-13 and MWI-14 samples effected by cloud ice.

	Backus-Gilbert footprint matching methodology applied on MWI and ICI observations	Code: TR/BG/MWI-ICI
		Issue: 1.0
		Date: June 5, 2019
		File: optimal-interpolation-applied.tex
		Page: 162 / 200
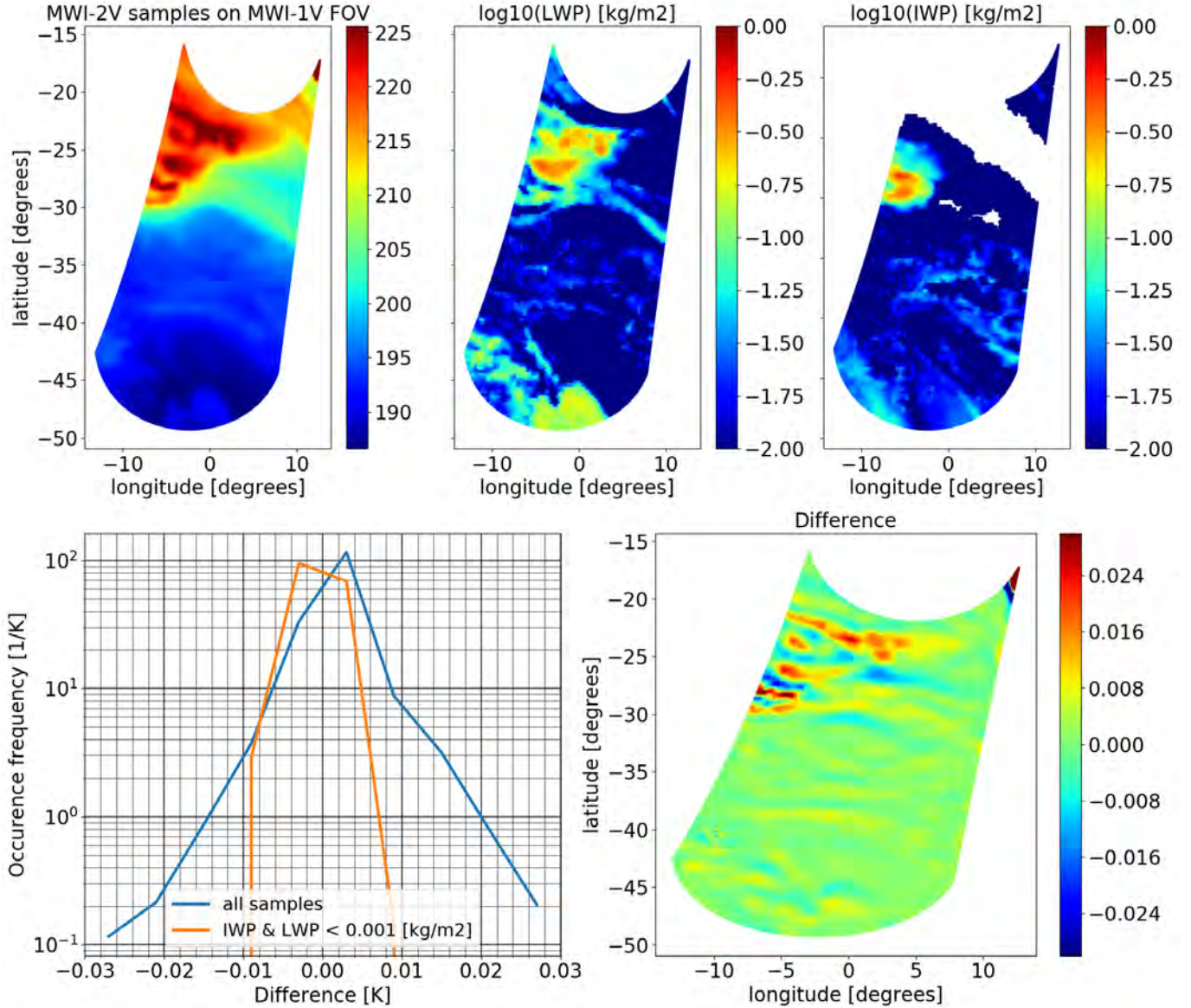
Figure 72: MWI-2V samples remapped to MWI-1V FOV for a cloudy scene. Upper left panel shows "true" antenna temperatures, and upper middle and right panel shows liquid and ice water path (ERA5 data) of the scene, respectively (the white feature in the IWP field indicates that the IWP is 0). The right bottom panel shows the difference (remapped - "true"), and the left bottom panel shows the frequency of occurrence of various differences. The unit associated to the colorbars is K.

	Backus-Gilbert footprint matching methodology applied on MWI and ICI observations	Code:	TR/BG/MWI-ICI
		Issue:	1.0
		Date:	June 5, 2019
		File:	optimal-interpolation-applied.tex
		Page:	163 / 200
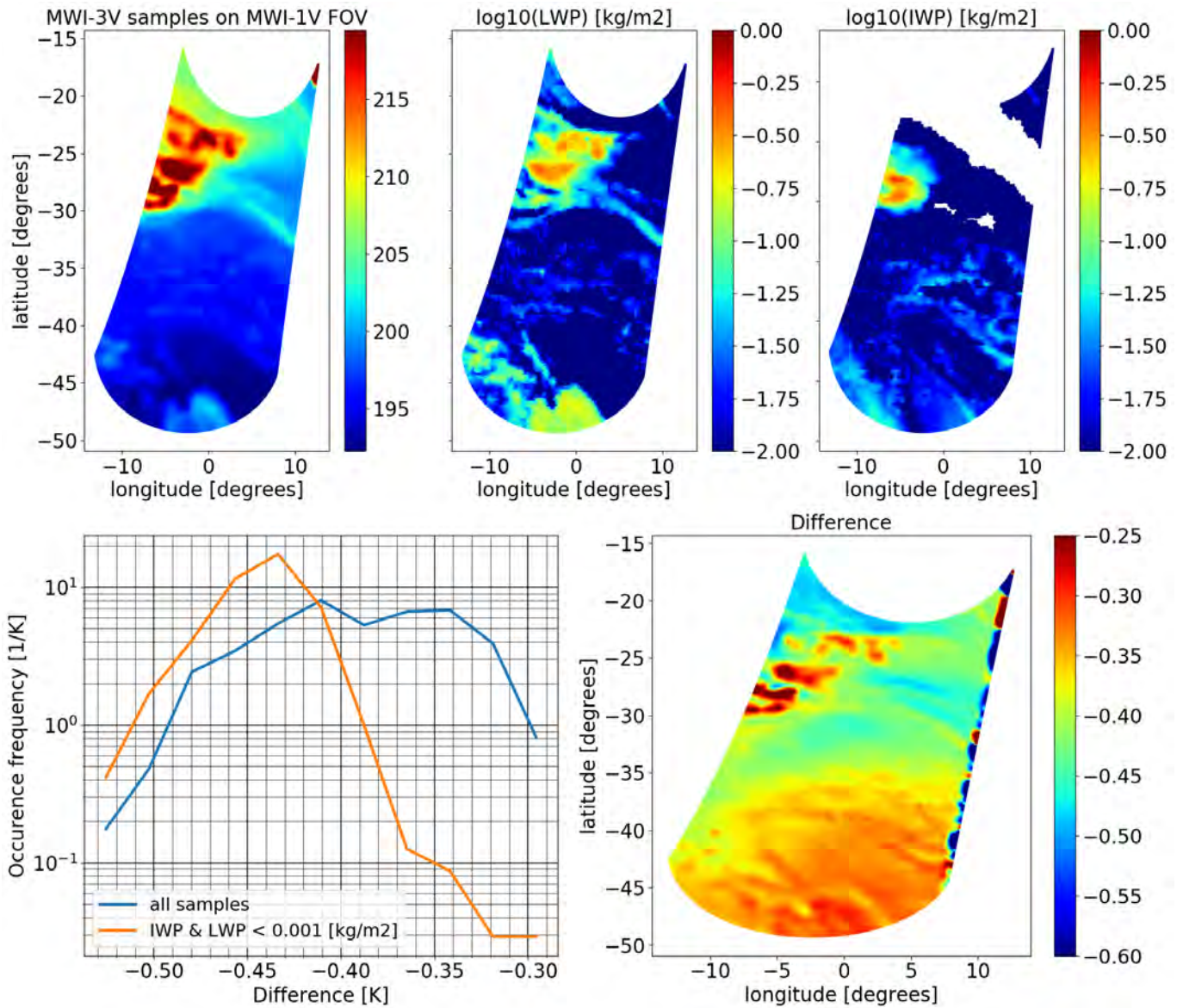
Figure 73: As Figure 72 but showing data for MWI-3V remapped onto MWI-1V FOV.

	Backus-Gilbert footprint matching methodology applied on MWI and ICI observations	Code:	TR/BG/MWI-ICI
		Issue:	1.0
		Date:	June 5, 2019
		File:	optimal-interpolation-applied.tex
		Page:	164 / 200
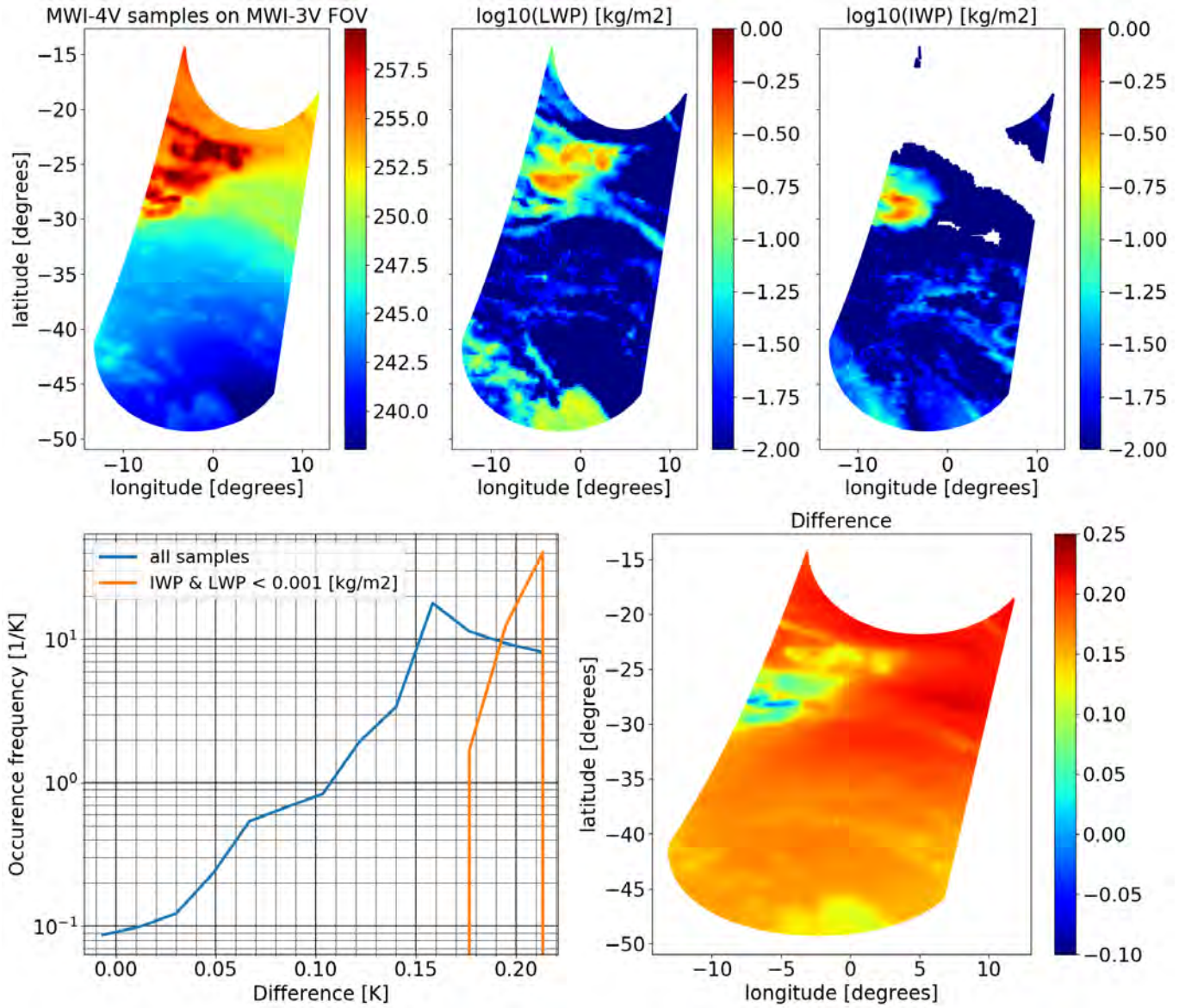
Figure 74: As Figure 72 but showing data for MWI-4V remapped onto MWI-3V FOV.

	Backus-Gilbert footprint matching methodology applied on MWI and ICI observations	Code:	TR/BG/MWI-ICI
		Issue:	1.0
		Date:	June 5, 2019
		File:	optimal-interpolation-applied.tex
		Page:	165 / 200
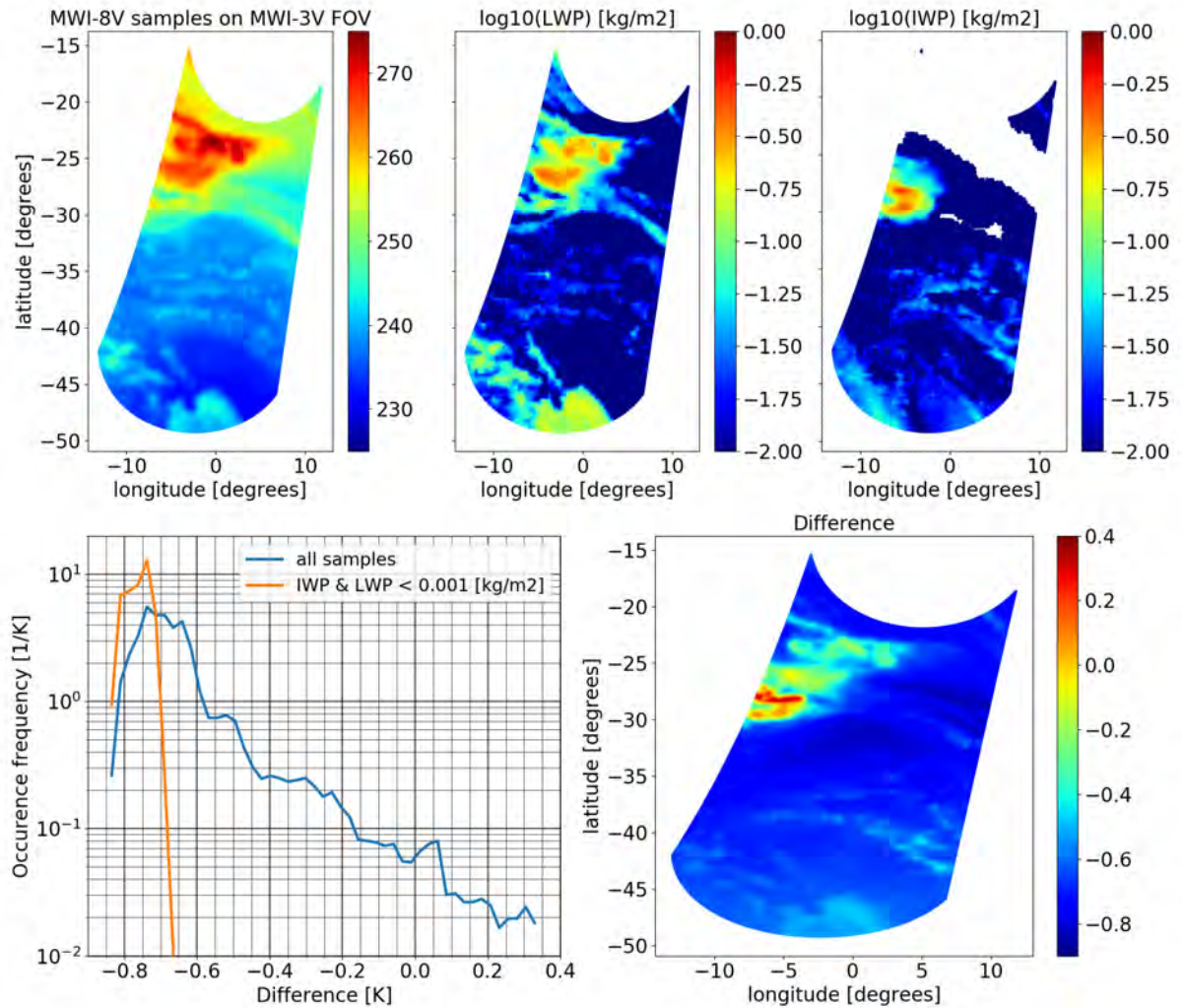
Figure 75: As Figure 72 but showing data for MWI-8V remapped onto MWI-3V FOV.

	Backus-Gilbert footprint matching methodology applied on MWI and ICI observations	Code:	TR/BG/MWI-ICI
		Issue:	1.0
		Date:	June 5, 2019
		File:	optimal-interpolation-applied.tex
		Page:	166 / 200
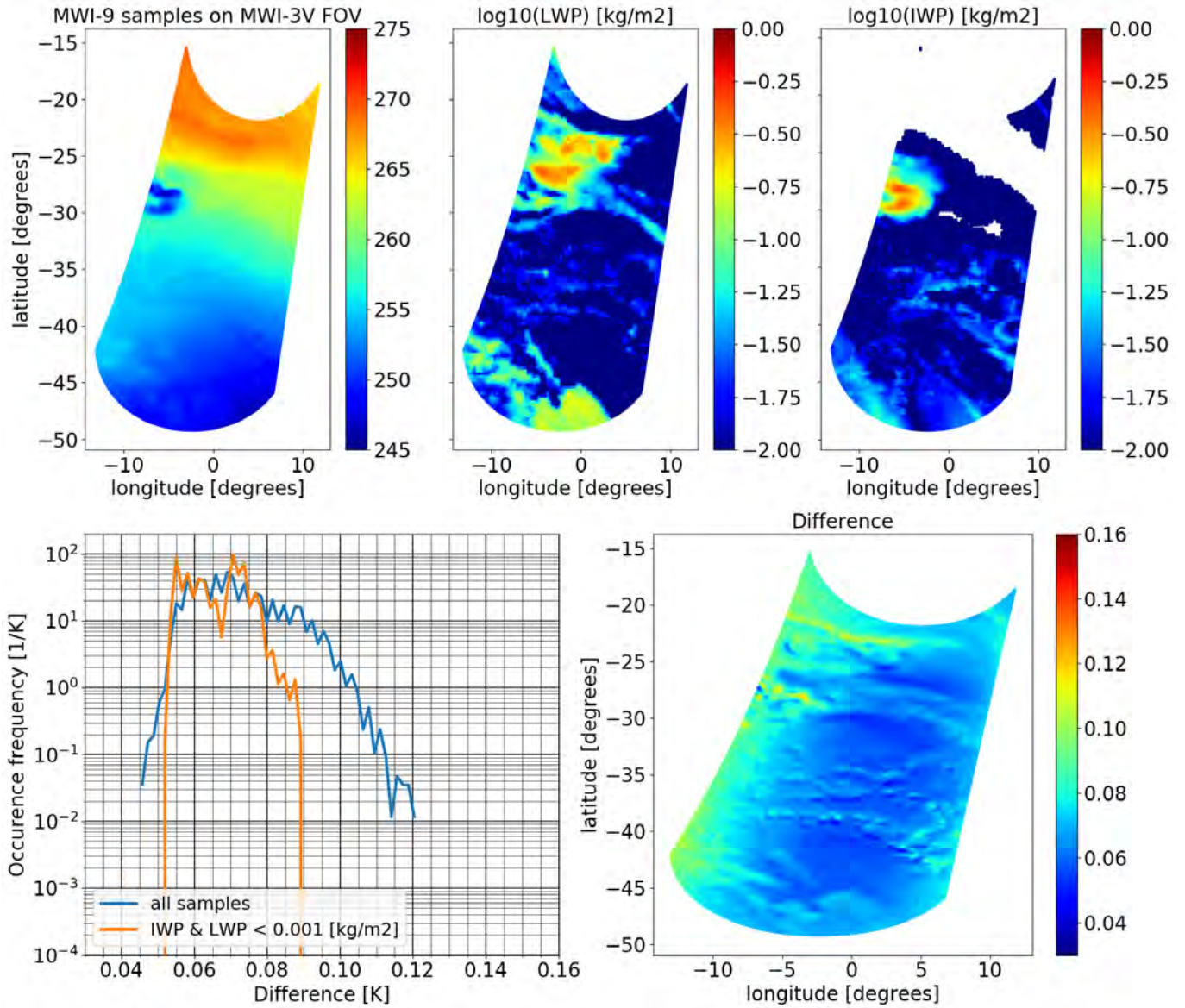
Figure 76: As Figure 72 but showing data for MWI-9 remapped onto MWI-3V FOV.

	Backus-Gilbert footprint matching methodology applied on MWI and ICI observations	Code: TR/BG/MWI-ICI
		Issue: 1.0
		Date: June 5, 2019
		File: optimal-interpolation-applied.tex
		Page: 167 / 200
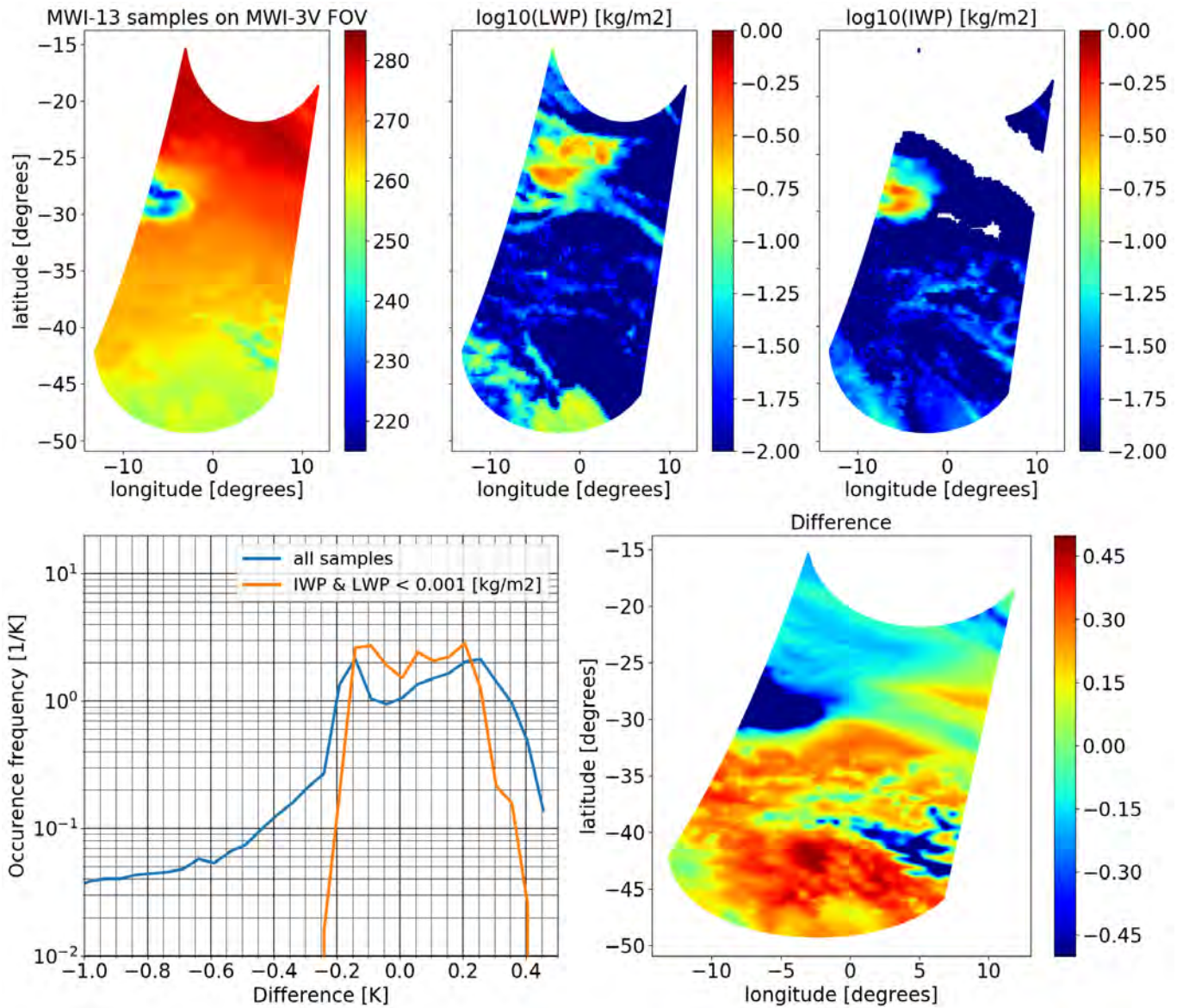
Figure 77: As Figure 72 but showing data for MWI-13 remapped onto MWI-3V FOV.

	Backus-Gilbert footprint matching methodology applied on MWI and ICI observations	Code:	TR/BG/MWI-ICI
		Issue:	1.0
		Date:	June 5, 2019
		File:	optimal-interpolation-applied.tex
		Page:	168 / 200

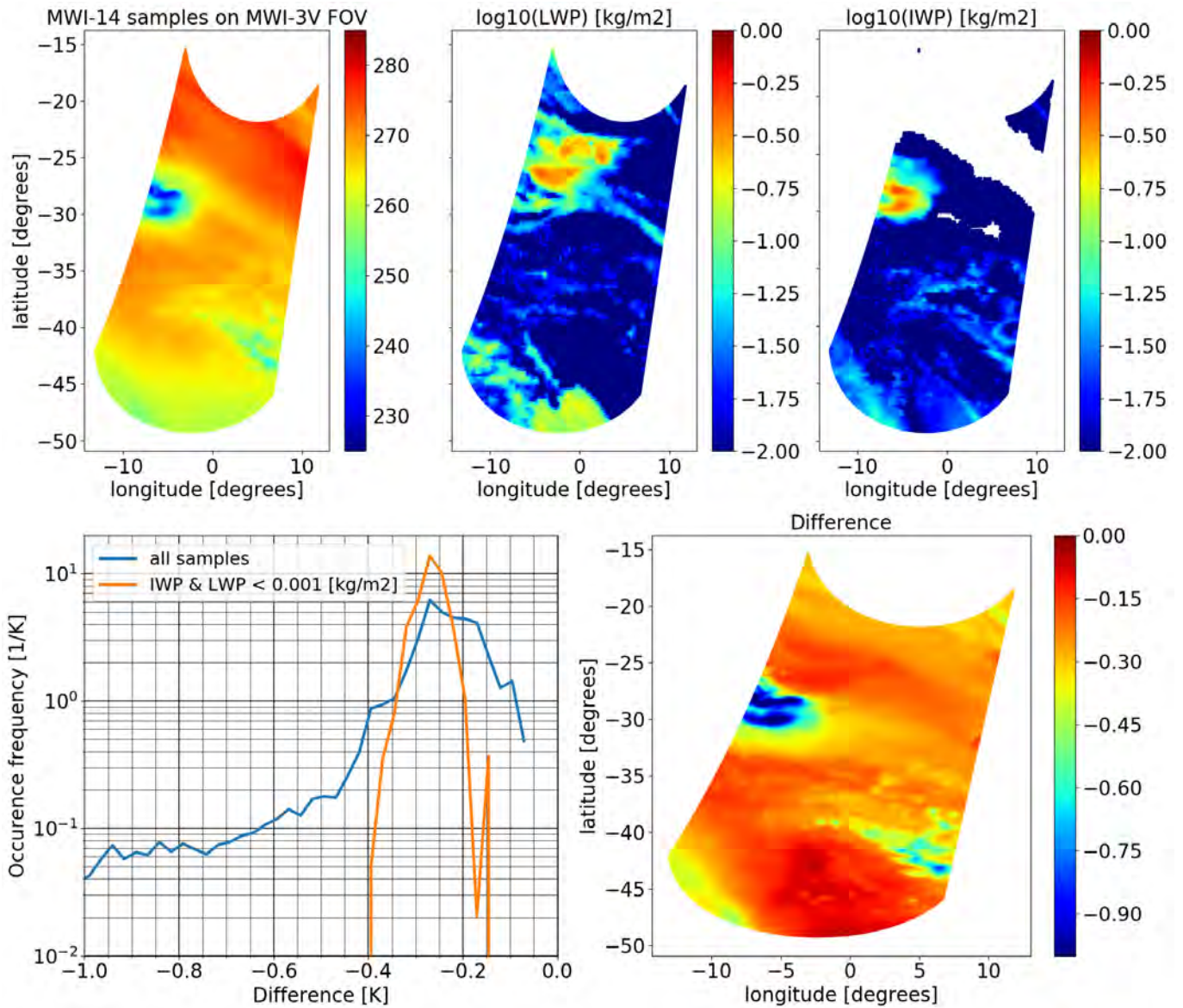Figure 78: As Figure 72 but showing data for MWI-14 remapped onto MWI-3V FOV.

	Backus-Gilbert footprint matching methodology applied on MWI and ICI observations	**Code:** TR/BG/MWI-ICI
MotHoW		**Issue:** 1.0
		Date: June 5, 2019
		File: optimal-interpolation-applied.tex
		Page: 169 / 200

10.2.3 Impact of BG convolution on L2 cloud retrieval

It has been shown that samples from MWI channels can be remapped onto MWI-3V FOVs for scan angles between about -66° to 65°. Outside this range, it is possible to remap data from some of the channels, but a possible retrieval will be limited to use a subset of MWI channels, and the retrieval performance should therefore be degraded. The effective noise of the remapped observations, within the -66° to 65° range, is well below the required Level1B noise levels for the MWI-3 to MWI-18 channels. The performance of the remapping of samples from MWI-1 and MWI-2 channels onto the MWI-3V FOVs is limited. The remapping results in clear fit-errors, even within the main beam, and primarily only the resolution in the across-track direction was possible to enhance, while at the same time keeping the effective noise at an acceptable level. On top of this, the remapping here results in that relatively large sidelobes are introduced. The usefulness of these remapped observations, for Level2 processing, can therefore be questionable. An alternative approach can be to remap MWI-1 and MWI-2 samples onto a modified MWI-3V FOV, using the effective MWI-1V antenna pattern as target (i.e. not aiming for increasing the resolution). The exact impact on the L2 cloud retrieval has not been studied, but generally, the impact should be negligible for a homogeneous scene, and mainly impact scenes with variations within the FOV, in whatever way the MWI-1 and MWI2 channels are used.

A bias-free convolution has been demonstrated as long as the remapping does not involve a change in incidence angle (i.e. when the incidence angle of the samples to be remapped agree to that of the target channel). However, several MWI channels have an incidence angle that do not exactly match that of the target (the variation in incidence angle is around 1.2° among the MWI channels), and hence, non-negligible biases, even for cloud free conditions, were found for some of the channels. The reason for this is due to the fact that both surface emissivity / reflectivity and atmospheric transmission varies with incidence angle (and with surface type and atmospheric condition), and this is not taken into account by the Backus-Gilbert footprint resampling methodology.

The cloud free bias were found to be state dependent, but no significant inter-FOV biases (or scan position dependent biases) were found for any channel within the MWI-3V scan angle range of -66° to 65°.

Clouds within the FOV can have a non negligible influence, on top of the cloud free bias, and the impact varies between channels and phase of cloud. The impact of liquid phase clouds tend to decrease the bias related to surface emissivity / reflectivity variation with incidence angle, as the observation becomes less sensitive to the surface contribution. The impact of cloud ice tends to be to increase the bias. Cloud ice will have an impact both through a "pure" incidence angle difference effect that applies to a homogeneous cloud layer, but also at the edges of areas with hydrometeors where even higher errors were found. This is also related to differences in viewing angles, and due to the fact that slightly different parts of the atmosphere may be observed by the the target channel and the samples convolved to the target FOV. This gives primarily that samples around cloud system edges may be biased (low or high).

Biases described above should be taken into account of in Level2 processing. The bias related to the pure incidence angle difference effect, that applies to a homogeneous state, should be possible to take into account of by applying the original incidence angle for each channel in the retrieval calculation. This should effectively remove most of this bias.

The "cloud free" bias, and its variation with state, should be the important component of

	Backus-Gilbert footprint matching methodology applied on MWI and ICI observations	**Code:** TR/BG/MWI-ICI
		Issue: 1.0
		Date: June 5, 2019
		File: optimal-interpolation-applied.tex
		Page: 170 / 200

the bias, for cloud detection, as it should be fairly uncomplicated to detect clouds with high LWP, even though samples may be biased. The bias varies only slightly with state, for channels having only a small incidence angle difference to MWI-3V, and the variation is smaller than $NE\Delta T$. This gives that as long as the "cloud free" bias can be taken into account of, the impact of BG convolution on cloud detection should be low.

The biases related to the fact that slightly different parts of the atmosphere are observed by the various channels and for a given FOV is a bit more challenging to take into account. This is particularly true for a 1DVar retrieval, as this bias is related to the 3-dimensional variability of the atmosphere. Potentially, this can even result in that a 1DVar retrieval can have difficulties in finding a solution, for observations around a cloud system edge. A possible solution for this is that remapped samples from channels having a different effective incidence angle than that of MWI-3V are given an additional noise term, arising from the fact that these are sensitive to a slightly different part of the atmosphere than MWI-3V, and the retrieval is assumed to be valid for the FOV of MWI-3V.

Table 15: ICI remapping bias for clear sky condition over ocean and land surface. Note that the bias is state dependent and applies to the data described in this section, and it is described by the 16th and 84th percentile. Incidence angle is varying with sensor altitude and is given for a height of 822.14[km].

Channel	Frequency [GHz]	Incidence angle [degrees]	Bias (ocean) [K]	Bias (land) [K]
ICI-3	183.31 ± 2.0	53.7453	[-0.001, 0.001]	[-0.001, 0.001]
ICI-4V	243.2 ± 2.5	51.7720	[-0.13, 0.40]	[0.32, 0.54]
ICI-4H	243.2 ± 2.5	51.7427	[-0.08, 0.40]	[0.34, 0.54]
ICI-5	325.15 ± 9.5	53.8021	[-0.02, -0.01]	[-0.02, 0.01]
ICI-10	448.0 ± 1.4	53.8006	[-0.02, -0.01]	[-0.03, -0.02]
ICI-11V	664.0 ± 4.2	51.7166	[0.36, 0.50]	[0.46, 0.60]
ICI-11H	664.0 ± 4.2	51.5542	[0.39, 0.53]	[0.48, 0.63]

10.3 ICI

10.3.1 Cloud free condition

In this section we repeat the bias analysis presented in Sect. 10.2.1, but for ICI samples convolved onto ICI-1 FOV. ICI samples were remapped onto the FOV of ICI-1 for sample positions $1, 4, ..., 784$ using weighting coefficients with characteristic described in Sect.9.3. The "true" FOV value, for each channel and FOV, was simulated using the ICI-1 target antenna pattern and viewing angle.

Figure 79 to Figure 82 display comparison between the remapped and the "true" FOV antenna temperatures for a scene over ocean and land, respectively, both having a relatively low cloud coverage, and Figure 83 and 84 show statistics of difference as function of scan position. Small biases (less than 0.02[K]), more or less constant for all positions within the scan, are found for the remapping from ICI-3, ICI-5, and ICI-10 onto ICI-1 FOV. Thus, inter-channel and inter-FOV biases between remapped samples from these channels are more or less negligible small.

Larger biases (up to 0.6[K]) are found for the ICI-4V, ICI-4H, ICI-11H, and ICI-11V remapping onto ICI-1 FOV. This difference, compared to the other channels, can be explained by the fact that the viewing angles (and consequently incidence angles) differs between the various channels, due to the instrument configuration of ICI, and these angles are displayed in Table 15. Samples from the dual polarized ICI-4 and ICI-11 channels have a $\sim 2[°]$ difference in incidence angle compared to that of the target, while the remaining ICI channels have only a $\sim 0.05[°]$ difference to the target.

Figure 80 and 82 show that biases for the ICI-4 and ICI-11 channels are not constant. The brightness temperature of a cloud free scene is strongly related to to water vapor for ICI-4 and ICI-11. Both ICI-4 and ICI-11 are "window" channels, but the atmospheric transmission is higher for ICI-4, and ICI-11 is only sensitive to the upper part of the troposphere. This gives that cloud free biases between ICI-4V and ICI-4H is more or less perfectly correlated, as well as biases between ICI-11V and ICI-11H. However, biases between ICI-4 and ICI-11 are seen to be not so correlated. It can further be noted that the bias varies significantly with latitude (from

0.4 to -0.2[K]) for ICI-4V and for the ocean scene (Figure 80). Figure 85 shows derivative of brightness temperature (Tb) as function of viewing angle from nadir for different type of clear sky atmospheres at a frequency around 246[GHz]. It can be noted that different atmospheres gives different results, and thus an atmosphere dependent bias is expected between remapped and "true" values. For a tropical atmosphere, and around 45[°], the Tb change is 0.25[K/°] and about 0.4[K] for a 1.5[°] change, and for a southern Atlantic Ocean winter atmosphere this value is -0.75[K].

The state dependency of the bias makes it non-trivial to assess inter-FOV biases for ICI-4 and ICI-11. However, for ICI-4H and ICI-11H and for the most easterly part of swath (see Figure 80 and 82) a clear bias is seen, but this corresponds to sample numbers above 750 where the remapping was shown to generate in inaccurate results for these channels (see Sect. 9.3). Figure 83 shows the bias variability with scan position for the ocean scene, and for the ICI-4 channels the 84th percentile is about 0.05[K] greater for the greatest sample numbers compared to the lowest, but for the land scene (Figure 84) the situation is reversed. A similar feature can be seen for the ICI-11 channels. The conclusion is therefore that these biases are more likely to be due to state variability, than to a systematic bias introduced by the BG application, and for a hypothetical scene with no state variability no significant scan dependent biases are expected to be found for the ICI-4 and ICI-11 channels (and for all other ICI channels) within the ICI-1 scan angle range of 59° to -59°, where the remapping is anticipated to work well (see Sect. 9.3).
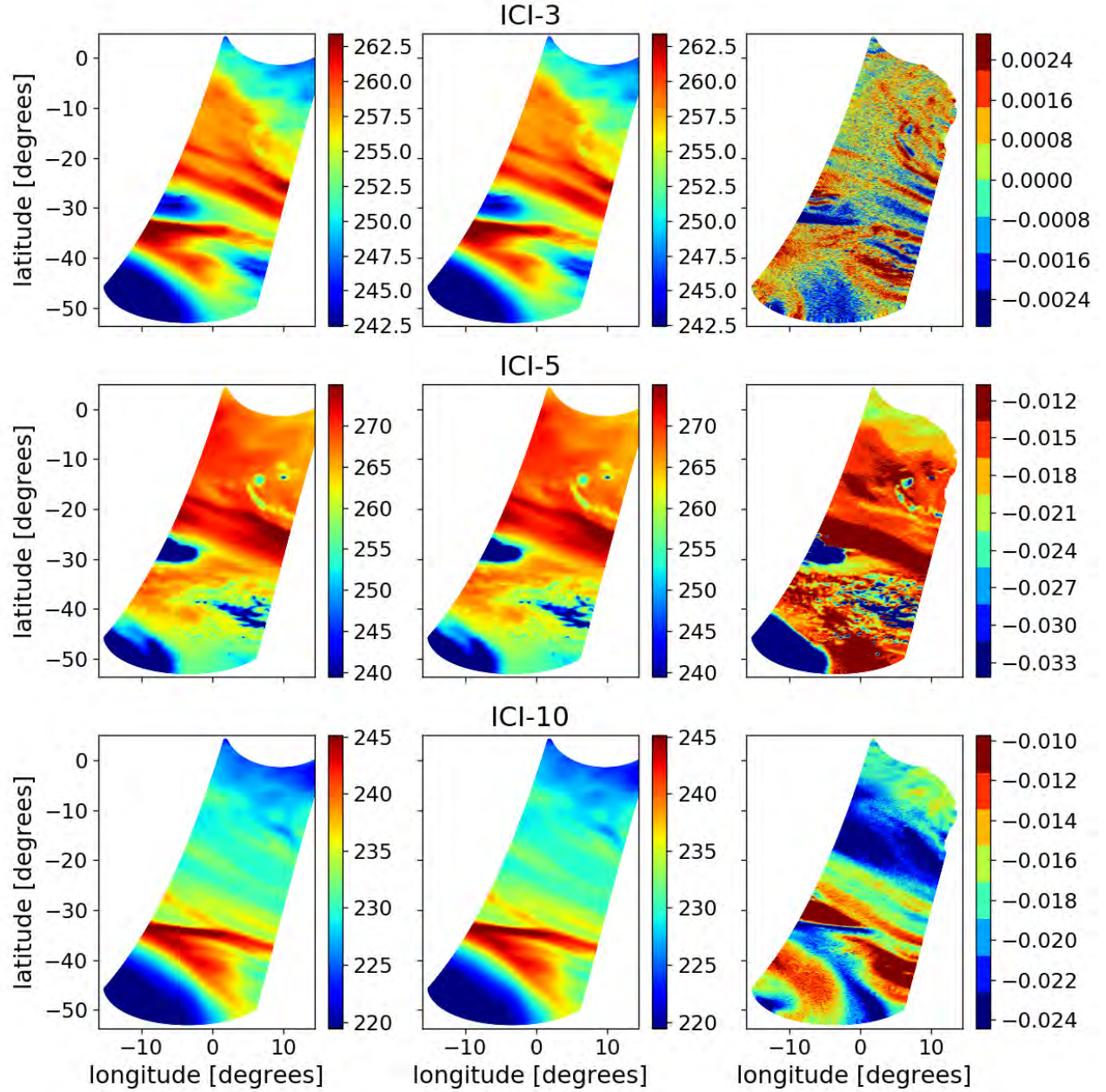
Figure 79: Bias between samples from ICI-3, ICI-5, and ICI-11 remapped onto ICI-1 FOV and the "true" antenna temperature, based on simulation of a section of Metop-A orbit 4655 (2007-09-12) over southern part of Atlantic Ocean. Left and middle column show "true" and remapped antenna temperature (described in text), respectively, and the right column shows the difference (remapped - "true"). The unit associated to the colorbars is K.

	Backus-Gilbert footprint matching methodology applied on MWI and ICI observations	Code: TR/BG/MWI-ICI
		Issue: 1.0
		Date: June 5, 2019
		File: optimal-interpolation-applied.tex
		Page: 174 / 200
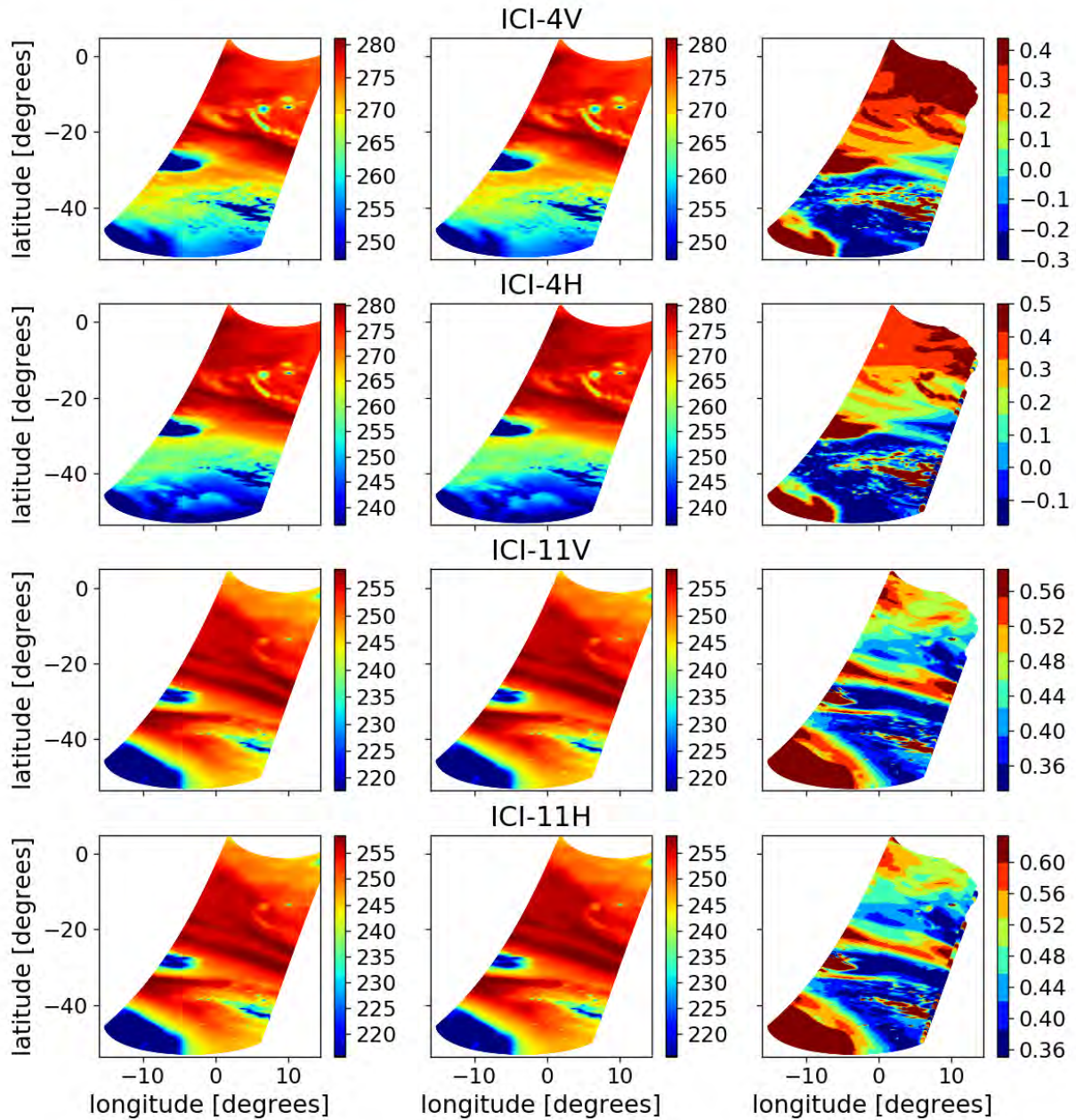
Figure 80: As Figure 79 but showing data for ICI-4 and ICI-11.

	Backus-Gilbert footprint matching methodology applied on MWI and ICI observations	Code:	TR/BG/MWI-ICI
		Issue:	1.0
		Date:	June 5, 2019
		File:	optimal-interpolation-applied.tex
		Page:	175 / 200
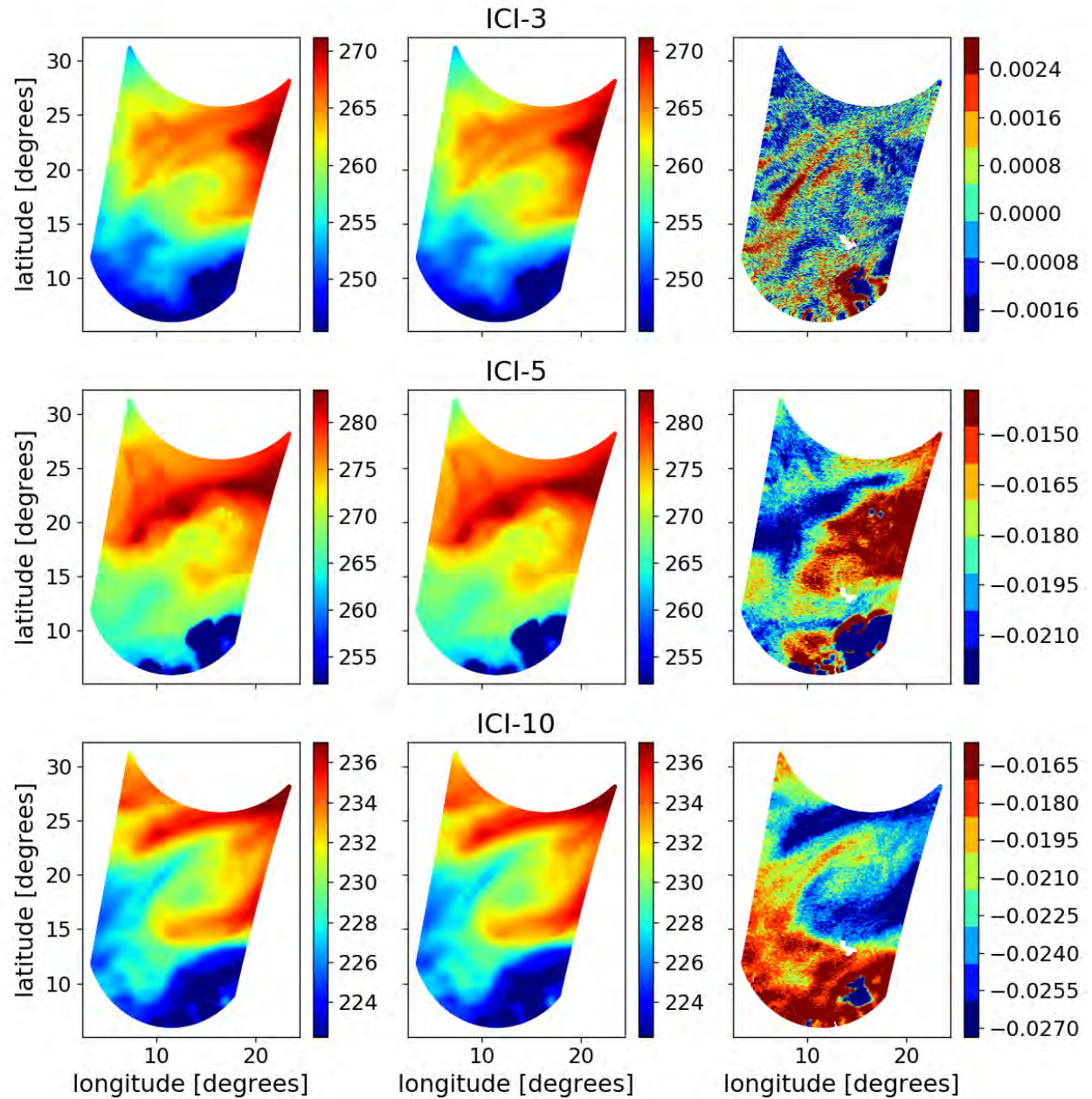
Figure 81: As Figure 79 but showing data for a scene over Africa.
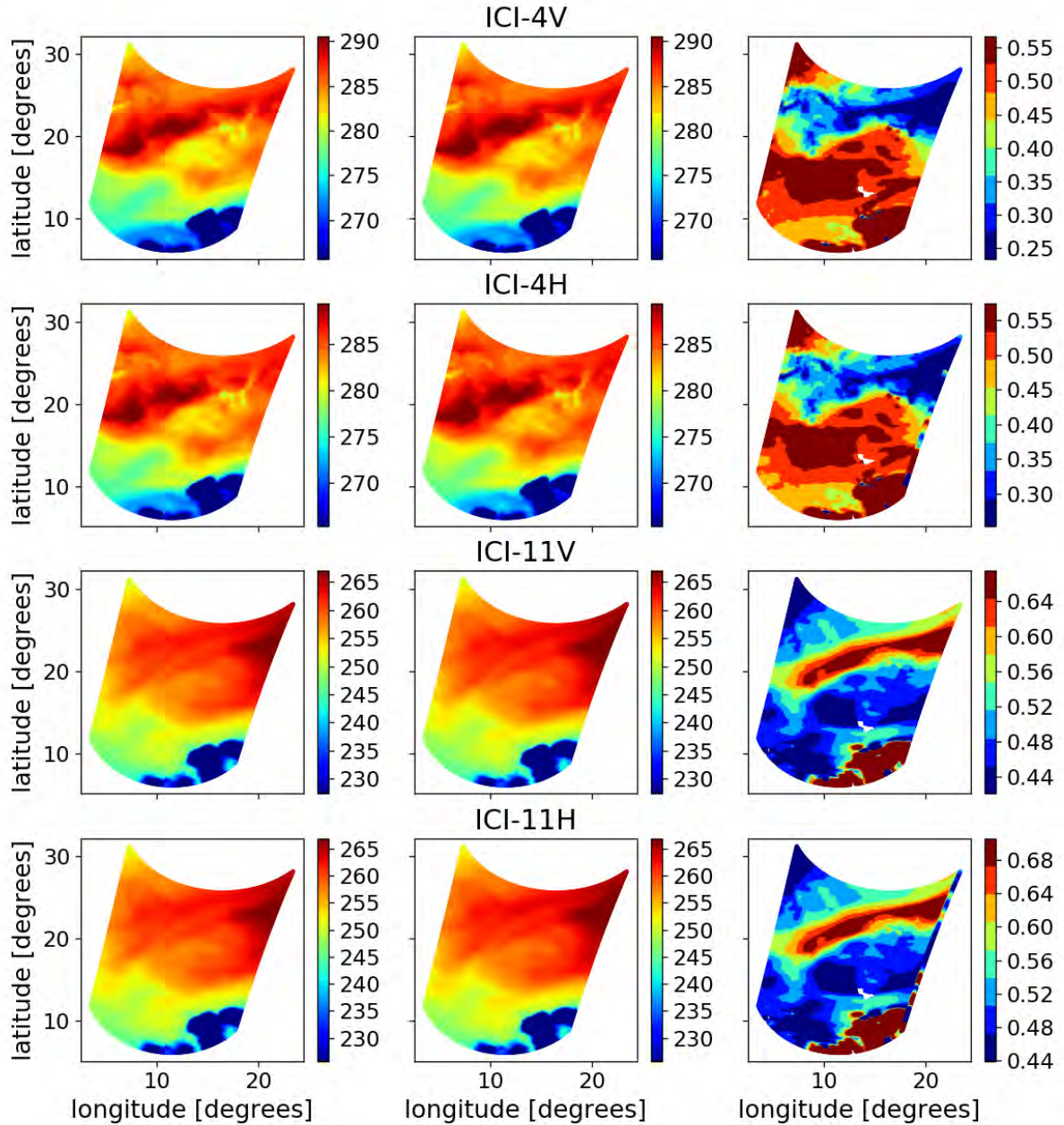
Figure 82: As Figure 79 but showing data for a scene over Africa for ICI-4 and ICI-11.
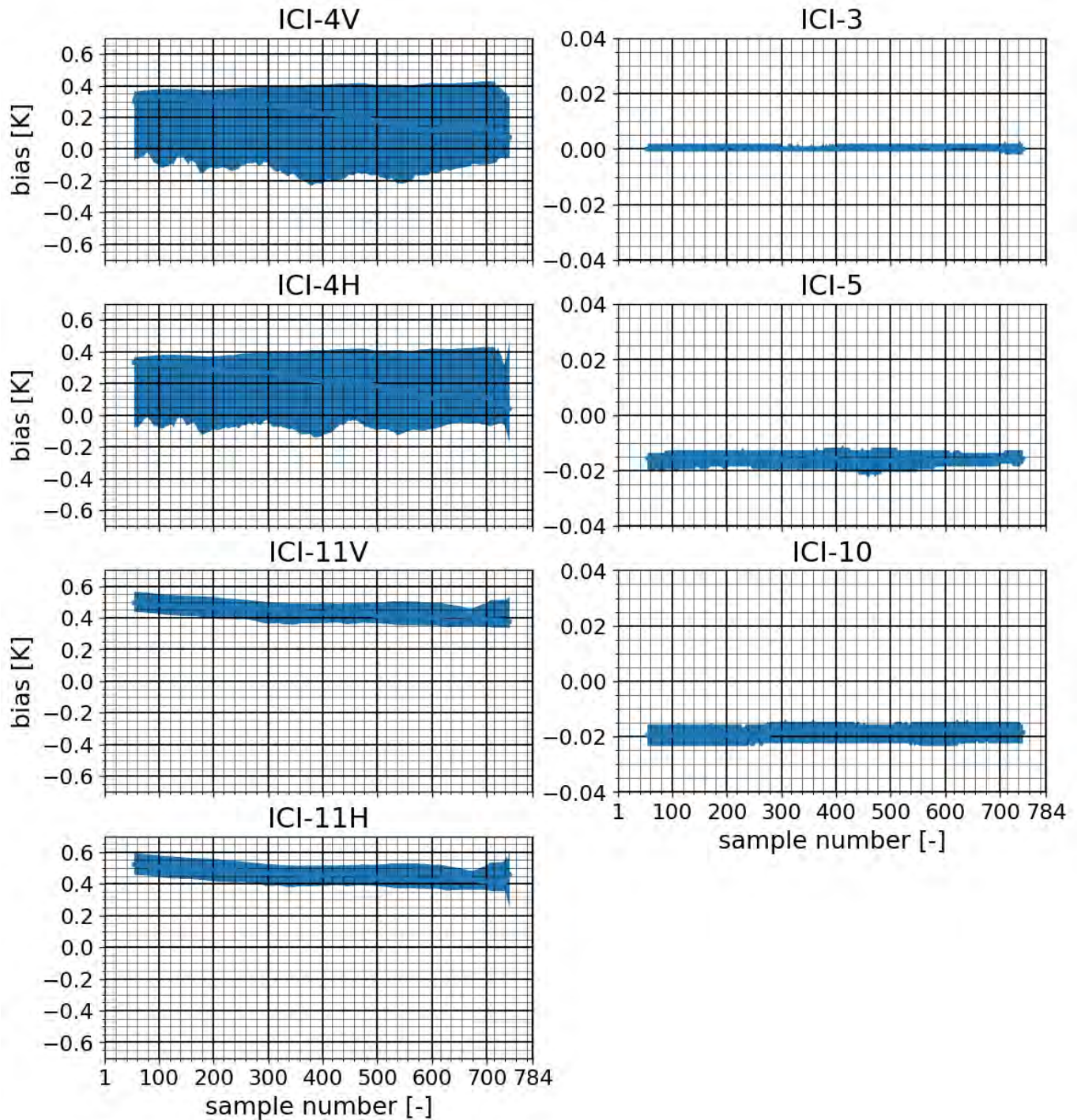
Figure 83: Bias between samples from ICI channels remapped onto ICI-1 FOV and the "true" antenna temperature as function of scan position for simulated observation over southern part of Atlantic Ocean (see Figure 79 and 80). The lower and upper bounds of the shaded area corresponds to the 16th to 84th percentile of the data points, respectively (corresponding to ±1σ).

	Backus-Gilbert footprint matching methodology applied on MWI and ICI observations	Code:	TR/BG/MWI-ICI
		Issue:	1.0
		Date:	June 5, 2019
		File:	optimal-interpolation-applied.tex
		Page:	178 / 200
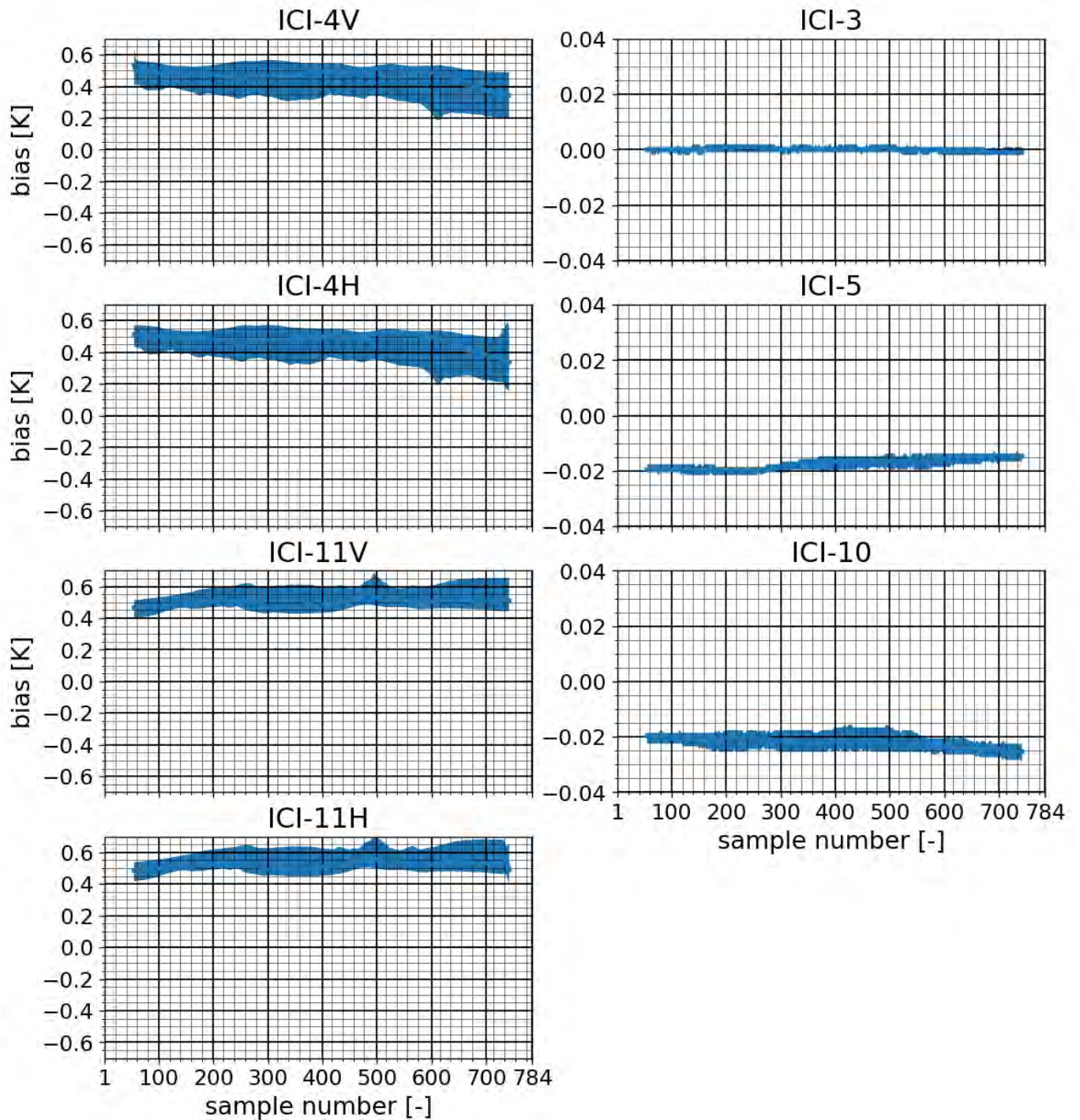
Figure 84: As Figure 83 but showing data for a scene over Africa (see Figure 81 and 81).

Figure 85: Derivative of brightness temperature as function of viewing angle from nadir for different type of clear sky atmospheres and for a frequency of 246[GHz] (tro=tropical, mls=mid-latitude summer, mlw=mid-latitude winter, sas=Southern Atlantic Ocean Summer, saw=Southern Atlantic Ocean winter). The dashed line lies close to viewing angle from nadir of ICI.

	Backus-Gilbert footprint matching methodology applied on MWI and ICI observations	Code:	TR/BG/MWI-ICI
		Issue:	1.0
		Date:	June 5, 2019
		File:	optimal-interpolation-applied.tex
		Page:	180 / 200

10.3.2 Impact of cloud on biases

Figure 86 to Figure 89 show comparisons between "true" and remapped samples for a cloudy scene (high altitude cloud ice over Africa and Atlantic ocean) for ICI-3, ICI-4V, ICI-5, and ICI-11V. First and foremost, it can be noted that cloud ice can have a strong imp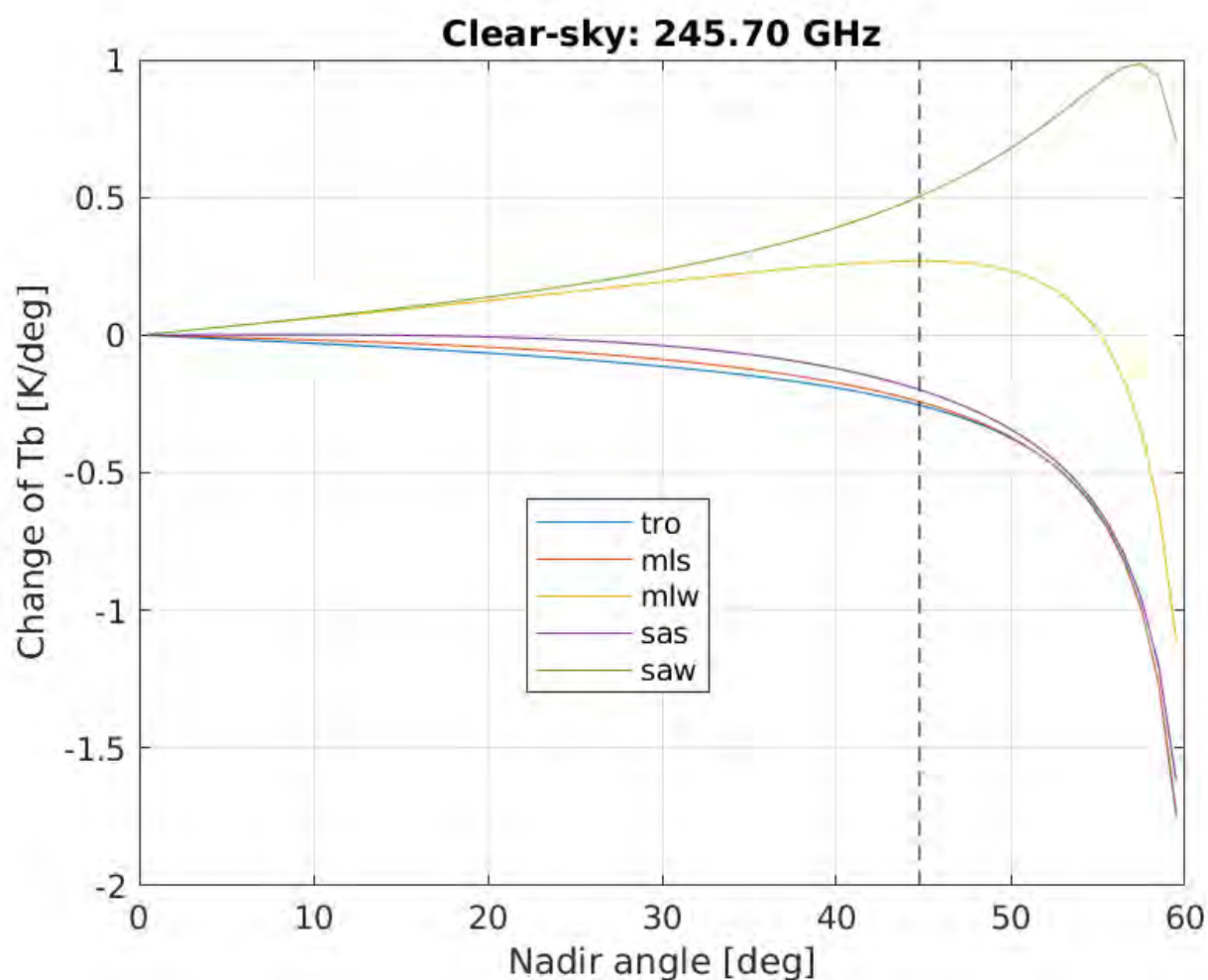act on the "observed" antenna temperature. For example, the antenna temperature is above 270[K] for the cloud free part and around 140[K] around the center of one of the cloud system for ICI-4V. Furthermore, it can clearly be seen that clouds can introduce a bias that is different from that for cloud free condition, and biases of samples that are influenced by clouds can be several times greater than clear sky biases, and biases can also be seen to vary between the various channels.

The target footprint on ground is not perfectly matched, as the matching is a compromise between noise and fit error. It can be noted that even ICI-3 is slightly biased (although negligible small) around cloud system edges, and this should be due to this "smoothing" error.

Biases for ICI-4V and ICI-11V are much greater than for ICI-3 and ICI-5 and that is due to the difference in incidence angle match to the target channel that was discussed in the previous section.

The cloud induced biases are partly explained by Figure 90, that shows the derivative of Tb as function of angle from nadir for cloudy (ice) conditions at ICI-4 frequencies. The figure indicate that we can expect a bias from roughly 0.5 up to 2.5[K] due to the 1.5[°] difference in nadir viewing angle, even for a completely homogeneous cloud layer.

However, Figure 87 shows that the bias is greater than this, and varies between about -0.2 to 4[K], and clear features, correlated to cloud features in antenna temperature fields are seen. Observations north and south of the cloud systems tends to biased low and high, respectively. This can also be explained by the incidence angle difference through a slight mismatch in what part of the atmosphere a remapped and "true" observation is sensitive to.

A remapped observation (from samples having a greater incidence angle than that of the target) can possibly "detect" a cloud slightly before the "true" observation, and this will result in a cold bias (remapped - "true") when the "observations are approaching" a cloudy scene. The situation than becomes reversed when "leaving" the cloudy scene, and the bias will than be high. The antenna pattern projected on e.g. a 12[km] altitude is shifted horizontally by about 1[km], given that the FOV is matched (on the surface) and there is a 2[°] difference in incidence angle. It can further be noted that this bias is correlated between ICI-4V and ICI-11V, and anti-correlated to that of ICI-5.

The conclusion from here is that clouds can have a big impact on biases (as derived from cloud free observations) of samples convolved to the target FOV, if the incidence angle is not close to that of the target. The cloud induced bias is heavily state dependent and give rise to systematic biases around cloud systems.
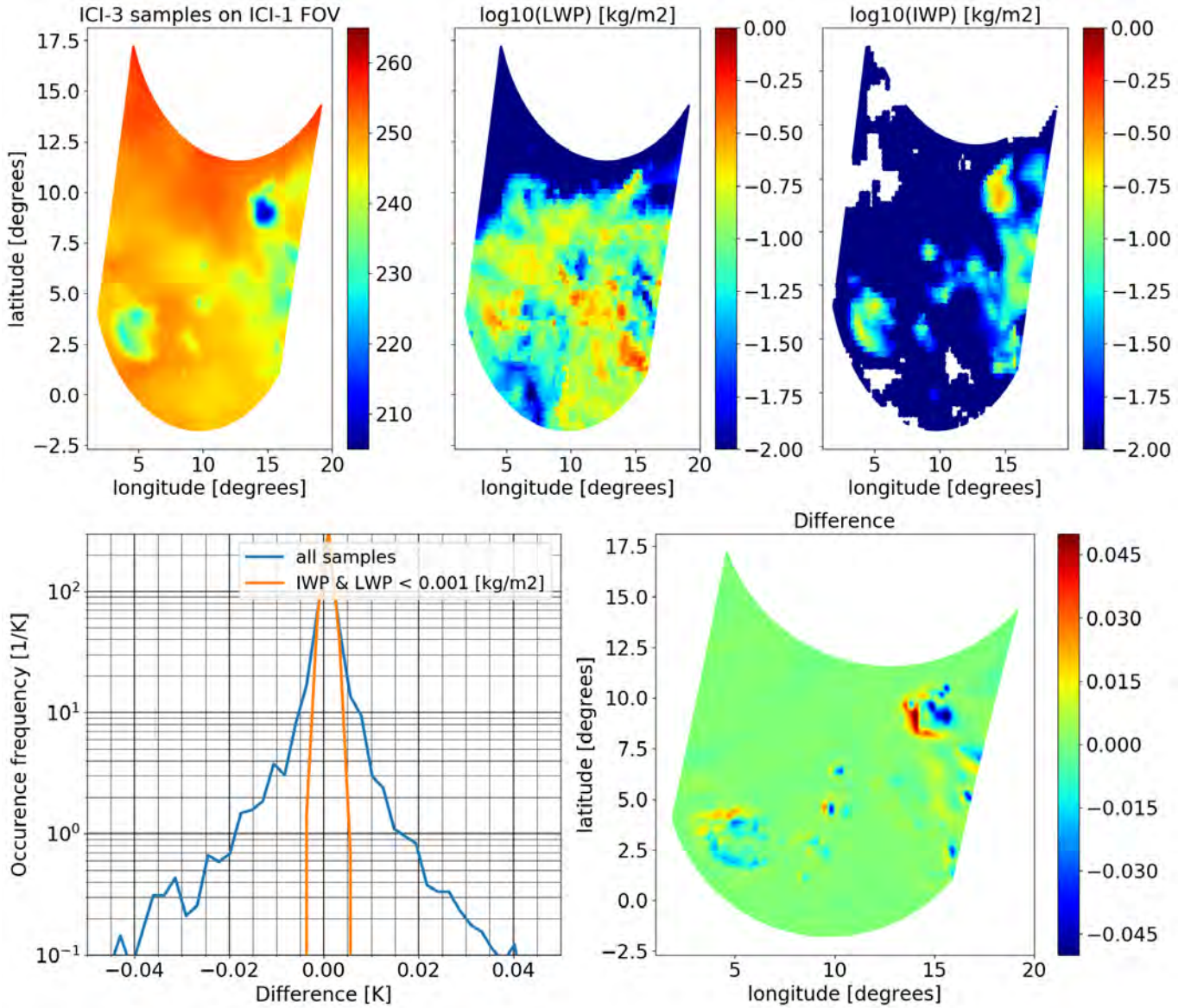
Figure 86: ICI-3 samples remapped to ICI-1 FOV for a cloudy scene. Upper left panel shows "true" antenna temperatures, and upper middle and right panel shows liquid and ice water path of the scene, respectively. The right bottom panel shows the difference (remapped - "true"), and the left bottom panel shows the frequency of occurrence of various differences. The unit associated to the colorbars is K.

	Backus-Gilbert footprint matching methodology applied on MWI and ICI observations	Code: TR/BG/MWI-ICI
		Issue: 1.0
		Date: June 5, 2019
		File: optimal-interpolation-applied.tex
		Page: 182 / 200
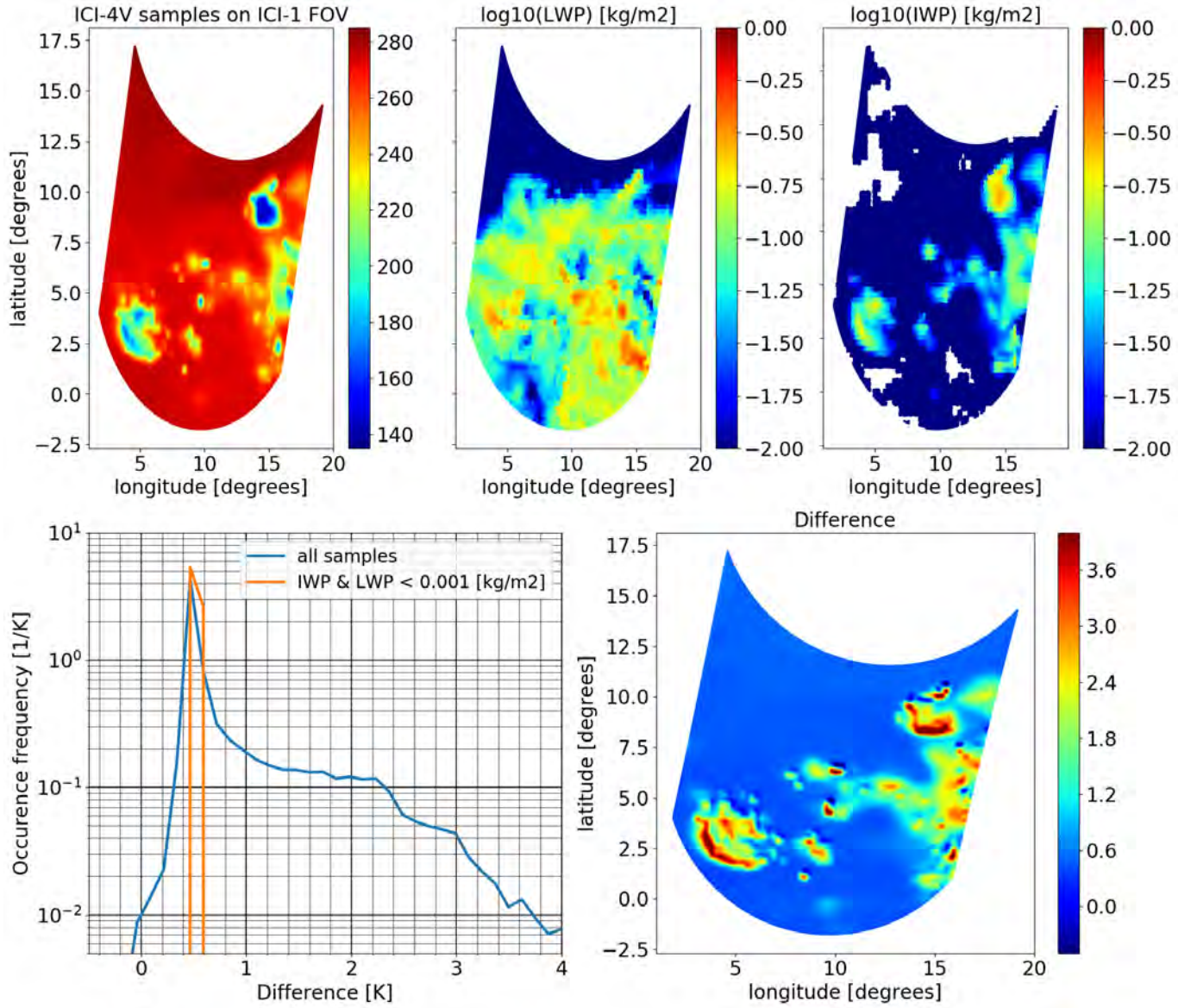
Figure 87: As Figure 86 but for ICI-4V.

	Backus-Gilbert footprint matching methodology applied on MWI and ICI observations	Code:	TR/BG/MWI-ICI
		Issue:	1.0
		Date:	June 5, 2019
		File:	optimal-interpolation-applied.tex
		Page:	183 / 200

Figure 88: As Figure 86 but for ICI-5.

	Backus-Gilbert footprint matching methodology applied on MWI and ICI observations	Code:	TR/BG/MWI-ICI
		Issue:	1.0
		Date:	June 5, 2019
		File:	optimal-interpolation-applied.tex
		Page:	184 / 200

Figure 89: As Figure 86 but for ICI-11V.

Figure 90: Derivative of brightness temperature as function of viewing angle from nadir for a tropical atmosphere containing a cloud layer around 12 Km and for a frequency of 246 GHz

10.3.3 Impact of BG convolution on L2 cloud retrieval

It has been shown that samples from all ICI channels can be remapped onto ICI-1 FOVs for scan angles between about 59° to -59°. The effective noise of the remapped observations are here well below the required Level1B noise levels for all channels.

A bias-free convolution has been demonstrated as long as the remapping does not involve a change in incidence angle. However, the incidence angles of the dual polarized ICI-4 and ICI-11 channels differs by about 2° relative to that of ICI-1 and this results in non negligible biases even for cloud free conditions. The reason for this is primarily due to the fact that atmospheric transmission varies with incidence angle and this is not taken into account by the Backus-Gilbert footprint resampling methodology.
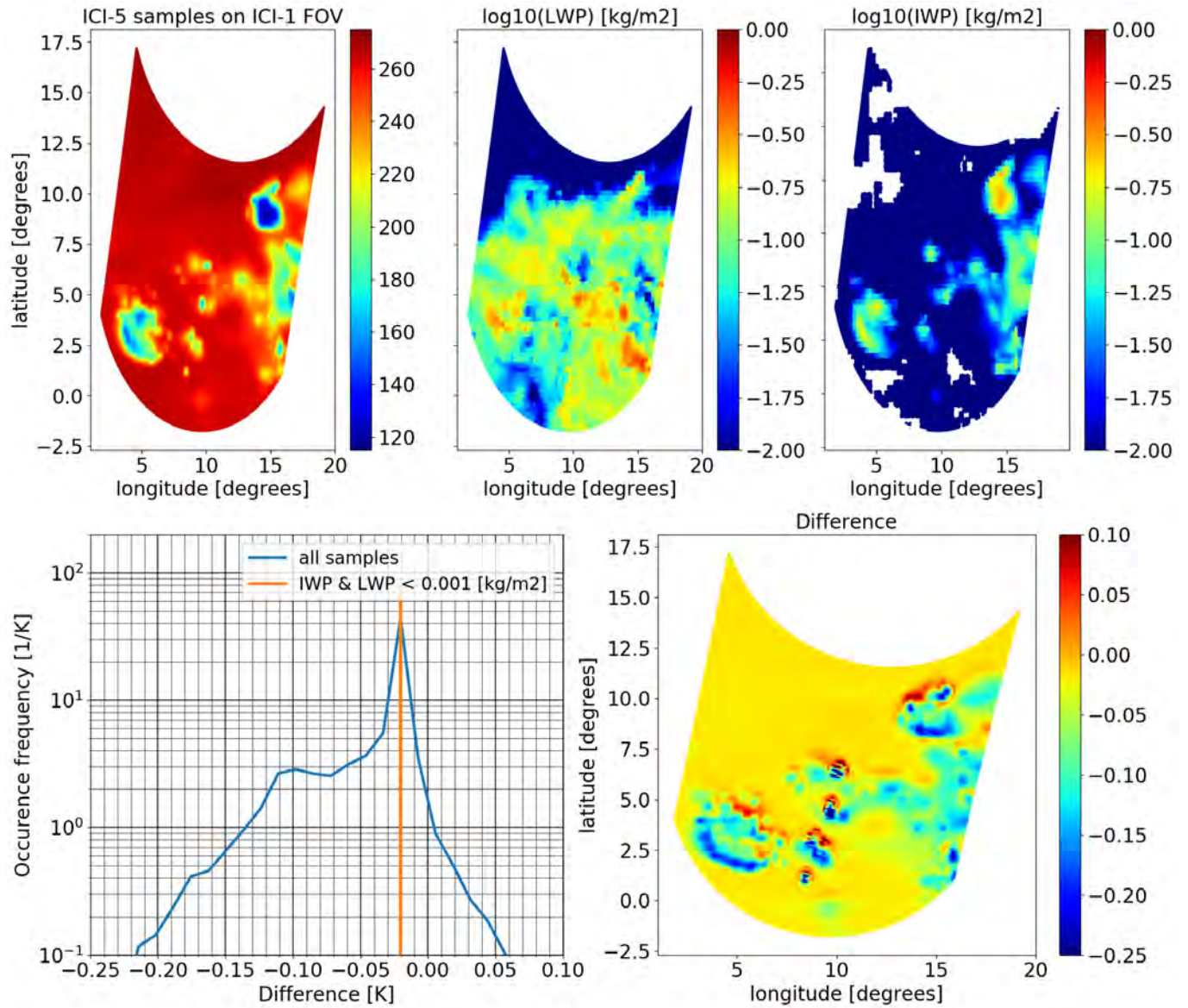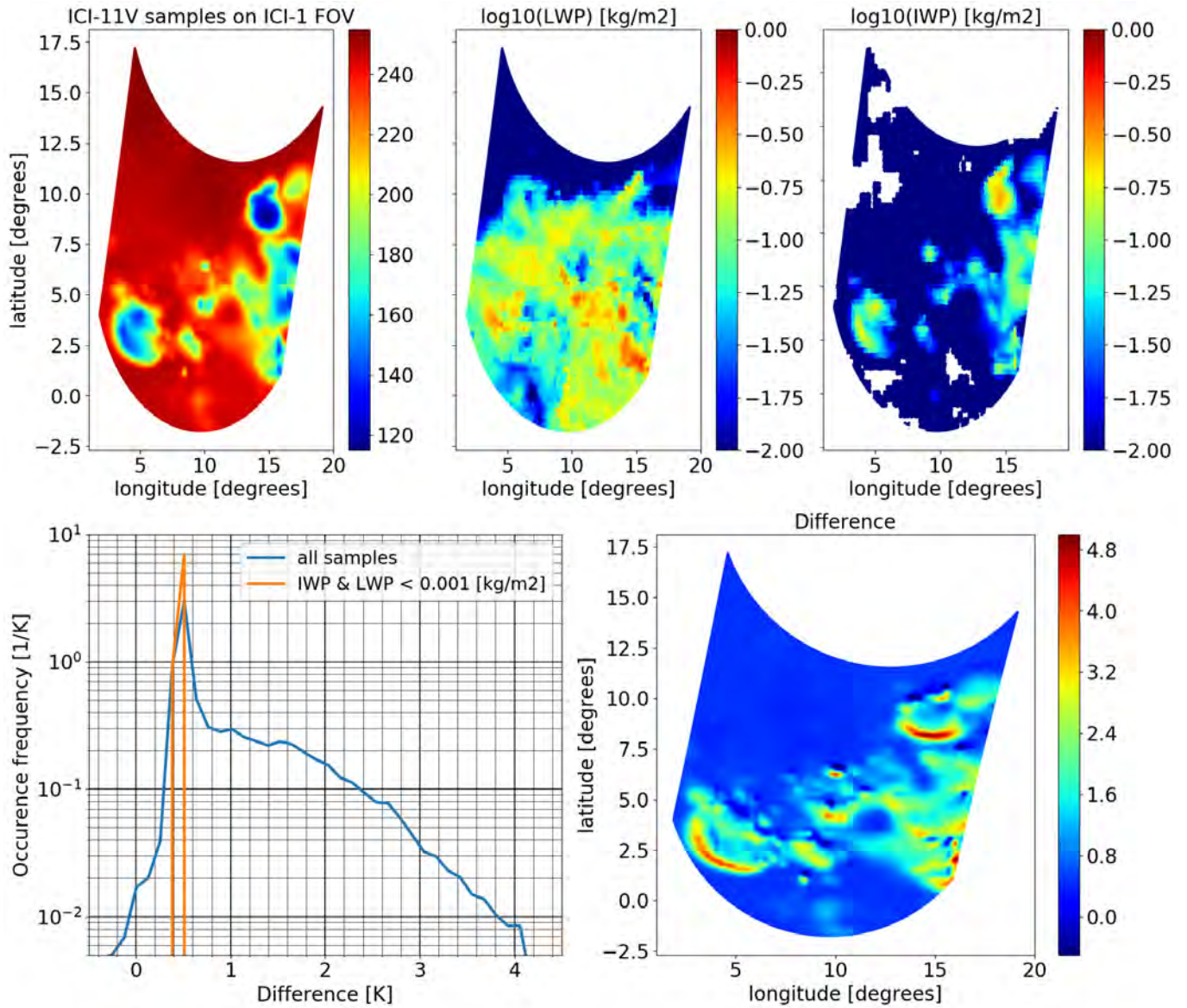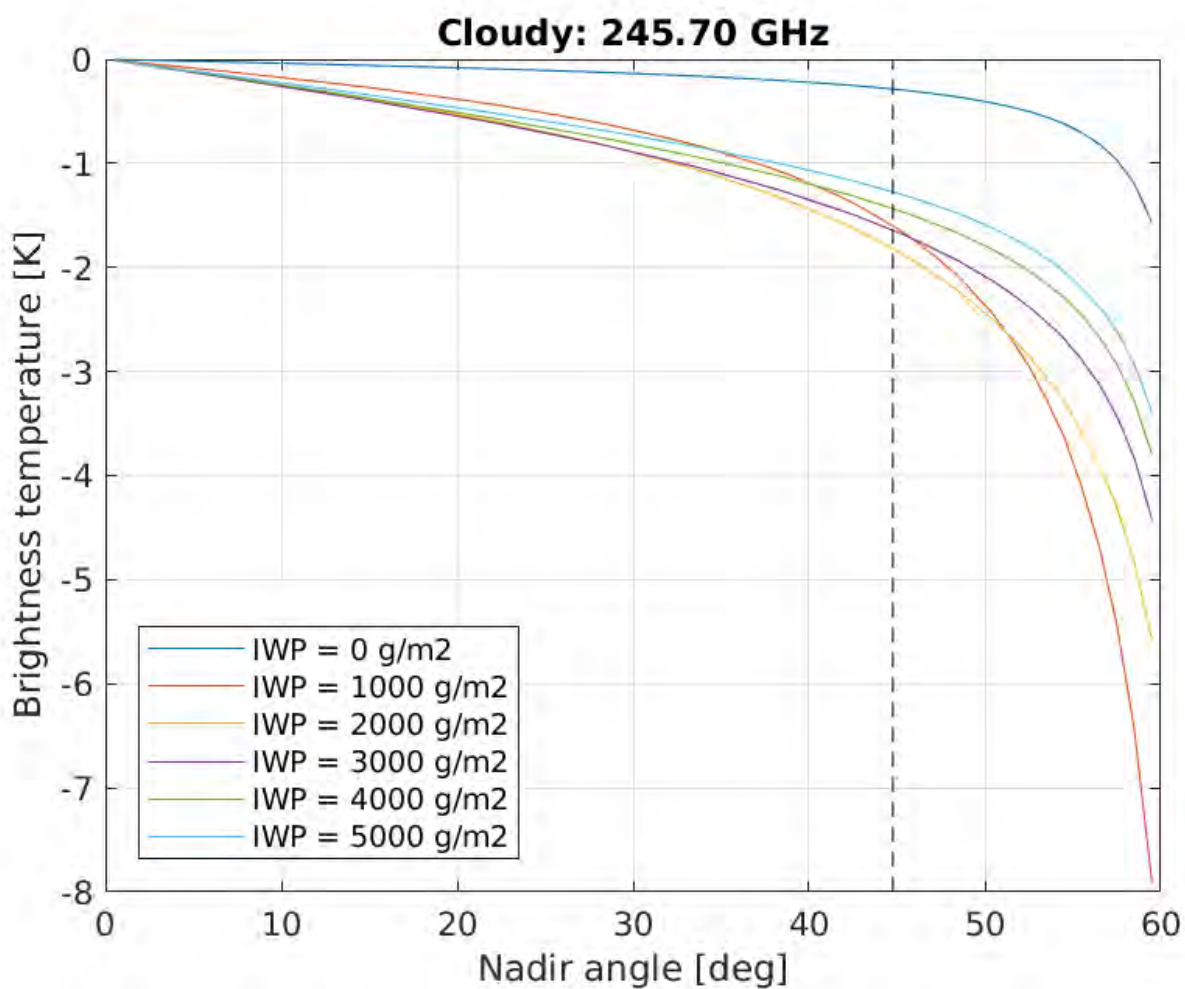
The cloud free bias were found to be state dependent, but no significant inter-FOV biases (or scan position dependent biases) were found for any channel within the ICI-1 scan angle range of 59° to -59°.

Clouds within the FOV can have a non negligible influence, on top of the cloud free bias. Cloud ice will have an impact both through a "pure" incidence angle difference effect (up to about 2 K for ICI-4 and ICI-11 channels) that applies to a homogeneous cloud layer, but also at the edges of areas with hydrometeors where even higher errors were found. This is also related to differences in viewing angles, and due to the fact that slightly different parts of the atmosphere may be observed by the the target channel and the samples convolved to the target FOV. This gives primarily that samples around cloud system edges may be biased (low or high).

Biases described above should be taken into account of in Level2 processing. The ICI retrieval algorithm is based on a precalculated retrieval database consisting of synthetic states and corresponding simulated ICI observations. The bias related to the pure incidence angle difference effect, that applies to a homogeneous state, should be possible to take into account of by applying the original incidence angle of each channel when generating the retrieval database. The bias related to the fact that slightly different parts of the atmosphere are observed by the various channels and for a given FOV is a bit more challenging to take into account. The ICI channel and scanning characteristic can potentially be taken into account when generating this retrieval database, but this requires that the simulation is based on 3-dimensional varying states. Alternatively, the bias can be taken into account of by increasing the noise values for the ICI-4 and ICI-11 channels in the retrieval calculation.

	Backus-Gilbert footprint matching methodology applied on MWI and ICI observations	Code:	TR/BG/MWI-ICI
		Issue:	1.0
		Date:	June 5, 2019
		File:	optimal-interpolation-applied.tex
		Page:	187 / 200

10.4   MWI and ICI

10.4.1   Cloud free condition

Here we focus on estimate inter-channel biases between samples from ICI-1 / MWI-14, ICI-2 / MWI-17, and ICI-3 / MWI-18 convolved to the ICI-1 FOV. These pairs of channels are overlapping in frequency range, and are, hence, handy to compare in a Cal/Val activity. MWI samples were remapped to the FOV of ICI-1 for sample positions $1, 4, ..., 784$ using weighting coefficients with characteristic described in Sect.9.4. It was assumed that the start time of each MWI and ICI scan was synchronized.

Figure 91 and 92 show biases between these pairs of channels for a scene covering ocean and land, respectively. It can be noted that ICI "observations" are a bit warmer ($\sim$0.06 - 0.15[K]) than that of MWI, that is due to that ICI samples having a lower incidence angle. A given scene is seen is seen by a slightly greater ($\sim$0.3[°]) incidence angle by the MWI channels compared to the ICI channels. It can be seen that the inter-channel bias is state dependent, and fairly correlated between the pairs of channels.

Figure 93 and 93 show the bias as function of scan position for these channels for ocean and land, respectively. For the ocean scene no scan position bias is observed, while a slope ($\sim$0.04[K] across the scan) is seen for the land scene, for ICI-1 / MWI-14. However, as this slope only can be seen for ICI-1 / MWI-14 this is likely to be related to the bias generated by the scene variation. It is anyhow a relatively small variation.

	Backus-Gilbert footprint matching methodology applied on MWI and ICI observations	Code:	TR/BG/MWI-ICI
		Issue:	1.0
		Date:	June 5, 2019
		File:	optimal-interpolation-applied.tex
		Page:	188 / 200

Figure 91: Bias between samples from ICI-1 / MWI-14, ICI-2 / MWI-17, and ICI-3 / MWI-18 remapped to ICI-1 FOV, based on simulation of a section of Metop-A orbit 4655 (2007-09-12) over southern part of Atlantic Ocean. Left and middle column show ICI and MWI antenna temperature, respectively, and the right column shows the difference (MWI - ICI). The unit associated to the colorbars is K.

	Backus-Gilbert footprint matching methodology applied on MWI and ICI observations	**Code:** TR/BG/MWI-ICI
		Issue: 1.0
		Date: June 5, 2019
		File: optimal-interpolation-applied.tex
		Page: 189 / 200
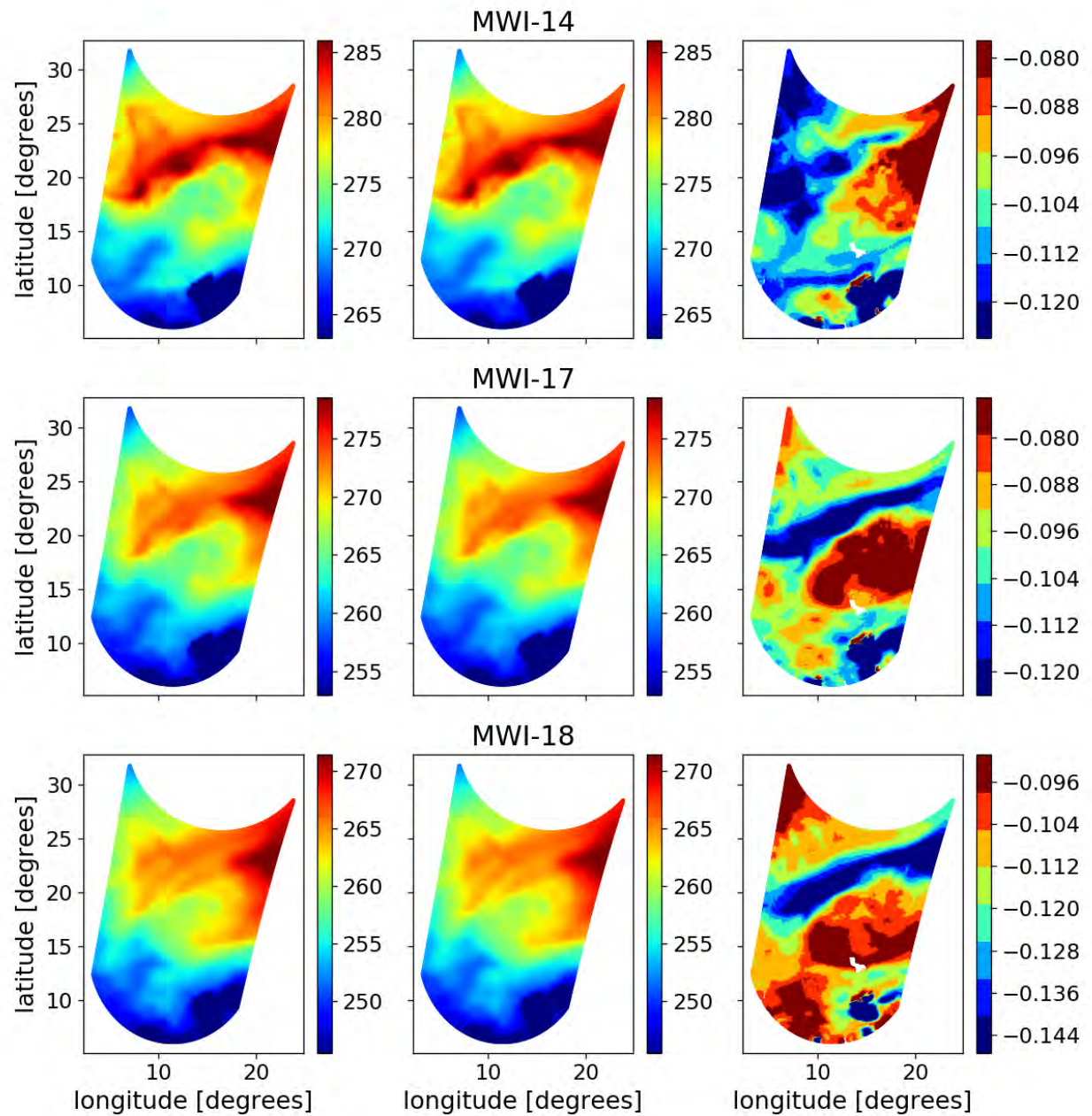
Figure 92: As Figure 91 but showing data for a scene over Africa.

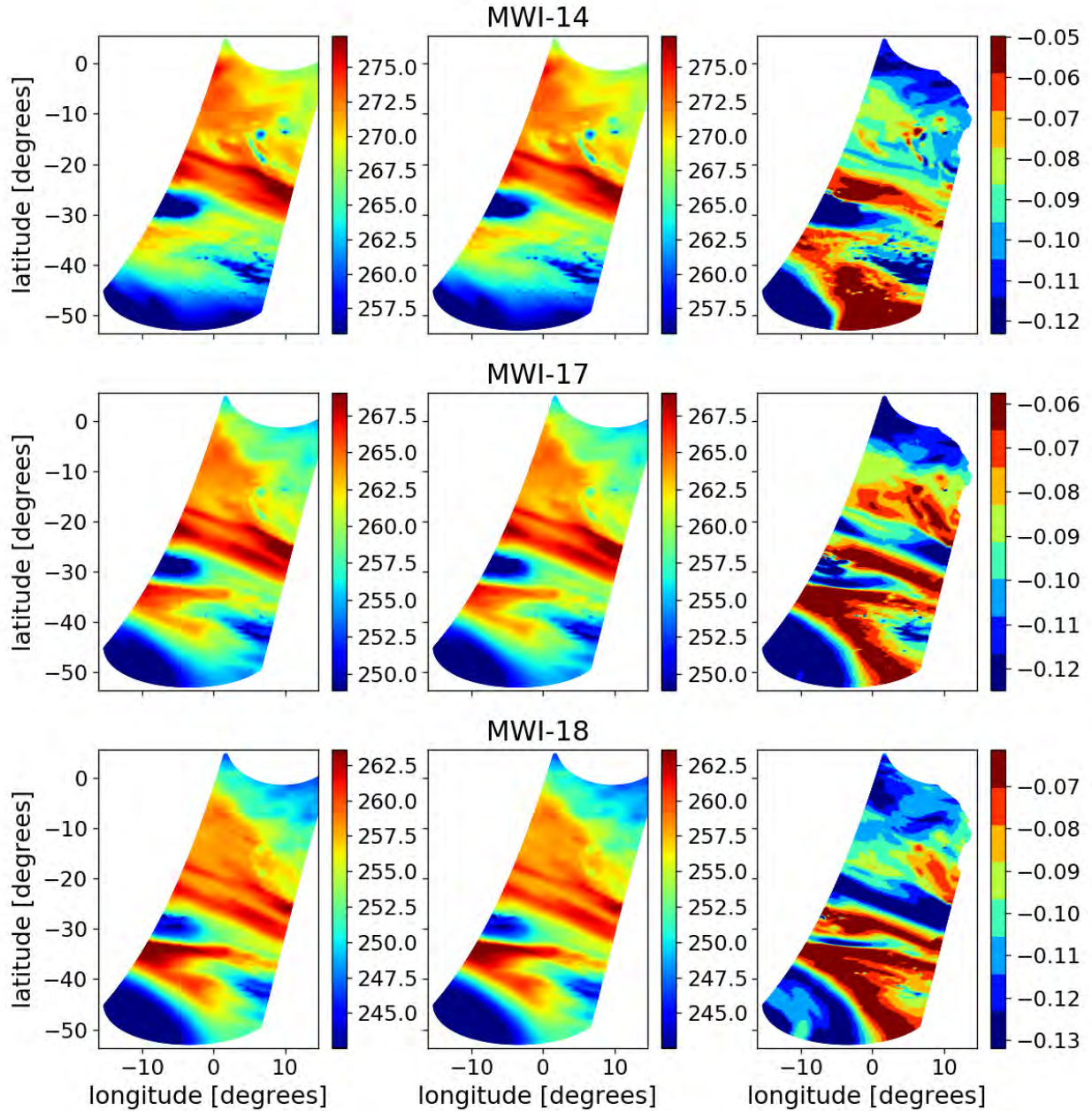|	**Backus-Gilbert footprint matching methodology applied on MWI and ICI observations**	Code: TR/BG/MWI-ICI
		Issue: 1.0
		Date: June 5, 2019
		File: optimal-interpolation-applied.tex
		Page: 190 / 200
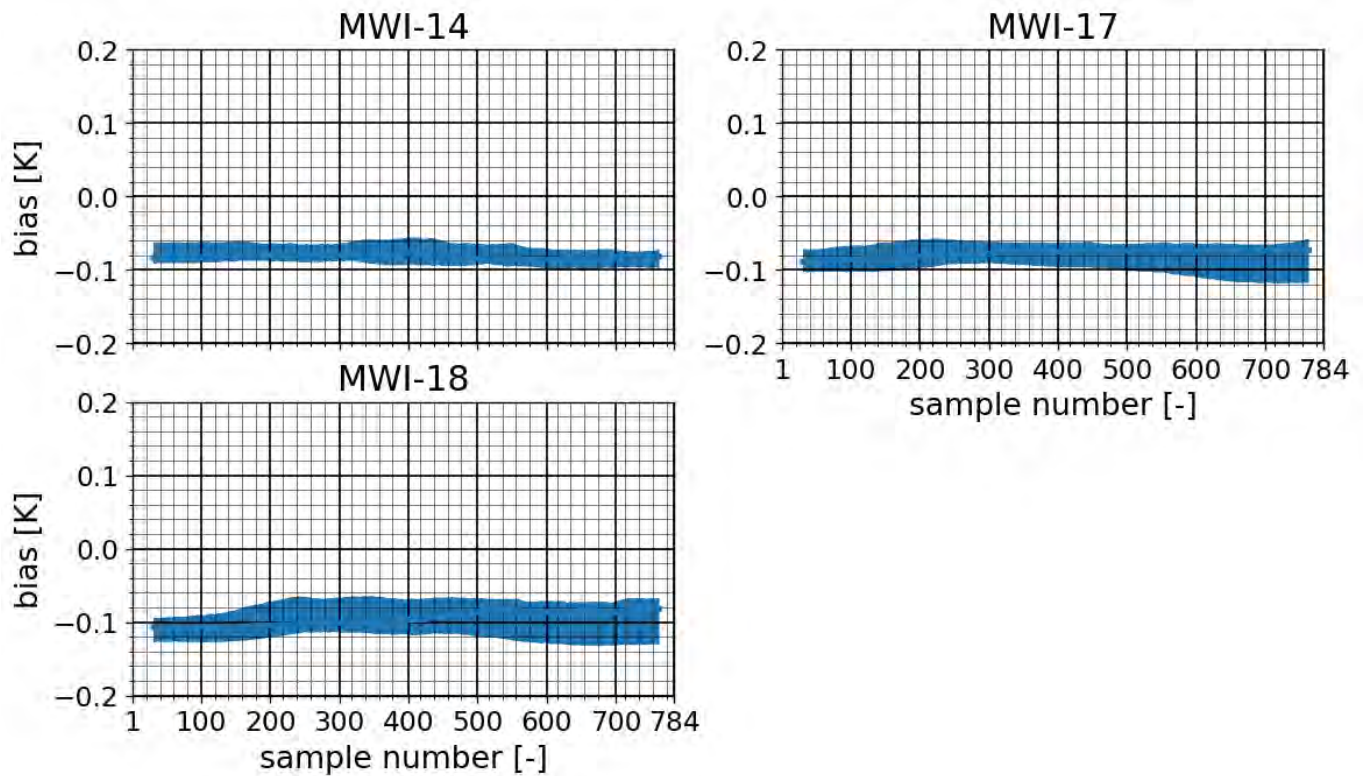
Figure 93: Bias between samples from ICI-1 / MWI-14, ICI-2 / MWI-17, and ICI-3 / MWI-18 channels remapped to ICI-1 FOV as function of scan position for simulated observation over southern part of Atlantic Ocean (see Figure 91). The lower and upper bounds of the shaded area corresponds to the 16th to 84th percentile of the data points, respectively (corresponding to $\pm 1\sigma$).

	Backus-Gilbert footprint matching methodology applied on MWI and ICI observations	Code: TR/BG/MWI-ICI
		Issue: 1.0
		Date: June 5, 2019
		File: optimal-interpolation-applied.tex
		Page: 191 / 200
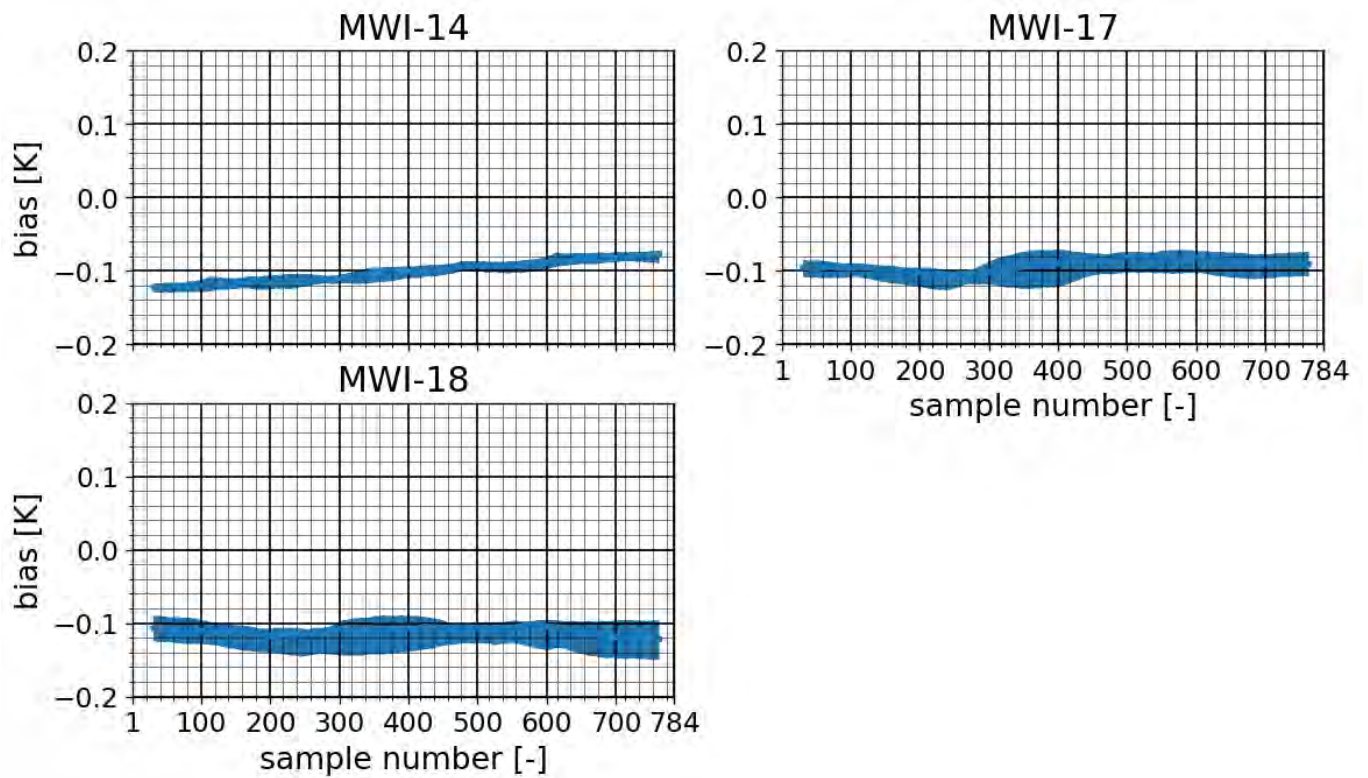
Figure 94: As Figure 83 but showing data for a scene over Africa (see Figure 92).

10.4.2   Impact of cloud on biases

Figure 95 to Figure 97 show comparisons between "true" and remapped samples for a cloudy scene (over Africa and Atlantic ocean) for ICI-1 / MWI-14, ICI-2 / MWI-17, and ICI-3 / MWI-18. In general, the cloud induced bias is highly correlated for the three combination of channels, although the magnitude of the bias is somewhat greater for ICI-1 / MWI-14 compared to the two others. Similar biases as seen in Figure 95 to Figure97 was explained Sect. 10.4 for the pure ICI to ICI-1 remapping.
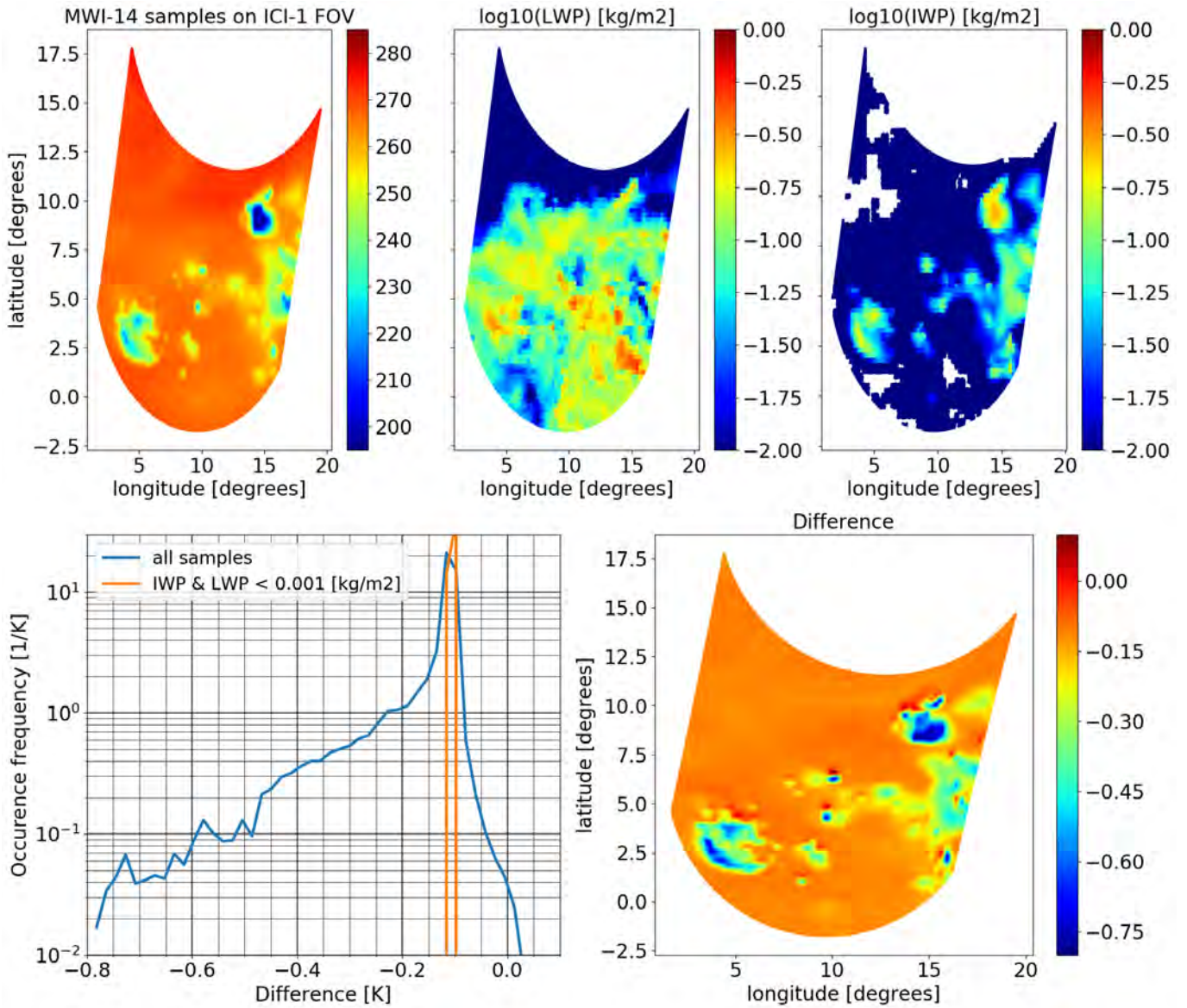
Figure 95: MWI-14 samples remapped to ICI-1 FOV for a cloudy scene. Upper left panel shows "true" antenna temperatures, and upper middle and right panel shows liquid and ice water path of the scene, respectively. The right bottom panel shows the difference (MWI-14 - ICI-1), and the left bottom panel shows the frequency of occurrence of various differences. The unit associated to the colorbars is K.

	Backus-Gilbert footprint matching methodology applied on MWI and ICI observations	Code:	TR/BG/MWI-ICI
		Issue:	1.0
		Date:	June 5, 2019
		File:	optimal-interpolation-applied.tex
		Page:	194 / 200
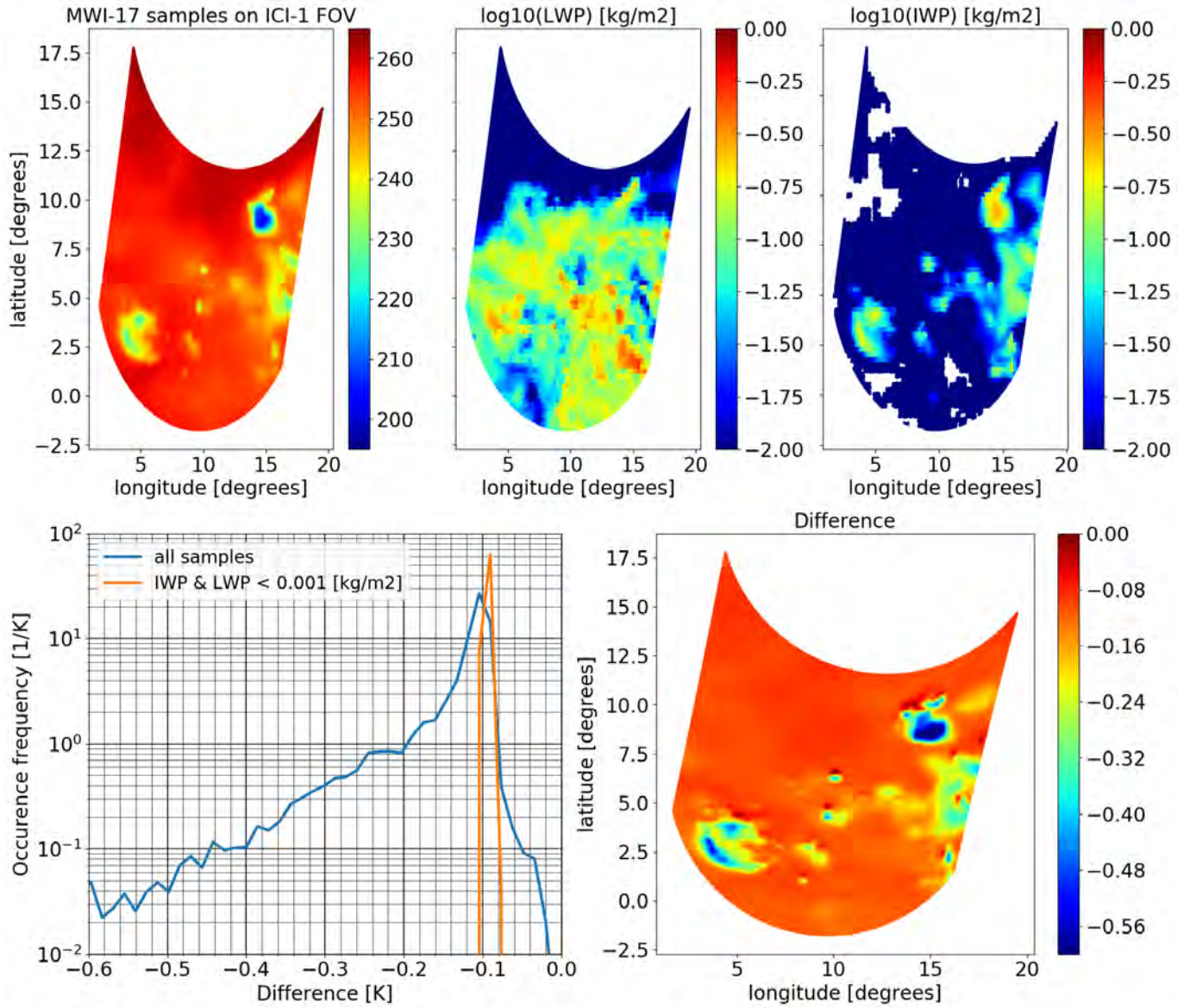
Figure 96: As Figure 95 but for ICI-2 / MWI-17.

	Backus-Gilbert footprint matching methodology applied on MWI and ICI observations	Code:	TR/BG/MWI-ICI
		Issue:	1.0
		Date:	June 5, 2019
		File:	optimal-interpolation-applied.tex
		Page:	195 / 200
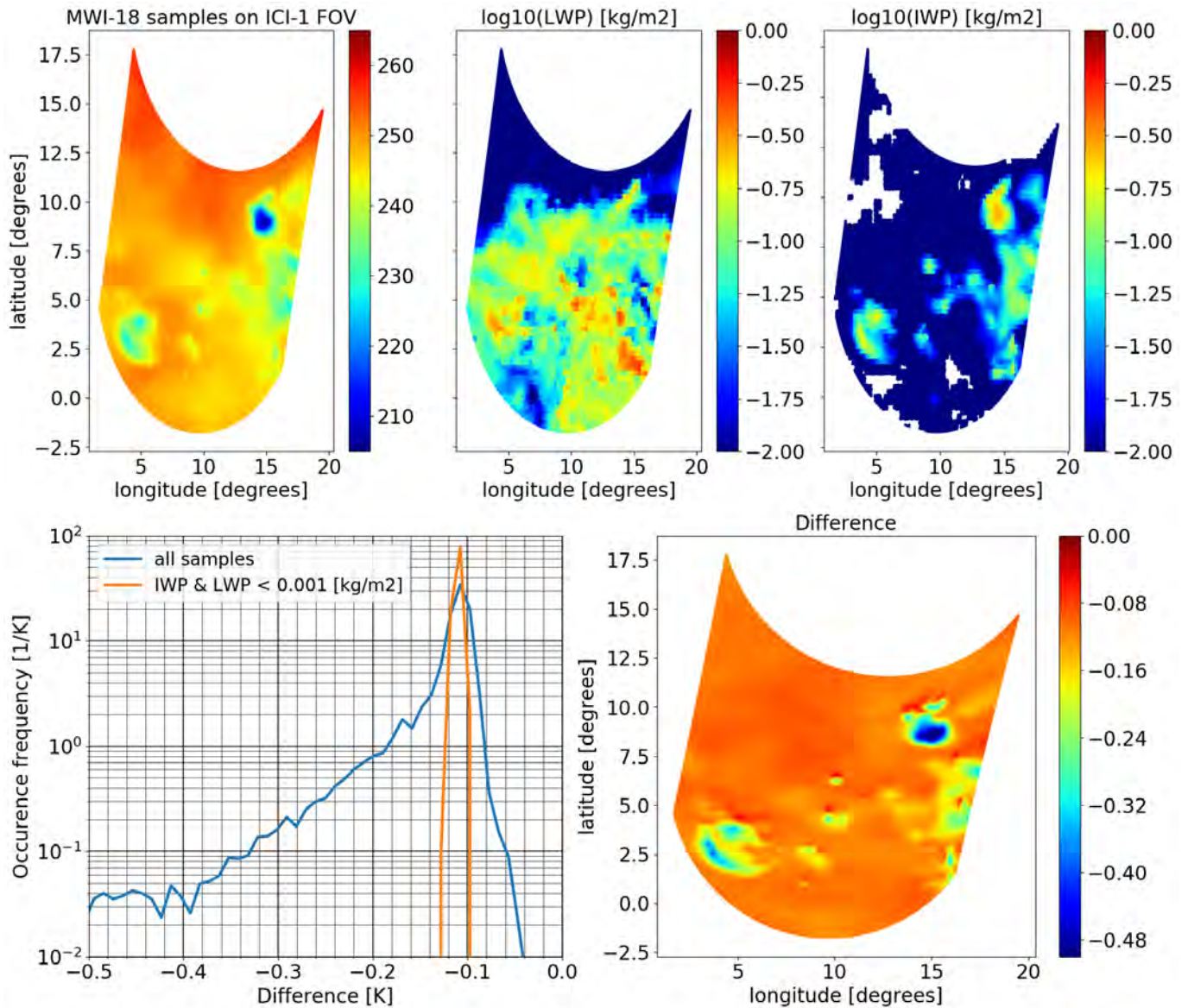
Figure 97: As Figure 95 but for ICI-3 / MWI-18.

	Backus-Gilbert footprint matching methodology applied on MWI and ICI observations	Code:	TR/BG/MWI-ICI
		Issue:	1.0
		Date:	June 5, 2019
		File:	optimal-interpolation-applied.tex
		Page:	196 / 200

References

S. J. Abel and I. A Boutle. An improved representation of the raindrop size distribution for single-moment microphysics schemes. *J. Quant. Spectrosc. Radiat. Transfer*, 128:2152–2162, 2012. doi: 10.1002/qj.1949.

Filipe Aires, Catherine Prigent, Frédéric Bernardo, Carlos Jiménez, Roger Saunders, and Pascal Brunel. A tool to estimate land-surface emissivities at microwave frequencies (telsem) for use in numerical weather prediction. *Q. J. R. Meteorol. Soc.*, 137(656):690–699, 2011.

G. Backus and F. Gilbert. Uniqueness in the inversion of inaccurate gross Earth data. *Phil. Trans. R. Soc. Lond. A*, 266(1173):123–192, 1970.

R. Bennartz. Optimal convolution of AMSU-B to AMSU-A. *J. Atmos. Oceanic Technol.*, 17: 1215–1225, 2000. doi: 10.1175/1520-0426(2000)017⟨1215:OCOABT⟩2.0.CO;2.

S. A. Buehler, J. Mendrok, P. Eriksson, A. Perrin, R. Larsson, and O. Lemke. ARTS, the Atmospheric Radiative Transfer Simulator – version 2.2, the planetary toolbox edition. *Geosci. Model Dev.*, 11(4):1537–1556, 2018. doi: 10.5194/gmd-11-1537-2018.

WJ Ellison. Permittivity of pure water, at standard atmospheric pressure, over the frequency range 0–25 thz and the temperature range 0–100 c. *Journal of physical and chemical reference data*, 36(1):1–18, 2007.

P. Eriksson, S. A. Buehler, C. P. Davis, C. Emde, and O. Lemke. ARTS, the atmospheric radiative transfer simulator, version 2. *J. Quant. Spectrosc. Radiat. Transfer*, 112:1551–1558, 2011. doi: 10.1016/j.jqsrt.2011.03.001.

P. Eriksson, R. Ekelund, J. Mendrok, M. Brath, O. Lemke, and S. A. Buehler. A general database of hydrometeor single scattering properties at microwave and sub-millimetre wavelengths. *Earth Syst. Sci. Data*, 10(3):1301–1326, 2018. doi: 10.5194/essd-10-1301-2018.

K. F. Evans and G. L. Stephens. Microwave radiative transfer through clouds composed of realistically shaped ice crystals. Part ii: remote sensing of ice clouds. *J. Atmos. Sci.*, 52: 2058–2072, 1995.

P. R. Field, A. J. Heymsfield, and A. Bansemer. Snow size distribution parameterization for midlatitude and tropical ice clouds. *J. Atmos. Sci.*, 64:4346–4365, 2007. doi: 10.1175/2007JAS2344.1.

S. Fox, J. Mendrok, P. Eriksson, R. Ekelund, S. J. O'Shea, K. N. Bower, R. C. Harlow, and J. C. Pickering. Airborne validation of radiative transfer modelling of ice clouds at millimetre and sub-millimetre wavelengths. *Atmos. Meas. Tech. Discuss.*, 2018:1–29, 2018. doi: 10.5194/amt-2018-308.

A. J. Geer and F. Baordo. Improved scattering radiative transfer for frozen hydrometeors at microwave frequencies. *Atmos. Meas. Tech.*, 7:1839–1860, 2014. doi: 10.5194/amt-7-1839-2014.

	Backus-Gilbert footprint matching methodology applied on MWI and ICI observations	Code:	TR/BG/MWI-ICI
		Issue:	1.0
		Date:	June 5, 2019
		File:	optimal-interpolation-applied.tex
		Page:	197 / 200

P. C. Hansen and D. P. O'Leary. The use of the L-curve in the regularization of discrete ill-posed problems. *SIAM J. Sci. Comput.*, 14(6):1487–1503, 1993. doi: 10.1137/0914086.

T. Maeda and Y. Taniguchi K. Imaoka. GCOM-W1 AMSR2 level 1R product: Dataset of brightness temperature modified using the antenna pattern matching technique. *IEEE Geosci. Remote Sens.*, 54:770–782, 2016.

C Prigent, F Aires, D Wang, S Fox, and C Harlow. Sea-surface emissivity parametrization from microwaves to millimetre waves. *Quarterly Journal of the Royal Meteorological Society*, 143 (702):596–605, 2017.

P. W. Rosenkranz. Absorption of microwaves by atmospheric gases. In M. A. Janssen, editor, *Atmospheric remote sensing by microwave radiometry*, pages 37–90. John Wiley & Sons, Inc., 1993.

P. W. Rosenkranz. Water vapor microwave continuum absorption: A comparison of measurements and models. *Radio Sci.*, 33(4):919–928, 1998. (correction in 34, 1025, 1999), ftp://mesa.mit.edu/phil/lbl_rt.

B. Rydberg and P. Eriksson. Simulation of MWI and ICI level1b data. Technical report, Molflow, 2018.

A. Stogryn. Estimates of brightness temperatures from scanning radiometer data. *IEEE Trans. Antennas Propag.*, AP-26(5):720–726, 1978.

D. A. Vallado, P. Crawford, R. Hujsak, and T.S. Kelso. Revisiting spacetrack report 3. Technical report, AIAA 2006-6753, 2006. URL https://celestrak.com/publications/AIAA/2006-6753/AIAA-2006-6753-Rev2.pdf.

Appendices

	Backus-Gilbert footprint matching methodology applied on MWI and ICI observations	**Code:** TR/BG/MWI-ICI
		Issue: 1.0
		Date: June 5, 2019
		File: optimal-interpolation-applied.tex
		Page: 198 / 200

A   File format description

A.1   Orbit/Scan file

The orbit/scan file is saved as netcdf format database file and described in Table 16. To allow for a simplification (or speed up) of the generation of antenna temperatures a variable named *group* (size = channel) is introduced. For ICI group = [1, 1, 1, 2, 3, 4, 4, 4, 5, 5, 5, 6, 7], and hence seven different groups of channels are defined. Each group share a common antenna pattern function and have approximately identical viewing directions for a given sample in a gviven scan. The calculation of antenna temperatures from swath Tb data can be done in parallell for channels from a common group.

A.2   Antenna temperature file

The antenna temperature file is connected to the orbit/scan file and is saved as netcdf format database file and described in Table 17.

A.3   Orbit state vector file

The orbit state vector file is connected to the orbit/scan file and is saved as netcdf format database file and described in Table 18.

Table 16: Orbit/scan file description.

Attributes	Type	Description
instrument	char	MWI or ICI
orbit	char	orbit number
start_time	char	start time of first scan (YYYY-MM-DDThh:mm:ss)

Dimension	Length	Description
channel	13 / 26	number of unique channels (13 / 26 for ICI / MWI)
scan	e.g 4591	number of scans in orbit
sample	784 / 1402	number of samples in a scan (784 / 1402 for ICI / MWI)
string	14	number of characters in string data
theta	201	number of theta angles in antenna_pattern
phi	201	number of phi angles in antenna_pattern

Variable(Dimension)	Type	Description
channel(channel)	int	channel number
group(channel)	int	group number (see text for moee details)
scan_number(scan)	int	scan number
sample_number(sample)	int	sample number
polarisation(channel)	char	V or H
frequency(channel, string)	char	channel frequency
theta(theta)	float	elevation angle grid of antenna pattern (-10 - 10)
phi(phi)	float	azimuth angle grid of antenna pattern (-10 - 10)
time(channel, scan, sample)	double	acquisition_time: milliseconds since start_time
latitude(channel, scan, sample)	float	sensor geodetic latitude (-90 - 90)
longitude(channel, scan, sample)	float	sensor geodetic longitude (-180 - 180)
altitude(channel, scan, sample)	float	sensor geodetic altitude [km]
azimuth_angle(channel, scan, sample)	float	line of sight azimuth angle (0 - 360 Degrees), 0 = North, 90 = East, 180 = South, 270 = West
zenith_angle(channel, scan, sample)	float	line of sight zenith angle (Degrees), 0 = zenith, 180 = towards Earth center
geoloc_latitude(channel, scan, sample)	float	geodetic latitude of geolocation, or point of observation (-90 - 90)
geoloc_longitude(channel, scan, sample)	float	geodetic longitude of geolocation, or point of observation (-180 - 180)
geoloc_solar_za(channel, scan, sample)	float	solar zenith angle at point of observation (degrees)
geoloc_solar_az(channel, scan, sample)	float	solar azimuth angle at point of observation (degrees)
geoloc_satellite_za(channel, scan, sample)	float	satellite zenith angle at point of observation (degrees)
geoloc_satellite_az(channel, scan, sample)	float	satellite azimuth angle at point of observation (degrees)
pitch(channel, scan, sample)	float	platform pitch angle (degrees)
roll(channel, scan, sample)	float	platform roll angle (degrees)
yaw(channel, scan, sample)	float	platform yaw angle (degrees)
antenna_pattern(channel, phi, theta)	double	antenna pattern, normalised such that the integral over the unit sphere is 1

	Backus-Gilbert footprint matching methodology applied on MWI and ICI observations	Code:	TR/BG/MWI-ICI
		Issue:	1.0
		Date:	June 5, 2019
		File:	optimal-interpolation-applied.tex
		Page:	200 / 200

Table 17: Antenna temperature file description.

Attributes	Type	Description
instrument	char	MWI or ICI
orbit	char	orbit number
channel	char	channel number
Dimension	**Length**	**Description**
scan	4591	
sample	784	
Variable(Dimension)	**Type**	**Description**
TA(scan, sample)	float	Antenna Brightness Temperature [K]

Table 18: Orbit state vector file description.

Attributes	Type	Description
instrument	char	MWI or ICI
orbit	char	orbit number
start_time	char	start time of first scan (YYYY-MM-DDThh:mm:ss)
Dimension	**Length**	**Description**
channel	13 / 26	number of unique channels (13 / 26 for ICI / MWI)
scan	e.g 4591	number of scans in orbit
sample	784 / 1402	number of samples in a scan (784 / 1402 for ICI / MWI)
space	3	x,y,z coordinates
Variable(Dimension)	**Type**	**Description**
r_spacecraft(channel, scan, sample, space)	float	Spacecraft location in ECEF coordinates
v_spacecraft(channel, scan, sample, space)	float	Spacecraft velocity in ECEF coordinates